ISSN 1590-2595

quaderni di geofisica

n. 35

Preliminary Results from the EPOT Project

TECHNOLOGICAL INNOVATION AND AUTOMATION IN THE INTEGRATED APPLICATIONS OF ELECTROMAGNETIC AND POTENTIAL FIELD METHODS IN ACTIVE VOLCANIC AREAS

Papers Presented at the Second Year Workshop

Edited by
Ciro Del Negro

Istituto Nazionale di Geofisica e Vulcanologia

2004

PRELIMINARY RESULTS FROM THE EPOT PROJECT

Technological innovation and automation in the integrated applications of electromagnetic and potential field methods in active volcanic areas

Papers Presented at the Second Year Workshop

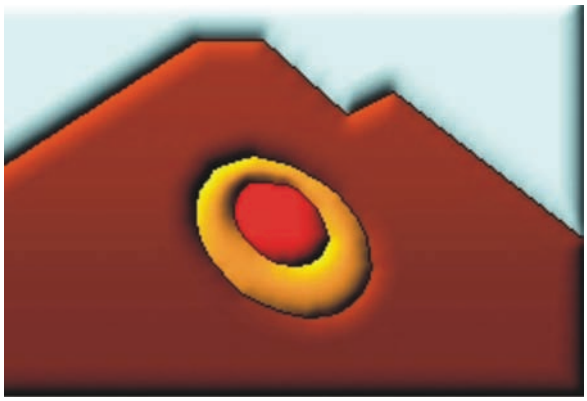

Edited by
Ciro Del Negro

Istituto Nazionale di Geofisica e Vulcanologia, Catania, Italy

Table of Contents

Preface: The EPOT Project

This special issue of "Quaderni di Geofisica" collects proceedings from the Second Year Workshop of the Coordinated Project "Technological innovation and automation in the integrated applications of electromagnetic and potential field methods in active volcanic areas" (EPOT) organized at Catania on December 13, 2002. The EPOT project was supported by Dipartimento di Protezione Civile in the frame of the GNV Programme 2000-2003 of the INGV. This research began as a joint project between Research Institutes and Universities with the aim of improving the investigative capability of electromagnetic and potential field methods in their various possible applications in active volcanic areas. Progress achieved in the geophysics of volcanoes over the past few decades, and the rapid technological development of recent years, have made a decisive effort both possible and necessary to introduce automation and a multi-methodological approach as fundamental for the monitoring of active volcanoes. The integrated approach is probably the only procedure capable of giving a global response to the volcanological problem and to minimize interpretative ambiguities. In order to achieve these objectives we have been working to strongly improve the investigative power of the electromagnetic and potential field methods through: (a) development of suitable methods of integrated inversion, (b) application of advanced technologies to process continuously recorded signals, and (c) automation of monitoring and management systems and of surveys in real time.

The EPOT project, though centrally coordinated, is separated in 10 Research Units characterized by homogeneous objectives. The activity reports offer a good summary of the on-going activities in the three main tasks. The project appears to be moving successfully toward the achievement of the proposed goals. During this meeting all partners presented their preliminary results and discussion followed on how to ensure that the algorithms developed in this project are implemented in real-time monitoring procedures and may be used during volcano crises. I wish to thank the authors not only for their contributions but also for stimulating a fruitful discussion among participants. A comprehensive view of our present scientific knowledge on the advances in geophysical researches on major Italian volcanoes was provided. The web site for the project is available at the address: **http://maglab.ct.ingv.it/epot** since July 2002. It is maintained by Geomagnetism Laboratory of INGV-Sezione di Catania and provides updated information about the project, proposed architecture, meetings, etc.

I am grateful to all those who were co-opted for their expertise and to all those who provided time and energy in assisting in this project. Special thanks are expressed to the GNV Evaluation Committee, including Domenico Giardini of ETH Zurich, Gudmundur Sigvaldasson of NVO Rejkjavik, and Marjorie Wilson of Leeds University, for all their support and valuable contributions in setting the direction for this project.

I also wish to acknowledge here Enzo Boschi and Paolo Gasparini for having suggested the publication of workshop proceedings on "Quaderni di Geofisica".

We would like to express our gratitude to several colleagues for their collaborative efforts. Special thanks is addressed to the reviewers for their fine work: Salvatore Baglio (DIEES-University of Catania, Italy), Paolo Baldi (DF-University of Bologna, Italy), Tommaso Caltabiano (INGV-Catania, Italy), Daniele Carbone (INGV-Catania, Italy), Angelo De Santis (INGV-Roma, Italy), Maurizio Fedi (DST-University of Naples, Italy), Giovanni Florio (DST-University of Naples, Italy), Vincenzo Lapenna (IMAA-CNR, Italy), Adele Manzella (IGG-CNR, Italy), Giuseppe Nunnari (DIEES-University of Catania, Italy), Domenico Patella (DSF-University of Naples, Italy), Antonio Rapolla (DST-University of Naples, Italy), Andre Revil (CNRS-CEREGE, France), Agata Siniscalchi (DGG-University of Bari, Italy).

I am appreciative of the help given by all staff members of the Geomagnetism Laboratory of INGV-CT, and in particular by Rosalba Napoli for her editorial support and assistance throughout the production of the special issue.

Ciro Del Negro
Coordinator of EPOT

On the Resolution of Electromagnetic Induction Methods in Marine Exploration of Complex Volcanic Structures

Antonio Troiano[1], Zaccaria Petrillo[2], Maria Giulia Di Giuseppe[1] and Domenico Patella[1]

[1] *Department of Physical Sciences, University Federico II, Naples, Italy*
[2] *National Institute of Geophysics and Volcanology, Vesuvian Observatory, Naples, Italy*

Abstract

The realisation of a standard magnetotelluric (MT) sounding requires the measurements of the horizontal components of the local electric and magnetic fields on the Earth's surface in order to obtain the frequency-dependent apparent resistivity curve. The application of the MT method in marine research has, however, serious difficulties as for the measurement of the electric field in sea water. The magnetovariational (MV) method seems more appropriate, since only the magnetic components are measured at two different levels, generally the sea surface and the sea bottom. By these measurements it is possible to obtain MV apparent resistivity sounding curves against frequency, carrying similar information about the electrical structure underwater as with the MT method. Using the MV approach, the difficulties of the MT method are avoided, but a difficulty still exists owing to the motional noise of the magnetometer hanged near the sea surface. In order to eliminate this last inconvenience, a sea-to-ground magnetovariational (SGMV) method has recently been proposed, based on the mesurements of only the magnetic components at two different places, namely the sea bottom and a remote land station opportunely placed over a 1D structure. This paper investigates the capability of the SGMV method to resolve 2D and 3D prismatic bodies approximating a magma chamber placed beneath a sea-water layer, in view of an application to the Campi Flegrei caldera (Naples, Italy), in particular to the portion of the caldera extending offshore in the Gulf of Pozzuoli. The modelling, performed by a finite difference algorithm, has allowed a comparison to be made between the standard free-surface MT representations and similar MT images reconstructed by the SGMV approach. In all cases, the modelling has confirmed the general capability of the electromagnetic induction methods to resolve complex volcanic structures and the comparison has shown the reliability of the SGMV method in simulating MT soundings in marine environment.

Key words *electromagnetic induction – marine geophysical exploration - volcano geophysics*

1. Introduction

The application of magnetotellurics (MT) to the study of volcanoes on land has gained in recent years a key role for its high resolution power with virtually no limitation as to the depth of investigation, and for its relatively simpler field work which allows costs to be sensibly reduced. Great interest has also been given to the possibility of exporting the MT method offshore to detect magma chambers residing beneath the sea-water layer.

A pioneer approach to MT sounding with electric and magnetic sensors immersed in sea water at a depth of few tens of meters dates back to the late 50s of last century, but a series of technical problems have always made the application of standard MT a difficult task in marine environment. The main difficulty is related to the measurement of the electrical (**E**) field in sea water. On land, the **E**-field is approximated as the ratio of the potential drop across a pair of electrodes to the separation between them, which must be not less than 100 m, in order for the **E**-field to represent the dominant resistivity in the surface layer [Kaufman and Keller, 1981]. Obviously, the necessity of such a long bipole cannot easily be satisfied at sea.

A way to avoid the difficulty related to the electric line layout is the use of the magnetovariational (MV) method, which allows an MT-like apparent resistivity representation to be retrieved using only two magnetic sensors [Patella and Siniscalchi, 1994]. The two sensors are normally aligned vertically with the top one, $S^{(t)}$, close to the sea surface and the lower one, $S^{(b)}$, anchored at the sea bottom, as sketched in fig.1a. Nonetheless, a difficulty still arises related, this time, to the measurement of the magnetic (**H**) field, due to lack of stability of the top sensor $S^{(t)}$ hanging in sea water, generating records heavily contaminated by motional noise.

Recently, a new way has been paved to deal with electromagnetic (em) induction in marine research using the so called sea-to-ground magnetovariational (SGMV) layout [Patella et al., 1999]. The new layout consists in displacing the magnetic sensor at the air-water boundary from station $S^{(t)}$ to a remote site S_2 on land where the subsoil conforms to a 1D struc-

ture, as in fig.1b. Using the basic MT hypotheses that the total **H**-field at the surface of a 1D layered earth is two times the primary **H**-field, independently of the underlying 1D resistivity sequence [Kaufman and Keller, 1981] and that the primary **H**-field is uniform over largely extended areas [Zelwer and Morrison, 1972], a new MT-like apparent resistivity representation can be retrieved without incurring the previously mentioned limitations of the MT and MV methods [Patella et al., 1999]. The critical point of the SGMV method is the hypothesis that the subsoil below S_2 has to conform to a 1D structure. This can result in a restriction for the applicability of the SGMV method, requiring an a priori knowledge of the geology in the reference site on land, not always available or totally reliable.

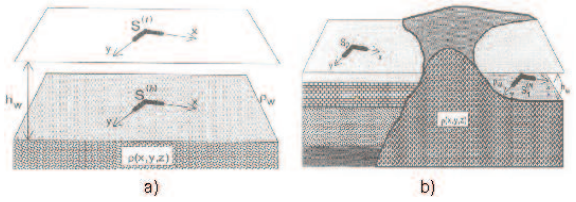

Figure 1. (a) The magnetovariational array configuration in marine exploration. (b) The sea-to-ground magnetovariational array configuration.

In this paper we study the SGMV response of 2D and 3D structures approximating a magma chamber. It is a preliminary investigation aiming at establishing the resolution power of the SGMV method in view of an application to the Campi Flegrei caldera, in particular to the portion of the caldera extending offshore in the Gulf of Pozzuoli, which has so far never been explored. We simulate an application of the SGMV method by a finite difference algorithm [Mackie et al., 1993], and compare the MT responses derived from the SGMV method (from now on the MT-by-SGMV responses) with the synthetic standard MT responses on the same structures, in order to highlight the performance of the new layout. In this preliminary investigation, all synthetic standard MT and MT-by-SGMV responses in marine environment are always computed as they were obtained on the free surface of the sea-water layer.

An outline of the SGMV theory [Patella et al., 1999] precedes the numerical simulations, in order to let the reader be acquainted with the formal approach followed to compute the MT-by-SGMV synthetic responses.

2. Theoretical outline

Neglecting displacement currents, the solution of Helmholtz equation for the plane magnetic field components with $e^{i\omega t}$ time behavior in a uniform, highly conductive sea-water layer overlying any complex resistivity structure, is

$$H_{x1}(\omega) = A_{x1}(\omega)e^{k_z z} + B_{x1}(\omega)e^{-k_z z} \qquad (1a)$$

$$H_{y1}(\omega) = A_{y1}(\omega)e^{k_z z} + B_{y1}(\omega)e^{-k_z z} \qquad (1b)$$

where the wavenumber k_z is given as

$$k_z = (i\omega\mu/\rho_w)^{1/2} \qquad (2)$$

and z, ω, μ and ρ_w are the depth positive downwards, the angular frequency, the magnetic permeability taken equal to that of free-space and the resistivity of the sea water layer, respectively. In writing eq.s 1a and 1b we have tacitly admitted that the horizontal wavenumbers in the sea water layer are negligible with respect to k_z.

Using eq.s 1a and 1b, the magnetic components

$$H_{x1}^{(s)}(\omega) \qquad \text{and} \qquad H_{x1}^{(g)}(\omega)$$

at the sea-floor station can easily be written as

$$H_{x1}^{(s)}(\omega) = A_{x1}(\omega)e^{k_z h_w} + B_{x1}(\omega)e^{-k_z h_w} \qquad (3a)$$

$$H_{y1}^{(s)}(\omega) = A_{y1}(\omega)e^{k_z h_w} + B_{y1}(\omega)e^{-k_z h_w} \qquad (3b)$$

where h_w is the thickness of the sea water layer. We suppose ρ_w and h_w are known parameters.

Assuming that S_2 is located at the top of a horizontally layered medium, the magnetic field at S_2 can be used to estimate the primary magnetic field [Kaufman and Keller, 1981]. As a consequence of eq.s 1a and 1b and due to a general uniformity of the primary magnetic field over extended areas [Zelwer and Morrison, 1972], the magnetic field components and at the top of the sea water layer (z=0) are estimated as follows

$$H_{x1}^{(g)}(\omega) = A_{x1}(\omega) + B_{x1}(\omega) = H_{x2}(\omega) \qquad (4a)$$

$$H_{y1}^{(g)}(\omega) = A_{y1}(\omega) + B_{y1}(\omega) = H_{y2}(\omega) \qquad (4b)$$

Eq.s 3a and 3b and eq.s 4a and 4b can be easily manipulated in order to estimate the electric components in the sea water layer. These estimates can be used to simulate a standard MT sounding at any level in the sea water layer. For the aim of this study, the electric field compo-

nents at the top of the sea water layer are readily obtained as

$$E_{x1}^{(0)}(\omega) = \rho_w k_w \left[B_{y1}(\omega) - A_{y1}(\omega) \right] \quad (5a)$$

$$E_{y1}^{(0)}(\omega) = \rho_w k_w \left[A_{x1}(\omega) - B_{x1}(\omega) \right] \quad (5b)$$

where

$$B_{x1}(\omega) = \frac{H_{x1}^{(1)}(\omega) - H_{x1}^{(0)}(\omega) e^{-k_0 h_0}}{1 - e^{-2k_0 h_0}} \quad (6a)$$

$$B_{y1}(\omega) = \frac{H_{y1}^{(1)}(\omega) - H_{y1}^{(0)}(\omega) e^{-k_0 h_0}}{1 - e^{-2k_0 h_0}} \quad (6b)$$

and

$$A_{x1}(\omega) = H_{x1}^{(1)}(\omega) e^{-k_0 h_0} - B_{x1}(\omega) e^{-2k_0 h_0} \quad (7a)$$

$$A_{y1}(\omega) = H_{x1}^{(1)}(\omega) e^{-k_0 h_0} - B_{y1}(\omega) e^{-2k_0 h_0} \quad (7b)$$

The standard MT formulas can thus be used to get reliable estimates of the MT apparent resistivities.

3. Numerical simulations

2D model

We show now the results of a simulation carried out on a 2D model of magma chamber using the finite difference approach. The 2D model consists of a prismatic body with rectangular section and infinite extent in a horizontal direction, immersed in a 1D hosting medium with 3 layers, as in fig.2. The first layer of the hosting medium simulates a sea-water stratum, with thickness of 200 m and resistivity of 0.3 Ωm. The second and third layer represent a conductive sedimentary bed, with thickness of 400 m and resistivity of 5 Ωm, and a resistive sedimentary substratum with resistivity of 100 Ωm, respectively. The 2D prismatic body is placed within the substratum and is given a 4×3.4 km^2 section and a resistivity of 2 Ωm. Three cases are considered by putting the top of the prismatic body at 1, 3 and 5 km of depth below sea level (models 1, 2, and 3 in fig.2).

The simulations consisted in retrieving the MT-by-SGMV and MT pseudosections along a profile perpendicular to the strike of the 2D chamber, in order to test at first the possibility of detecting the target body (the magma chamber) and then the performance of the SGMV method compared with the standard MT method. Fig.3 shows the results of the simulation for the three cases sketched in fig.2. In detail, fig.3a refers to model 1, fig.3b to model 2 and fig,3c to model 3. In all cases, the simulation allows the capability of the standard MT method in detecting a magma chamber to be verified, and the reliability of the MT-by-SGMV approach to be ascertained.

3D model

We consider now a 3D magma chamber model and introduce also a 2D coastal effect in order to better represent the expected situation in the Campi Flegrei area across the Gulf of Pozzuoli. A 100 Ωm homogenous rock environment, laterally in contact with a 100 m thick sea-water stratum with resistivity of 0.3 Ωm, is assumed to host a 3D magma chamber, assimilated to a 4×4×4 km^3 cubic body with resistivity of 1 Ωm and the top side buried at 4 km of

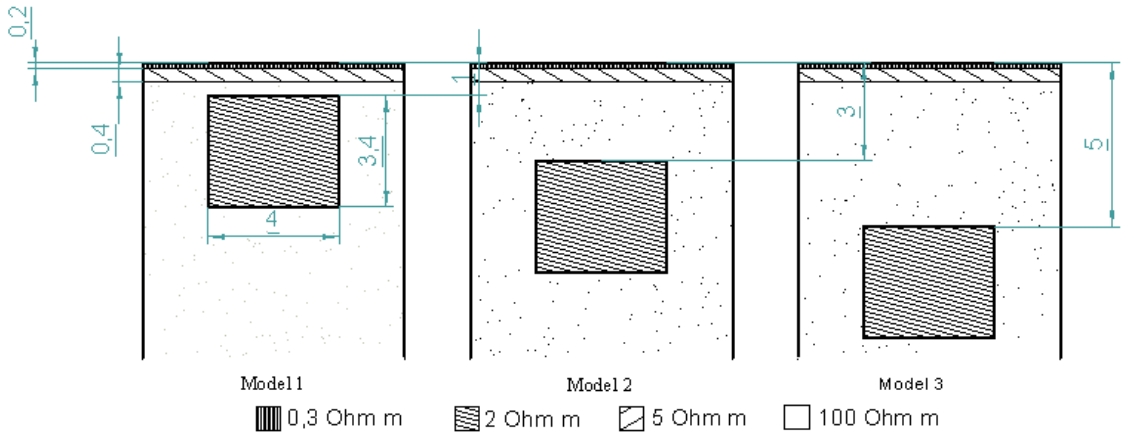

Figure 2. A 2D model of magma chamber immersed within the substratum of a three-layer sequence, whose first layer characterises a sea water layer. Thicknesses of the layers and side dimensions of the 2D prismatic body are expressed in km.

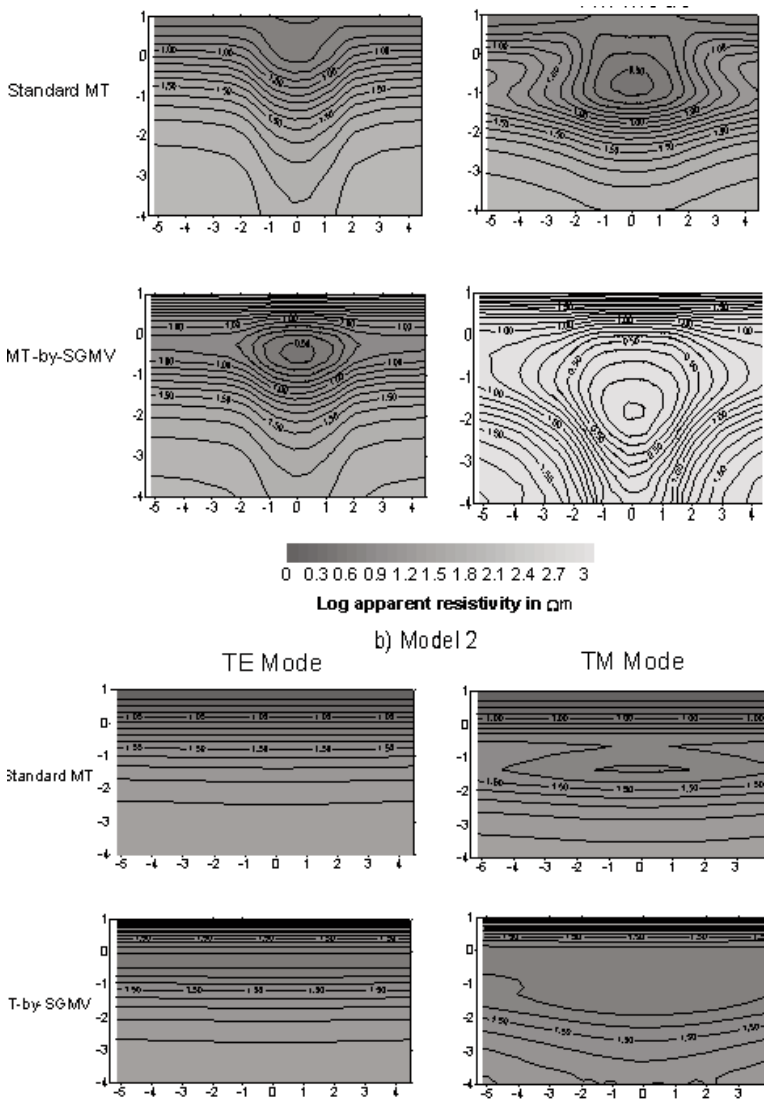

Figure 3a and 3b. Sea-surface MT and MT-by-SGMV apparent resistivity pseudosections for models 1 and 2 of fig.2. The vertical scale is logarithm of frequency in Hz and the horizontal scale is distance in km.

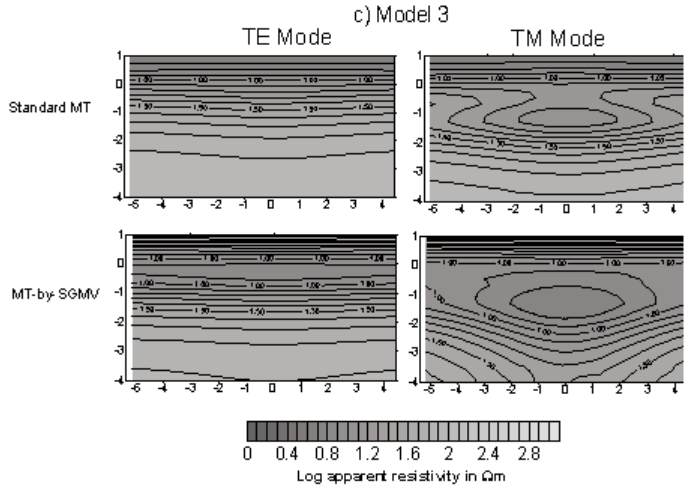

Figure 3c. Sea-surface MT and MT-by-SGMV apparent resistivity pseudosections for model 3 of fig.2. The vertical scale is logarithm of frequency in Hz and the horizontal scale is distance in km.

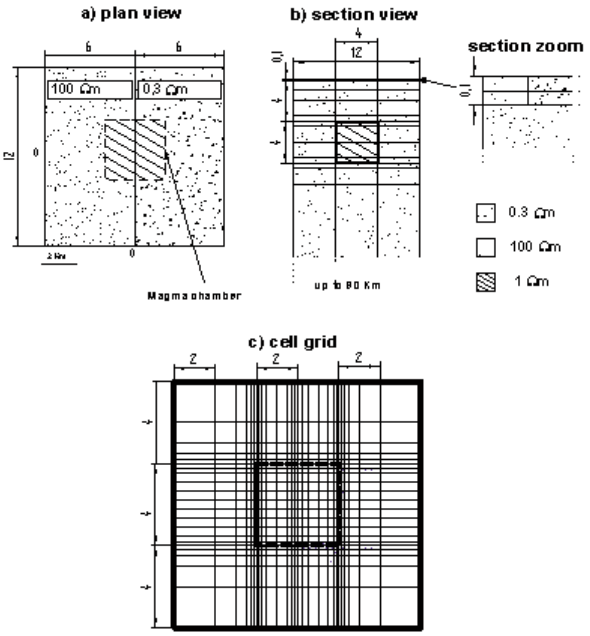

Figure 4. Section (a) and plan (b) views of a complex 3D model simulating the Campi Flegrei volcanic area (Naples). The cell gridding for the application of the finite difference algorithm is shown (c). All distances are expressed in km.

depth below sea level. The cubic chamber is placed in such a way as to lie partly below the sea-water layer, as in fig.4 which shows a plan (a) and section (b) view of this complex 3D model. For computation, the horizontal section of the 2D model simulating the coastal scarp effect (the first 100 m of the whole model) has been subdivided into two sectors of 14×21 cells each, by assigning a resistivity of 100 Ωm in each cell of the left-hand land sector, and 0.3 Wm in each cell of the right-hand marine sector, as depicted in fig.4c.

We have repeated for this 3D model the same finite difference process used for the previous 2D simulation. Before illustrating the performance of the SGMV method, we delineate the behaviour of the standard MT method applied to such a complex situation. Fig.5 shows a sequence of horizontal slices at different periods, where the standard MT apparent resistivity maps in the more resolutive TM mode are depicted, starting from 1 s up to 10,000 s. In order to better highlight the effect of the cubic chamber on the MT response, the images obtained without the cubic body are also illustrated. It results that the presence of the magma chamber can possibly be appreciated looking at two effects appearing in the left-hand land sector. The first effect consists in an apparent distortion of the isolines, starting from 10 s upward, tending to isolate a closed anomaly reflecting the boundary of the cubic body, placed vertically beneath the resistive land sector of the model. The second effect consists in a drop of the resistivity value of the isolines up to about 37% in the same area where they tend to encircle the target anomaly.

Apparently, there is no signal coming from the right-hand marine sector. Actually, this silence seems to be due to the fact that in the marine sector the apparent resistivity values are so very low as to be undistinguishable with the adopted scale for the isolines, which favour the left-hand isoline pattern. In a next representation, regarding a profile at sea parallel to the shoreline, the choice of a logarithmic scale for the isolines will better focus the apparent resistivity pattern inside the marine sector.

The analysis of fig.5 allows a final comment to be made regarding the presence of the coast lateral effect. The strong resistivity lateral contrast, assumed to characterise the passage from land to sea, generates an intense crowding of the isolines in correpondence of the shoreline. This effect propagates virtually with the same intensity in all horizontal slices for both the situations with and without magma chamber.

In order to visualise the above results as pseudosections, we consider two profiles on

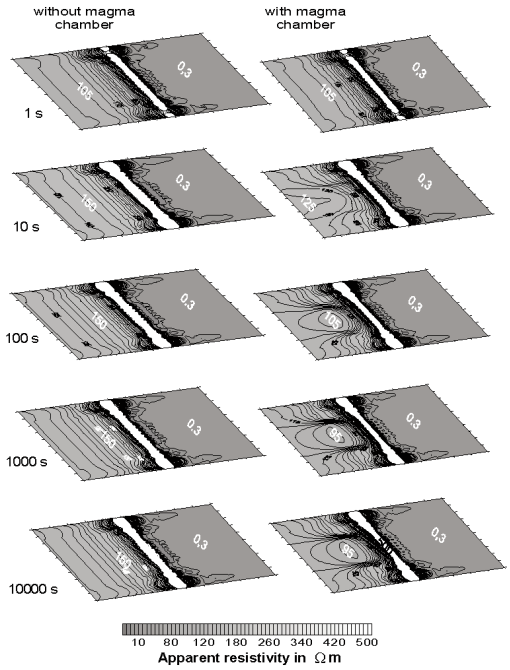

Figure 5. Standard MT TM mode apparent resistivity horizontal maps at different periods for the model of fig.4 with (right-hand column) and without magma chamber (left-hand column). Tips along the sides of the slices are every 1 km.

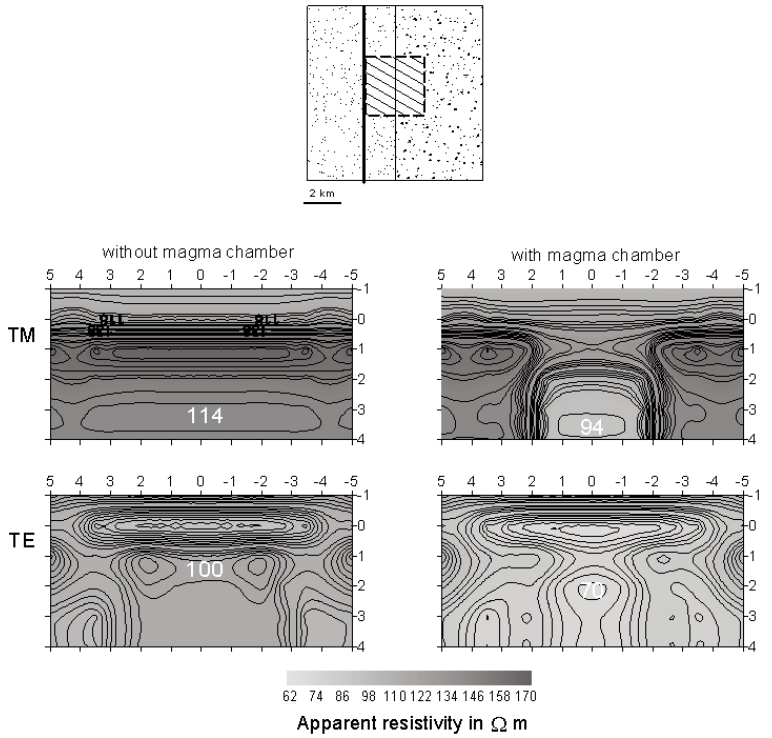

Figure 6. Standard MT TM and TE mode apparent resistivity pseudosections drawn across a profile running on land parallel to the shoreline at a distance of 2 km, with (right-hand column) and without magma chamber (left-hand column). In all pseudosections, the vertical scale is logarithm of period in s, and the horizontal scale is distance in km.

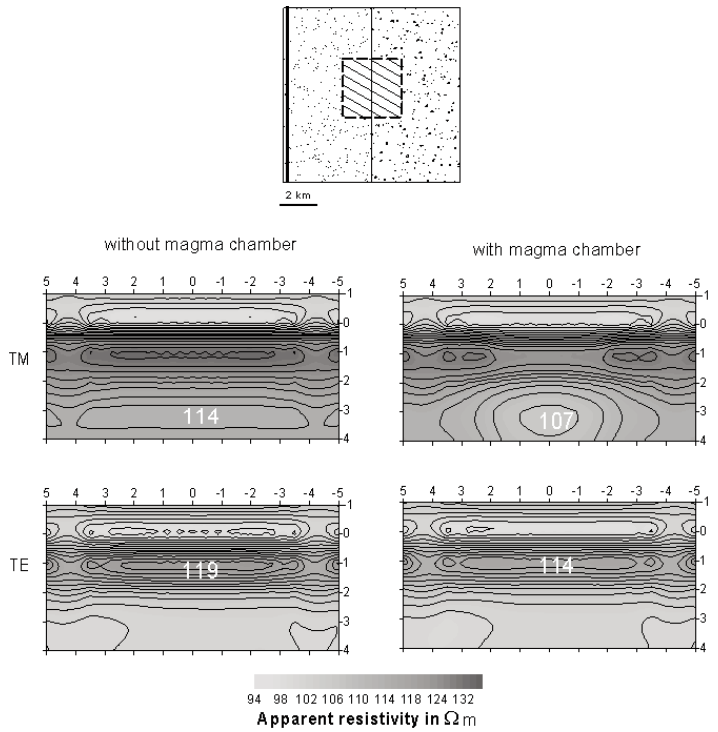

Figure 7. Standard MT TM and TE mode apparent resistivity pseudosections drawn across a profile running on land parallel to the shoreline at a distance of 5 km, with (right-hand column) and without magma chamber (left-hand column). In all pseudosections, the vertical scale is logarithm of period in s, and the horizontal scale is distance in km.

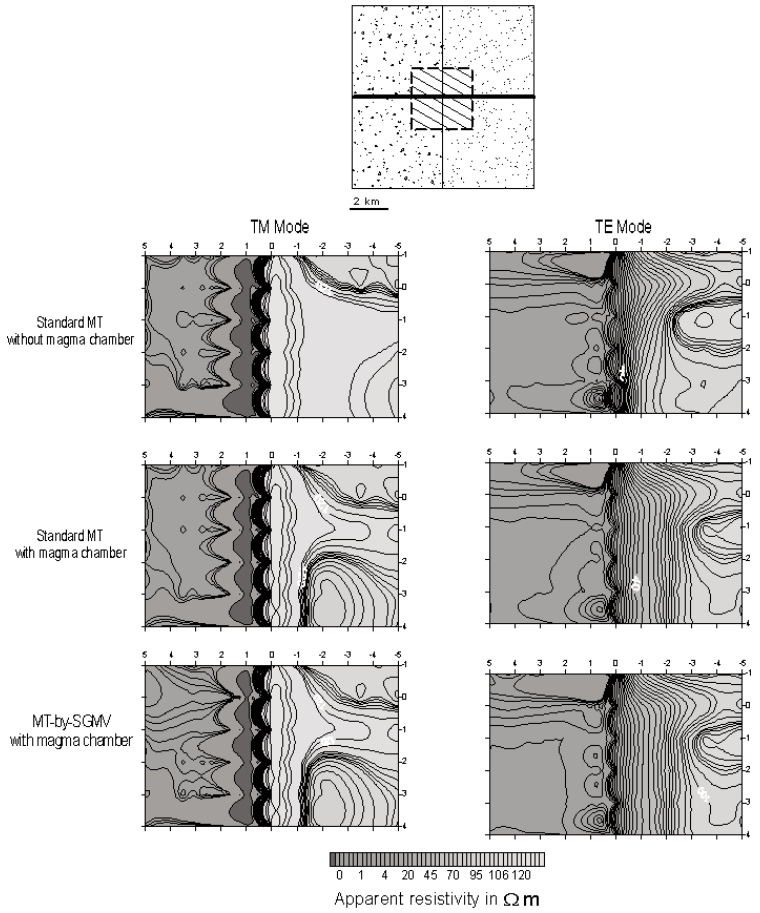

Figure 8. Standard MT TM and TE mode apparent resistivity pseudosections drawn across a profile running along the symmetry axis perpendicular to the shoreline without (top line) and with magma chamber (middle line). The bottom line shows the TM and TE pseudosections along the same profile obtained using MT-by-SGMV data in the portion at sea, for the case with magma chamber. In all pseudosections, the vertical scale is logarithm of period in s, and the horizontal scale is distance in km.

land parallel to the coast line, one distant 2 km from the shoreline, placed over the continental border of the magma chamber (fig.6), and the other displaced 5 km on land from the shoreline (fig.7). Again the comparison of the MT responses with and without magma chamber is made. Moreover, the less resolutive TE mode is also reported. In the former profile (fig.6), the TM signature of the magma body is very evident and also its geometry appears well delineated, whereas in the latter profile (fig.7) the target anomaly tends to become evanescent, as expected.

We consider now the TM and TE pseudosections across a profile through the axis of symmetry of the model, perpendicular to the shoreline (fig.8). For the portion of the profile at sea, MT-by-SGMV data have been used (bottom line in fig.8). A comparison is also made with standard MT TM and TE pseudosections for the case without (top line in fig.8) and with magma chamber (middle line in fig.8). The MT-by-SGMV image at sea is quite consistent with the corresponding standard MT image. In the land sector, the boundary of the magma body is again very well outlined in the correct lateral position, especially in the TM mode. Again, the distortion of the isolines in the top level of the pseudosections at periods around 1 s, can likely be associated with the presence of the coastal boundary. The sea-scarp effect is now well evident also in the marine sector, but only in the TE mode, in addition to the back-projected similar, but much stronger effect appearing in the land sector, mainly in the TM mode.

Finally, we consider the MT-by-SGMV TM and TE pseudosections (top line in fig.9), across a profile running parallel to the shoreline and placed at a distance of 2 km over the marine border of the magma chamber, compared with the standard MT TM and TE pseudosections (bottom line in fig.9). In order to emphasise the apparent resistivity variations around values less than 2.5 Ωm, a logarithmic scale has been now

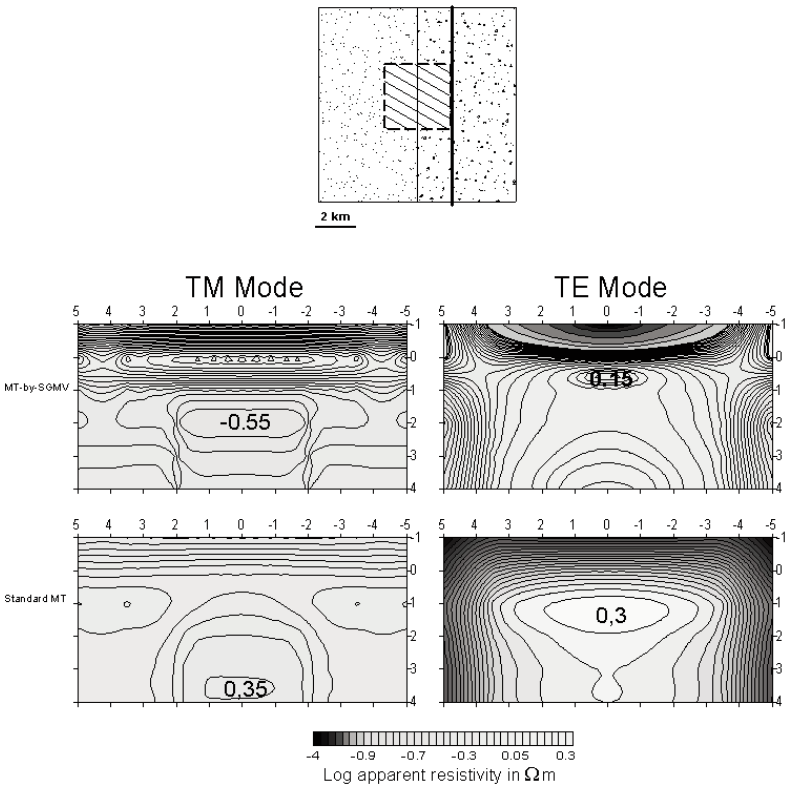

Figure 9. MT-by-SGMV TM and TE pseudosections (top line) compared with standard MT TM and TE pseudosections (bottom line), drawn across a profile offshore parallel to the shoreline at a distance of 2 km. The vertical scale is logarithm of period in s, and the horizontal scale is distance in km.

adopted for the isolines. Even though with a not complete coicidence of the isolines, the comparison between standard MT and MT-by-SGMV images can again be considered satisfactory. The MT-by-SGMV pseudosections seem now to possess a slightly greater resolution of the magma body, which appears equivalent in both TM and TE imaging modes.

4. Conclusion

We have studied the capability of the SGMV geophysical method to resolve 2D and 3D prismatic bodies approximating a magma chamber placed beneath a sea-water layer, in view of an application to the Campi Flegrei caldera (Naples, Italy), in particular to the portion of the caldera extending offshore in the Gulf of Pozzuoli. The modelling has been performed using a finite difference algorithm, and has allowed a comparison to be made between standard free-surface MT representations and an equivalent MT imaging retrieved by the SGMV approach. In all cases, the modelling has confirmed the general capability of the em induction methods to resolve complex volcanic structures and the comparison has shown the reliability of the SGMV method in simulating MT soundings in marine environment. However, it must be emphasised that, in real cases, this kind of results implies the need of disposing of accurate field data with small error bars in order for a conductive magma chamber, residing beneath a sea-water layer, to be detected as reliably as possible.

Acknowledgements

This work was partially supported by the GNV through the Epot project.

References

Kaufman, A.A. and Keller, G.V., (1981). *The magnetotelluric sounding method*. Elsevier, Amsterdam.

Mackie, R.L., Madden, T.R. and Wannamaker, P.E., (1993). *Three-dimensional magnetotelluric modeling using difference equations - Theory and comparisons to integral equation solutions*. Geophysics, 58, 215-226.

Patella, D., Mauriello, P. and Siniscalchi, A., (1999). *A sea-to-ground magnetovariational method.* Proceedings of the 1999 Offshore Technology Conference, 845-850.

Patella, D. and Siniscalchi, A., (1994). *Two-level*

magnetovariational measurements for the determination of underground resistivity distributions. Geophysical Prospecting, 42, 417-444.

Zelwer, R. and Morrison, H.F, (1972). *Spatial characteristics of mid-latitude geomagnetic micropulsations*: Journal of Geophysical Research, 77, 674-694.

Characterization of the Coherent EM Noise due to Moving Sources on Magnetotelluric Data

Maria Giulia Di Giuseppe[1], Zaccaria Petrillo[2], Antonio Troiano[1] and Domenico Patella[1]

[1] *Department of Physical Sciences, University Federico II, Naples, Italy*
[2] *National Institute of Geophysics and Volcanology, Vesuvian Observatory, Naples, Italy*

Abstract

The magnetotelluric (MT) sounding method includes as a fundamental step during data processing the correct estimate of the impedance tensor elements on the ground surface. Soundings performed in areas of intense urbanization often show a not negligible tensor instability, which manifests in a given station as widely differring apparent resistivity curves beyond any confidence limit, according to the data vector subset used. As discussed in literature, the reason for such instability stands on the non-stationarity of coherent contributions from electromagnetic (EM) sources not approximable to a plane wave field (near-field). A way to overcome such a serious drawback is based on the use of the multivariate technique of data analysis, which allows the details of the EM noise structure to be fully investigated, and the estimate of the number of coherent sources to be ascertained. In many instances, by such technique, the MT useful signal can even be extracted from a complex mixing of the useful plane wave field with coherent signals from near sources. The multivariate technique is based on a robust analysis of multichannel data expanded in terms of empirical orthogonal functions. In this paper, we approach this problem using Egbert's robust multivariate errors-in-variables (RMEV) technique. We show some examples of the application of Egbert's algorithm to the optimum estimate of MT apparent resistivity curves, using at first a synthetic data structure in order to fix management criteria of the various steps of the algorithm, and then a field dataset belonging to an MT sounding very recently carried out in the Campi Flegrei volcanic area. The performance of the RMEV technique on our field data is considered quite satisfactory at the present stage of the research.

Key words *magnetotelluric sounding - RMEV technique - Campi Flegrei*

1. Introduction

The most important step in magnetotelluric (MT) data processing is the correct estimate of the surface impedance tensor, which is a difficult task in critical frequency bands for soundings carried out in proximity of electrical railroads [Egbert, 1997]. Sometimes, criticality extends to the whole MT frequency band in areas of also intense urbanization [Qian and Pedersen, 1991]. The non-stationarity of coherent noise can be an explanation of the different behaviour of MT sounding curves carried out in different periods in the same place by different groups [e.g. Di Maio et al., 1998; Manzella et al., 2000].

The structure of the electromagnetic (EM) noise is generally local (near-field), but with a scale reaching tens or more km and an amplitude comparable to that of the MT source [Fraser-Smith et al., 1978]. Its characterisation is a necessary step to extract the MT signal. In particular, the bias due to trains in the 0.001÷1 Hz frequency band, which is the band within which the deep crustal features of primary geophysical interest can be explored, is a fundamental problem for our research purposes.

After the introduction of the remote reference [Gamble et al., 1979a, 1979b], by which the EM field at a local site is correlated with the horizontal magnetic components recorded simultaneously at a remote station, and the application of various robust data-adaptive weighting tools [e.g. Huber, 1981; Jones and Jodicke, 1984; Egbert and Booker, 1986; Chave et al., 1987], the robust multivariate errors-in-variables (RMEV) estimator was at last proposed [Egbert, 1997], which allows the background noise level to be estimated and the bias due to coherent noise to be diagnosed.

The use of a multivariate technique of data analysis allows details of the EM noise structure to be explored, including an estimate of the number of coherent series in the data vector. In some cases it is also possible to extract the MT signal, i.e. the two series relative to the two orthogonal polarizations of the plane wave, even out of a complicate mixing with near-field terms due to trains and electric powerlines in the 0.001÷1 Hz and 1÷1000 Hz band, respectively.

The multivariate technique, borrowed from meteorology where it is also known as principal component analysis or spectral decomposition, is based on a robust analysis of multiple components recorded at multiple stations (multi-channels) and then represented as empirical orthogonal functions. Data vectors with anomalous distance from the mean value are

excluded from the statistical sample, and the most suitable norm is used according to the error distribution. The algorithm estimates the eigenvectors of the spectral density matrix (SDM) constructed with all available channels (magnetic and electric channels are dealt with in the same way) [Egbert, 1997]. A source is finally associated to each eigenvalue emerging above the threshold of the incoherent noise. The fundamental step within the theoretical apparatus is the estimation of the level of the incoherent noise in each channel, in order to avoid for eigenvalues without any physical significance to emerge out of it. It can also be demonstrated that using the eigenvector representation it is possible to extract all the linear relationships which connect channel to channel and group of channels to group of channels, like e.g. the impedance tensor elements in the case of local magnetic to local electrical channels, the magnetic transfer functions in the case of magnetic channels of different sites, and the tipper in the case of local magnetic channels. The prerequisite of the technique is the use of multiple records (two or three complete simultaneous MT stations), since it is heavily conditioned by the coherent sources-to-channels ratio in case of finite time series. Practice suggests to use a number of channels which doubles the number of sources. A limit of the SDM analysis is, however, the inability to associate an eigenvector to a single source when, in a given band, two or more eigenvalues are very close. In such a case, an eigenvector can be a linear combinations of eigenvectors related to single sources.

In this paper, firstly we give a short outline of the RMEV theory, then we assess the performance of the RMEV algorithm on an EM synthetic data structure upon which a high control can be exerted, and finally export the experience thus acquired to a real field case.

2. Outline of the RMEV technique

Following Egbert [1997], in the multivariate approach the frequency-domain MT array data vectors $\mathbf{X}_i$, where i=1,2,…,N with N being the total number of samples, can be put in matrix notation as

$$\mathbf{X}_i = \mathbf{U}\boldsymbol{\beta}_i + \mathbf{V}\boldsymbol{\gamma}_i + \boldsymbol{\varepsilon}_i \qquad (1)$$

where, indicating with K the total number of channels in the array, the columns of the K×2 **U** matrix are complex vectors, representing the magnetic and electrical fields that would be observed at all sites for idealized quasi-uniform magnetic sources, linearly polarized in the N-S and E-W directions, the columns of the K×L **V** matrix represent the L coherent noise sources, and the vector $\boldsymbol{\varepsilon}_i$ represents the incoherent noise. The vectors $\boldsymbol{\beta}_i$ and $\boldsymbol{\gamma}_i$ define the polarizations of the MT signal and coherent noise sources, respectively.

The impedance tensor **Z** for a site is given in terms of the elements of **U** corresponding to the x- and y-component of the electric and magnetic fields observed at the local station in polarisation states 1 and 2, as follows

$$\mathbf{Z} = \begin{pmatrix} E_{x1} & E_{x2} \\ E_{y1} & E_{y2} \end{pmatrix} \begin{pmatrix} H_{x1} & H_{x2} \\ H_{y1} & H_{y2} \end{pmatrix}^{-1} \qquad (2)$$

Solving the generalized eigenvalue problem

$$\mathbf{Su} = \lambda \Sigma_N \mathbf{u} \qquad (3)$$

where Σ_N is the covariance matrix of the incoherent noise and

$$\mathbf{S} = \frac{1}{K} \sum_i \mathbf{x}_i \mathbf{x}_i^*$$

is the spectral density matrix of the data, we can obtain the estimates of the eigenvalues λ.

3. The RMEV technique applied to synthetic data

We illustrate at first the results obtained using Egbert's RMEV algorithm to a synthetic data structure. The target has been the discrimination between a plane wave field source of signal MT_S and a moving near-field source of coherent noise MT_N. The MT_S datasets (Comdat Project) consist of five local channels and two remote channels. Firstly, only the MT_S datasets have been processed in order to test the computer program and verify the hypothesis of existence of two eigenvalues. Once ascertained the good quality of the results come out from this preliminary check, we have passed to contaminate the local channels by adding the coherent noise.

To simulate a moving near-field source (train), we have assumed that the effect of a dipolar source turning around the local MT station can be represented by a MT_N signal modulation on the electric (E_x and E_y) and magnetic (H_x and H_y) axes as follows

$$H_x = R \sin\left[\left(\frac{i-1}{N}\right)\frac{\pi}{2}\right] \qquad (4a)$$

$$H_y = R\cos\left[\left(\frac{i-1}{N}\right)\frac{\pi}{2}\right] \quad (4b)$$

$$E_x = R\sin\left[\left(\frac{i-1}{N}\right)\frac{\pi}{2}+\frac{\pi}{20}\right] \quad (4c)$$

$$E_y = R\cos\left[\left(\frac{i-1}{N}\right)\frac{\pi}{2}+\frac{\pi}{20}\right] \quad (4d)$$

where i=1,2,....,N with N being the total number of samples, and R is a random function with elements normally distributed around a zero mean value.

In order to have an idea of what kind of records we are dealing with, fig.1 shows the signal and noise power spectra, relative, for simplicity, to only the H_x component. In particular, we let notice the relative noise level at different periods in the range 1-10^4 s.

Fig.2 displays the obtained diagrams of the eigenvalues of the relative SDM expressed in dB, plotted versus period. Three eigenvalues significantly greater than unity appear in the period range from 4 s to about 60 s. The third largest eigenvalue is a clear evidence of the added coherent noise. In full agreement with the

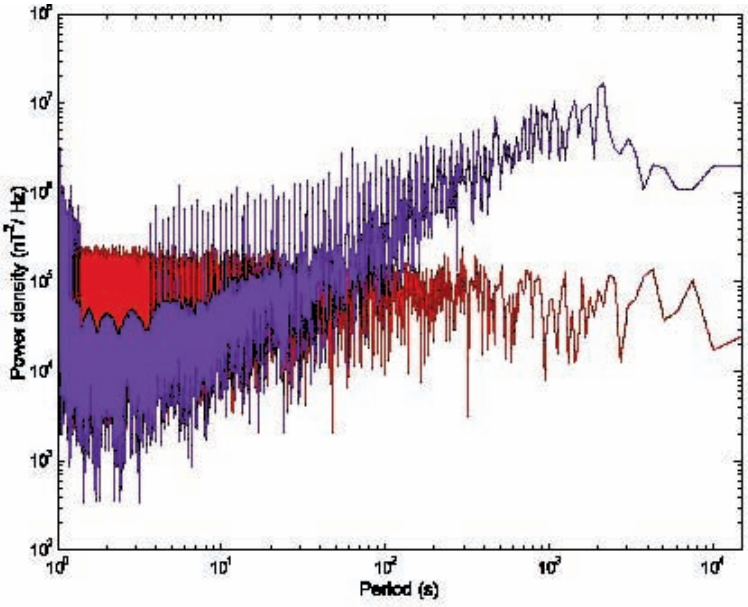

Figure 1. Power spectra of the magnetic *x*-component of a synthetic MT signal (dark grey line) and a coherent noise due to a mobile near-field source (light grey line).

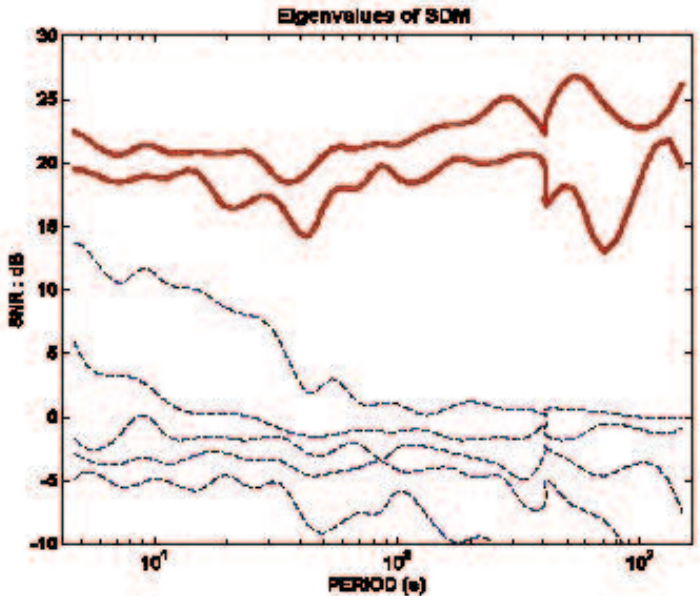

Figure 2. Eigenvalues of the spectral density matrix, relative to the corrupted MT dataset analysed in fig.1.

noise power spectra of the coherent noise for all local channels (fig.1 shows only the H_x component), the third eigenvalue decreases as period increases, until at about 60 s it definitely falls around the zero level, i.e. the background incoherent noise top level.

We have then analysed the polarization of the three main eigenvectors at different periods within four time windows corresponding to four distinct angular positions of the mobile noise source in the range 0°-90°.

Fig.3 is a plot of the electric (dashed lines) and magnetic (solid lines) eigenvectors in the band T=20 s. Although the noise level is similar to the signal level (see fig.1), the first two eigenvectors appear very stable, as expected, being representative of the MT source, while the third eigenvector rotates following the MT_N mobile source. As period decreases the noise contribution tends to become stronger and the eigenvectors become a linear combinations of the three sources, losing directivity.

Finally, fig.4 shows the apparent resistivity and phase curves for the TM and TE modes, computed by the RMEV method using the synthetic MT dataset without and with coherent noise, and assuming that the eigenvectors associated with the largest two eigenvalues of the SDM define the MT source.

Though a residual bias effect, indicative

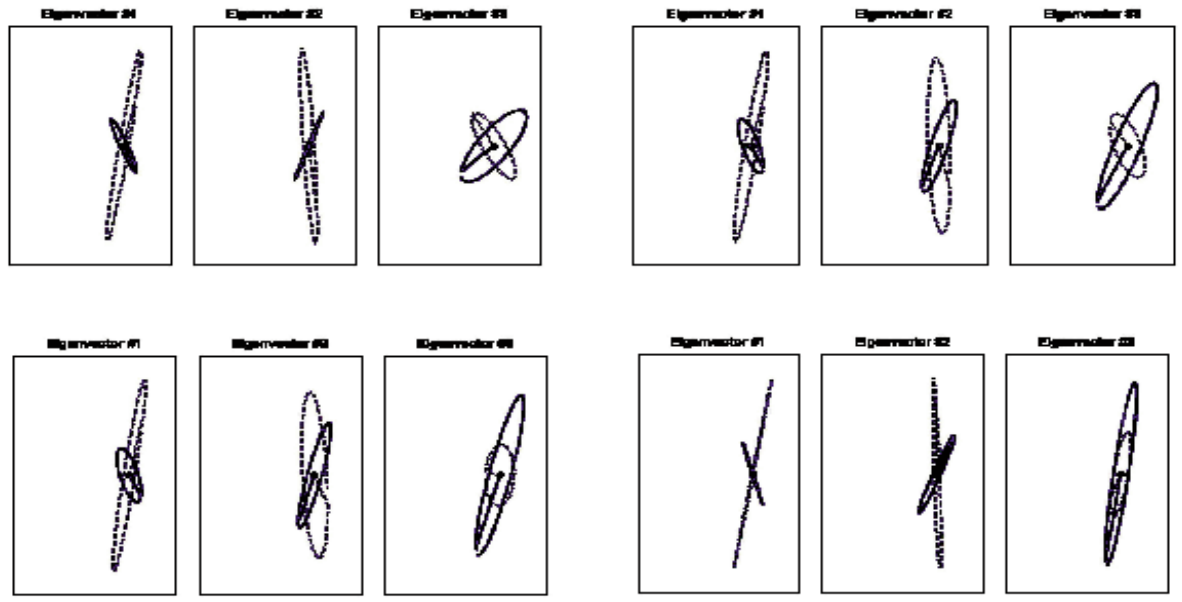

Figure 3. Eigenvector polar diagrams, computed in the band T=20 s within four contiguous time windows, relative to the corrupted MT dataset analysed in fig.1.

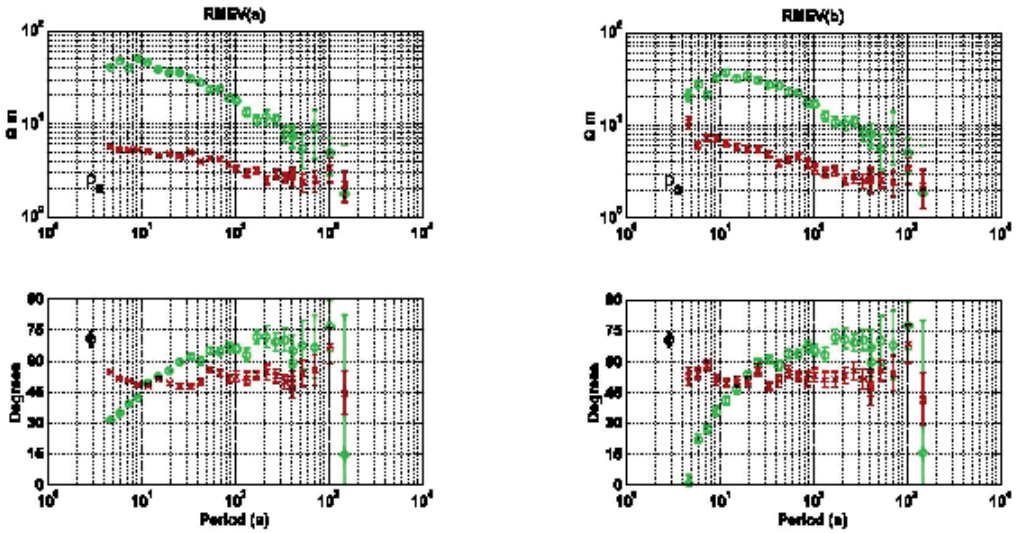

Figure 4. Apparent resistivity and phase curves computed by the RMEV method using the MT dataset analysed in fig.1, with only incoherent noise (a) and incoherent plus coherent noise (b).

of the participation of the coherent noise source in the estimate, is still present in both the apparent resistivity and phase curves in the high frequency band, the quality of the RMEV computation algorithm can be retained quite satisfactory, compared with other standard computation tools.

4. The RMEV technique applied to experimental data

We illustrate now the application of the RMEV analysis to experimental data relative to a two-station MT sounding carried out at Astroni (Campi Flegrei, Naples, Italy). In real field cases, the application of Egbert's technique is more complicated, since eigenvalues significantly greater than unity may not represent the MT source and/or result nearly equal, making the distinction between MT signal and coherent noise problematic.

Fig.5 shows a plot of the SDM eigenvalues obtained at Astroni using a 600 s time window. We have evidence of a coherent noise at low frequencies (2-30 s). In this case, the greater angular stability of the eigenvectors associated with the second and third eigenvalues in the band T=6.4 s (Fig.6) allows us to assume that they are the representative eigenvectors of the MT source. The first eigenvector, which shows changes of direction, is probably related to a coherent noise source due to trains. This conclusion is in agreement with the circumstance that the signal level associated with electrical railways results higher than the MT signal level when the distance between the MT site and the railroad is less than about 10 km.

Finally, fig.7 shows the apparent resistivity and phase curves computed using the WLS (weighted least-square) and RMEV methods. In both cases the curves exhibit a distorted behaviour in the period range 4-40 s. The apparent resistivity increases steeply and phases fall down to -90°. This behaviour is typical of an MT signal contaminated by non-uniform EM cultural noise sources [Mackie and Madden, 1992; Qian and Pedersen, 1991]. This conclusion is in agreement with the number of dominant SDM eigenvalues (see fig.5) in the same period range.

5. Conclusion

In this work we have tried to find a way to discriminate the MT signal from coherent noise in order to reconstruct the actual apparent resistivity and phase curves. The strongest contribution to the distortion of MT curves is likely due to electric railroads, which generate coherent noise extending up to tens of km.

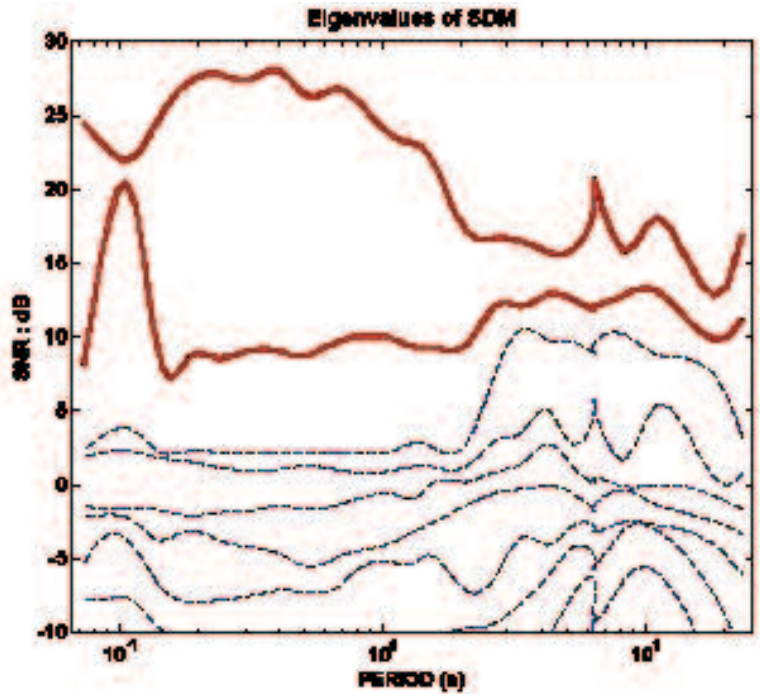

Figure 5. Eigenvalues of the spectral density matrix, relative to a two-station MT field sounding at Astroni (Campi Flegrei, Naples, Italy) within a time window of 600 s and with a sampling rate of 64 Hz.

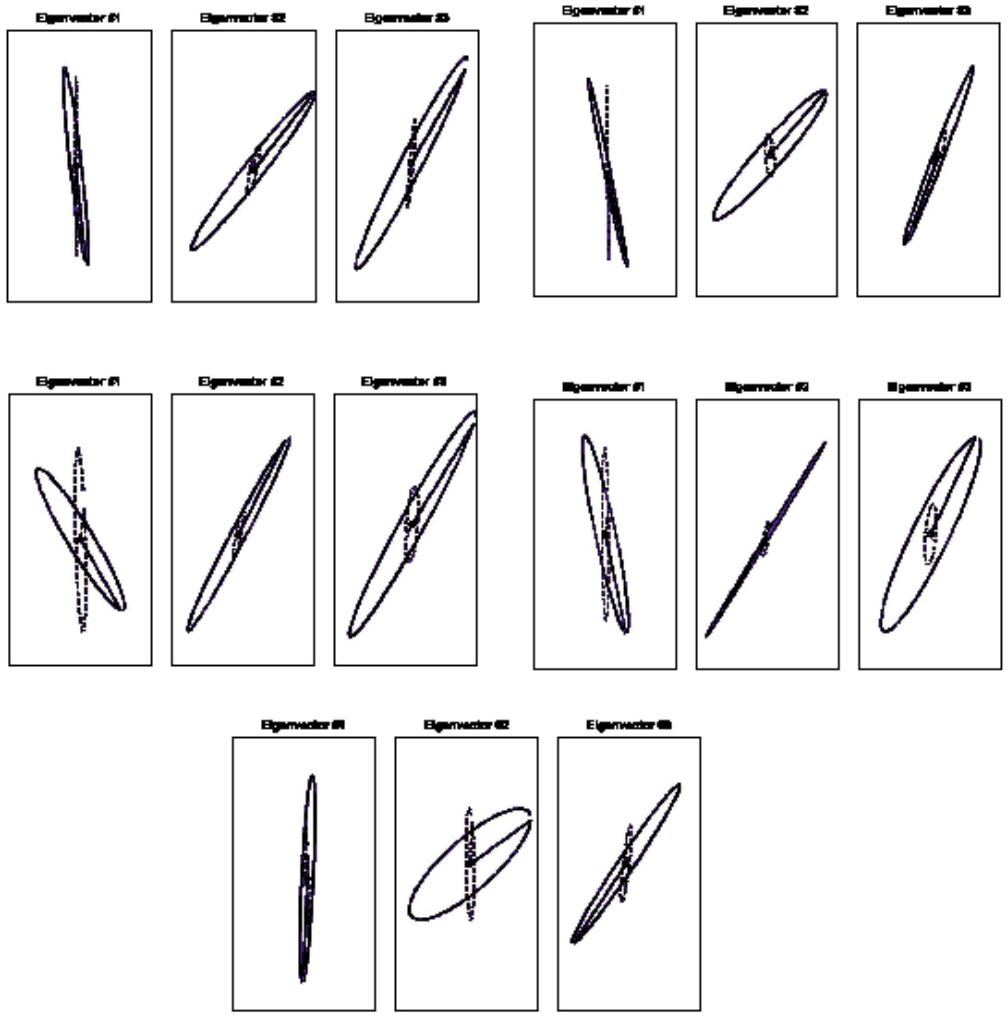

Figure 6. Eigenvector polar diagrams, computed in the band T=6.4 s within five contiguous time windows each with duration of 600 s, relative to the MT sounding performed at Astroni (Campi Flegrei).

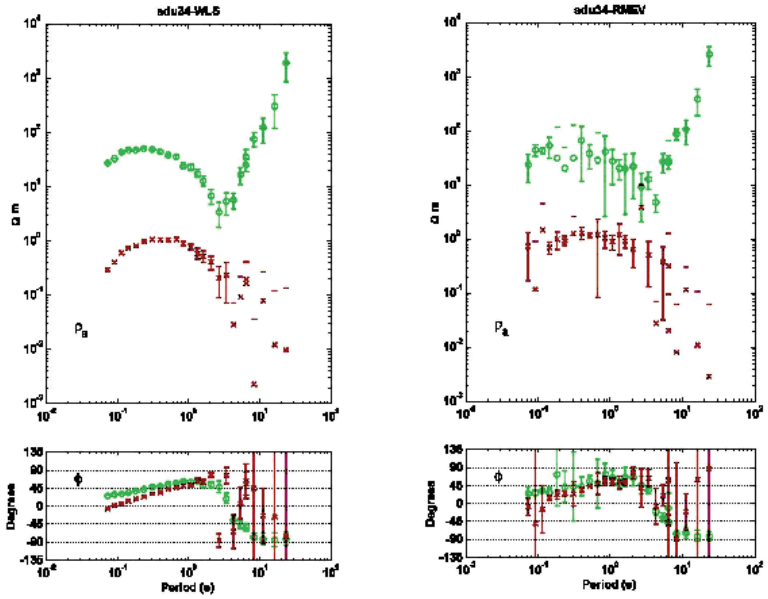

Figure 7. Apparent resistivity and phase curves computed by the WLS (a) and the RMEV (b) methods, relative to the MT sounding performed at Astroni (Campi Flegrei).

We have shown that the RMEV method allows an estimate of the number of coherent sources (signal and noise) to be obtained within data vectors, but only in few cases the MT signal to be easily extracted. The limit of the RMEV analysis is, in fact, the inability to associate a given eigenvector to a single source; eigenvectors related to near eigenvalues can be linear combinations of the specific eigenvectors of the single sources.

By analysing the behaviour of the eigenvectors associated with synthetic data we have been able to infer that a useful interpretative element is the rotation of the vectors related to moving sources. This information, even if limited to some period bands, can help to reconstruct the true MT impedance curves, using the not rotating eigenvectors.

Acknowledgements

This research was supported in part by the Epot project of the GNV.

References

Chave, A.D., Thomson, D.J., and Ander, M.E., 1987. *On the robust estimation of power spectra, coherences, and transfer functions*, Journal of Geophysical Research, 92, 633-648.

Di Maio, R., Mauriello, P., Patella, D., Petrillo, Z., Piscitelli, S., and Siniscalchi, A., 1998. *Electric and electromagnetic outline of the Mount Somma-Vesuvius structural setting*, Journal of Volcanology and geothermal Research, 82, 219-338.

Egbert, G.D., 1997. *Robust multiple-station magnetotelluric data processing*, Geophysical Journal International, 130, 475-496.

Egbert, G.D., and Booker, J.R., 1986. *Robust estimation of geomagnetic transfer functions*, Geophysical Journal of the Royal Astronomical Society, 87, 173-194.

Fraser-Smith, A.C., and Coates, D.B., 1978. *Large amplitude ULF electromagnetic fields from BART*, Radio Science, 13, 661-668.

Gamble, T.D., Goubau, W.M., and Clarke, J., 1979a. *Magnetotellurics with a remote reference*, Geophysics, 44, 53-68.

Gamble, T.D., Goubau, W.M., and Clarke, J., 1979b. *Error analysis for remote reference magnetotellurics*, Geophysics, 44, 959-968.

Huber, P.J., 1981. *Robust statistics*, J. Wiley & Sons, New York.

Jones, A.G., and Jodicke, H., 1984. *Magnetotelluric transfer function estimation improvement by a coherence-based rejection technique*, Paper presented at 54th SEG annual meeting.

Mackie, R.L , and Madden, T.R , 1992. *A magnetotelluric survey around the Loma Prieta fault zone*, EOS, Transactions of the American Geophysical Union, 73, 99.

Manzella, A., Volpi, G., and Zaja, A., 2000. *New magnetotelluric soundings in the Mt. Somma-Vesuvius volcanic complex: preliminary results*, Annali di Geofisica, 43, 259-270.

Qian, W, and Pedersen, L.B., 1991. *Industrial interference magnetotellurics: an example from the Tangshan area, China*, Geophysics, 56, 265-273.

On the Localisation of Long-Standing Self-Potential Sources at Vulcano (Italy) by Probability Tomography

Boris Di Fiore[1], Paolo Mauriello[2] and Domenico Patella[1]

[1]*Department of Physical Sciences, University Federico II of Naples, Italy*
[2]*Department of Science and Technology for Environment and Territory, University of Molise, Italy*

Abstract

We consider 7 self-potential (SP) areal surveys performed in the period 1991-1994 at Vulcano and show the results of the application of the 3D SP probability tomography method aimed at localising in the subsoil the presence of long-standing sources of the SP anomalies. The long-standing character is associated to sources showing the highest probability of residing in fixed positions underground, during the 1991-1994 observation period. The most important features resulting from the application of the 3D probability tomography are: (i) the presence of sources spread along the Piano and Fossa Caldera rims located in a very shallow depth interval, not extending below sea level; (ii) the presence of a negative source at the eastern side of Vulcanello, which shows the highest occurrence probabilities in the depth range 0.1-0.3 km bsl, with maximum occurring around 0.2 km bsl; (iii) the presence of a negative source close to Grotta Palizzi, which shows the highest occurrence probabilities in a depth range not extending below 0.1 km bsl, with maximum occurring around sea level.

Key words *self-potential – probability tomography - volcano geophysics*

1. Introduction

During the 1985-1995 volcanic unrest at the island of Vulcano (Aeolian Arc, Southern Italy) abnormal changes of physical and chemical parameters were detected in the active area of the Fossa Cone (see fig.1). Mostly, a remarkable increase of temperature (up to 650°C) and emission rate (up to 1395 tons/day) of the persistent fumaroles along the northern crater rim and slopes of the Fossa Cone was recorded, indicating an increase of flux of magmatic gases [Barberi et al., 1991]. A renewed awareness about the volcanic hazard in this touristic island was stimulated by these events and an intense research and monitoring activity was consequently promoted by the Italian Civil Defense Authority.

Among the many geophysical studies that were proposed, a Self-Potential (SP) investigation was included, consisted of an areal survey repeated 7 times in the period 1991-1994. The motivation was the SP study might have revealed the sites of polarised electrical charges, which in volcanic areas are assumed to correspond to pressure and/or heat sources [e.g. Revil and Pezard, 1998]. The resulting SP maps are reported in previous papers [Di Maio et al., 1996, 1997], where details of the data acquisition technique are outlined.

In this paper, we reconsider the 7 SP surveys at Vulcano and show the results of the application of the 3D SP probability tomography method [Patella, 1997a,b], aimed at localising in the subsoil the presence of long-standing sources of the SP anomalies. It is worth anticipating that the long-standing character will here be associated to sources showing the highest probability of residing in fixed positions underground during the 1991-1994 observation period. The probability tomography method has already been tested on SP field datasets collected in the volcanic areas of Mount Vesuvius (Naples, Italy) [Di Maio et al., 1998; Iuliano et al., 2002] and Phlegraean Fields (Naples, Italy) [Di Maio et al., 2000].

2. Structural and volcanological outline of Vulcano

The arc of Aeolian islands is located in the Tyrrhenian sea about 40 km north of Sicily (fig.1). The islands were formed since Late Pleistocene (130000 y.b.p.) through a series of alternating lava flows and pyroclastic fall and flow deposits, which originated typical strato-volcanoes. The Aeolian arc was formed on a NW-SE structural alignment, which marks the transition from the westwards downdipping Tyrrhenian basin to the eastwards uprising Apennines chain. The three-tip star-like shape of the arc indicates the existence of radial fractures, which favoured magma outpouring [Keller, 1980].

Vulcano is one of the seven islands of the arc and is located at its southernmost edge (fig.1). It raises up to 1500 m above sea floor (500 m a.s.l.) with an extension of 22 km^2. From Late Pleistocene the main strato-volcano, called Primordial Vulcano, whose remnant is the Piano Caldera, was originated. Then, at the end of Pleistocene the Lentia Mountains were formed

and later, during Holocene, the Fossa Caldera collapse occurred where the present active Fossa Cone (391 m a.s.l.) resides. Since 183 b.C. the formation of Vulcanello started as a separate small island, which in 1550 a.C. joined Vulcano due to accumulation of sands filling the narrow isthmus [Frazzetta et al. 1983].

In historical times, the Fossa Cone and Vulcanello were the sites of frequent and vigorous eruptions; mostly those occurred in the 6th and 16th century at Vulcanello and that occurred in 1888-1890 at the Fossa Cone. Vulcanello manifested intense fumarolic activity at least until 1878, as testified by the abundant sulphurous deposits around its slopes. The Fossa Cone is the present most active center, characterised by a persistent fumarole activity along the northern crater rim and slope, which was particularly intense in the period 1985-1995.

The volcanic history of the Fossa Cone includes various cycles of activity with a typical eruptive pattern. Frazzetta et al. [1984] firstly maintained that in case of further eruption, a volume smaller than that emitted during the last event of 1888-1890 ought to be released from an eruptive centre displaced either to west or to north of the present crater, in an area of greater structural weakness due to the persistent fumarole activity. Successively, Frazzetta and La Volpe [1991] stated that nature and volume of products emitted in the 1888-1890 event suggest that no further eruption should occur, having the Fossa Cone most likely concluded its evolution. The abnormal, alarming intensification of fumarole activity started in 1985, culminated in 1995 without eruption.

3. Presentation of the SP surveys at Vulcano

The 7 SP surveys were performed from May 1991 to December 1994, using a network of interconnected circuits spread over the whole island (dots in fig.2*a*). The SP maps are shown in fig.2*b* through fig.2*h* [redrawn after Di Maio et al., 1997].

A low wavenumber and roughly NW-SE oriented SP dipolar anomaly dominates over the whole island, subject to sign reversal, as *e.g.* from the map of fig.2*f* to the map of fig.2*g*. Superimposed on this field, high wavenumber anomalies are present, the most intense of which appear along the Fossa Cone rim and the eastern slopes of Vulcanello. Time migration and space shift of the local anomalies inside the Fossa Caldera can also be observed. A noteworthy anomaly with intermediate wavenumber appears in the area of Grotta Palizzi, across the Fossa Cone southern foothill and the Fossa Caldera rim. It is quite evident in the maps of fig.2*f* and fig.2*h*.

In order to enhance long-standing SP signals correlatable with the sources of the persistent volcanic activity, the steady component of

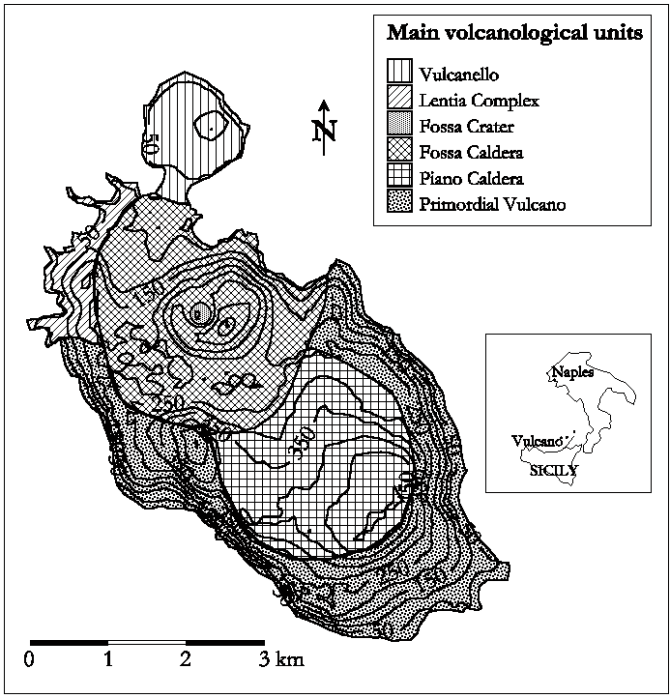

Figure 1. Sketch map of the outcropping volcanic units at Vulcano (Aeolian Arc, Italy).

the SP time varying field has been drawn by assigning at each station the weighted time average of the original SP values. Fig.3a shows the stationary SP map, in conjunction with the structural map of Vulcano [Ventura, 1994] sketched in fig.3b. The most interesting features are:

a) the chains of weak, short wavelength positive and negative anomalies along the whole Piano Caldera rim and western portion of the Fossa Caldera rim, both outlined in fig.3b;
b) two strong negative anomalies with higher wavelength, one located along the eastern side of Vulcanello and the other along the southwestern slopes of the Fossa Cone towards Grotta Palizzi.

4. Outline of the 3D probability tomography theory

In order to get information on the location of the sources of the SP anomalies shown in fig.3a, the 3D probability tomography (PT) method [Patella, 1997a,b] has been applied. An outline of the 3D PT theory is given at first, as follows.

Consider a Cartesian coordinate system with the (x,y)-plane placed at sea level and the z-axis positive downwards. Suppose to dispose of N SP datasets, collected in different times over the same grid of stations located at $\mathbf{r}\equiv(x,y,z)\in S$, where S is the survey surface defined by the elevation function $z(x,y)$. Indicate with $\mathbf{E}(\mathbf{r})=\langle\mathbf{E}_n(\mathbf{r})\rangle$ the weighted time average of the N natural electric field vectors $\mathbf{E}_n(\mathbf{r})$ $(n=1,2,..,N)$ over S, and assume that $\mathbf{E}(\mathbf{r})$ can be discretised as [Patella, 1997a,b]

$$\mathbf{E}(\mathbf{r}) = \sum_{q=1}^{Q} a_q \mathbf{s}(\mathbf{r}-\mathbf{r}_q) \qquad (1)$$

i.e. as a sum of partial effects due to Q source poles. The qth pole located at $\mathbf{r}_q\int(x_q,y_q,z_q)$ is given an average source strength a_q and its effect at $\mathbf{r}$ is governed by the function

$$\mathbf{s}(\mathbf{r}-\mathbf{r}_q) = \frac{\mathbf{r}-\mathbf{r}_q}{|\mathbf{r}-\mathbf{r}_q|^3} \qquad (2)$$

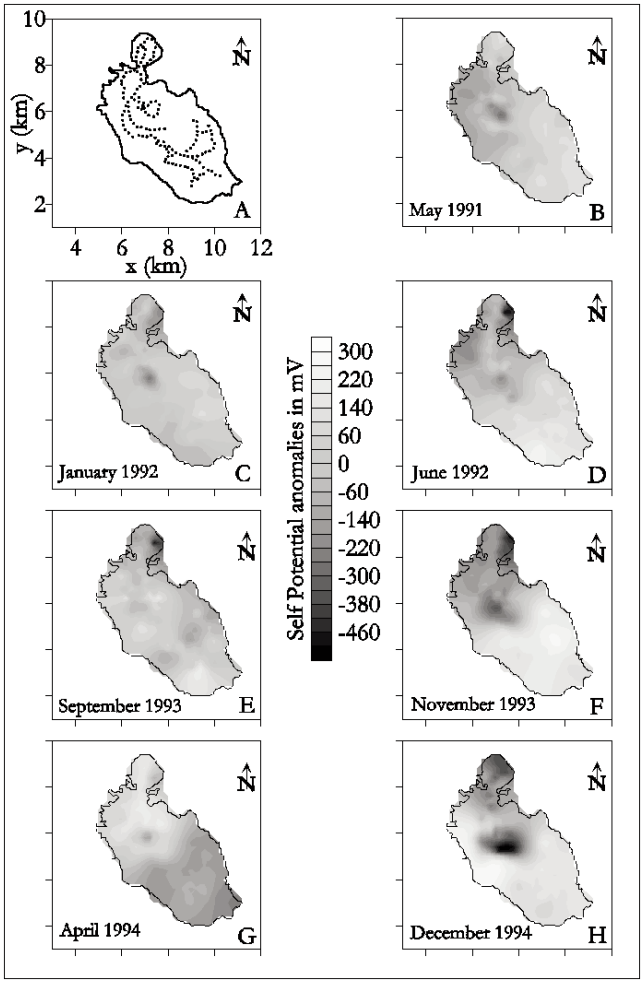

Figure 2. (a) The circuit network used to obtain the SP maps reported in pictures (b)-(h).

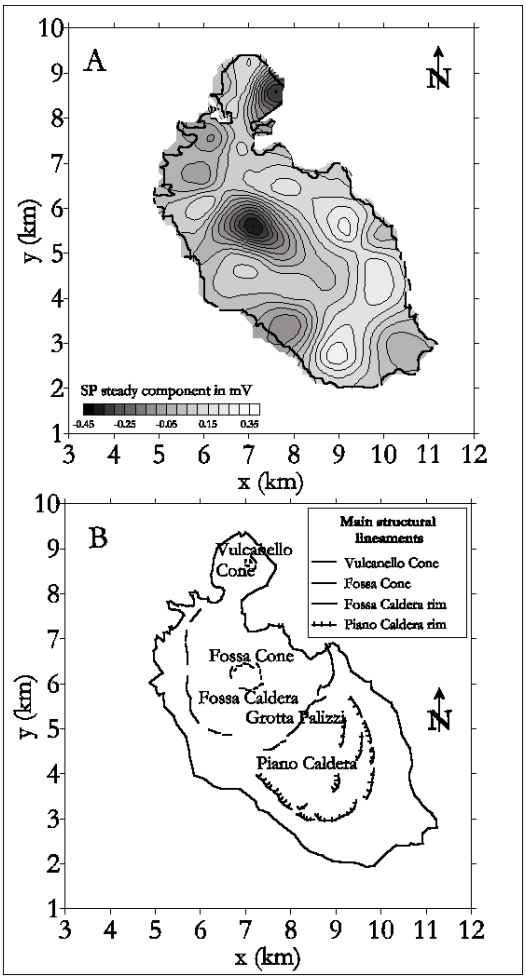

Figure 3. (a) The SP stationary map, obatained as weighted time average of the SP surveys drawn in fig. 2. (b) Schematic structural map of Vulcano.

Consider now the total signal power Λ associated with $\mathbf{E}(\mathbf{r})$ over S

$$\Lambda = \int_S \mathbf{E}(\mathbf{r}) \cdot \mathbf{E}(\mathbf{r}) dS \qquad (3)$$

which, using eq.1, can be expanded as

$$\Lambda = \sum_{q=1}^{Q} a_q \int_S \mathbf{E}(\mathbf{r}) \cdot \mathbf{s}(\mathbf{r} - \mathbf{r}_q) dS \qquad (4)$$

Take the generic qth term of eq.4 and apply Schwarz's inequality (5)

$$\left[\int_S \mathbf{E}(\mathbf{r}) \cdot \mathbf{s}(\mathbf{r} - \mathbf{r}_q) dS\right]^2 \le \int_S E^2(\mathbf{r}) dS \int_S s^2(\mathbf{r} - \mathbf{r}_q) dS$$

from which, indicating with $2X$ and $2Y$ the sides along the x- and y-axis, respectively, of the smallest rectangle containing the projection of S onto the x,y-plane [Patella, 1997b], a long-standing charge occurrence probability function $\eta(\mathbf{r}_q)$ is defined as

$$\eta(\mathbf{r}_q) = C_q \int_{-X}^{X} \int_{-Y}^{Y} \mathbf{E}(\mathbf{r}) \cdot \mathbf{s}(\mathbf{r} - \mathbf{r}_q) g(x) dx dy \qquad (6)$$

where (7)

$$C_q = \left[\int_{-X}^{X} \int_{-Y}^{Y} E^2(\mathbf{r}) g(x) dx dy \int_{-X}^{X} \int_{-Y}^{Y} s^2(\mathbf{r} - \mathbf{r}_q) g(x) dx dy\right]^{-1/2}$$

and

$$g(z) = \sqrt{1 + (\partial z/\partial x)^2 + (\partial z/\partial y)^2} \qquad (8)$$

The $\eta(\mathbf{r}_q)$ function, satisfying the condition $-1 \le \eta(\mathbf{r}_q) \le +1$, gives a measure of the average probability, which a negative ($\eta_n<0$) or positive ($\eta_n>0$) source pole obtain at $\mathbf{r}_q$ as responsible of the average $\mathbf{E}(\mathbf{r})$ field.

The role of probability attributed to $\eta(\mathbf{r}_q)$ is motivated as follows. In general, a probability measure $\mathbf{P}$ is defined as a function assigning to every subset g of a space of states G a real number $\mathbf{P}$(g) such that [Gnedenko, 1979]

$\mathbf{P}(\gamma) \ge 0$, for every γ, (9a)
$\mathbf{P}(\Gamma)=1$, (9b)
if $\gamma=\alpha\cup\beta$, with $\alpha\cap\beta\equiv 0$, $\mathbf{P}(\gamma)=\mathbf{P}(\alpha\cap\beta)=\mathbf{P}(\alpha)+\mathbf{P}(\beta)$. (9c)

Assuming that the presence of a source at $\mathbf{r}_q$ is independent of the presence of a source at another point, the function

$$\mathbf{P}(\mathbf{r}_q) = \frac{|\eta(\mathbf{r}_q)|}{\int_V |\eta(\mathbf{r}_q)| dV} \qquad (10)$$

where V is a generic volume including all non-null values of $|\eta(\mathbf{r}_q)|$, can be defined as a probability density, allowing a measure of the probability to find a pole at $\mathbf{r}_q$ to be made in agreement with axioms (9a,b,c).
Actually, eq.6 differs from eq.10 only for an unknown constant factor, appearing at the denominator of eq.10, and has the advantage of giving information on the sign of the sources. Therefore, $\eta(\mathbf{r}_q)$ can conventionally be assumed as a measure of the charge occurrence probability.

5. Analysis of the SP tomography at Vulcano

Fig. 4 shows the result of the application of the 3D PT imaging method to the average SP surface map, drawn in fig.3a. The horizontal tomoslices give a 3D representation of the $\eta(\mathbf{r}_q)$ function. Without imposing a priori constraints, a structural pattern of the most probable locations of electrical charge accumulations in the shallow part of the volcanic complex has thus

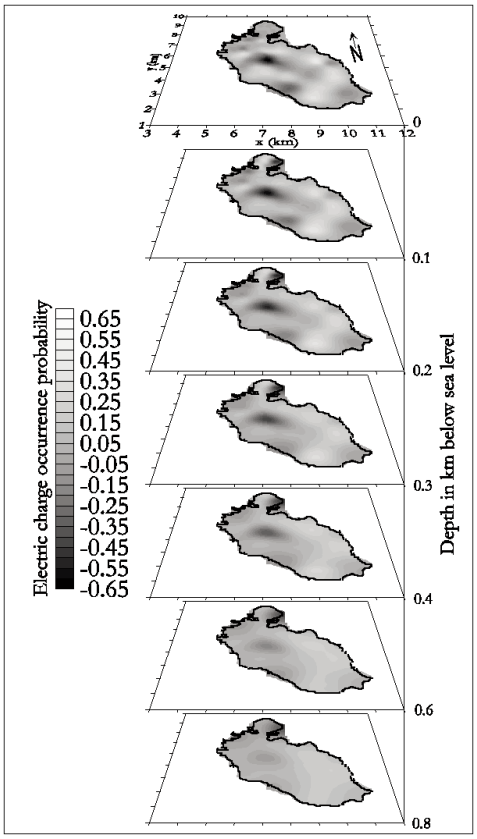

Figure 4. The 3D probability tomography of the average SP survey map drawn in fig. 3a.

been retrieved.

The most important features are:

a) the sources of the weak anomalies spread along the Piano and Fossa Caldera rims appear to be most probably located in a very shallow depth interval, not extending below sea level;
b) the intense anomaly at the eastern side of Vulcanello has a negative source, which shows the highest occurrence probabilities in the depth range 0.1-0.3 km bsl, with maximum occurring around 0.2 km bsl;
c) the Grotta Palizzi large anomaly has also a negative source, which shows the highest occurrence probabilities in a depth range not extending below 0.1 km bsl, with maximum occurring around sea level.

6. Conclusion

We have shown the results of the application of the 3D SP probability tomography method to the weighted average SP survey, calculated from 7 SP surveys performed in the period 1991-1994 at Vulcano, in order to highlight the presence of long-standing SP sources in fixed positions underground. The most important result of this analysis has been the presence of a negative source close to Grotta Palizzi, which is considered a place of great importance to understand the volcanic structure and dynamics of the Fossa cone. This source shows the higher occurrence probabilities in a depth range not exceeding 0.1 km bsl, with the maximum occurring around sea level. The next step will be the analysis of this SP source in the framework of the coupled flows theory, in order to establish if the SP anomalous and stable signal close to Grotta Palizzi is originated and fed by a stable pressure source.

Another important application will be the probability tomography analysis using an elementary dipole source scanner, in addition to the pole source scanner approach described in this paper, in order to assess the possible existence of zones where SP sources of electrochemical nature occur [Revil et al., 2001] and to resolve permeability boundary zones [Iuliano et al., 2002].

Acknowledgements

This work was supported by the Epot project of the GNV.

References

Barberi, F., Neri, G., Valenza, M. and Villari, L., (1991). *1987-1990 unrest at Vulcano*. Acta Vulcanol., 1, 95-106.

Di Maio, R., Di Sevo, V., Giammetti, S., Patella, D., Piscitelli, S. and Silenziario, C., (1996). *Self-potential anomalies in some Italian volcanic areas*. Ann. Geofis., 39, 179-188.

Di Maio, R., Mauriello, P., Patella, D., Petrillo, Z., Piscitelli, S., Siniscalchi, A. and Veneruso, M., (1997). *Self-potential, geoelectric and magnetotelluric studies in Italian active volcanic areas*. Ann. Geofis., 40, 519-537.

Di Maio, R., Mauriello, P., Patella, D., Petrillo, Z., Piscitelli, S. and Siniscalchi, A., (1998). *Electric and electromagnetic outline of the Mount Somma-Vesuvius structural setting*. J. Volcanol. Geotherm. Res., 82, 219-238.

Di Maio, R., Patella, D., Petrillo, Z., Siniscalchi, A., Cecere, G. and De Martino, P., (2000). *Application of lectric and electromagnetic methods to the definition of the Campi Flegrei caldera (Italy)*. Ann. Geofis., 43, 375-390.

Frazzetta, G., La Volpe, L. and Sheridan, M.F., (1983). *Evolution of the Fossa Cone*. J. Volcanol. Geotherm. Res., 17, 229-260.

Frazzetta, G., Gillot, P.Y., La Volpe, L. and Sheridan, M.F., (1984). *Volcanic hazards at Fossa of Vulcano: Data from the last 6000 years*. Bull. Volcanol., 47, 106-124.

Frazzetta, G. and La Volpe, L., (1991). *Volcanic history and maximum expected eruption at "La*

Fossa di Vulcano" (Aeolian Islands, Italy). Acta Vulcanol., 1, 107-114.

Gnedenko, B.V., (1979). *Kurs teorii verojatnostej*. Mir, Moscow.

Keller, J., (1980). *The Island of Vulcano*. Rend. Soc. It. Miner. Petrol., 32, 369-414.

Iuliano, T., Mauriello, P. and Patella, D., (2002). *Looking inside Mount Vesuvius by potential fields integrated geophysical tomographies*. J. Volcanol. Geotherm. Res., 113, 363-378.

Patella, D., (1997a). *Introduction to ground surface self-potential tomography*. Geophys. Prospect., 45, 653-681.

Patella, D., (1997b). *Self-potential global tomography including topographic effects*. Geophys. Prospect., 45, 843-863.

Revil, A. and Pezard, P.A., (1998). *Streaming electrical potential anomaly along faults in geothermal areas*. Geophys. Res. Lett., 25, 3197-3200.

Revil, A., Ehouarne, L. And Thyreault, E., (2001). *Tomography of self-potential anomalies of electrochemical nature*. Geophys. Res. Lett., 28, 4363-4366.

Ventura, G., (1994). *Tectonics, structural evolution and caldera formation on Vulcano Island (Aeolian Archipelago, Southern Tyrrhenian Sea)*. J. Volcanol. Geotherm. Res., 60, 207-224.

New Magnetotelluric Response on the Mt. Etna Volcano

Annalisa Zaja[1] and Adele Manzella[2]

[1]Dipartimento di Geologia, Paleontologia e Geofisica, Università di Padova,Via Giotto 1, 35123 Padova, Italy
[2]CNR-Istituto di Geoscienze e Georisorse, Via Moruzzi 1, 56124 Pisa, Italy

Abstract

During autumn 2001 some MT soundings, in a remote-reference mode, were carried out on the Mt. Etna volcano. Data were collected with 3 Metronix acquisition systems, one unit was located on the remote site in Calabria and the others on the Mt. Etna volcano along a W-E profile centred at Rifugio Sapienza. The obtained electrical resistivity section shows a conductive zone between 0 to 4000 m b.s.l. The lowest resistivity values, of the order of 1 Ωm, has been detected in the western part of the section. The conductor is interpreted as being due to magmatic intrusion at shallow depth. This intrusion was probably a remnant of the previous eruption that took place few months before the fieldwork, which did not emptied the magma stored at shallow level. This hypothesis would be also testified by the strong eruption started one year after the MT survey.

Key words *magnetotelluric sounding - 1D resistivity section - Mt. Etna volcano*

1. Introduction

In the last decade many geophysical methods have been applied to investigate the structure of the Mt. Etna volcano. The seismic model of Sharp et al. [1980] and the modeling of the deformation of Mt. Etna during its 1991-1993 major eruption from radar interferometry measurements [Massonnet et al., 1995] hypothesised a large magma chamber located at depth of 15-25 km within a crust of continental thickness. Seismic data [Hirn et al.,1997] suggested the presence of a upwelling mantle, capped by a lens of melt, located at a depth range of 15-20 km below Mt. Etna. Murru et al., [1999], using *b*-values of earthquakes recorded before 1997, suggested the presence of at least two major active magma reservoirs with radii less than 2 and 5 km, respectively, one located WSW of the summit at about 2km b.s.l., the other 2 km E of the summit at about 11 km b.s.l.

The structure beneath the volcano from the surface down to 18 km depth has been recently defined from seismic tomographic modeling [Chiarabba et al, 2000]. The main structural features defined by this recent seismic tomography consists of a high-velocity body located beneath the central craters, whose lateral extension is about 12 km between 3 and 9 km depth and about 6 km between 9 and 18 km depth. At shallow depth this body appears split in two high-velocity anomalies, located below the summit craters and the eastern flank (Valle del Bove), respectively. This high velocity body is interpreted as being due to solidified magma intrusions. Within this broad body, the authors hypothesise thin feeding systems below 9 km and small sized magma storage at depth shallower than 9 km.

Loddo et al., [1989], using deep dipole geoelectrics, excluded the presence of a shallow magmatic chamber as suggested by the absence of any geophysical markers down to about 3 km b.s.l. Mauriello et al. [2000] suggested, from 1D Bostick inversion of MT soundings, the existence of a wide conductive zone, with resistivities as low as few Ωm, located below the southern side of the volcano in the depth range 15-30 km.

The whole set of geophysical data suggests that the shallow volcanic structure cannot be considered in a static condition, and that the very dynamic nature of the structure is reflected by the clear and periodic change of physical parameters at depth.

This paper describes the result of a magnetotelluric (MT) survey on the southern flank of the volcano, with the aim of characterize the magmatic and still melted intrusion at depth. The conductive anomaly that has been defined is interpreted and discussed.

2. Data analysis

MT soundings were recorded with three Metronix acquisition systems during autumn 2001. One system recorded data in the remote site of Verzino, located in Calabria, while eleven soundings were carried out on the southern side of the Mt. Etna volcano, along a W-E profile centred approximately at Rifugio Sapienza (site 1). Figure 1 shows the location of the MT soundings.

Data were recorded in the frequency band of 40960 – 0.002 Hz. The high frequency bands were acquired during the daytime, whereas the lower frequency band was acquired during the night simultaneously on the volcano and the remote site.

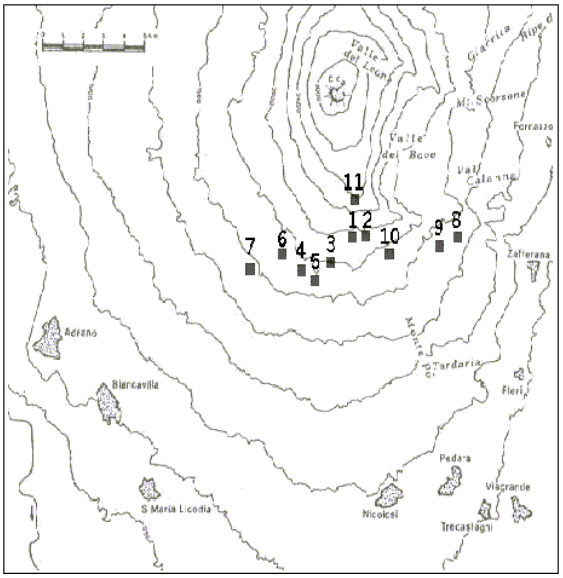

Figure 1. Location of the MT soundings on the Mt. Etna volcano

Due to presence of radio and telephone transmitters, MT data appeared affected by noise, especially in the high frequency range.

In order to remove the noise, data were processed using a robust code [Larsen et al., 1996]. Data could be processed in single-site mode, and the noise could be removed from data of all the sites except those recorded in the central part of the profile (site 1, 2 and 3 in Fig. 1) The obtained apparent resistivity and phase response curves of the MT soundings are shown in Figs. 2 and 3. For some not yet clear reason, the data acquired in the remote site appears scattered and out of phase with the data acquired simultaneously on the Etna volcano, and could not be used.

Beside the very noisy central sites, the MT sounding curves show a low scattered data and a regular behaviour for all soundings along the whole profile. These curves show high apparent resistivity values (500-1000 Ωm) at higher frequencies and low values (10 Ωm) at lower frequencies. This evidence suggests that below a resistive cover the detected volcanic structure is very conductive.

The use to plot data in the form of apparent resistivity and phase pseudosections helps to image the structure along the profile at different frequencies. The calculated apparent resistivity

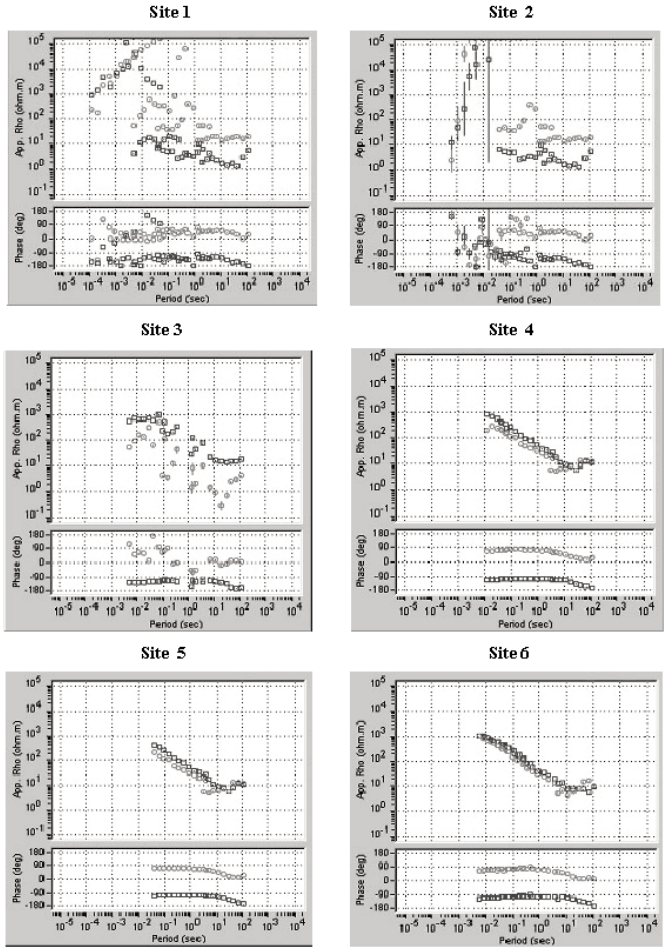

Figure 2. Apparent resistivity and phase curves along N-S and E-W directions

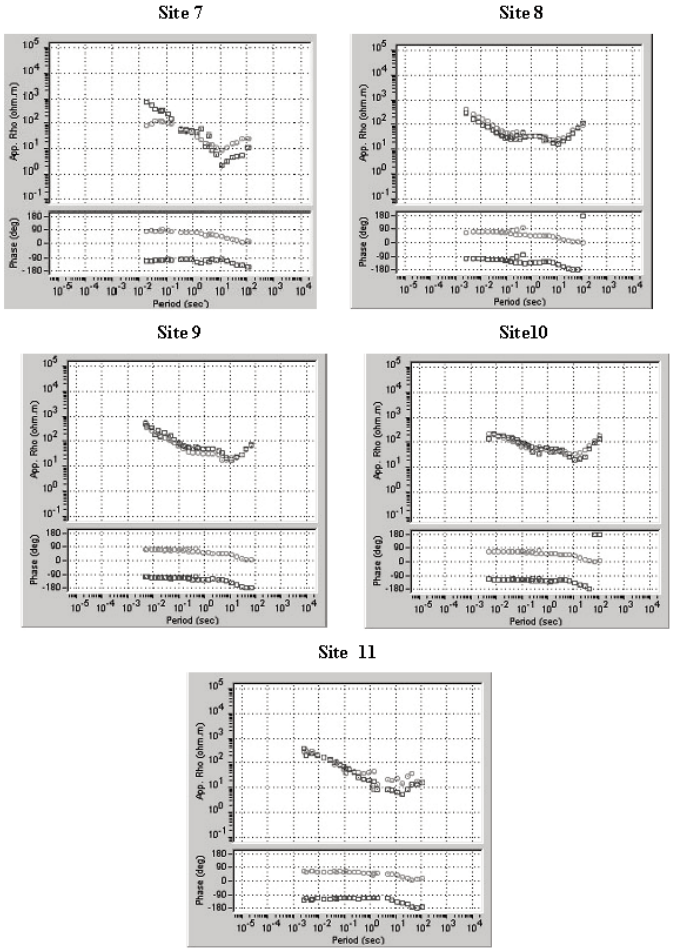

Figure 3. Apparent resistivity and phase response curves along N-S and E-W directions

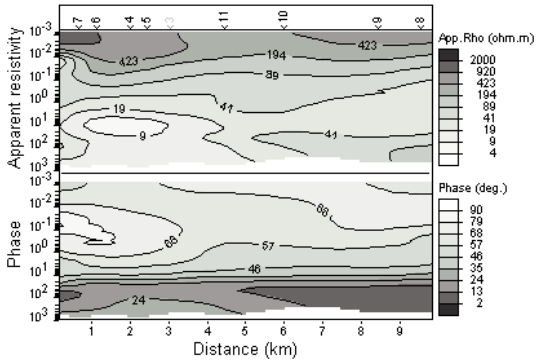

Figure 4. Apparent resistivity and phase pseudosections in the N-S direction

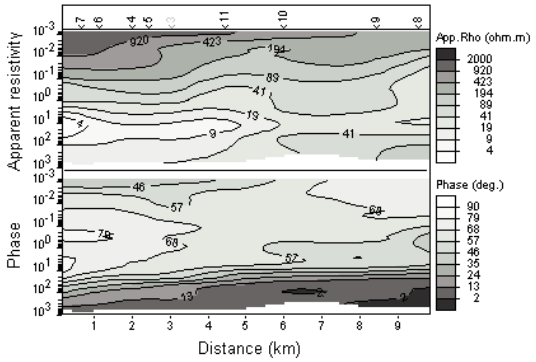

Figure 5. Apparent resistivity and phase pseudosections in the W-E direction

and phase pseudosections in the N-S and W-E directions are presented in Fig. 4 and Fig.5, respectively.

On both the apparent resistivity pseudosections, a very conductive area, for frequencies between 1 and 0.01 Hz and a maximum of phase anticipated for frequencies between 100 to 1 Hz is clearly visible on the western side of the profile. The very low values of phase, at very long periods, are possibly due to the presence of coherent noise on the recorded data which was not removed by a single site data processing.

To image the electrical volcanic structure at depth, data have been modeled using the 1D Bostick and the layered inversions.

In the 1D interpretative resistivity section, presented in Fig.6, it is possible to recognize:

• a very resitive shallow layer (~ 1000 Ωm).

The highest resistivity values are detected on

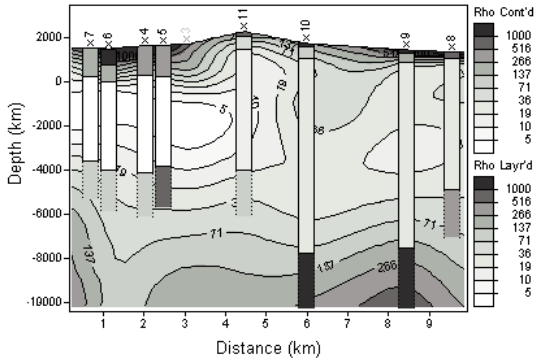

Figure 6. 1D Resistivity Section

the western flank of the volcanic apparatus;
• a very conductive layer (2-20 Ωm) at depth ranging between 0-4000 m b.s.l. The highest resistivity values are detected on the western side of the profile.

3. Discussion

The near surface resistive layer represents the volcanic cover. Its resistivity agrees with the shallow resistivity defined by Loddo et al. [1989], and Mauriello et al. [2000]. The very interesting and new feature defined in this survey with respect to those performed in the past is the very conductive body at a depth of 0-4 km, where previous survey indicated the presence of high resistivity. This body is shallower, thicker and more conductive on the western side of the investigated section. The conductive anomaly can be interpreted as being due to a magmatic intrusions, in the shallow crust, with a very high fluid fraction. In order to understand why we define such a different structure with respect to those defined in the past, we must take into account the particular period of our survey. The measurements were carried out only 3 months after the spectacular eruption of July 2001, and one year before the very long eruption of 2002-2003, which is still active at the moment. We hypothesise that the shallow magmatic intrusion storage that fed the 2001 eruption was not totally emptied during the eruption, and that a large quantity of melted material was present at shallow level during our survey. This hypothesis is proved by the fact that one year after the survey a new eruption started, and the amount of material that has been and is still being erupted could have never been accumulated in just one year.

4. Conclusion

The new MT soundings, collected during autumn 2001, produced a resistivity section along a W-E profile centred at the Rifugio Sapienza, on the southern side of the Mt. Etna volcano. This section defines the resistivity distribution of the volcanic structure down to the depth of 8 km. It shows a very conductive area between 0 to 4000 m b.s.l. that indicate the presence of melted material at shallow depth. We believe that the magma intruded at shallow level in the crust, which was imaged by our survey, has been then erupted during the 2002-2003 eruption. To support this interpretation, a repetition of the MT soundings is planned in next future. If the magma stored at shallow level has been totally erupted during the eruption of 2002-2003, the new resistivity section should be characterized by higher resistivity values corresponding to the real values of the near surface volcanic formations of the area. This image would be comparable with the one depicted by Mauriello et al. [2000]. This study testify the strong potentiality of MT method in defining the shallow volcanic structure of Etna volcano, and for monitoring the magmatic activity.

Acknowledgements

Metronix Company is acknowleged for providing the three systems for the demo project, and in particular Bernhard Friedrichs for the technical support during the survey. We thank Nicola Praticelli, Giampaolo Girardi and Alessandro Maretto for their help during the fieldwork. This research was financially supported by the GNV through the Epot project.

References

Chiarabba C., Amato A., Boschi E., (2000). *Recent seismicity and tomographic modeling of the Mount Etna plumbing system.* Journal of Geophysycal Research, Vol.105, No. B5, p.10,923-10,938.

Hirn A., Nicolich R., Gallart J., Laigle M., Cernobori L., ETNASEIS Scientific Group (1997). *Roots of Etna volcano in faults of great earthquakes.*Earth and Planetary Science Letters, 148, p.171-191.

Larsen J.C., Mackie R., Manzella A., Fiordelisi A., Rieven S., (1996). *Robust smooth magnetotelluric transfer function.*Geophys. J. Int., 124, p.801-819

Loddo M., Patella D., Quarto R., Ruina G., Tramacere A., Zito G. (1989).*Application of gravity and deep dipole geoelectrics in the volcanic area of Mt. Etna (Sicily).* Journal of

Volcanology and Geothermal Research , 39, p.17-39

Massonnet D., Briole P. And Arnaud A. (1995).*Deflation of Mount Etna monitored by spaceborne radar interferometry.* Nature, 375, p.567-570.

Mauriello P., Patella D., Petrillo Z., Siniscalchi A. (2000) *An integrated studies of M.te Etna volcanic structure.* Annali di Geofisica, 43, N.2, p.325-342.

Murru M., Montuori C., (1999). *The location of magma chamber at Mt. Etna, Italy, mapped by b-values.* Geophys. Res. Lett., vol.26, N.16, p 2553-2556.

Sharp A.D.L., Davis P.M.and F.Gray (1980). *A low velocity zone beneath Mount Etna and magma storage.*Nature 287, p.587-591.

Electrical Modelling of the Shallow Structural Setting of the Cisternazza-Montagnola Area (Mt. Etna)

Giuseppe Della Monica[1], Rosa Di Maio[2], Roberto Scandone[1], Gianpaolo Cecere[3], Ciro Del Negro[4], Prospero De Martino[3], Francesco Santochirico[2]

[1]*Dipartimento di Fisica, Università Roma Tre, Roma, Italy*
[2]*Dipartimento di Scienze Fisiche, Università di Napoli Federico II, Napoli, Italy*
[3]*Istituto Nazionale di Geofisica e Vulcanologia - Osservatorio Vesuviano, Napoli, Italy*
[4]*Istituto Nazionale di Geofisica e Vulcanologia – Sezione di Catania, Italy*

Abstract

We present the results of a study concerning the definition of the main structural lineaments and the dynamic processes characterising the shallower crustal portion of the south-eastern sector of the Mt.Etna by electric-type geophysical methods. At this end, using the self-potential and the geoelectrical techniques, a geophysical exploration was performed in a test-site (Cisternazza-Montagnola area) interested by the eruption events of July-August 2001. In particular, a self-potential survey, in an area of about 2 km^2, and a geoelectrical tomography, along a profile 1200 m long, have permitted to model the buried volumes down to a depth of about 300 m below ground level. The presence of low resistivity and high charge occurrence probability values in the central portion of the investigated area, to a depth of about 150 m b.g.l., seems to indicate the occurrence of a shallow groundwater flow.

Key words *applied geophysics - electric methods - volcanology*

1. Introduction

During the recent Etna eruption of July-August 2001, the vent at height of 2550 m a.s.l. had a moderate explosive activity probably caused by magma-water interaction. On 19 July 2001, two days after the beginning of the eruption, two pit craters opened at 2550 m a.s.l. on the SE flank of Etna. The initial eruptive activity was characterised by frequent explosion with the emission of ashes which were dispersed to the SE of the volcano in direction of Catania. Between 24 and 31 July the activity of these craters was characterised by strombolian explosion and the emissions of several lava flows. The strombolian activity built an impressive scoria cone. The lava flows destroyed the upper station of the cableway, and menaced the touristic settlement of Rifugio Sapienza. On the 31 of July, in coincidence with the end of the lava flow emission, there was a renewal of ash explosions. This activity slowly subsided with the general trend of the eruption. Overall this activity may be due to different degree of interaction between magma and water, depending on the height of the magma head in the conduit.

As the main damages of the eruption were caused by the ash dispersion coming from this vent, it is necessary a better knowledge of the mechanisms dominating this kind of Etnean activity by the individuation, if any, of the shallow groundwater circulation network. Since the electric parameters are strongly dependent on temperature and pressure, as well as on the presence and abundance of mineral particles and fluids, a relevant role is played, in principle, by the electric geophysical methods in investigating volcanic environments. Recent studies, performed in the main Italian volcanic areas [Di Maio et al., 1997, 1998a, 1998b, 2000], have demonstrated that a joint use of high resolution tomographic geoelectrical methodologies, in particular of self-potential (SP) and dipolar geoelectrics (DG), seems capable of revealing the most important shallow-sited electrical charge polarisation and resistivity variations, most probably caused by rock-water-magma interactions in active areas, and more generally, by invasion and circulation of hot fluids in porous media and/or along permeable fracture systems.

Indeed, the analysis of the SP signals, observed on the surface with multi-channel acquisition techniques along profiles or by sensor areal distribution, can fruitfully put in evidence double layer like anomalies across fractures, particularly enhanced in presence of fluid flows through them. With an appropriate integral transformation of the observed SP data (cross-correlation power analysis) according to a sectional tomographic representation, it is possible to obtain the structural configuration of the electrokinetic paths and further delineate the buried geometries, as well as to understand the role of water solutions and their interaction in the deep dynamics of the fractured systems.

An important contribute to a better definition of the structural features depicted by the above mentioned SP prospecting is provided by the DG tomography. Indeed, it is deputed to give a high-resolution image of the subsoil structural pattern on the basis of the resistivity contrasts characterising the various geologic

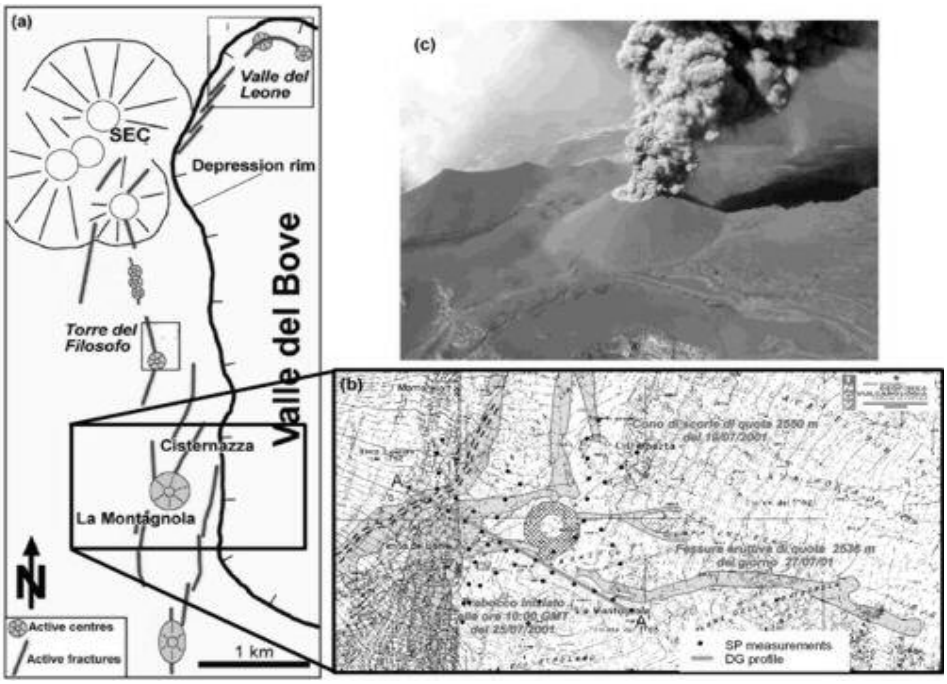

Figure 1. (a) Schematic map of fractures and volcanic centres developed during the July-August 2001 eruption of Mt.Etna (from Billi et al., 2003, modified). (b) Geophysical survey area. The dotted circuits and the AA' full line refer, respectively, to the self-potential survey and the dipolar geoelectric profile. (c) Eruptive vent at 2550 m a.s.l. (from INGV-CT).

bodies in contact to each other inside the maximum lateral and vertical investigation ranges. Besides this fundamental property, the DG tomographic approach, gets also useful information helping to understand the meaning of some SP anomalies, particularly those which are related to charge distributions along resistivity discontinuity planes, induced by the SP primary sources.

In this paper, we present the results of self-potential and geoelectrical measurements performed in the Cisternazza-Montagnola area, in the framework of a study concerning the definition of the main structural lineaments and the dynamical behaviour of the feeding and uprising systems characterising the shallower crustal portion of the south-eastern sector of the Mt. Etna.

2. Self-potential survey

The SP data were obtained by measuring the potential difference existing between two grounded copper rod electrodes, which were continuously displaced along the circuits reported in fig. 1b. The mutual distance between every two consecutive electrode positions was taken constantly equal to 50 m. A total of 96 SP drop measurements, distributed over an area of about 2 km^2, were collected. Figure 2 shows the elaborated SP final map. Separation between negative and positive SP anomalies is marked by the black zero-valued thick line, which was drawn after shifting the SP zero, originally attributed to an arbitrary reference station for the calculation of the initial set of SP mapping values, to all points corresponding to the average SP value of the initial set. For further details about the SP measuring system, survey technique and data processing the reader is referred to a previous paper [Di Maio et al., 1996].

From a qualitative point of view, the SP map shows the investigated area characterised by a low wavenumber regional trend with prevailing "negative" SP values in the western sector and "positive" SP values in the central-eastern sector. The demarcation band of this bipolar field is defined by a crowding of the SP isolines in the westernmost part of the surveyed area, along a nearly N-S direction. Superimposed on this regional trend there appear high wavenumber local anomalies. It is interesting to note the pattern of the isolines in some transition zones from positive to negative SP values, that sounds correlated to the fracture systems, so as displayed in fig.1a. Therefore, such a feature could be indicative of shallow electric charge accumulations along the structural discontinuity planes, where in primary electrokinetic fluid streams could be the sources of the observed anomalies. Finally, the negative SP anomaly in the north-

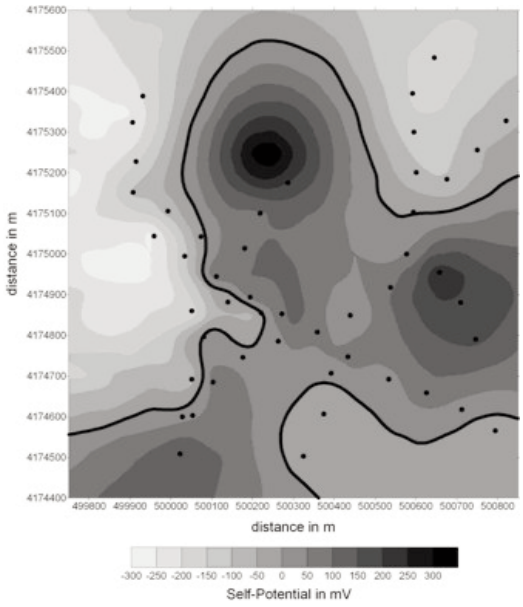

Figure 2. The self-potential survey map.

eastern part of the map, seems well delineate the border of the Cisternazza caldera, interested by fluid circulation.

In order to elicit from the SP survey map of fig. 2 the most quantitative information on the depth location of the polarisation field sources, we have adopted a tomographic imaging procedure [Di Maio and Patella, 1994, Patella, 1997a] of the SP anomalies including topographic effects [Patella, 1997b]. Briefly, the 3D tomographic approach aims at the recovering of the underground electric charge distributions through a cross-correlation procedure between the observed natural electric field and a theoretical *scanner* function, representing the synthetic SP response on surface of an elementary positive charge with unitary intensity, located in any generic point of the subsoil. Then, by a normalisation procedure of the cross-correlation operator based on Schwarz's inequality, it is possible to define a *charge occurrence probability func-*

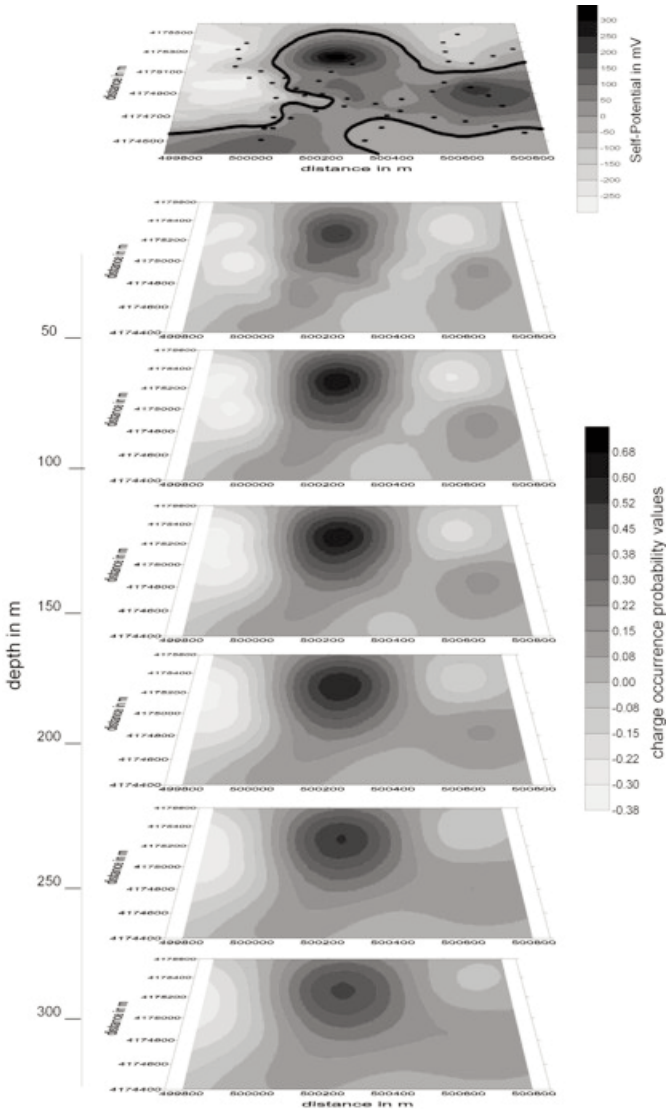

Figure 3. 3D self-potential probability tomography in the depth interval from 50 m to 300 m b.g.l.

tion (COP) [Patella, 1997a], constrained to vary inside the interval [-1,1]. Positive values are the result of a major influence from positive charge accumulations, while negative values result from negative charge concentrations. Finally, by a suitable 3D grid distribution of probability values in the investigated volume, the tomographic image can be drawn for inspecting the pattern of the polarisation source centres in a probabilistic sense.

Figure 3 shows the 3D tomographic inversion of the SP data displayed in the map of fig. 2, and here reported again at the top of the figure. The tomography refers to shallow images between 50 m and 300 m below the ground level (b.g.l.). As for the shallowest part of the underground investigated volume, it is interesting to note, in the north-eastern sector of the first slice of the tomographic sequence, a negative charge accumulation, whose maximum COP values are observed at depth of about 70 m b.g.l. According to our previous hypothesis, this depth indicates the bottom of the Cisternazza crater.

Moreover, the E-W oriented dipolar field, already shown by the SP isoline pattern of fig. 2, now appears clearly evident. The charge accumulations have the highest absolute COP values in the range 100-150 m b.g.l. for both negative and positive nuclei. The depth location and intensity of these clusters seem to outline a structural discontinuity characterised by a conspicuous fluid circulation, very likely ascribable to the N-S fracture system (Fig.1a) developed on top of Mt.Etna during the July-August 2001 eruption [Billi et al., 2003].

3. Geoelectrical tomography

In order to verify the occurrence of a significant underground fluid circulation, as suggested by the results of the SP survey, a ultra-high resolution (u.h.r.) geoelectrical tomography [Worthington, 1984] has been carried out along the profile indicated in fig.1b with the AA' full line. This technique is able to give an extremely detailed picture of the electric resistivity behaviour across the vertical plane through the profile. In fact, following Worthington [1984], the u.h.r. geoelectrical pseudosection can be classified as a first-order tomography, for it can provide, in a truly objective way and prior to any data inversion program, symptomatic resistivity anomaly images across the investigated section. Indeed, sophisticated 2D and 3D inversion procedures applied to many field examples have shown that the complex geometries of the interpreted models are closely reflected in the original pseudosection images [see, *e.g.*, Loke and Barker, 1995, 1996; Turberg and Barker, 1996; Dahlin, 1996].

Figure 4 shows the DG apparent resistivity pseudosection across the selected profile. The DG data were obtained with dipoles of 100 m of length and the measured dipolar apparent resistivities were attributed at a pseudodepth equal to half the spacing between the centres of the emitting and receiving dipoles, along the median axis through the line joining the two dipoles. Continuous displacement of the dipoles along the selected profile of 1200 m of length provided a very dense network of about 54 experimental data points in the vertical pseudosection.

Looking at the fig. 4, relatively high apparent resistivity values (higher than 1000 Ωm) characterise the shallower portion of the pseudosection, very likely ascribable to fractured volcanics saturated with waters. In fact, the resistivity values describing dry volcanic materials generally exceed the observed values

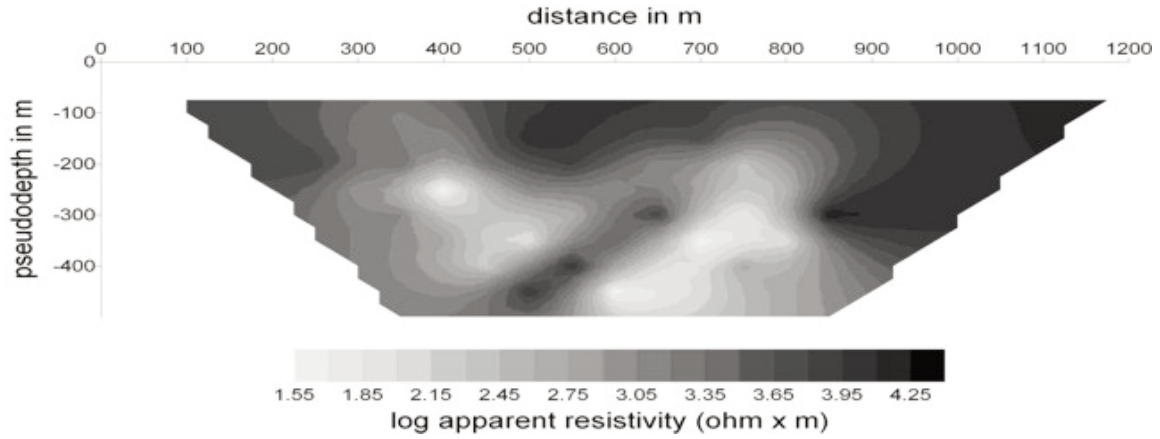

Figure 4. DG apparent resistivity pseudosection along the AA' profile shown in Fig. 1b.

of about two orders of magnitude. This hypothesis is in agreement with the V_p and V_p/V_s models given by Patane et al. [2002]. The authors, indeed, observe in the shallower part of the investigated area low P-wave velocities and high V_p/V_s values, which they correlate to sedimentary rocks where water-filled pores and cracks exist. Moreover, very interesting appears, for the purposes of our study, the resistivity anomaly pattern in the deeper zone of the pseudosection: a resistive dyke-like configuration seems to intrude inside conductive walls. The resistivity values characterising the conductive blocks bring to hypothesise the presence of a groundwater flow, while the values describing the resistive body seem to suggest the presence of solidified lava, due to magma uprising which originated the eruptive vent at 2550 m a.s.l.. Therefore, the presence of a local water table, outlined by the electric investigation at a depth of about 150 m b.g.l, could justify a magma-water interaction [Taddeucci et al., 2002], which conferred to the 2001 eruption an explosive character.

4. Concluding remarks

We have presented and discussed the results of an electric-type geophysical survey in the south-eastern sector of the Mt.Etna (Cisternazza-Montagnola area). Self-potential (SP) and dipolar geoelectrics (DG) were used to investigate the shallower crustal portion of the area site of July-August 2001 eruption.

As it concerns the SP method, the main result was the evidence of a roughly N-S fracture system (Fig. 3) to west of the vent opened during the eruption at 2550 m a.s.l.. The successive SP data analysis, through a tomographic imaging procedure, has been able to define the depth of the fluid flow, which probably feeds the outlined fracture system. Indeed, the occurrence of electric positive and negative charge accumulations in the depth range 100-150 m b.g.l. (Fig. 4), brought to hypothesise the presence of a shallow aquifer, responsible of the phreatomagmatic activity observed in some phases of the July-August 2001 eruption. This interpretation conforms to the result pointed out by the DG tomography, performed along a profile crossing the quoted fracture system. The presence, in fact, of a largely extended relatively low resistivity zone at a depth of about 150 m b.g.l. seems ascribable to a local water table, which caused magma-water interactions.

Noteworthy was also the evidence of a high-resistivity intrusive body in the deep central portion of the DG pseudosection (Fig. 4). The pattern of this resistive anomaly lets foresee the occurrence of the dyke that fed the activity of the vent.

Acknowledgements

We thank A. Bonaccorso for help provided to realise the measurement campaign and G. Macedonio who authorised personnel of the Osservatorio Vesuviano to participate in the geophysical survey. Sincere thanks to S. Riccioli and P. Aloe for the invaluable help in the field work. Study performed with financial support from INGV (Catania Section).

References

Billi, A., Acocella, V., Funiciello, R., Giordano, G., Lanzafame, G. and Neri, M., (2003). *Mechanisms for ground-surface fracturing and incipient slope failure associated with the 2001 eruption of Mt.Etna, Italy: analysis of ephemeral field data*. Journal of Volcanology and Geothermal Research, 122, 281-294.

Dahlin, T., (1996). *2D resistivity surveying for environmental and engineering applications*. First Break, 14, 275-283.

Di Maio, R. and Patella, D., (1994). *Self-potential anomaly generation in volcanic areas. The Mt.Etna case-history*. Acta Vulcanologica, 4, 119-124.

Di Maio, R., Di Sevo, V., Giammetti, S., Patella, D., Piscitelli, S. and Silenziario, C., (1996). *Self-potential anomalies in some Italian volcanic areas*. Annali di Geofisica, 39, 179-188.

Di Maio, R., Mauriello, P., Patella, D., Petrillo, Z., Piscitelli, S., Siniscalchi, A. and Veneruso, M., (1997). *Self-potential, geoelectric and magnetotelluric studies in Italian active volcanic areas*. Annali di Geofisica, 40, 519-537.

Di Maio, R., Mauriello, P., Patella, D., Petrillo, Z., Piscitelli, S. and Siniscalchi, A., (1998a). *Etna: Self-potential, geoelectric and magnetotelluric measurements*. In: Data related to eruptive activity, unrest phenomena and other observations on the Italian active volcanoes - 1993-1995 (P.Gasparini, ed), Acta Vulcanologica, 10(1), 187-193.

Di Maio, R., Mauriello, P., Patella, D., Petrillo, Z., Piscitelli, S. and Siniscalchi, A., (1998b). *Electric and electromagnetic outline of the Mount Somma-Vesuvius structural setting*. Journal of Volcanology and Geothermal Research, 82, issue 1-4, 219-238.

Di Maio, R., Patella, D., Petrillo, Z., Siniscalchi, A., Cecere, G. and De Martino, P., (2000). *Application of electric and electromagnetic methods to the definition of the Campi Flegrei caldera (Italy)*. Annali di Geofisica, 43, 375-390.

Patane, D., Chiarabba, C., Cocina, O., De Gori, P., Moretti, M. and Boschi, E., (2002). *Tomographic images and 3D earthquake*

locations of the seismic swarm preceding the 2001 Mt.Etna eruption: Evidence for a dyke intrusion. Geophysical Research Letters, 29, 135-1÷135-4.

Patella, D., (1997a). *Introduction to ground surface self-potential tomography.* Geophysical Prospecting, 45, 653-681.

Patella, D., (1997b). *Self-potential global tomography including topographic effects*. Geophysical Prospecting, 45, 843-863.

Taddeucci, J., Pompilio, M. and Scarlato P., (2002). *Monitoring the explosive activity of the July-August 2001 eruption of the Mt. Etna (Italy) by ash characterization*. Geophysical Research Letters, 29, 71-1÷71-4.

Turberg, P. and Barker, R., (1996). *Joint application of radio-magnetotelluric and electrical imaging surveys in complex subsurface environments*. First Break, 14, 105-112.

Worthington, M.H. (1984). *An introduction to geophysical tomography*. First Break, 2, 20-26.

Bouguer Correction for a Spherical Earth: Application to the Etna Data

Mariano Loddo and Domenico Schiavone

Dipartimento di Geologia e Geofisica, Università di Bari

Abstract

The procedures to perform complete Bouguer corrections are a critical concern mainly when rugged topographies and large investigation areas are interested. These corrections generally include the simple slab and terrain corrections. In recent years it was recognized that a curvature correction is necessary also for exploration surveys. In order to standardize the correction parameters and to allow the joining together of different data sets, the choice of an outer radius of 166.7 km was suggested for the complete Bouguer correction. This paper presents an automatic procedure to perform the Bouguer correction considering as reference the spherical surface through each gravity station. The terrain correction in the "outer zone" (from 2.5 km to 166.7 km) is performed calculating, from gridded average elevation data, triangular polyhedra with a face on the reference sphere. For the "inner zone" (station to 2.5 km) triangular polyhedra are constructed by modelling the topographic surface with a triangular faceted surface resulting from the Delaunay triangulation of the digitized elevation data. An example of the application of the proposed procedure to the Etna gravimetric data is shown.

Key words *Bouguer correction - gravimetric data - Mt. Etna*

1. Introduction

As it is well known the Bouguer anomaly represents the residual values between the observed gravity and the gravity components generated by a simple earth model (the ideal earth model). As stated by Chapin (1996) the gravity corrections, adopted for obtaining the Bouguer anomalies, "attempt to make up for the incorrect assumptions made in the original earth model". It was lengthy debated in the last ten years in the scientific community on the procedures to carry out the corrections for prospecting targets, mainly as regards the earth model to adopt for the simple Bouguer correction (a planar model or a spherical one) and the limit to which the terrain corrections should be applied [LaFehr, 1991a, 1991b, 1998; Talwani, 1998]. Following LaFehr (1998), if major changes in elevation occur between stations also for local surveys a spherical cap with surface radius of 166.7 km from a station must be considered both for the simple Bouguer correction and the terrain one. The selection of this distance, although arbitrary, is justified by the need of standardization in the correction procedures. As a consequence of this choice it is (1) avoided the introduction of fictitious elevation-dependent anomalies and (2) eliminated the occurrence of misties between independently conducted adjacent or overlapping surveys [LaFehr, 1991a, 1998].

We consider the argumentations of LaFehr well founded and his standardization requirement to be observed for gravity surveys in a large part of the Italian territory.

In this paper we present a procedure for the complete Bouguer correction with an example of application to the Etna field data.

2. Complete Bouguer correction

The classical complete Bouguer correction is a three-step procedure [Bullard, 1936]:

- Simple Bouguer correction (Bullard A) – it is an elevation correction where the air in the Free-air correction is replaced by an infinite slab filled with rock.
- Curvature correction (Bullard B) – it attempts to correct the physically unaccountable slab model of the earth making its shape more realistic; it is not generally used.
- Terrain correction (Bullard C) – it accounts for the topography around the station out to the maximum distance assumed to produce a meaningful contribution to the data values.

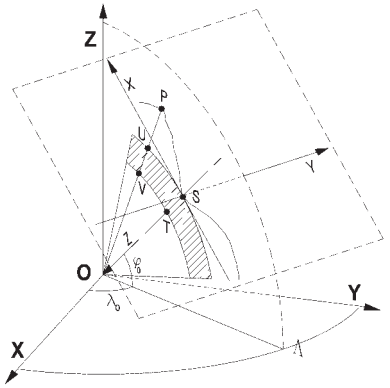

Figure 1. Sketch of the topographic surface and the spherical cap (dashed area) in the meridian plane ZOΛ and geometrical relationship between ellipsoidal coordinates and Cartesian coordinates used for terrain correction.

2.1. Bullard A+B correction

The simple Bouguer correction and the curvature one can be unified in a single step considering directly a spherical cap. Fig.1 shows, in a meridian plane, a sketch of the topographic surface and the spherical cap around a station S. See LaFehr (1991b) for the algorithms to calculate the attraction of a spherical cap.

2.2.Terrain correction

The procedure to correct gravimetric data for the topographic relief around the stations is the processing step more susceptible to introduce errors in the computed anomalies. This accounts for the large number of papers on this subject published in the last several decades.

Considering, for simplicity, only the completely automated methods, the difference among them is the way the topographic surface is mathematically represented.

The starting point is a digital representation of the topographic surface. The digital earth models (DEM or DTM) represent the surface at the nodes of a regular grid through elevation or mean values. The used gridded data come from databases, when available, or are specially constructed for a study area.

Considering the inverse square distance law for gravitational attraction, an increasing accuracy in the surface approximation is necessary, the distance from the station decreasing. To take into account this requirement, moving out from the station the area is generally divided into different zones in which different strategies are adopted for the correction. Thus, an inner or near zone and an outer or distant zone are generally considered. In some cases one or more intermediate zones are introduced between the previous ones [Blais and Ferland, 1984; Ma and Watts, 1994].

Fundamentally, for the inner zone, the gridded data are fitted with a mathematical surface – a set of Gaussian functions [Herrera-Barrientos et al. 1991], a multiquadric equation [Krohn, 1976], a triangle-based surface [Cogbill, 1990] – and interpolated values computed at a more dense grid points distribution [Blais and Ferland, 1984] or mean values calculated in circular sectors similar to the Hammer's chart [Herrera-Barrientos and Fernandez, 1991]. Once this is done, corrections are calculated using different approximations of the surface: flat-top prisms [Hammer, 1939], inclined-top circular prisms [Olivier and Simard, 1981], dipping triangular elements [Zhou et al., 1990].

While for the distant zones a regular structure of the data could be justified by data storage needs in the framework of databases covering large areas (at a regional, state or global scale), the complex procedures adopted to represent the topography in the area nearest a station seem to us unjustified for the nowadays computer memory and power capabilities.

Our reasoning is the following. The original digital terrain data are produced from maps or aerial photographs by manual digitizing, semi-automatic line following or automatic raster scanning or provided by digital satellite imageries. Whatever be the method to generate surfaces from the data, the accuracy of the reconstruction cannot be better than the original data. Any other processing step applied to the data is likely to misrepresent the terrain model and to introduce errors in the terrain correction. Besides, with reference to the application of the surface modelling to gravity data correction, we must consider that hardly the position of the gravity stations coincide with the nodes of a DTM, requiring a supplemental approach to introduce them into computation [Ma and Watts, 1994]. Hence, a method directly using the irregular distribution of the original data is, to our opinion, more suitable to perform, at the maximum accuracy contained into the elevation data and in a simpler way, the modelling of the topography.

Triangulated Irregular Networks (TINs) represent a data structure that directly relies on data. Terrain models are consequently represented by triangular faceted surfaces. Triangulated surface models are the most widely used in many different application domains, including computer graphics, geographic data processing, computer vision and computer aided design. The advantage of this method is the possibility of including surface features and on the simplicity of the topological structure. In the framework of digital terrain modelling, triangle-based models allow for the variable resolution connected with different topography behaviours. Thus, TINs succeed in representing a surface at a certain level of accuracy using a smaller amount of data.

Among the methods for triangulating a set of irregularly spaced points in 2-D and 3-D spaces, the Delaunay one satisfies some optimality criteria. In particular, the method generates triangles that are as much equiangular as possible [Lawson, 1977; Preparata and Shamos, 1985], thus avoiding thin and elongated triangular facets, it minimizes the maximum circumcircle [D'Azavedo and Simpson, 1989] and the maximum contained circle [Rajan, 1994] (the last two conditions can be equivalently

expressed as follows: considering any four points, such points do not belong to the same circle).

Using the triangulation method, the terrain correction can be carried out through triangular prisms [see, for example Zhou et al. 1990].

3. Terrain correction method

Fig. 2 shows the scheme adopted for the terrain correction. The inner zone is defined as the 5 km^2 square region centred at each station. In this zone the height field is approximated from digitized 1:25000 topographic maps through Delaunay triangulations.

There are many Delaunay triangulations algorithms with different computer speed and memory requirements [see, for example: Barber et al. 1996; Bourke, 1989; Renka, 1984; Shewchuk, 1996, 1997, 2002]. Among the freely available computer routines we have preferred the Triangle program by Shewchuk (1996) for its efficiency and computational speed. Fig. 3 shows an example of digitized points and the resulting triangulations. For drawing clarity it is represented only the 1 km^2 area surrounding the station.

In the distant zone, between the inner one and the circular, 170 km radius, outer edge the topography is approximated by 7.5"x 10" gridded data representing mean elevation values. The gravity effect of the topography both in the inner and outer zones is evaluated considering triangular polyhedra. The relationships for homogeneous polyhedral bodies by Okabe (1979) are used. The faces of the polyhedra are

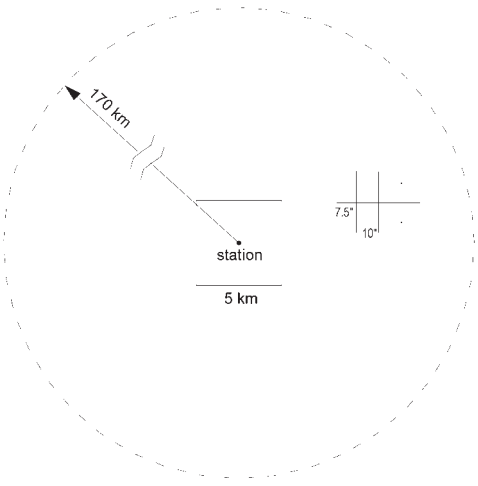

Figure 2. Definition of the inner and outer zone for topographic correction and grid spacing used to represent the topography in the outer zone.

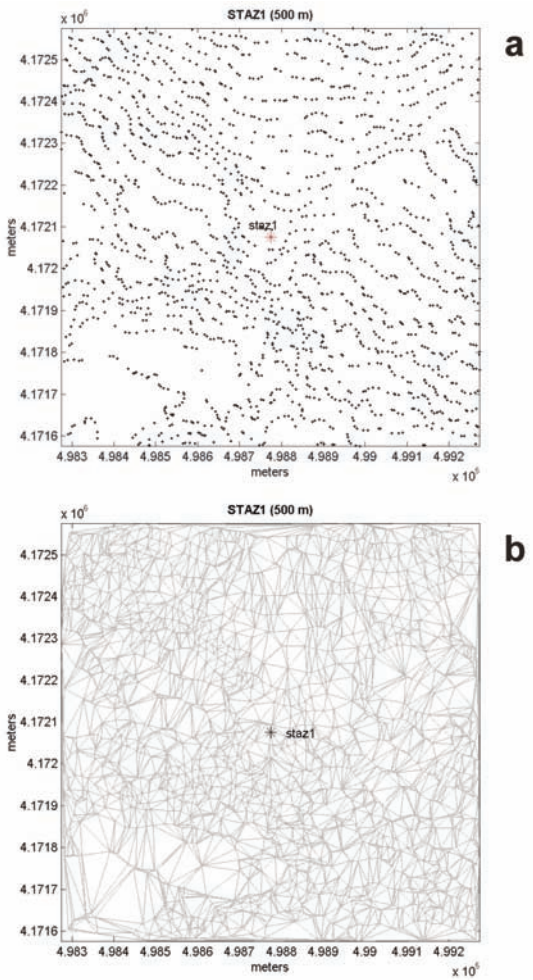

Figure 3. Method used to approximate the topographic surface in the inner zone; a) example of digitized elevation points around staz1 and b) resulting Delaunay triangulations.

the triangular facets in the inner zone and three neighbouring grid values in the outer zone, on the topographic surface, and their geocentric projections on the reference sphere, respectively. To apply the Okabe's formulae transformations from ellipsoidal to plane coordinates are needed. In particular, from figure 1, assuming the local sphere at each station to approximate the ellipsoid, a station S, a generic point P on the surface and its projection on the sphere U, have ellipsoidal coordinates $S(r_0,\varphi_0,\lambda_0)$, $P(r,\varphi,\lambda)$ and $U(r_0,\varphi,\lambda)$, respectively; where $OT=OV=R_0$ is the mean earth radius, $TS=h_0$ and $VP=h$ are the heights above the mean sea level of the station and the point, respectively, $r_0=R_0+h_0$ and $r=R_0+h$. φ_0 and φ are the ellipsoidal latitudes and λ_0 and λ the ellipsoidal longitudes of the two points, respectively. For simplicity, Fig. 1 shows the points S and P in the same meridian plane.

Considering a Cartesian coordinate system with origin in S, the plane *XY* tangent to the

local sphere in S, *X* axis northward, *Y* axis eastward and *Z* axis toward the centre of the sphere, the coordinates of the points P and U become:

$$P\begin{cases} X = -r\cos\varphi\sin\varphi_0\cos(\lambda-\lambda_0)+r\sin\varphi\cos\varphi_0 \\ Y = r\cos\varphi\sin(\lambda-\lambda_0) \\ Z = -r\cos\varphi\cos\varphi_0\cos(\lambda-\lambda_0)-r\sin\varphi\sin\varphi_0+r_0 \end{cases}$$

$$U\begin{cases} X_1 = -r_0\cos\varphi\sin\varphi_0\cos(\lambda-\lambda_0)+r_0\sin\varphi\cos\varphi_0 \\ Y_1 = r_0\cos\varphi\sin(\lambda-\lambda_0) \\ Z_1 = -r_0\cos\varphi\cos\varphi_0\cos(\lambda-\lambda_0)-r_0\sin\varphi\sin\varphi_0+r_0 \end{cases}$$

4. Application to Etna data

The method previously described was used for reprocessing the gravity data surveyed for the study of the Mt. Etna volcano [Loddo et al. 1989]. The Bouguer anomaly shown in the cited paper was obtained performing the topographic correction with a manual chart method over a distance of 28 km from each station and using the 1930 International Gravity Formula. For the new processing step the original data were standardized using the IGSN71 system [Morelli et al., 1974] and the Italian First Order Gravity Network [Marson and Morelli, 1978]. Besides, the Geodetic Reference System 1980 [Moritz, 1984] was applied and the data corrected for the spherical cap and the topography out to 166.7 km. In order to numerically compare the old and the new processing procedures, the infinite slab and the old topographic corrections were applied to the transformed data.

Fig. 4 shows the approximate area over which the topographic corrections of all the Etna data were carried out. The Sicily mountain chains are completely contained in the area together with a large part of the calabrian Apennines. Besides, large sea-covered surfaces are present. For these last zones, the 7.5”x10” mean elevation gridded data were computed by digitizing the bathymetric maps. The obtained database was connected to the existing one for inland zones.

Considering the elevation values of the Etna stations, the maximum difference between the infinite slab and the spherical cap amounts to about 2-3 mGal. On the contrary, differences larger than 10 mGal result for the effect of the topography as figs. 5 and 6 indicate. The maps are constructed using a mass density of 2650 kg/m^3.

The differences between the complete Bouguer corrections obtained with the new processing method and the older one are mapped in fig. 7. As it was expected, the differences increase with the elevation resulting in substantial changes in the Bouguer anomalies.

To our knowledge, there are few papers that take into account the topographic effect out to 170 km [Krohn, 1976; Banerjee, 1998] and just one that shows, with a field example, the different contributions to the corrections by the topography in the first 20 km range and by the rest of the 170 km range area [Banerjee, 1998]. The survey presented in the last cited paper, carried out in an area with very large elevation changes, shows results similar to ours as regards the contribution of the elevation changes to the terrain correction. In particular, it was con-

Figure 4. Approximate extent of the 167 km radius area considered for the computation of the terrain effect on the Etna data.

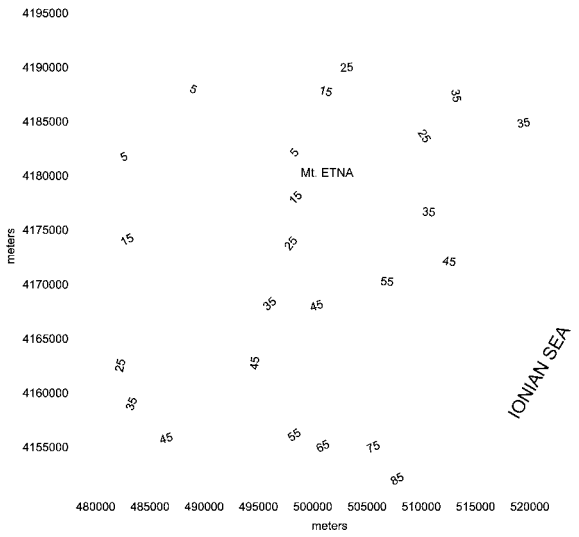

Figure 5. Topographic effect for the Etna stations evaluated with the manual chart method out to 28.8 km from each station. Contour lines in mGal.

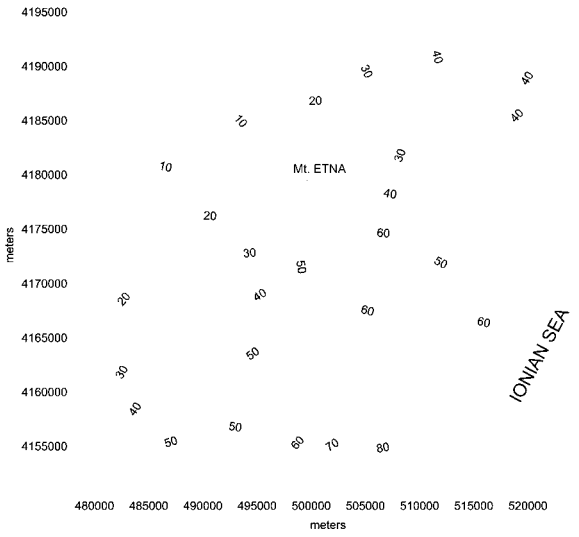

Figure 6. Topographic effect for the same stations of Fig. 5, computed through our processing method. Contour lines in mGal.

firmed the increase with the elevation rising both of the terrain correction and of the contribution to the total terrain correction, by the region between 20 km and 170 km from the gravity station.

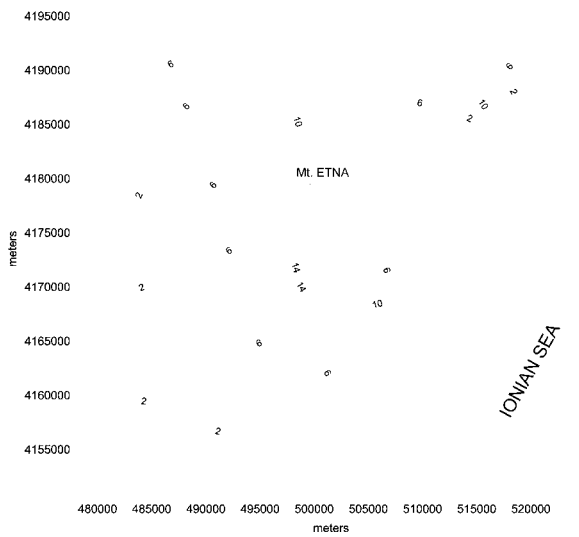

Figure 7. Difference in mGal between the complete Bouguer corrections for the Etna data resulting from the old and the new processing method.

5. Concluding remarks

We have presented an automatic method to perform the complete Bouguer correction on a spherical earth considering the effect of the topography out to 170 km from the stations. For the zone nearest the station (the inner zone), where the topography have the largest influence on the accuracy of the corrections, the earth surface is approximated by a TIN structure generated by digitized height values. The method is simple and does not introduce further approximations to the original elevation data.

Our results show that the contribution of the topographic correction to Bouguer anomalies changes with the elevation of the station resulting in a different effect over short distances. Besides, the influence of the distant topography cannot be ignored when large changes in elevation among stations exist. As standard the processing steps to obtain the Bouguer anomalies should include the effect of the earth curvature and of the terrain out to 170 km from the station.

Acknowledgments

This research was supported by the National Institute of Geophysics and Volcanology through the EPOT project.

References

Banerjee, P., (1998). *Gravity measurements and terrain corrections using a digital terrain model in the NW Himalaya*. Comput. And Geosci., 24 (10), 1009-1020.

Barber, C.B., Dobkin, D.P. and Huhdanpaa, H.T., (1966). *The quickhull algorithm for convex hulls*. ACM Trans. on Math. Software, 22 (4), 469-483.

Blais, J.A.R. and Ferland, R., (1984). *Optimization in*

gravimetric terrain corrections. Can. J. Earth Sci., 21, 505-515.

Bourke, P., (1989). *Efficient triangulation algorithm suitable for terrain modelling*. In: Pan Pacific Computer Conference, Beijing, China, 1989.

Bullard, E.C., (1936). *Gravity measurements in East Africa*. Phil. Trans. Roy. Soc. London, 235, 486-497.

Chapin, D.A., (1996). *The theory of the Bouguer gravity anomaly : a tutorial*. The Leading Edge, 15, 361-363.

Cogbill, A.H., (1990). *Gravity terrain corrections calculated using digital elevations models*. Geophysics, 55 (1), 102-106.

D'Azavedo, E.F. and Simpson, R.B., (1989). *On optimal interpolation triangle incidences*. SIAM Journal on Scientific and Statistic Computing, 20 (6), 1063-1075.

Hammer, S., (1939). *Terrain corrections for gravimetric stations*. Geophysics, 4, 184-194.

Herrera-Barrientos, J. and Fernandez, R., (1991). *Gravity terrain corrections using Gaussian surfaces*. Geophysics, 56 (5), 724-730.

Krohn, D.H., (1976). *Gravity terrain corrections using multiquadric equations*. Geophysics, 41 (2), 266-275.

LaFehr, T.R., (1991). *An exact solution for the gravity curvature (Bullard B) correction*. Geophysics, 56 (8), 1179-1184.

LaFehr, T.R., (1991). *Standardization in gravity reduction*. Geophysics, 56 (8), 1170-1178.

LaFehr, T.R., (1998). *On Talwani's "Errors in the total Bouguer reduction"*. Geophysics, 63 (4), 1131-1136.

Lawson, C.L., (1977). *Software for C^1 surface interpolation*. In: Mathematical Software III (J.R. Rice, ed.), pp. 161-194. Academic Press Inc., New York.

Loddo, M., Patella, D., Quarto, R., Ruina, G., Tramacere, A. and Zito, G., (1989). *Application of gravity and deep dipole geoelectrics in the volcanic area of Mt. Etna (Sicily)*. J. Volcanol. Geotherm. Res., 39, 17-39.

Ma, X.Q. and Watts, D.R., (1994). *Terrain correction program for regional gravity surveys*. Comput. And Geosci., 20 (6), 961-972.

Marson, I. and Morelli, C., (1978). *First order gravity net in Italy*. 8th Meeting of the international gravity commission, Paris, 12-16 Sept. 1978, 660-689.

Morelli, C., Gantar, C., Honkasalo, T., McConnel, R.K., Tanner, I.G., Szabo, B., Uotila, U. and Whalen, C.T., (1974). *The international gravity standardization net 1971 (IGNS71)*. International Association of Geodesy, IUGG, Spec. Publ. n° 4.

Moritz, H., (1984). *Geodetic Reference System 1980*. Bullettin Géodésique, 58, 388-398.

Okabe, M., (1979). *Analytical expressions for gravity anomalies due to homogeneous polyhedral bodies and translations into magnetic anomalies*. Geophysics, 44 (4), 730-741.

Olivier, R.J. and Simard, R.G., (1981). *Improvement of the conic prism model for terrain correction in rugged topography*. Geophysics, 46 (7), 1054-1056.

Preparata, F.P. and Shamos, M.I, (1985). *Computational geometry: an introduction*. Springer Verlag, Berlin.

Rajan, V.T., (1994). *Optimality of the Delaunay triangulation in R^d*. Discrete and Computational Geometry, 12, 189-202.

Renka, R.J., (1984). *Algorithm 624, Triangulation and interpolation at arbitrary points in a plane*. ACM Trans. On Math. Software, 10, 440-442.

Shewchuk, J., (1996). *Triangle: Engineering a 2D quality mesh generator and Delaunay triangulator*. In: First Workshop on Applied Computational Geometry, May 1996, Philadelphia, Pennsylvania, pp. 124-133.

Shewchuk, J., (1997). *Delaunay refinement mesh generation*. Ph. D. Thesis, Technical Report CMU-CS-97-137, School of Computer Science, Carnegie Mellon University, Pittsburg, Pennsylvania, 18 May 1997.

Shewchuk, J., (2002). *Delaunay refinement algorithms for triangular mesh generation*. Computational Geometry: Theory and Applications, 22 (1-3), 21-74.

Talwani, M., (1998). *Errors in the total Bouguer reduction*. Geophysics, 63 (4), 1125-1130.

Zhou, X., Zhong, B. and Li, X., (1990). *Gravimetric terrain corrections by triangular-element method*. Geophysics, 55 (2), 232-238.

Data Concerning Magnetic Susceptibility Changes in Powdered Rock Induced by Temperature. Results from Mount Etna and Ustica Island Specimens

Antimo Angelino[1], Ciro Del Negro[2], Alberto Incoronato[3], Rosalba Napoli[2] and Pasquale Tiano[3] *

[1] *CNR-IAMC Istituto per l'Ambiente Marino Costiero, Napoli, Italy*
[2] *Istituto Nazionale di Geofisica e Vulcanologia, Sezione di Catania, Italy*
[3] *Dipartimento di Scienze della Terra, Università di Napoli, Italy*

Abstract

The variation of the magnetic susceptibility with temperature of volcanic samples collected at Etna, and Ustica Island have been investigated and possible explanations of the magneto-mineralogical changes have been suggested. The magnetic susceptibilities of powdered specimens have been measured during heating in air, from room temperature up to 700 °C, and subsequent cooling. The continuous susceptibility curves (k-T curves) are generally not reversible and appear to be sensitive to the magnetic mineralogy. Although, two main groups of behaviours have been distinguished (A and B groups), it is shown that very significant variations of the magnetic susceptibilities can occur even as a result of a temperature increasing of some hundred degrees above ambient temperature.

Keywords *Etna – Ustica - magnetic susceptibility - temperature*

1. Introduction, apparatus and measurements

Generally low field magnetic susceptibility, k, measured at room temperature is used in interpreting magnetic anomalies. However it is known that k can change with temperature significantly. Samples from Mount Etna and Ustica Island have been collected (Fig.1) in order to provide information on these changes. Variations in air of k with temperature of powdered specimens were measured, in the Laboratorio di Paleomagnetismo e Magnetismo delle Rocce of Dipartimento di Scienze della Terra of Università degli Studi di Napoli "Federico II", using a Bartington apparatus (Fig. 2) consisting in:

1) Magnetic susceptibility meter MS2. It works on the principle of a.c. induction.
2) Water jacketed sensor type MS2W30. This has a 30 mm internal diameter sample cavity and the passage of water within the probe screens it from extremes of temperature which may be present within the sample cavity.
3) Furnace type MS2WF. This comprises a non-inductively wound platinum wire furnace with a maximum operating temperature of 900 °C and a maximum sample capacity of 15 mm diameter.
4) Power supply type MS2WFP. This unit supplies electrical power to the furnace and provides either preset thermostatic control of temperature or slowly varying linear increasing or decreasing of temperature.

The heating or cooling cycle is selected on the front panel of the power supply unit MS2WFP. The initial, maximum and final temperature values, the rate of heating and cooling, the measurement steps are selected via software. The MS2WFP unit is computer controlled and connected to both the heating unit MS2WF and to the susceptibility meter unit MS2. The latter is connected to the water cooled MS2W30 sensor within which the specimen is located. The drift is corrected by taking two background measurements at the beginning and at the end of process.

All the powdered specimens, 5 cm^3 each, were heated up to 700 °C, starting from 35 °C, and cooled down at a constant rate of 8 °C/min and the measurements were carried out with 5 °C step.

2. Discussion

The variations of k with temperature, normalised with reference to the value measured at the start of the heating, k_{start}, are plotted in figures 3 and 4. The value of k for each untreated specimen of standard size (cylinder: 2.54 cm, diameter, x 2.20 cm, height) are also indicated. The variations of k with temperature can be grouped into 2 main groups called A (Fig. 3) and B (Fig. 4) respectively.

The behaviour of type A specimens (Fig. 3) during heating is generally similar to that exhibited during cooling. However, the value of the magnetic susceptibility at the end of cooling, k_{end}, is much lower than the value measured at

* To whom correspondence should be addressed, e-mail: tiano@unina.it

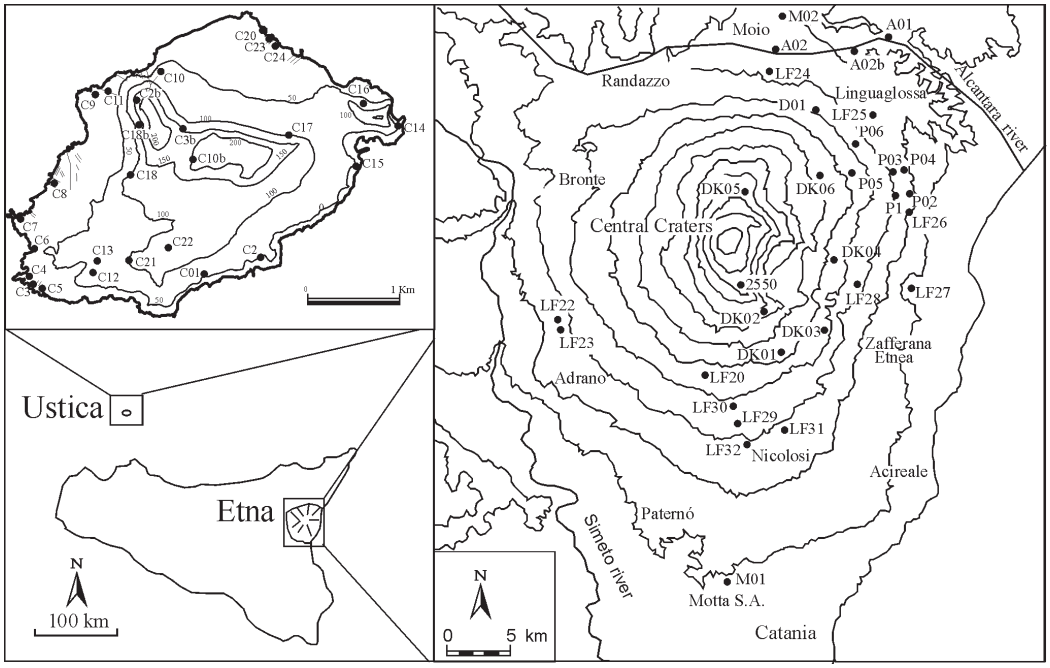

Figure 1. Sites location maps of Ustica Island and Mount Etna.

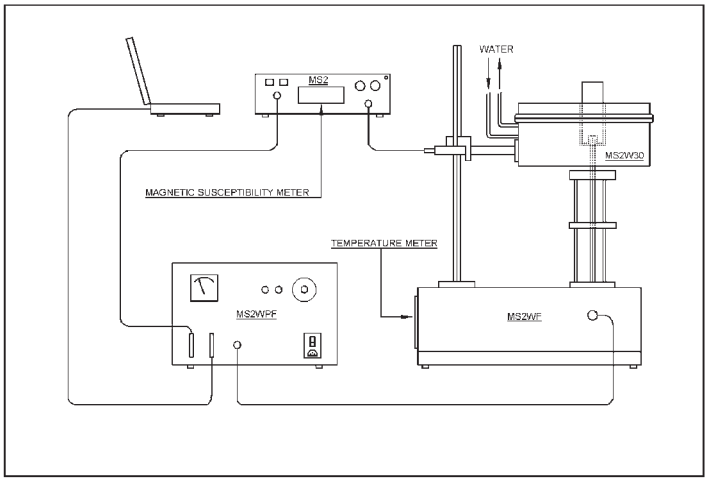

Figure 2. Bartington apparatus for measuring variation of k during heating and cooling (Redrawn from Bartington manual).

the start of the heating, k_{start}. The overall behaviour during the entire heating-cooling process suggests that the dominant magnetic carrier is magnetite and/or Ti-poor titanomagnetite [Goguitchaichvili et al., 2001; Orlicky, 1990; Tarling, 1983].

The lower value of k observed during the cooling can be the result of partial transformation occurred above 500 °C of the main magneto-mineralogical phase into a new phase characterised by an higher Curie temperature, T_C, and lower k, such as hematite [Dunlop and Özdemir, 1997; Tarling, 1983; France et al., 1999]. Differences of behaviour exhibited by A type specimens during heating can related to different magnetic grain sizes. In fact, specimens characterized by predominant SD magnetic carrier exhibit variations of the k values that in approaching the T_C can be 35 to 40 % higher than k_{start}. In fact, according to Thompson and Oldfield [1986] MD carrier are characterized by a much smaller increasing of k values.

The behaviour of type B specimens (Fig.4) during heating is generally characterised by increasing of k_{start} of 40 to 50% in the range 100-200 °C.

Generally a rapid and significant decreasing of k_{star}, even 70 to 80%, follows in the range 250 to 300 °C. Such low values are retained until the end of treatment although few

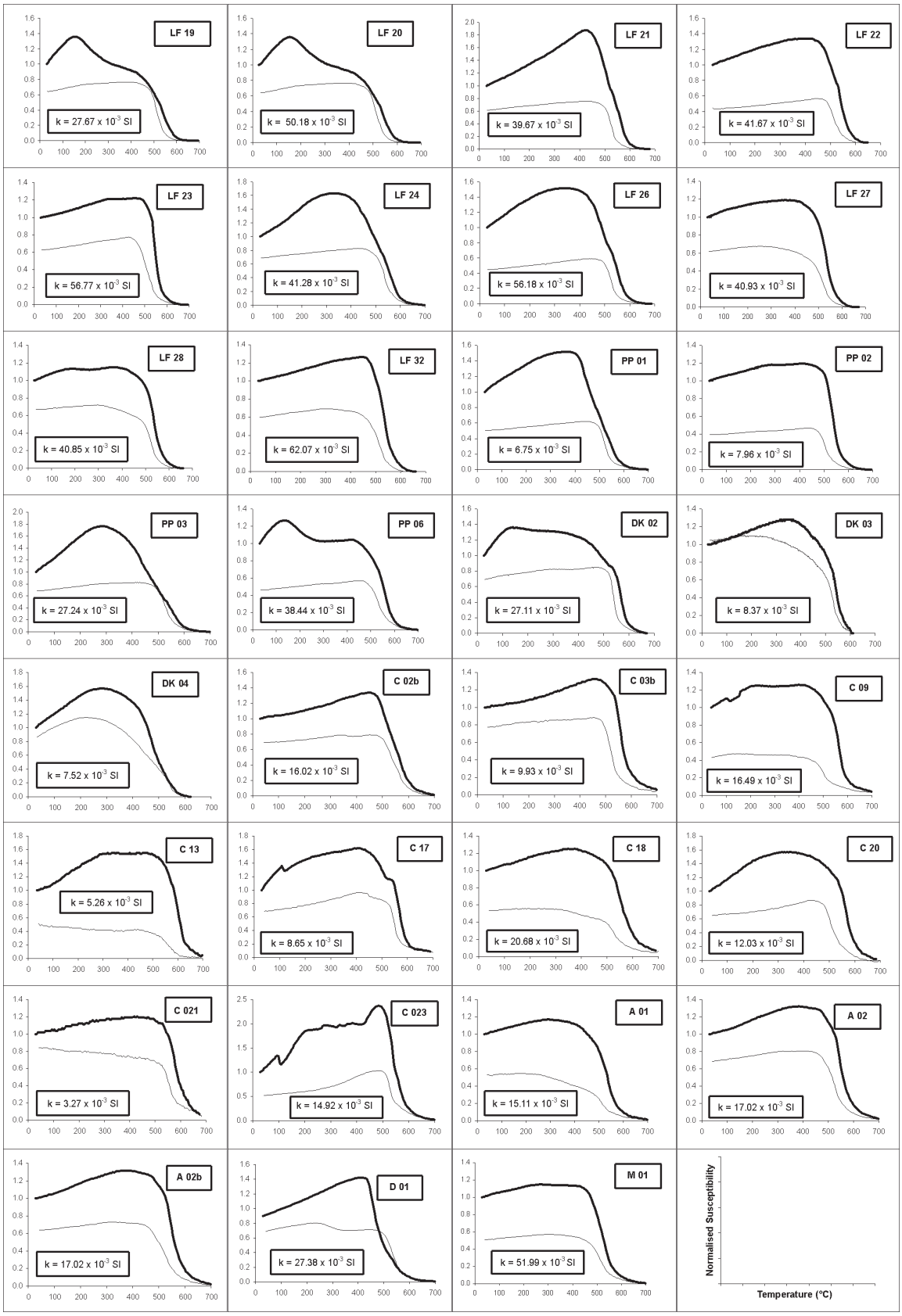

Figure 3. Normalised magnetic susceptibility (k/k_{start}) versus temperature (°C) of Etna and Ustica specimens (Group A, see text). The value of k of each untreated specimen of standard size (see text) is also indicated. Thick (thin lines) indicate heating (cooling) curves. Etna specimens labels: LF = lava flows, DK = dykes, A = Alc.antara, M = Moio/Motta S.A., D = Mt. Dolce, PP = Provenzana-Pernicana fracture system. Ustica specimens labels: C. Site location in Fig.1.

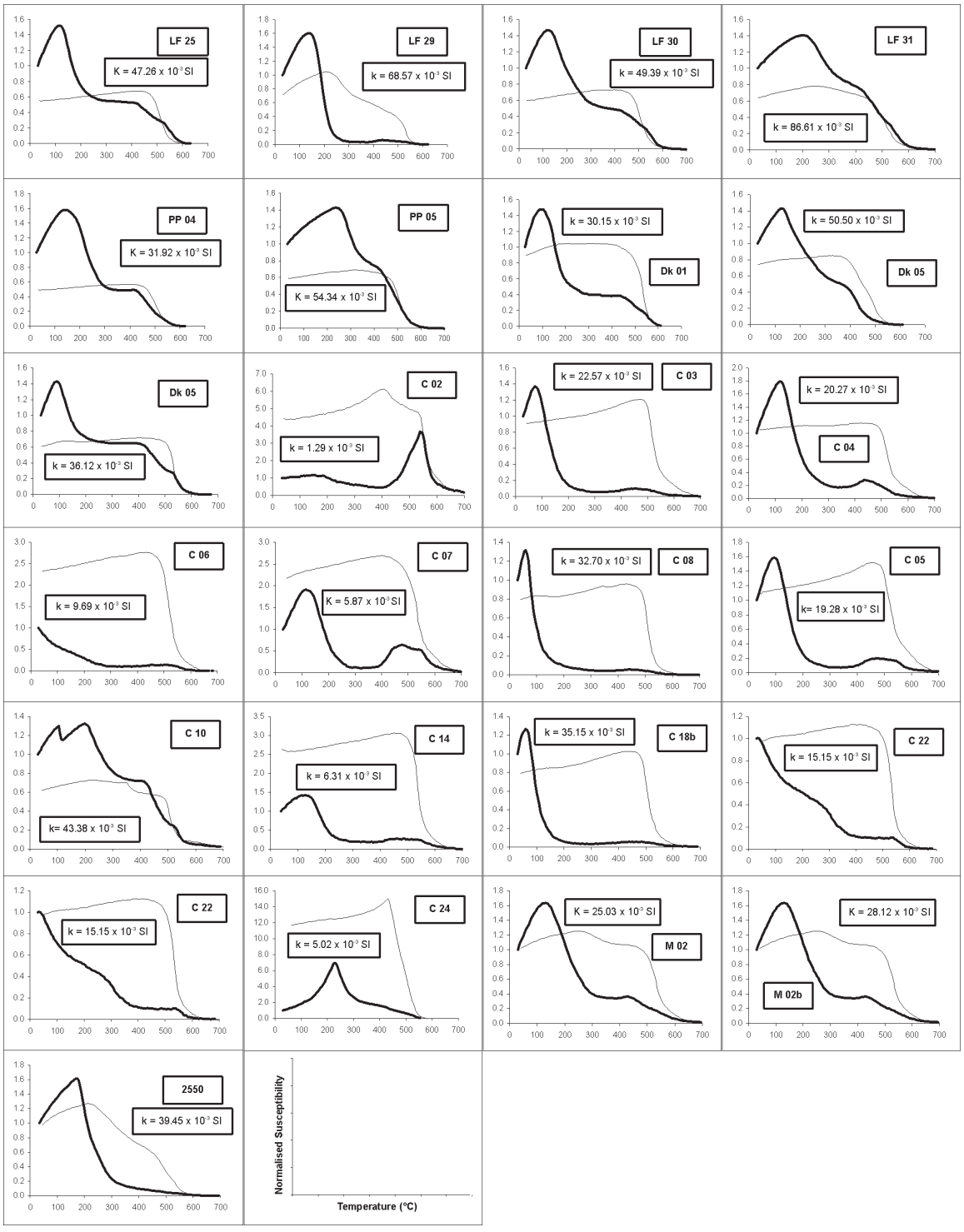

Figure 4. Normalised magnetic susceptibility (k/k_{start}) versus temperature (°C) of Etna and Ustica specimens (Group B, see text). Specimens labels as in Fig. 3.

specimens exhibit further increasing and decreasing (however much smaller than the previous ones) between 400 and 500 °C. The behaviour of k during the cooling is very similar for almost all the specimens. In fact, k increases between 600 and 500 °C and keeps either constant or lowers very little as cooling proceeds. In few cases, the sharp increasing during the early stages of the cooling is followed by a smaller one that ends at about 250-200 °C after which it decreases. The observed behaviours can be ascribed to Ti-rich titanomagnetite, characterised by T_C of about 250 °C, that at about 400 °C changes into maghemite, possibly [Özdemir, 1987; King, 2000]. In many cases it is evident that further changes, into hematite, occur at

about 450 °C [Özdemir, 1987; King, 2000]. The presence of hematite is clearly detected from the initial path of the cooling curves in all cases. However, the steep increasing of the k value between 550 and 500 °C can be clearly be associated to Ti-poor titanomagnetites [Thompson and Oldfield, 1986; Orlicky, 1990]. However these titanomagnetites could only form during the very late stages of the heating. The bell type shape exhibited around 300 °C can be ascribed to MD Ti-rich titanomagnetites [Thompson and Oldfield, 1986; Shcherbakova and Shcherbakov, 2000; Day et al., 1977; Radhakrishnamurty et al., 1977]

3. Conclusion

The study of the variations of k with temperature carried out on Ustica Island and Mount Etna specimens has allowed to highlight 2 main groups: A and B. As far as type A specimens are concerned, their k values during heating are much higher than those during the cooling. On the contrary, B type specimens show k values during heating that are lower than those during the cooling, except the 200-250 °C interval where the Ti-poor titanomagnetite contribution prevails. It must be stressed that during the heating k values increase significantly. In B type specimens such increasing occurs up to 200-300 °C while in A type specimens they last even up to 500 °C. The magnitude of these variations may be of interest in interpreting magnetic anomalies in volcanic areas, particularly when the modelling effects active volcanic areas.

Acknowledgements

This work was developed in the frame of the Geomagnetism Laboratory of INGV-CT.

References

Day, R., Fuller M. and Schmidt V.A., (1977). *Hysteresis properties of titanomagnetites: grain size and compositional dependence.* Phys. Earth. Plan. Int., 13, 260-267.

Dunlop, D.J. and Özdemir Ö., (1997). *Rock Magnetism: Fundamentals and frontiers.* Cambridge University Press. pp. 573.

France D., Hu Y., Snowball I, Rolph T., Oldfield F. and Walden, J., (1999) *Additional rock magnetic measurements*. In: Enviromental Magnetism: a practical guide. (J. Walden, F. Oldfield and J.P. Smith, eds.), Quaternary Research Association, Technical Guide, No. 6., London, 197-211.

Goguitchaichvili, A., Morales J., Urrutia-Fucugauchi J. and Soler A.M., (2001). *On the use of continuous thermomagnetic curves in paleomagnetism: a cautionary note.* Earth Planet. Sc. Lett., 333, 699-704.

King, J. G. and Williams W., (2000). *Low-temperature magnetic properties of magnetite.* J. Geophys. Res., 105, N. B7, 16,427-16,436.

Orlicky, O., (1990). *Detection of magnetic carriers in rocks: results of susceptibility changes in powdered rock samples induced by temperature.* Phys. Earth. Plan. Int., 63, 66-70.

Özdemir, Ö., (1987). *Inversion of titanomaghemites.* Phys. Earth. Plan. Int., 46, 184-196.

Radhakrishnamurty, C., Likhite S.D. and Sahasrabudhe P.W., (1977). *Nature of magnetic grains and their effect on the remanent magnetization of basalts.* Phys. Earth. Plan. Int., 13, 289-300.

Shcherbakova, V.V. and Shcherbakov V.P., (2000). *Properties of partial thermoremanent magnetization in pseudosingle domain and multidomain magnetite grains.* J. Geophys. Res., 105, N. B1, 767-781.

Tarling, D.H., (1983). *Palaeomagnetism* – London and New York, Chapmann & Hall. pp 379.

Thompson R. and Oldfield F., (1986). *Enviromental Magnetism* – London, Boston and Sydney, Allen & Unwin. pp 227.

Exploring the Time Dynamics of Geoelectrical and Geomagnetical Signals

Marianna Balasco, Gerardo Colangelo,
Vincenzo Lapenna and Luciano Telesca

Istituto di Metodologie per l'Analisi Ambientale del CNR, Tito Scalo (PZ)

Abstract

Fractal tools have been used to investigate the time dynamics of hourly geomagnetic and geoelectrical data, recorded during the year 2000 and 2001 respectively, by a monitoring network located in the seismic area of Irpinia and in the volcanic area of Etna, both in southern Italy. Scaling behaviour has been revealed by means of different statistics: the Lomb Periodogram method, the Detrended Fluctuation Analysis and the Higuchi analysis. The values of the scaling exponents estimated by means of these methods indicate that the temporal fluctuations of the geoelectrical signals are not typical of purely random stochastic processes (i.e. white noise), but evidence the presence of long-range correlations.

Keywords *electromagnetic time series - fractal methods*

1. Introduction

The dynamics underlying tectonic processes could be directly revealed by the investigation of the temporal fluctuations of self-potential signals, which may be useful to monitor and understand many seemingly complex phenomena linked to seismic and volcanic activity [Park, 1997; Johnston, 1997]. Self-potential field variability may be induced by stress and fluid flow field variability [Scholz, 1990], therefore, the analysis of these induced fluctuations could contribute to gain information on the governing geophysical mechanisms characterizing normal as well as intense volcano-seismic activity. In this context, in this work we investigate the dynamical properties of geoelectrical signals, as they can be detected from observational time series.

Self-potential signals are the result of the interaction among very heterogeneous and not well known mechanisms which can be influenced by the particular structure of the monitored zone [Patella et al., 1997]. This means that local features can be mixed to the general ones so increasing the difficulty of rightly characterising and interpreting the signal time variations. In addition, as occurs for many environmental signals, observational data are made even more erratic by the presence of anthropic phenomena: electrical signals coming from anthropic sources may be added, e.g., to the natural signal so making harder its dynamical characterization [Cuomo et al., 1998].

In a previous paper Cuomo et al. [1998] analyzed the geoelectrical daily means in order to give information about the statistical features of the geoelectrical background noise and the inner dynamics of geophysical processes producing the electrical phenomena observed on earth surface in seismic areas. They discussed the statistical analysis of dynamical systems based on the estimation of their degree of predictability, distinguishing randomness from chaos and providing a parsimonious representation in terms of autoregressive models of observations, by means of the only information coming from the time series itself.

In the study of seemingly complex phenomena, as those generating self-potential signals, methodologies able to capture the dynamical peculiarities in observational time series are particularly useful tools to obtain information on the features and on the causes of signal time variability. In particular, fractal techniques, developed to extract qualitative and quantitative information from time series, have been applied recently to the study of a large variety of irregular, erratic signals and by now have demonstrated to be very useful to reveal deep dynamical features. Cuomo et al. [2001] detected scaling behaviour in the power spectra of geoelectrical time series, revealing the antipersistent character of the self-potential fluctuations. Telesca et al. [2001] proposed a new approach to investigate correlation between geoelectrical signals and earthquakes, analyzing the time variations of the fractal parameters, characterizing their dynamics. Balasco et al. [2001] found that self-potential measurements seem to be featured by long-range correlations with scaling exponents which indicate that the underlying geophysical process is characterized by stabilizing mecahnisms.

In the frame of the EPOT project the main contribute of this Research Unit concerned the development of innovative and robust methods to explore the time dynamics of geoelectrical time series measured in seismic areas. Firstly, techniques to denoise time series have been developed, and software packages to remove climatic and cultural noises from geoelectrical time series have been designed. In particular, great attention has been devoted to the analysis

of the influence of data missing, that is a typical situation in the framework of geophysical monitoring activities. To overcome the problem related to the application of conventional FFT analysis, we applied the Lomb Periodogram Method. Fractal techniques have been applied for searching scaling invariance laws in the time series.

The algorithms have been designed and validated using the data-base of geophysical time series available at Geophysical Lab of IMAA, in a second step these techniques have been successfully applied to extract quantitative dynamics from time series recorded by means of the magnetic network of Etna volcano.

2. Methods

To quantitatively characterize geoelectrical signals, we need to use techniques able to extract robust features hidden in these complex fluctuations.

Various methods for analyzing the correlation properties of a time series are available, and many techniques have been developed to detect and quantify fractal features in experimental and observational data.

The spectral analysis represents the standard method to evaluate the presence of purely random fluctuations in time series. Signals, whose samples are uncorrelated among them, are characterized by a flat power spectrum (white noise); while signals, whose samples are long-range correlated, are characterized by a power spectrum decreasing with the frequency, $S(f) \propto f^{-\alpha}$, where α indicates the degree of correlation (coloured noise). For unevenly sampled time-series the power spectrum can be calculated by means of the Lomb Periodogram method [Lomb, 1976]. Denoting as x_n the datum measured at instant t_n, the Lomb Periodogram is defined by the following formula:

$$P(\omega) = \frac{1}{2\sigma^2}\left\{\frac{\left[\sum_n (x_n - \bar{x})\sin\omega(t_n - \tau)\right]^2}{\sum_n \sin^2\omega(t_n - \tau)} + \frac{\left[\sum_n (x_n - \bar{x})\cos\omega(t_n - \tau)\right]^2}{\sum_n \cos^2\omega(t_n - \tau)}\right\} \quad (1)$$

where $\omega = 2\pi f$ is the angular frequency and τ is given by

$$\tan(2\omega\tau) = \frac{\sum_n \sin 2\omega t_n}{\sum_n \cos 2\omega t_n} \quad (2)$$

The slope of the line fitting the log-log plot of the power spectrum by a least square method in the linear frequency range gives the estimate of the spectral index α.

A more stable estimate of the spectral exponent can be performed by the calculation of the fractal dimension of the signal using the Higuchi method [Higuchi, 1988; Higuchi, 1990]. In the literature, many papers have been devoted to find methods capable of giving stable estimations of the power-law spectral index. Burlaga and Klein [1986] presented a method to calculate stable values of the fractal dimension D of large-scale fluctuations of the interplanetary magnetic field; the relationship between the fractal dimension D and the spectral exponent α is given by Berry's expression $D=(5-\alpha)/2$ [Berry, 1979], for $1<\alpha<3$. They defined the length $L_{BK}(\tau)$ of the B(t) curve as

$$L_{BK}(\tau) = \sum_{k=1}^{N} \left| \bar{B}(t_k + \tau) - \bar{B}(t_k) \right| / \tau \quad (3)$$

where

$$\bar{B}(t_k)$$

denotes the average value of B(t) between $t=t_k$ and $t=t_k+\tau$. This length is a function of τ, and for statistically self-affine curves, the length is expressed as $L_{BK}(\tau) \propto \tau^{-D}$. Using this relation, the value of D can be estimated, as the slope of the log-log plot of the length $L_{BK}(\tau)$ vs. the time interval τ. Then, using Berry's, the spectral exponent estimation can be estimated.

Another method which also gives a stable value of the fractal dimension has been presented by Berry [1979]. A new time-series is constructed from the given time series X(i), (i=1, 2, ..., N),

$$X_m^\tau : X(m), X(m+\tau), X(m+2\tau), \ldots, X(m+[(N-m)/\tau]\tau), \quad (m = 1, \ldots, \tau) \quad (4)$$

where [ ] denotes Gauss' notation. The length of the curve is defined as

$$L_m(\tau) = \left\{ \left(\sum_{i=1}^{[(N-m)/\tau]} \left| X(m+i\tau) - X(m+(i-1)\tau) \right| \right) \frac{N-1}{[(N-m)/\tau]\tau} \right\} \frac{1}{\tau} \quad (5)$$

The average value $\langle L(t) \rangle$ over t sets of $L_m(\tau)$ is defined as the length of the curve for the time interval τ. If $\langle L(\tau) \rangle \propto \tau^{-D}$, within the range $\tau_{min} \le \tau \le \tau_{max}$ then the curve is fractal with dimension D in this range. He examined the relationship between the fractal dimension D and the power law index α, by calculating the fractal dimension of the simulated time series which follows a single power-law spectrum density. Even in this case, the spectral exponent estimation could be carried out using Berry's expression.

Recently, the method of Detrended

Fluctuation Analysis (DFA) has been developed to reveal long-range correlation structures in observational time series. This method was proposed by Peng et al. [1995], and it avoids spurious detection of correlations that are artifacts of nonstationarity, that often affects experimental data. Such trends have to be well distinguished from the intrinsic fluctuations of the system in order to find the correct scaling behaviour of the fluctuations. Very often we do not know the reasons for underlying trends in collected data and we do not know the scales of underlying trends. DFA is a well-established method for determining the scaling behaviour of data in the presence of possible trends without knowing their origin and shape [Kantelhart et al., 2001]. The methodology operates on the time series x(i), where i=1,2,...,N and N is the length of the series. With x_{ave} we indicate the average value

$$x_{ave} = \frac{1}{N}\sum_{i=1}^{N} x(i) \qquad (6)$$

The signal is first integrated

$$y(k) = \sum_{i=1}^{k}[x(i) - x_{ave}] \qquad (7)$$

Next, the integrated time series is divided into boxes of equal length n. In each box a least-squares line is fit to the data, representing the trend in that box. The y coordinate of the straight line segments is denoted by $y_n(k)$. Next we detrend the integrated time series y(k) by subtracting the local trend $y_n(k)$ in each box. The root-mean-square fluctuation of this integrated and detrended time series is calculated by

$$F(n) = \sqrt{\frac{1}{N}\sum_{k=1}^{N}[y(k) - y_n(k)]^2} \qquad (8)$$

Repeating this calculation over all box sizes n, we obtain a relationship between F(n), that represents the average fluctuation as a function of box size, and the box size n. If F(n) behaves as a power-law function of n, data present scaling:

$$F(n) \propto n^d. \qquad (9)$$

Under these conditions the fluctuations can be described by the scaling coefficient d, representing the slope of the line fitting log F(n) to log n. The values of exponent d may represent a range of processes. For example d=0.5 means that the signal samples are uncorrelated or short-range-correlated variable. An exponent d≠0.5 in a certain range of scales n suggests the existence of long-range correlations. If d=1.0 the temporal fluctuations are of flicker-noise type; if d=1.5 the temporal fluctuations are of Brownian type. The DFA scaling exponent d and the spectral exponent α are related to each other as described in Buldirev et al. [1994] and Havlin et al. [1988] by the following equation:

$$d = \frac{1+\alpha}{2} \qquad (10)$$

3. Data analysis and results

Fig. 1 shows a typical power spectrum of a geoelectrical signals, calculated by means of the Lomb Periodogram method. The time series shows a very clear scale-invariance, denoted by the power-law behaviour of the spectrum versus frequency, with the scaling exponent α indicating that the temporal fluctuations of the signal

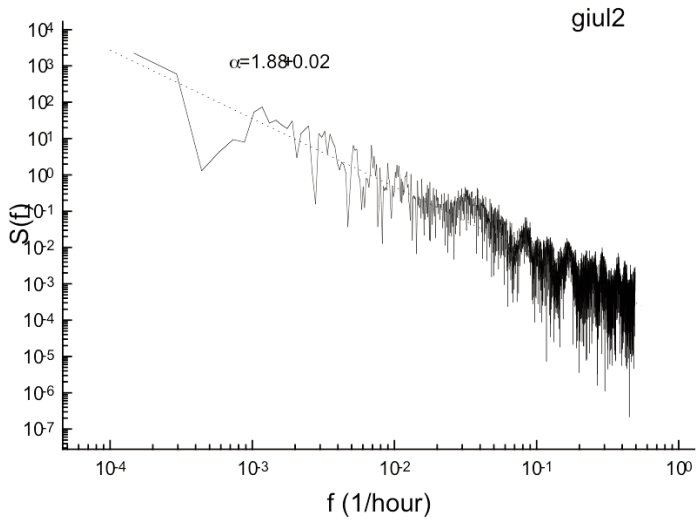

Figure 1. Lomb Periodogram of one geoelectrical time series measured in Giuliano station (southern Italy) during 2001.

are not purely random (flat spectrum), but present long-range correlations.

Fig. 2 shows the results of the Higuchi analysis performed on one of the four geoelectrical time series measured by Tito station. The plot evidence scaling behaviour with scaling exponent D approximately 1.8. A divergence from the linear behaviour is present at larger timescales; this could be due to edge effect, that gives rise to an increase of the $<L(\tau)>$ at those scales.

Fig. 3 shows the results of the Detrended Fluctuation Analysis performed on the geoelectrical time series measured by Marsico station. The scaling behaviour is apparent with scaling exponent d approximately 1.3.

We analysed the time dynamics of one time series of geomagnetic data measured during 2000 by one station installed on the Etna (southern Italy). Fig. 4 shows the hourly signal variation.

Fig. 5 shows the Lomb periodogram: it is evident the scaling behaviour, characterized by a flicker-noise-type dynamics of the temporal fluctuations, indicated by the unitary value of the spectral exponent α. This 1/f-like behaviour is mainly due to solar-terrestrial interaction, which is the external origin for the fluctuations of the magnetic field until periods of monthly order.

Fig. 6 shows the results obtained applying the Detrended Fluctuation Analysis to the CSR geomagnetic signal; it is clear the appearance of two different scaling regimes, with different val-

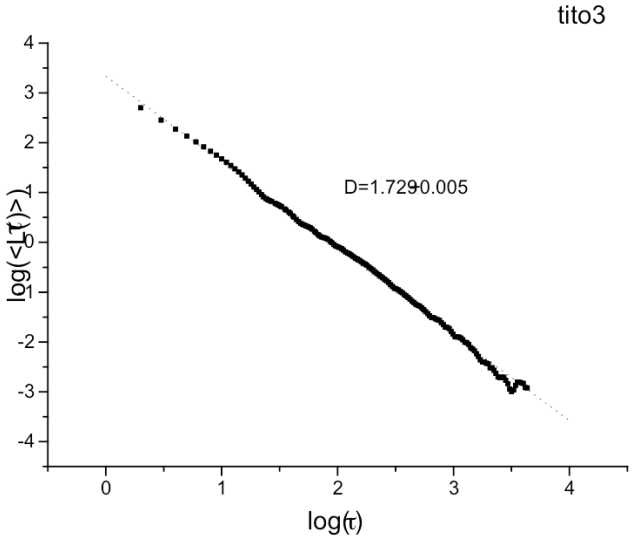

Figure 2. Higuchi analysis of one of the geoelectrical time series measured in Tito station (southern Italy) during 2001.

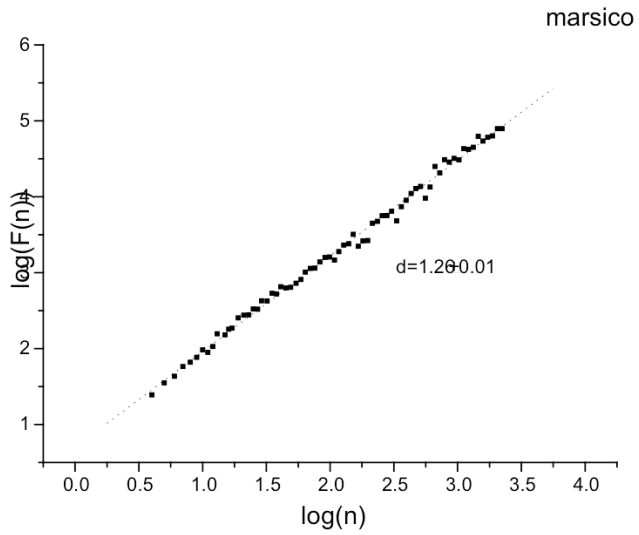

Figure 3. Detrended Fluctuation Analysis of the geoelectrical time series measured in Marsico station (southern Italy) during 2001.

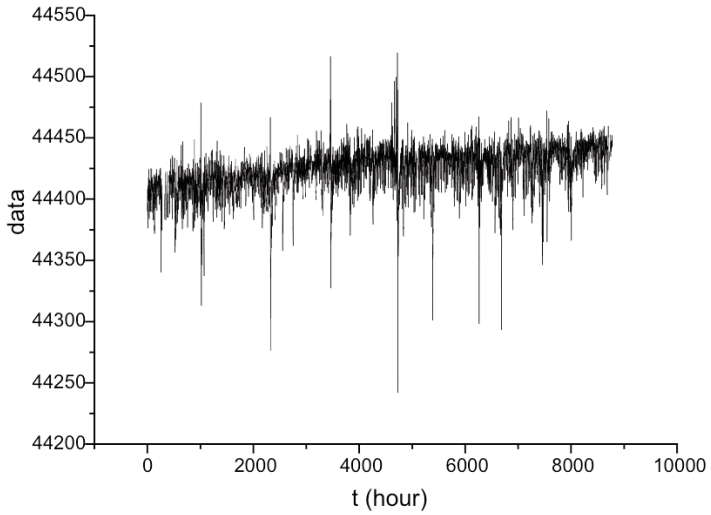

Figure 4. Hourly time variability of geomagnetic signal measured during 2000 at the station CSR located on Mount Etna (southern Italy).

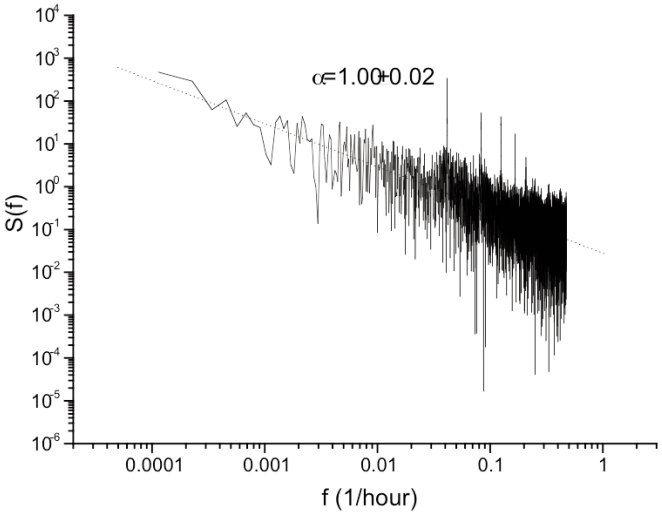

Figure 5. Lomb Periodogram of the geomagnetic signal measured by station CSR.

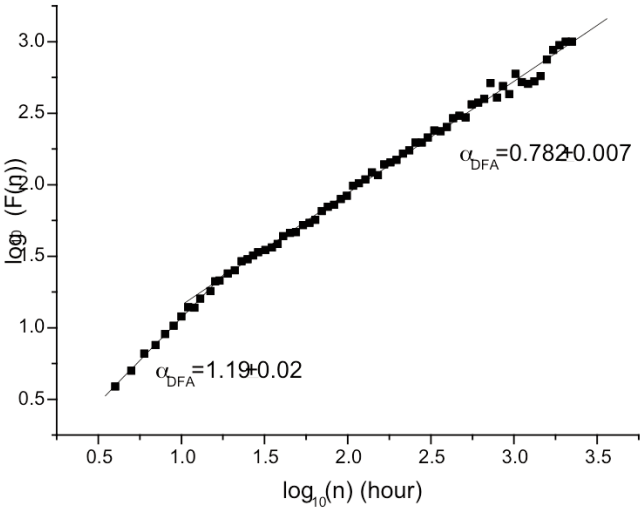

Figure 6. Detrended Fluctuation Analysis performed on the CSR geomagnetic signal.

ues for the scaling exponents, with a crossover located approximately at 24 hours. This crossover effect indicates that different dynamics govern the same geophysical phenomenon at small and long timescales. The crossover can be associate to the diurnal variation, induced by pressure and temperature.

4. Conclusions

We have shown that the time dynamics of the geoelectrical and geomagnetic time series measured in a seismic and volcanic active areas of Southern Italy are not realizations of a purely random stochastic process. The power spectra have the power-law form typical of colored-noise with the spectral exponent measuring the degree of correlations in the signals, this indicating the presence of memory effects in the geophysical system generating geoelectrical and geomagnetic signals. The spectral results are confirmed by applying fractal methods of analysis. The Higuchi analysis has revealed that the signals present typical features of fractal curves with scaling exponents D consistent with the spectral indices. The DFA has shown the presence of long-range correlations in the data, characterizing the temporal fluctuations of the signals as persistent.

Acknowledgements

The authors are grateful to Ciro Del Negro for providing us of the geomagnetic data. This research was supported in part by the Epot project of the GNV.

References

M. Balasco, V. Lapenna and L. Telesca, (2001). *1/f$^{\alpha}$ fluctuations in geoelectrical signals observed in a seismic area of southern Italy*. Tectonophysics, 347, 253-268.

Berry, M.V., (1979). *Diffractals*. J. Phys. A Math. Gentile., 12, 781-792.

Buldyrev, S.V., Goldberger, A.L., Havlin, S., Peng, C.-K. and Stanley, H.E., (1994). *Fractals in biology and medicine*. In: Fractals in Science (A. Bunde and S. Havlin S, eds). Springer-Verlag.

Burlaga, L.F. and Klein, L.W., (1986). *Fractal structure of the interplanetary magnetic field*. J. Geophys. Res., 91, 347-351.

Cuomo, V., Lapenna, V., Macchiato, M., Serio, C. and Telesca, L., (1998). *Linear and non linear dynamics in electrical precursory time series: implications with earthquake prediction*. Tectonophysics, 287, 279-298.

Cuomo, V., Di Bello, G., Heinecke, J., Lapenna, V., Martinelli, G., Piscitelli, S. and Telesca, L., (2001). *Investigating the temporal fluctuations in geoelectrical and geochemical signals jointly measured in a seismic area of southern apennine chain (Italy)*. Annali di Geofisica, 44, 179-191.

Havlin, S., Selinger, R., Schwartz, M., Stanley, H.E. and Bunde, A., (1988). *Random multiplicative processes and transport in structures with correlated spatial disorder*. Phys. Rev. Lett., 61, 1438-1441.

Higuchi, T., (1988). *Approach to an irregular time series on the basis of the fractal theory*. Physica D, 31, 277-283.

Higuchi, T., (1990). *Relationship between the fractal dimension and the power-law index for a time series: a numerical investigation*. Physica D, 46, 254-264.

Kantelhardt, J.W., Koscienly-Bunde, E., Rego, H.H.A., Havlin, S. and Bunde, A., (2001). *Detecting long-range correlations with detrended fluctuation analysis*. Physica A, 295, 441-454.

Johnston, M.J.S., (1997). *Review of electric and magnetic fields accompanying seismic and volcanic activity*. Survey in Geophysics, 18, 441-475.

Lomb, N.R., (1976). *Least-squares frequency analysis of unequally spaced data*. Astrophyisics and Space Science, 39, 447-462.

Park, S.K., (1997). *Monitoring resistivity change in Parkfield, California: 1988-1995*. J. Geophys. Res., 102, 24545-24559.

Patella, D., Tramacere, A. and Di Maio, R., (1997). *Modelling earth current precursors in earthquake prediction*. Annali di Geofisica, 40, 495-517.

Peng, C.-K., Havlin, S., Stanley, H.E. and Goldberger, A.L., (1995). *Quantification of scaling exponents and crossover phenomena in nonstationary heartbeat time series*. CHAOS, 5, 82-87.

Scholz, C.H., (1990). *The mechanics of earthquakes and faulting*. Cambridge University Press, 439 pp.

Telesca, L., Cuomo, V., Lapenna, V. and Macchiato, M., (2001). *A new approach to investigate the correlation between geoelectrical time fluctuations and earthquakes in a seismic area of southern Italy*. Geophys. Res. Lett., 28 , 4375-4378.

Non-Stationary Analysis of Geomagnetic Field Variations for the Identification and Characterisation of Volcanomagnetic and Seismomagnetic Events

Maurizio Fedi and Mauro La Manna

Dipartimento di Scienze Della Terra, Università di Napoli

Abstract

Some geomagnetic variations, termed volcanomagnetic (VM) and/or seismomagnetic (SM) effects, are linked to volcanic and seismic activity. Here, we analyse real geomagnetic time series to detect the VM and/or SM effects caused by historical volcanic and/or seismic events. We apply to geomagnetic signals two signal processing techniques, called CWTSA (Continuous Wavelet Transform Singularity Analysis) and TVANS (Time-Variant Analysis of Non Stationary Signals). Both techniques are very effective in identifying the geomagnetic variations at the time instants linked to volcanic and/or seismic activity. The main feature of the methods is that they work inherently in a local sense, i. e. they do not need time averaging and are not global estimates on time windows, like Fourier spectral techniques. But CWTSA may also work in a global sense, which gives in practice similar results to conventional spectral analysis. We tested these methodologies on seismomagnetic real data to which we added five theoretical singularities in order to simulate geomagnetic anomalies due to a piezomagnetic effect from a seismomagnetic model of a fault rupture. CWTSA and TVANS were then applied to real geomagnetic time sequences recorded in North Palm Springs during the seismic event of 8 July 1986. The results evidence a good agreement between detected and known event.

Key words *non-stationary analysis – geomagnetic anomalies - North Palm Springs*

1. Introduction

It is known that volcanic activity and/or seismic events can cause time variations of the geomagnetic field of a few nT. They are termed seismomagnetic (SM) and volcanomagnetic (VM) effects. A clear relation between SM and VM effects and volcanic and seismic events is often discussed in literature. [Davis et al. 1983, Johnston et al. 1981, Johnston et al. 1987, Johnston 1997, Zlotnicki & Le Mouel. 1988, Zlotnicki et al. 1998].

The SM and VM effects can be caused by several physical phenomena. The most common mechanisms are the piezomagnetism and thermomagnetism, but also other mechanisms play a very important rule to generate geomagnetic variations: electrokinetic effects and resistivity variations in the rocks. Moreover, other phenomena can generate important geomagnetic variations in volcanic area, like the removal of magnetized materials [Johnston et al. 1981] and the interactions between the eruptive shock waves and Earth's ionosphere [Zlotnicki 1995].

To understand the possible duration of the SM and VM effects it is very important to know the origin of these. It is known that they can accompany the volcanic and seismic events but also they can precede and follow these ones. The events with a duration very quick (hours) are associated to piezomagnetic effects, while those very intense, in volcanic areas, are usually caused by thermomagnetic effects. Instead, the long period effects are related to electrokinetic effects [Zlotnicki et al. 1998].

Actually, in several volcanic and seismic areas in the world are installed geomagnetic networks of surveillance that continuously monitor the geomagnetic field variations (SM and VM effects). Some of these are located along San Andreas fault system in California (USA), on the Mt. S. Helens (USA), on the Merapi (Indonesia), on various volcanoes in Japan, on the Mt Etna (Italy), etc. Usually, the variations of the geomagnetic field are studied considering the simultaneous difference between the magnitudes of the geomagnetic fields measured in two or more stations which are often spaced several kilometres apart. This primary operation aims at removing or reducing the slow variations of the main and transient magnetic fields due to the inner and external part of this one respectively. Instead, it is very difficult the reduction of the irregular transitory variations due to anomalous resistivity variations in the rocks. Actually, the usual method applied to reduce of 1-2 nT the irregular transitory variations is based on the hourly and daily mean values of the difference of the magnetic fields [Del Negro et al.. 1997, Del Negro et al. 2002, Zlotnicki et al. 1998].

Here, we propose two methodologies of analysis to study the real geomagnetic time sequences recorded in stations of geomagnetic networks. The first one is based on the continuous wavelet transform (CWT), it allows the detection singularities of the signal; the second one, instead, is based on a time-varying adaptive predictor which provides information about "innovation" events in the time. We do not only

consider the difference between more signals but we try to analyse the separated signals.

These methodologies were first tested on seismomagnetic real data where we simulated the geomagnetic variations adding theoretical singularities. Then, just like example, we applied them to real geomagnetic time series recorded during the North Palm Springs earthquake. We found a good correlation among historical data and the seismic event detected by our signal processing techniques. In the following sections we describe two techniques of analysis which allow the detection of geomagnetic time variations linked to possible volcanic and/or seismic activity.

2. Non-stationary analysis

2.1 CWTSA analysis of non-stationary signals instead than conventional Fourier analysis

The first technique, called CWTSA (Continuous Wavelet Transform Singularity Analysis), is based on the computation of continuous wavelet transform of a signal. The continuous wavelet transform allows for a localized decomposition of measured physical quantities (as well logs or field data) into their multiscale constituents.

This obviously is more able to study much more complexity of geophysical data than that we can deal with other techniques, such as Fourier analysis. In practice, the scaling behaviour of a real process carries over the local scaling properties of its wavelet coefficients [Gonçalves et al., 1998]. Fourier analysis is inadequate to describe the local behaviour of a given signal, since it refers to a global and not local scale. The only way to make more local a conventional spectral analysis is to partition the signal and compute the power-law scaling exponent local for any sub-interval [Zhou and Thybo 1998]. But this has well known disadvantages and, in any case, it is a not inherently justified way to deal with a local problem. For instance, global analysis, like Fourier spectral analysis, gives all the information required to assess the fractal nature of a signal, but does not help to find and classify the singularities in a local sense.

Wavelet analysis, instead allows an inherent locally-posed analysis. Moreover, it may be also used to perform a global analysis, if required, as for instance using the Legendre transform and the related singularity spectrum. For a comparison between second order statistics (Fourier spectra) and wavelet analysis, see [Fedi 2002]. The continuous wavelet transform of $f(t) \in L^2$ ( ) at scale s and time t_0 is

(1)

$$W_f(t_0,s) = (f, \psi_{t_0,s}) = \int_{-\infty}^{+\infty} f(t) \frac{1}{\sqrt{s}} \cdot \psi\left(\frac{t-t_0}{s}\right) dt$$

where the kernel function $\Psi_{to,s}(t) = 1/(s)\text{-}1/2\ \Psi[(t- t_0)/s]$ is the analysing wavelet.

It provides a partition of the signal in the time-scale plane and it allows the detection of the rapid changes (usually steps, jerks, etc) present into the signal. These quick variations are defined singularities. Some theorems [Mallat and Hwang, 1992] prove that the wavelet transform is an optimal tool to define the local regularity of a function. The regularity can be estimated by the study of the local maxima of the modulus of the continuous wavelet transform, or as a whole, in a region of the time-scale plane called cone of influence by the continuous wavelet transform coefficients. The wavelet transform modulus maxima lines (WTMML) are the lines interconnecting the maxima of the modulus of the wavelet transform within the cone of influence and across the time-scale plane. They emanate from the abscissas where the singularities are located. The partitioning of the time-scale plain with WTMML provides an efficient measurement procedure of the local Holder exponents associated with singularities, through the slope of the WTMML at small scales [Mallat and Zhong 1992, Mallat 1998, Hermann 1997].

CWTSA is suitable to detect both isolated and not-isolated singularities. Obviously, it is known that real geomagnetic time sequences, as all real data, are very often characterized by not-isolated singularities.

2.2 TVANS analysis of non-stationary signals

The second technique, called TVANS (Time-Variant Analysis of Non-Stationary Signals), is based on time-variant analysis and it is based on a predictive analysis. This method deals with the general problem of estimation in which a sample of each of the several measured sequences is predicted, in adaptive way, from a weighted linear combination of past samples from other sequences. The mutual correlation between the signals can then be estimated. Considering that the phenomenology of the process is time-variant, a non-stationary approach is more useful to describe the physical processes tied to volcanic and seismic dynamics. For this reason it also has been utilised an

approach of adaptive type. In the non-stationary analysis all the variables are time-varying. Therefore also the weight vector of prediction will depend on time, as well as the cost function (least squares error). The technique of analysis consists in a set of adaptive mutual predictors trained on a sliding time-window that, via a "forgetting" mechanism, tracks the changing statistical characteristics of the observed time series [Haykin, 1996]. The TVANS uses an adaptive algorithm (RLS) that allows the detection of some time intervals where important statistical variations of the signal occur. These variation are termed "non-stationarity zones" and they could be associated to zones where SM and VM effects occur.

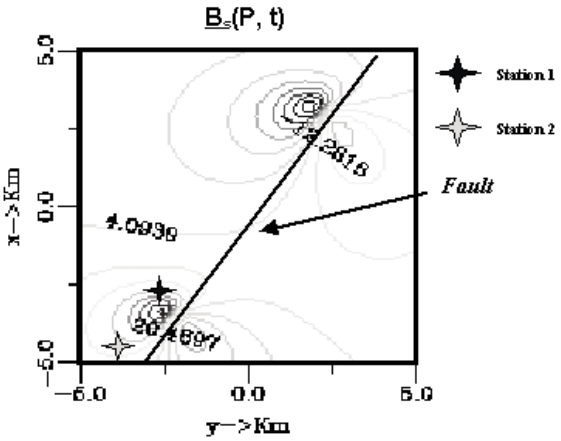

Figure 1. Seismomagnetic Model. Simulation of geomagnetic variation due to a piezomagnetic effect for a fault rupture of 10 Km.

3. Application of the techniques to seismomagnetic signals from a fault rupture model

The CWTSA and TVANS have been tested on two real seismomagnetic signals to which we added singularities in order to simulate geomagnetic anomalies from a seismomagnetic model of a fault rupture, figure 1 and table I.

The INGV- Catania has developed a MatLab code VMM (Volcano Magnetic Monitoring) that allows the building of seismomagnetic and volcanomagnetic models. We used this code to build our seismomagnetic model based on a fault rupture. Then we considered two real seismomagnetic signals at which we added five theoretical singularities to simulate the geomagnetic variations due to a piezomagnetic effect caused by a fault rupture of a 10 km length. The five singularities added are charcterized by different Holder exponents such as α_1= 0.2, α_2= -1, α_3= 0, α_4= 0.5 and α_5= -0.5. For the first sequence (station 1) we added the five singularities with a 10 nT amplitude, while for the second sequence (station 2) the amplitude was 11 nT.

First, we verified in which way the time averages applied to the signals affected the results. The differences of the geomagnetic signals at the two stations either before adding the five singularities (a) and then adding them (b) are shown in figure 2. It is clear that the differences are similar. Only for the singularity with an Holder exponent α_3=0 a different behaviour is clearly visible. The diagrams, in (b) and in (d), indicate the time average of the difference, with a window of 6 points, without singularities and adding them, respectively. These two diagrams evidence that only the singularities with α_3=0 is distinguishable while the information about the others is dramatically lost. In practice, the time average only detect the singularities associated to step function (α_3=0).

Subsequently, CWTSA and TVANS have been applied to the difference of the signals and to the signals themselves, respectively. We considered two cases: without the five theoretical singularities and with them. In figure 3 the CWT of the difference of the geomagnetic time series either without singularities (a) or adding them (b) is shown. It is clear that the wavelet transform detects well the time instant where the theoretical singularities are added. A net change between the two diagrams occurs. In fact, the CWT allows the detection of singularities different from the case (a). TVANS, instead, has been applied directly to the station signals.

Physical Parameters		**Source Parameters**
Magnetic	*Piezomagnetic*	*Geometry of the fault*
Incl: 60 °	Rigidity: 0.35 bar*1E6	Depth: 0.5 km
Dec: 0°	Stress Sensibility: 0.0002 bar^-1	Dip: 90°
Aver. Magnetiz.: 2 A/m	Poisson Ratio: 0.25	Length: 8 km
Curie depth: 25 Km		Width: 4 km
		Orient. in the N: 34 °
		Displacement 2 m
		Type of displacement.: Strike Slip

Table I - Physical parameters of the fault of the model.

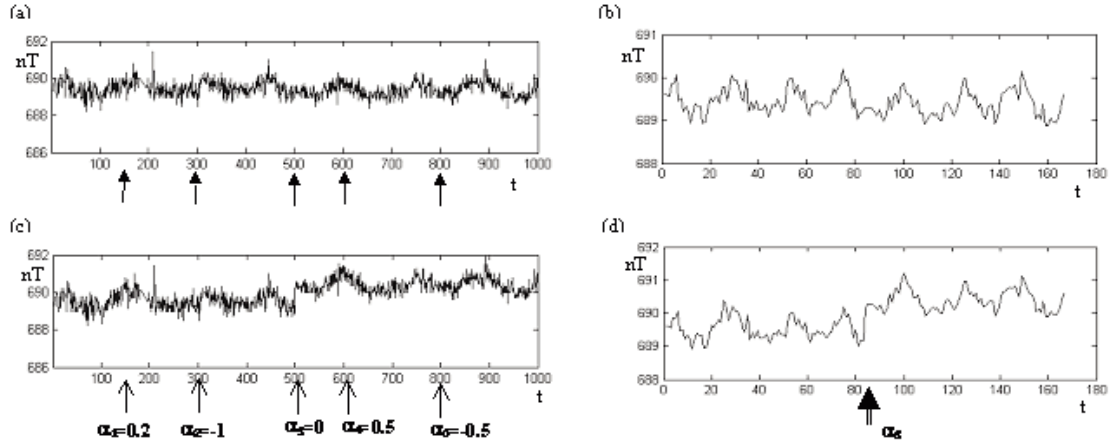

Figure 2. In (a) the difference of the geomagnetic fields measured in stations 1 and 2 without theoretical singularities is shown; black arrows indicate the positions where the singularities will be successively added. In (c) the difference of the geomagnetic fields shown in (a) after adding the singularities. In the diagram (b) the time average of the difference (a) performed on 6 points is shown. In (d) the same time average adding the singularities is visualized. The double arrow indicates the unique identified singularity α_3=0.

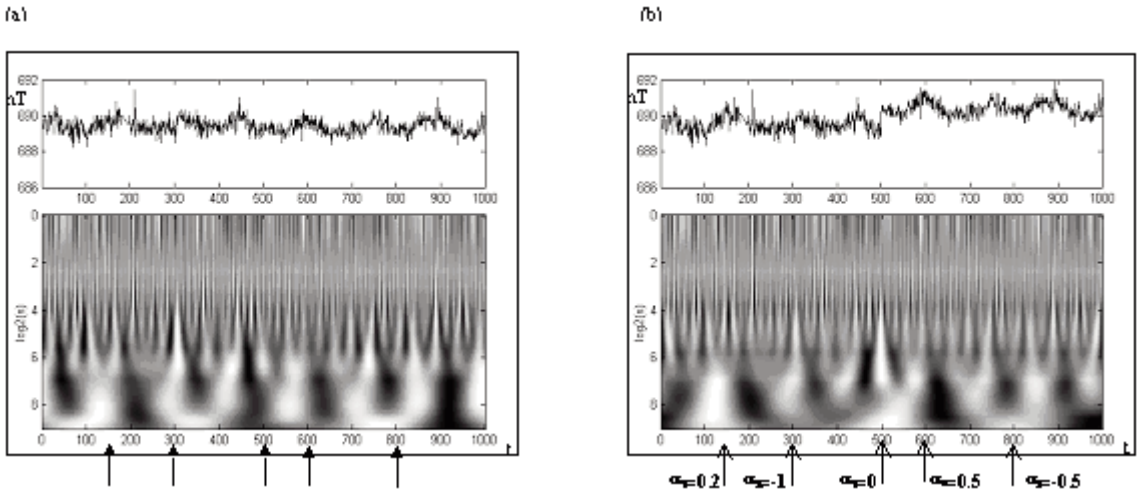

Figure 3. CWT of the geomagnetic field difference for stations 1-2 without the singularities. The arrows indicate the positions in the CWT where the singularities will be successively added (a) and adding them (b).

TVANS evidences some intervals where a statistical "innovation" occurs. Figure 4 shows the results of the time-variant analysis applied to the signals either in the case without the singularities (a) and (b) or in that where we added them (b) and (d). For the signal recorded in station 1 the five theoretical singularities are detected well. In the diagrams the least square minimum errors (LSME) of the signal 1 predicted by itself, by the signal 2 and by both, evidence that new non stationarity zones (b) occur, with respect to the TVANS before adding the singularities (a). The same thing happens for the signal 2 in (c) and (d).

In conclusion, the CWTSA and TVANS are very effective to identify well the geomagnetic variations (i.e. singularities).

4. Real geomagnetic time series recorded during the North Palm Springs earthquake.

Real seismomagnetic signals have been measured by two proton magnetometers of a geomagnetic networks of surveillance placed at distances of 3 km and 9 km from the epicentre of the North Palm Springs earthquake occurred on July 8 1986, magnitude 5.9, along San Andreas fault system, approximately 12 km NW of North Palm Springs, California, at 0921 UT

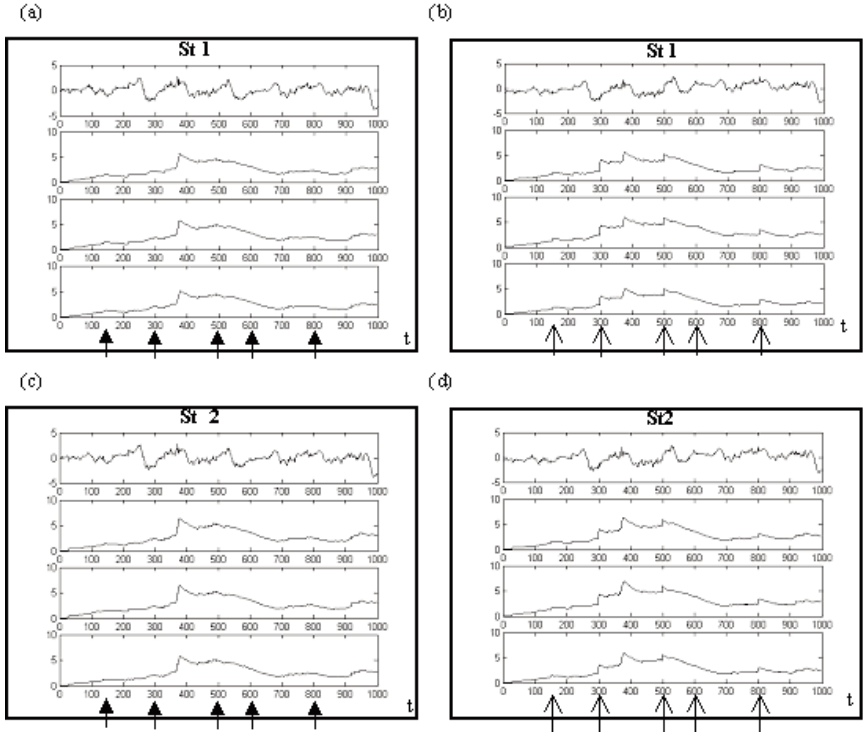

Figure 4. TVANS of the geomagnetic signal recorded in station 1 without theoretical singularities (a) and adding them (b). In (a) and (b) in order from top to bottom: signal 1, least square minimum error (LSME) of the predictor 1, LSME of the predictor 1-2, LSME del of the predictor 1-1-2. of the geomagnetic signal recorded in station 2 without theoretical singularities (c) and adding them (d). In (c) e (d) in order from top to bottom: signal 2, LSME of the predictor 2, LSME of the predictor 2-1, LSME of the predictor 2-2-1. The arrows in the diagrams (a) and (c) indicate the positions before adding the theoretical singularities, while those in (b) and (d) indicate the positions of the singularities added. Vertical axes refer to adimensional quantities.

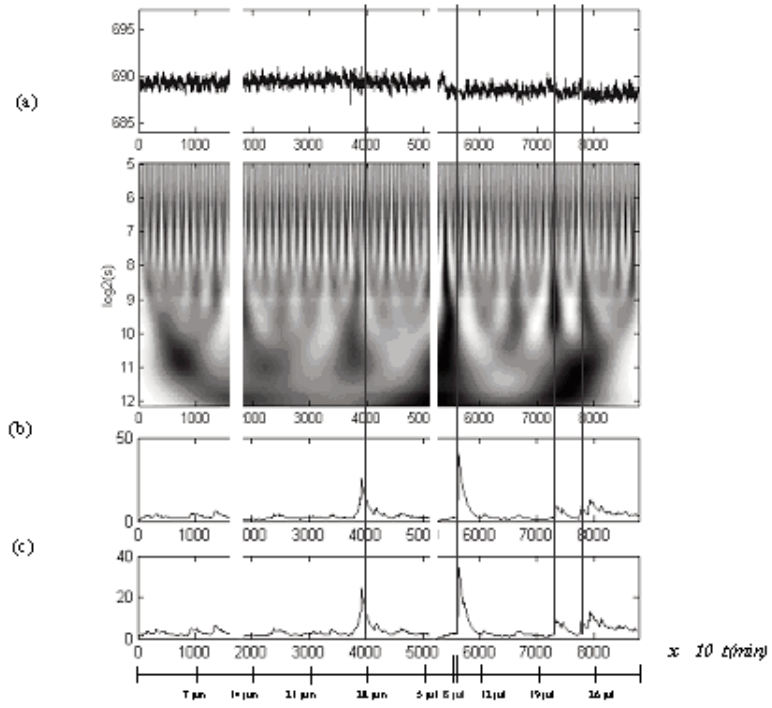

Figure 5. (a) CWT of the difference of the geomagnetic time series measured at stations (OCHM – LSBM). The LSME of the predictors 1-2 e 2-1 are shown in (b) and (c).

[Johnston et al., 1987]. Two stations, OCHM and LSBM, have been sampling and transmitting data every 10 minutes through a 16-bit digital telemetry system to Menlo Park, California.

The length of the analysed geomagnetic time sequences is two months (June-July 1986).

CWTSA was directly applied to the difference of geomagnetic time series without performing time averages. In figure 5a the CWT of the difference is visualized. Several cones of influence detect some singularities. The most evident cones are four; the first one around the June 28, the second one on July 8, the other two on July, 21 and 24 respectively. According to the singularity analysis, we observe a sharp variation of the signal (singularity) at the point of abscissa t_0, where the cones of influence begins.

Then, TVANS was applied to two geomagnetic time sequences recorded in OCHM and LSBM stations. They are indicated with x_1 and x_2 respectively. In the diagram (b) the LSME of the predictor 1-2 is visualized. In diagram (c), instead, the LSME of the predictor 2-1 is shown. The most important statistical variations of the sequences are evident: around June 28, around July 8 and between July 21 and 24.

Summarizing, the comparison of the results of CWTSA and TVANS show in agreement some important time intervals where important geomagnetic variations occur. The first around June 28, the second around July 8 and the third between July 21 and 24.

It is not possible, for the North Pam Springs data set, to correlate the results with other geophysical data because actually these were not available.

5. Conclusions

Some important magnetic variations occur during volcanic and seismic activity. Usually, the amplitude of the geomagnetic variations are very small, ranging 1-2 nT, so that it is very difficult to detect them.

In this work, two methodologies of non-stationary analysis, CWTSA and TVANS, have been applied to study geomagnetic time series. These methodologies, tested to seismomagnetic real data from a seismomagnetic model of a fault rupture, have shown a remarkable ability to detect simulated time variations. Such techniques, inherently superior to the usual second-order statistics methods (like Fourier spectra) may operate on either a local or a global scale. Fourier power spectra or other common techniques, like time averages, do not have this local performance: for instance, using different kinds of singularities, we have verified that the technique based on time averages is effective to evidence only singularities with $\alpha=0$.

CWTSA and TVANS have been applied to real geomagnetic time sequences. In particular, CWTSA has been applied to the difference of geomagnetic series while the TVANS has been applied to single station signals. The results have shown that these techniques have a good ability to detect geomagnetic variations that could be associated to SM and/or VM effects. Comparing the results from both techniques is evident a substantial agreement for the event relative to seismic activity recorded at North Palm Springs. Moreover, these two techniques allowed other particular temporal intervals to be detected, where the statistical characteristics of the signal change. In conclusion, the research has provided good results: using localized techniques of analysis, like CWTSA and TVANS, one may not only obtain the same results than conventional techniques like time averaging, but may also study other features of the signal, which are completely lost with conventional analysis. The characterization of the singular events is another potential feature of our approach and will be described in a different paper.

Finally, we note that while the CWTSA can be applied to the difference of geomagnetic time series, TVANS can be also applied to more stations. This technique is therefore potentially very interesting, since may allow to studying simultaneously time series recorded in multi-stations, as typically occurs for a geomagnetic networks of surveillance.

Acknowledgements

This research was supported in part by the Epot project of the GNV.

References

Davis, P.M. and Johnston, M.J.S. (1983). *Localised geomagnetic field changes near active faults in California 1974-1980*, Journal of Geophisycal Research, 88, No B11, 9452-9460.

Del Negro C., Ferrucc, F. and Napoli, R. (1997). *Retrieval of large volcanomagnetic effects observed during the 1981 eruption of Mt. Etna*, Annali di Geofisica, vol. XL, 2, 547-56.

Del Negro, C., and Currenti, G. (2002). *Volcanomagnetic signals associated with the 2001 flank eruption of Mt. Etna (Italy)*, accepted by Geophysical Research Letters.

Fedi, M. (2002). *Global and Local Multiscale*

Analysis of Magnetic Susceptibility Data. Pure Appl. Geophys., in press.

Gonçalvès P., Riedi R., Baraniuk R. (1998). *A simple statistical analysis of wavelet-based multifractal spectrum estimation*, in Proc. 32nd Conf. On Signals, System and Computers, (Asilomar, Pacific Grove, CA), Nov 1998.

Haykin,S. **(**1996). *Adaptive filter theory*, Info. and Sys. Scie. Ser. Prentice Hall, T. Kalaith editor, pp. 365-572.

Johnston, M.J.S., Mueller, R.J. and Dvorak J. (1981). *Volcanomagnetic observations during eruptions, May-August 1980*, US Geol. Sr. Prof. Pap. ,1250, 183-189.

Johnston, M.J.S. and Mueller R.J. (1987). *Seismomagnetic observation during the 8 July 1986 magnitude 5.9 North Palm Springs earthquake*, Science, 237, 1201-1203.

Johnston, M.J.S. (1989). *Review of magnetic and electric field effects near active faults and volcanoes in the U.S.A.*, Earth Planet. Sci. Lett., 57, 47-63.

Johnston, M.J.S. (1997). *Review of electric and magnetic fields accompanying seismic and volcanic activity*, Survey in Geophysics, 18, 441-475.

Mallat S. (1998). *A Wavelet Tour of Signal Processing*, Academic Press.

Mallat S. & Hwang W.L. (1992). *Singularity detection and processing with wavelets*, IEEE Transactions an Information Theory, 38, no 2, 617-643.

Mallat S. & Zhong S. (1992). *Characterization of signals from multiscale edges*, IEEE Transactions on Pattern an Machine Intelligence, 14, no 7, 710-732.

Zhou, S. and Thybo, H. (1998). *Power spectra analysis of aeromagnetic data and KTB susceptibility logs, and their implication for fractal behavior of crustal magnetization*, Pure Appl. Geophys., v. 151, 147-159.

Zlotnicki, J. and Le Mouel, J.L. (1988). *Volcanomagnetic effects observed on Piton de La Fournaise volcano (Réunion island): 1985-1987*, Journal of Geophysical Research, 93, 9157-9171.

Zlotnicki, J. (1995), *Monitoring active volcanoes, strategies, procedures and techniques*, edited by Mc Guire, C Kilburn & J. Murray, UCL Press.

Zlotnicki, J. and Bof, M. (1998). *Volcanomagnetic signals associated with the quasi-continuos activity of the andesitic Merapi volcano, Indonesia: 1990-1995*, Physics of the Earth and Planetary Interiors, 105, 119-130.

Nonlinear Identification and Modeling of Geomagnetic Time Series at Etna Volcano

Annamaria Vicari[1,2], Gilda Currenti[1,2], Ciro Del Negro[1], Luigi Fortuna[2] and Rosalba Napoli[1]

[1]Istituto Nazionale di Geofisica e Vulcanologia - Sezione di Catania, Italy
[2]Università di Catania – Dipartimento di Ingegneria Elettrica Elettronica e dei Sistemi, Italy

Abstract

Geomagnetic fluctuations observed on the ground are closely interrelated to external magnetic fields of ionospheric and magnetospheric origins. Theoretical studies have shown that the magnetosphere belongs to the class of dissipative chaotic systems. Assuming that the magnetosphere evolves in a coherent and organized way, a low-dimensional analogue model was studied to understand its dynamics. Following on from this description of the magnetosphere, we propose an innovative method for chaotic dynamical system identification from measured data. We firstly applied a nonlinear time series analysis to examine the behavior of geomagnetic signals and to obtain useful information about the internal deterministic component of magnetic time series from volcanic areas. We describe geomagnetic activity in terms of a relatively simple nonlinear dynamical analogue model, whose parameters are determined in such a way that the simulated output signal synchronizes with the data acquired from the magnetic monitoring network at Etna volcano. Finally, once a possible dynamic of the system has been evaluated, we make an estimate of possible external deterministic forces of the system.

Key words *geomagnetic fluctuations - chaotic dynamical system - Etna volcano*

1. Introduction

A wide variety of techniques have been developed to reconstruct dynamics from geomagnetic time series, and to characterize dynamics in terms of predictability or dynamical invariants such as the correlation dimension or spectrum of Lyapunov exponents. The true nature of geomagnetic variations is unknown [Barraclough and De Santis, 1997]. Variations in the Earth's magnetic field over different time scales are tied to different causative physical processes. The temporal variations in the geomagnetic field have extremely wide timescales, corresponding to a rich collection of physical mechanisms. We turn our attention to geomagnetic variations within shorter periods (from minutes to months). On these time scales, natural geomagnetic variations are due to secondary fields induced in the Earth by ionospheric and magnetospheric current systems. They introduce dissipativity and non-linearity, which are two necessary conditions for the existence of chaotic dynamics [Pavlos et al., 1994; 1999]. When the observed phenomenon is not obviously governed by some simple law, it is common practice to assume random behaviors. Starting from this assumption, statistical and spectral analyses are usually applied. Unfortunately, a statistical approach provides information only on the mean aspect of the geomagnetic field, and a conventional spectral analysis is not able to distinguish chaos from random signals since both have continuous broadband power spectra. These investigations are not able to detect any deterministic behavior, especially when the underlying process is expected to be chaotic. In the last decades different analyses have been devoted to reveal the presence of the chaotic motion in geomagnetic time series [Klimas et al., 1996], with particular attention to the behavior of magnetospheric processes [Vassiliadis, 1990]. The hypothesis of low-dimensional chaotic behavior of magnetospheric dynamics was examined and it was observed that magnetospheric data analysis highlighted an organized evolution. It appears that a relatively small number of magnetospheric state variables dominate the evolution. The tools of nonlinear time series analysis and chaos theory can be used with confidence in order to obtain useful information from apparently very irregular time series such as the geomagnetic sequences collected on Etna volcano. With this in mind, we firstly applied two different algorithms to detect determinism in the geomagnetic signal and then we propose a novel method for chaotic dynamical system identification using a procedure based on a master-slave synchronization approach. In this method, the complex geophysical system is considered as an autonomous one that evolves spontaneously. Nowadays, several studies have claimed that the magnetosphere can be handled as a non-autonomous system, indicating the significative role of the solar wind driver as external forcing [Horton et al., 2001; Doxas et al., 1999]. Therefore, we investigated the reliability of a possible non-autonomous model of the geo-

magnetic signal, taking the solar wind data from WIND satellite observations.

2. Detecting Determinism

Our purpose is to detect the presence of chaotic dynamics in geomagnetic time series. A wide variety of methods are often applied to experimental or real datasets to evaluate whether the signals are consistent with a low dimensional deterministic or stochastic mechanism. Particularly, we apply two different techniques: Kaplan Test and Local Linear Forecasting. These analyses allow us to examine the presence of deterministic dynamics and distinguish randomness from chaos.

We analyze 10-minute mean values of geomagnetic total intensity from the magnetic network on Mt. Etna during the period between January, 1999 and December, 2000. Each month is separately analyzed.

2.1 Kaplan Test

When deducing dynamics from a time series, continuity is often the only safe assumption one can make about a possible deterministic mechanism for a time series. To test for the continuity of the underlying system, a valuable technique involves examining all pairs of points z_j, z_k in terms of the distance $\delta_{j,k}=|z_j-z_k|$ and the distance between their images $\varepsilon_{j,k}=|z_{j+1}-z_{k+1}|$ [Kaplan, 1994].

It is useful to compute $\varepsilon(s)$ that is given by the average of the values $\varepsilon_{j,k}$ with corresponding $\delta_{j,k}<s$, where s sets the width of the 'bins'. The behavior of $\varepsilon(s)$, as s tends to zero, is evaluated. If

$$\lim_{s\to 0}\varepsilon(s)=0$$

it is supposed that the process is governed by a deterministic mechanism, otherwise a stochastic behavior is expected.

To explain the concept described above, the results of this test, applied on some random generator, are shown. It is worth noting that the $\varepsilon(s)$ never reaches zero value, maintaining values above 0.2 (Figure 1.a). Applying the Kaplan test to the geomagnetic time series, the results show that $\varepsilon(s)$ value goes down to zero value for each period as s decreases, revealing a possible deterministic behavior of the time series analyzed. In Figure 1.b the application of Kaplan test during August 2000 is reported.

2.2 Local Linear Forecasting

Sugihara and May [1990] developed a robust technique applied to real data. It employs a local linear forecasting in order to verify whether a time series is chaotic or not. The idea behind using prediction as an evidence of chaos is very intuitive. The limited predictive ability of a chaotic dynamical system is due to its sensitivity to initial conditions. Therefore it is expected that chaos is characterized by a decrease in the correlation between predicted and actual values as prediction time increases [Tsonis and Elsner, 1990]. If the system is chaotic, then the decrease in predictive ability with prediction time is equivalent to the presence of a positive Lyapunov exponent. This property can be used to distinguish chaotic behavior from randomness. In fact, for a random signal, it is expected that the forecasting property doesn't depend on the prediction interval.

The algorithm is based on predicting the future value of a data point by considering the future values of points, which are nearby in the reconstructed phase space.

The first step of the proposed algorithm is to choose an appropriate time delay and an embedding dimension in order to construct

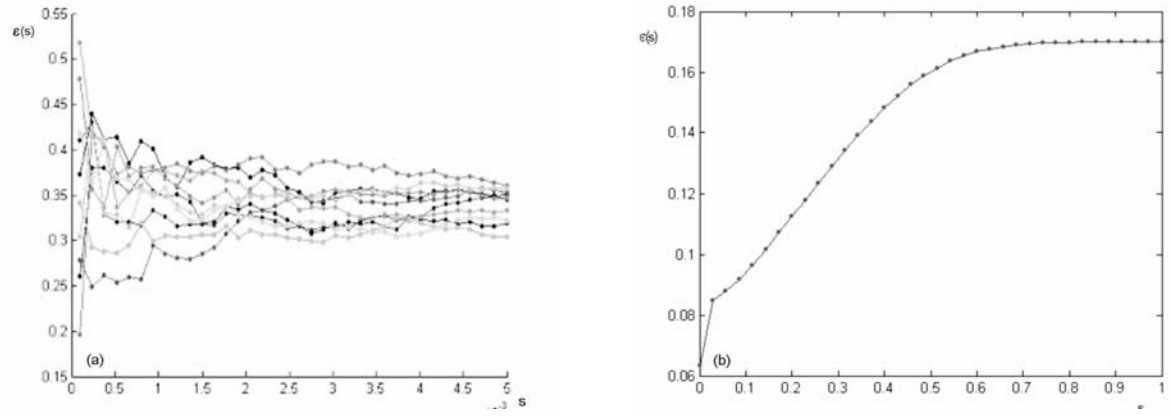

Figure 1. Kaplan test results for several random signals (a) and geomagnetic time series (b).

delay vectors in the phase space (1), using the embedding theorem by Takens [Takens F., 1981]. Given a time series x(t), the reconstructed delay vector is represented by:

$$X(t_n)= [x(t_n), x(t_n-\tau), x(t_n-2\tau), \ldots, x(t_n-(E-1)\tau)] \quad (1)$$

where τ is the time delay and E is the embedding dimension.

In order to predict a time L ahead of t_n, a neighborhood is selected around the point $X(t_n)$. For all points belonging to this neighborhood, that is, all points closer to $X(t_n)$ in the reconstructed phase space, the future values at time t_n+L are evaluated. The finally accepted prediction is the average of all these individual predictions. For each prediction all past points in the reconstructed phase space are considered, they are tested for closeness and most of them are rejected as too far away. The search of neighborhood must be repeated at each step in time to predict the future value. The correlation coefficient between predictors and true data is used to quantify the predictive ability. The correlation coefficient is dominated by the chaotic divergence of initially close trajectory and its rapid decay in relation to prediction time interval L is a strong signature of chaos.

The procedure to reconstruct the orbits in the pseudo-phase space is associated with the appropriate choice of the embedding dimension and the time delay. We use two methods, which are most common in nonlinear dynamics, the average mutual information (AMI) and the false nearest neighbors (FNN) methods [Abarbanel, H. D. I., 1995]. Since the AMI rapidly decays (Figure 2.a), the time delay cannot be determined choosing the first minimum of AMI, as is usually performed. Analyzing the AMI plot, a time delay τ=10 samples (1 sample corresponds to 10 minutes) seems to be a reasonable choice. In Figure 2.b the percentage of false nearest neighbors, as a function of the embedding dimension, is shown. The shape of FNN plot indicates an embedding dimension of about 3-4. These results have to be interpreted with great care, because of finite sets of noisy measurements. The embedding theorems mentioned pre-

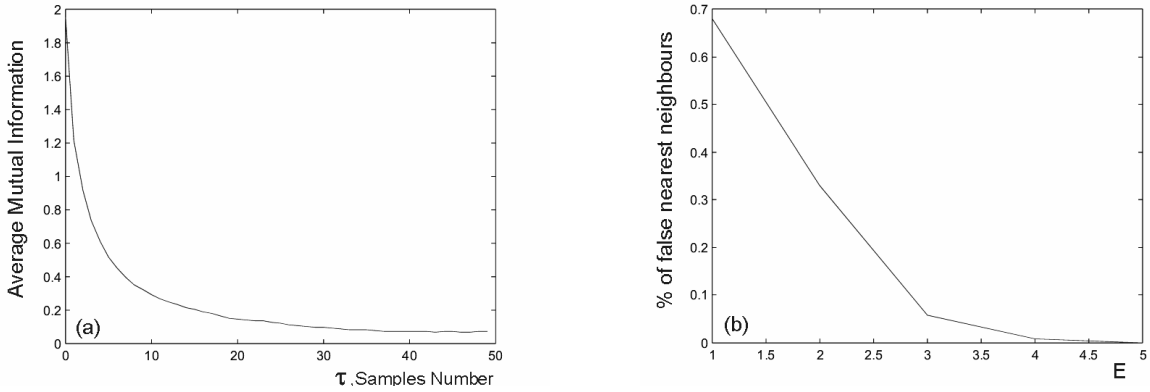

Figure 2. AMI plot for determining time delay (a) and FNN percentage versus Embedding dimension (b).

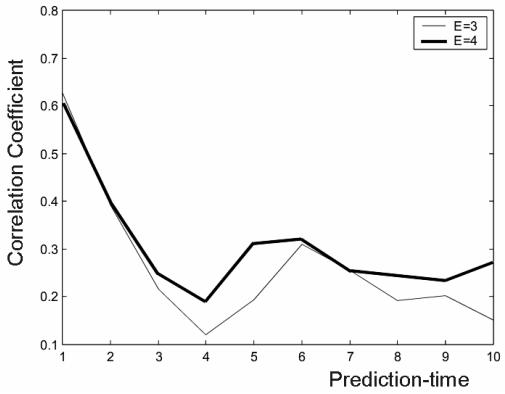

Figure 3. Correlation coefficient versus the prediction-time interval.

viously assume that the observations are available with arbitrary precision. Consequently, several authors have investigated what happens to the embedding procedure when noise is present and the sequence is of finite length. For the embedding procedure, noise seems to be the dominant limiting factor [Schreiber, T., 1999].

Having chosen the time delay and the embedding dimension, the nonlinear forecasting analysis is applied over the reconstructed phase space. The results show a quick decrease of the correlation coefficient as the prediction-time interval increases for both E=3 and E=4 (Figure 3). It is worth noting that the correlation coefficient strongly depends on the prediction time interval, revealing the unpredictability of future values for long time steps that is the most striking characteristic of chaotic behavior.

3. Nonlinear Identification

It is well known that the famous Lorenz 3-dimensional dynamical system is derived from the Navier-Stokes equations for studying the flow in fluids. If the magnetospheric system is considered as a magnetized fluid, the Navier-Stokes equations are to be generalized taking into account Maxwell's equations and the variables related to electromagnetic field [Armero and Simo, 1996]. Therefore a similarity exists between the Lorenz system and the magnetospheric one [Bhattacharjee, 1987].

With this in mind, we investigated if the state variables of the Lorenz system are able to follow the geomagnetic trajectories by opportunely setting its control parameters.

Recently, the search for synchronization has moved to chaotic systems. For a chaotic dynamical system, the evolution sensitively depends on the initial conditions. So, two trajectories starting from two different, but close initial conditions separate exponentially in the course of time. This is a relevant practical problem, in so far as experimental initial conditions are never known perfectly. By a synchronization approach, two (or many) chaotic systems (either equivalent or non-equivalent), starting from slightly different initial conditions, adjust a given property of their motion to a common behavior, due to coupling or forcing. In order to identify the control parameters of Lorenz system, we applied a combined method using a synchronization approach and Genetic Algorithm (GA) [Manganaro et al., 1999]. The synchronization can be obtained through different methods. After testing some of these, we prefer the Pecora-Carroll approach [Pecora and Carrol, 1990; 1991], based on coupling of two systems: the first one, the master, is independent from the other one, the slave, while the evolution of the second depends on the first, as illustrated in Figure 4. This arrangement is called master-slave configuration. In the Pecora-Carroll approach the *u* master system is partitioned into two subsystems, *w* and *v*. A slave system *w'* is created by duplicating the *w* system and replacing the set of variables *v'* by their corresponding *v*.

In this way the *w'* is forced by the *u* system by means of the *v* variables. As time tends to infinity, if *w'* tends to *w* then the master and slave are synchronized. Our chaotic system

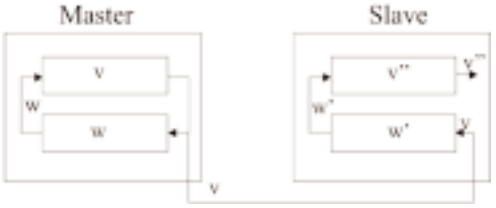

Figure 4. Mastaer-slave configuration.

identification, based on Pecora-Carroll cascaded synchronization, has been applied to identify the parameters of a Lorenz system, whose equations are reported in (3), in such a way that it synchronizes with the geomagnetic time series.

$$\begin{cases} \dot{X} = \sigma(Y - X) \\ \dot{Y} = \lambda X - Y - XZ \\ \dot{Z} = XY - rZ \end{cases} \tag{3}$$

Our geomagnetic signal, whose dynamics have to be estimated, is considered as a master system and is used to drive the Lorenz model, acting as a slave. The slave system responds to the driving signal in function of its parameters, which must be changed in order to minimize the difference between the geomagnetic sequence and the slave's state variable. To quantify this difference we define a performance index as:

$$r(p) = \sqrt{\sum_{i=1}^{M} (v - v'(p))^2} \tag{4}$$

where M is the length of data and p is the vector parameters to be identified.

The master and slave will be synchronized when the performance index has reached its global minimum. Therefore the synchronization problem can be formulated as an optimization problem, which can be solved by GA. When a genetic algorithm is used to solve an

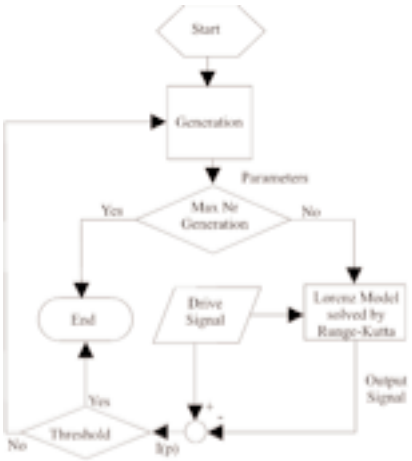

Figure 5. Modeling scheme.

optimization problem, the performance index must be opportunely chosen to obtain the best solution. Initially, the genetic algorithm will create a population of solutions based on provided sample data structure (Genome or phenotype).

The genetic algorithm then operates on the population to evolve to the best solution. The σ and λ parameters of Lorenz model represent the GA phenotype (p variables of I(p) index), whereas the r parameter is fixed at 8/3 value. Figure 5 shows the modeling scheme setup for identification of Lorenz parameters.

At each step of GA, the system of differential equations (3) is solved by a fourth-order Runge-Kutta algorithm with a time step of 0.01. It is important to note that Runge-Kutta algorithm receives the geomagnetic signal as input too. If the max number of generation is not reached, Runge-Kutta's output is compared with the geomagnetic signal to produce the performance index I(p). This process continues until I(p) goes down a threshold value (global minimum).

3.1 Results

The used data set represents a time series of 10-minute mean values from magnetic stations on Mt. Etna during the months of June 1999 (Figure 6a) and March 2000 (Figure 6b). The mean values are removed from the time series.

Each monthly data set of geomagnetic total intensity is analyzed separately and introduced as the driving signal in the master-slave configuration, therefore the number of data M is 4320 samples. The initial values of x, y, and z in Equation (3) are chosen arbitrarily because a synchronization approach is used. In particular, we have found that the best synchronization,

Algorithm Type	*Simple*	*Steady State*
Population Size	100	140
Mutation Probability	0.3	0.03
Crossover Probability	0.3	0.5
Repetition Percentage	0.8	0.8
Max Generation Number	100	100
Convergence Time (in Generation Number)	78	43

Table I - Setting parameters of GA for two different simulations.

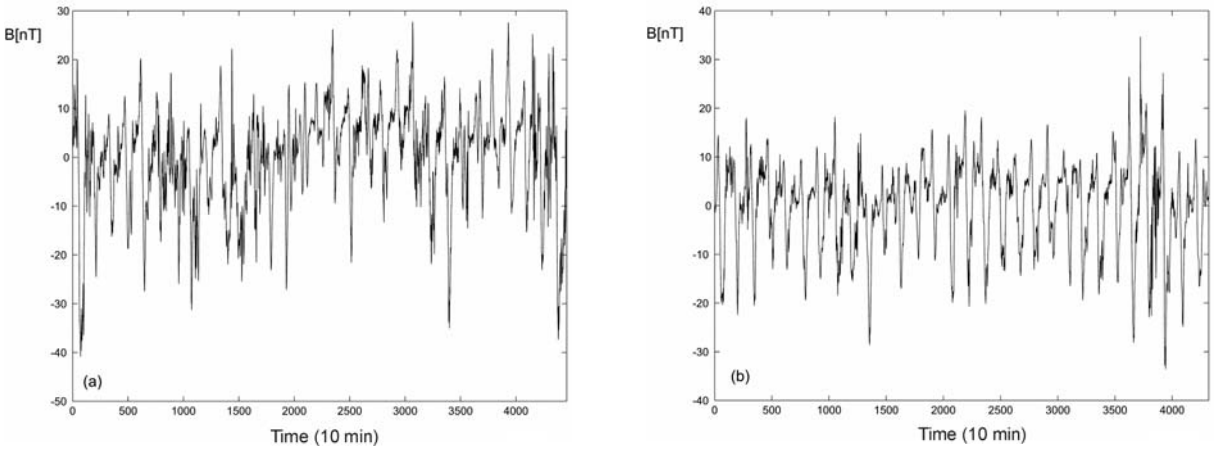

Figure 6. Time series of the geomagnetic field during June 1999 (a) and March 2000 (b).

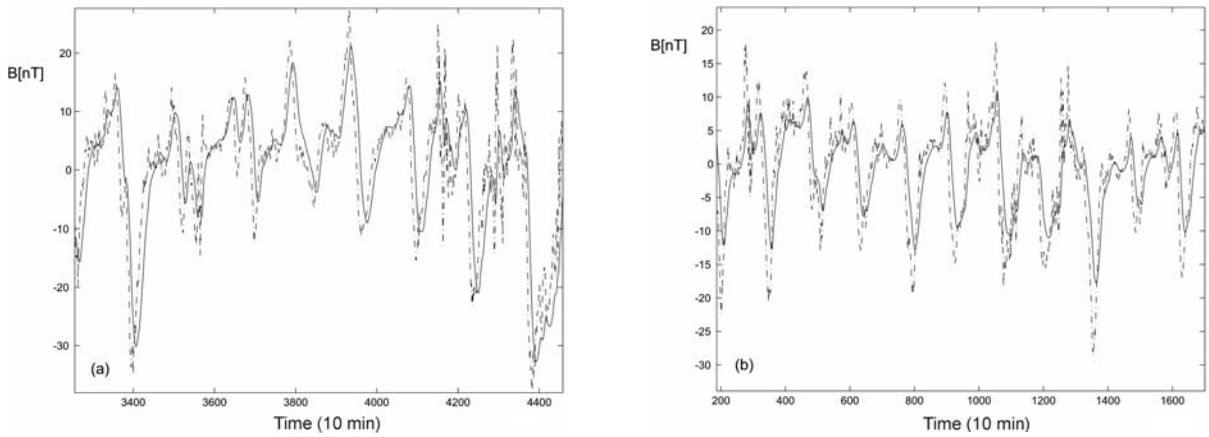

Figure 7. Geomagnetic data in dot-dash line and the x state variable of Lorenz model in solid line during June 1999 (a) and March 2000 (b).

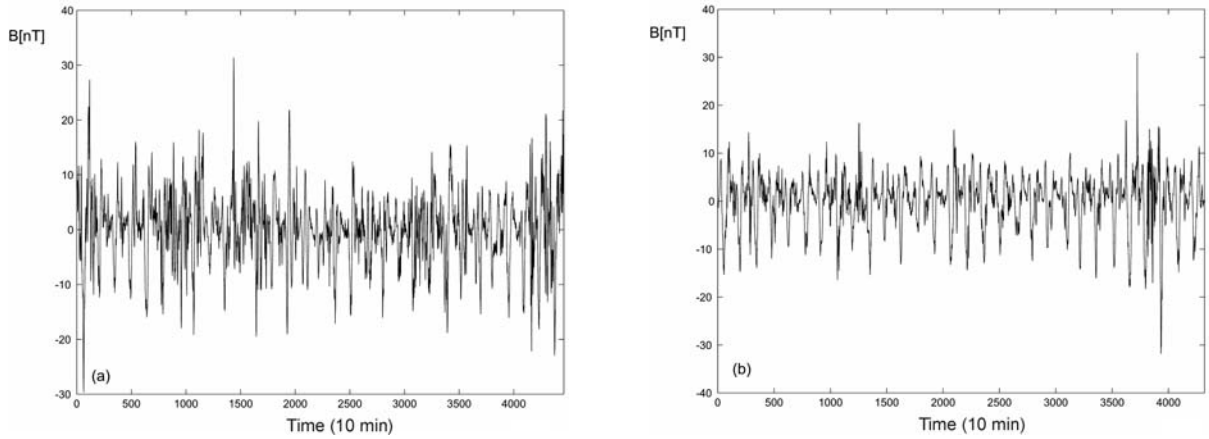

Figure 8. Synchronization error during June 1999 (a) and March 2000 (b). The STD values are respectively 4.97 and 2.98.

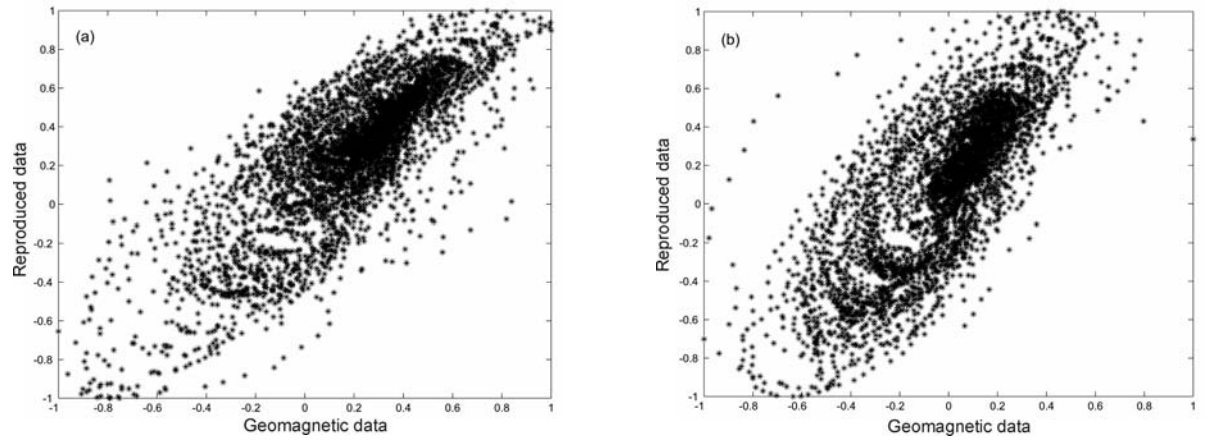

Figure 9. Geomagnetic data vs. reproduced signal of Lorenz model during June 1999 (a) and March 2000 (b). Data are normalized into [-1,1] interval.

that is the minimum I(p), is obtained when the x state variable of slave Lorenz system is driven. Two of the 'simple' and 'steady-state' ones, carried out varying the GA parameters, are written up here to show the major factors of impact.

The parameters of the Lorenz system, associated to the optimum value I(p), are reported in table II. In order to evaluate the results of the identification, the geomagnetic signal and the output signal obtained with the estimated

Period	σ	λ	I(p)
June 1999	10	29.87	15.2
March 2000	10	31.5	14

Table II - Lorenz's parameters and I(p) value obtained for two different geomagnetic sequences.

parameters have been superimposed in Figure 7. The associated synchronization errors are shown in Figure 8.

The quality of the synchronization can be appreciated by observing Figure 9, which shows the geomagnetic signal versus the output-simulated signal, after they have been normalized. In an ideal synchronization, we should see a straight line. But in real data applications, this is never going to happen owing to noise. To improve the results, we could filter the geomagnetic data by using a low-pass filter. We haven't applied any pre-processing procedure on the data to avoid losing useful information on the signal.

Although the input signal changes, our findings clearly reveal that the value of sigma and lambda always remains in the same ranges in which the Lorenz system shows the well-known butterfly attractor. Therefore, it permits us to not exclude the presence of a common dynamics, characterized by the obtained parameters.

4. Forcing Method

Once a possible dynamics of the geomagnetic signal has been estimated, we overcome the hypothesis of an autonomous model, and we suppose that the geophysical system can be modeled as a non-autonomous system [Lundstedt, 1997], namely one that evolves under the influence of some external deterministic forces. So, the question is: how to detect the external force? It is necessary to make some relevant considerations.

The analysis of geomagnetic series in the frequency domain reveals a composite spectrum that can be split into two parts: a sum of periodic terms (power concentrated in a discrete set of frequencies) and a continuous broadband spectrum (a continuous distribution of power over the whole frequency range). The broadened lines reveal the presence of harmonics with their fundamental oscillations, and a deterministic chaotic component in addition to noise (the broadband background) (Figure 10).

To fit regular variations, we justly choose a sinusoidal forcing with periodicity determined

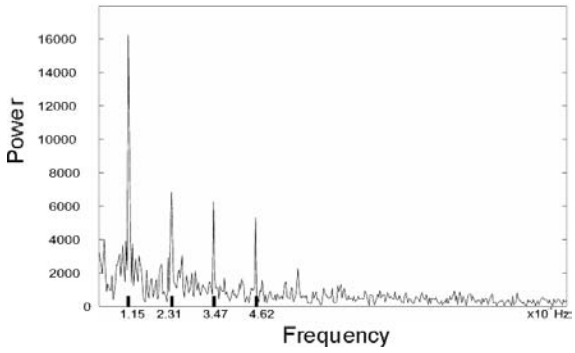

Figure 10. Power spectrum of geomagnetic time series.

by the fundamental oscillations of the spectrum, while the irregular geomagnetic external variations are given an account of solar wind velocity. Therefore the excitation (sinusoidal excitation and solar wind) is expressed by a linear combination of terms, as follows:

$$f(t) = a \times f_1(t) + b \times f_2(t) \tag{5}$$

where:

$f_1(t)$ is the solar wind component;

$f_2(t)$ is periodic components as:

$$f_2(t) = c_1 \times \sin(\Omega t) + c_2 \times \sin(2\Omega t) + c_3 \times \sin(3\Omega t) + c_4 \times \sin(4\Omega t) \tag{6}$$

a, b, c_i, with i = 1…4, are weight coefficients and Ω is the fundamental pulse.

The interaction between geomagnetic variations and the excitations is expressed by weight coefficients that are the GA phenotype. The term $f(t)$ makes the system non-autonomous: in such a way, we obtain an estimate of a possible external dynamic of the system. The external excitation is introduced in the Lorenz equation and best results are obtained when x-driven configuration is used:

$$\begin{cases} \dot{X} = \sigma(Y - X) + f(t) \\ \dot{Y} = \lambda X - Y - XZ \\ \dot{Z} = XY - rZ \end{cases} \tag{7}$$

As is shown in Figure 11, the modeling scheme is modified with respect to the previous one. At each step of GA, the system of differential equations (7) is solved by a fourth-order Runge-Kutta scheme with a time step of 0.01, but there are two considerable differences:

1. the phenotype of GA is composed of system parameters and the weight coefficients of the external forcing;
2. Runge-Kutta algorithm receives only solar wind velocity as input regardless of the geomagnetic signal.

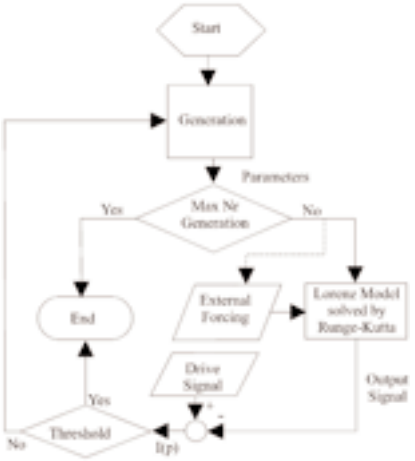

Figure 11. Modeling scheme with external forcing.

4.1 Results

We consider one of the geomagnetic data sets, used in the previous method, namely June 1999 (Figure 6). The external forcing is represented by the 10-minute mean measurements from WIND satellite observations for solar wind velocity during the same period (Figure 12).

The setting parameters of GA are the same as reported in Table I. The parameters of both the external forcing and the Lorenz system, in correspondence to the minimum value I(p), are reported in Table III. The geomagnetic signal and the output signal, obtained with the estimated parameters, have been superimposed in Figure 13 in order to estimate the results of the identification. The related identification error is shown in Figure 14.

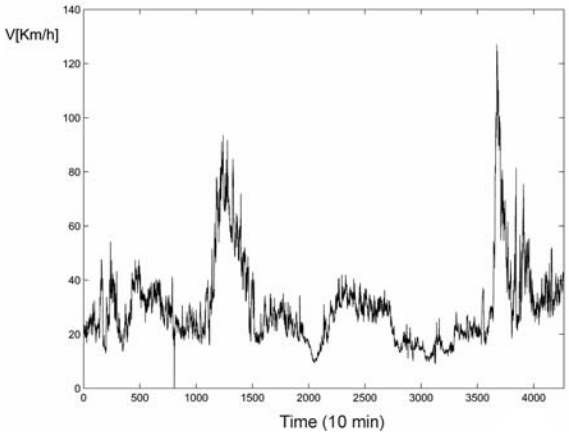

Figure 12. Solar Wind velocity from Wind satellite observations during June, 1999.

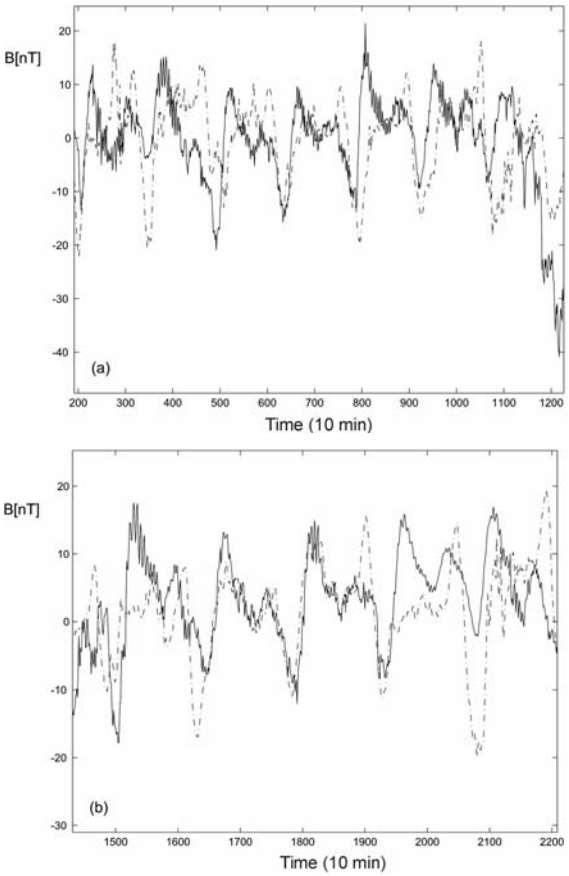

Figure 13. Geomagnetic data in dot-dash line and the x state variable of Lorenz model in solid line during June, 1999.

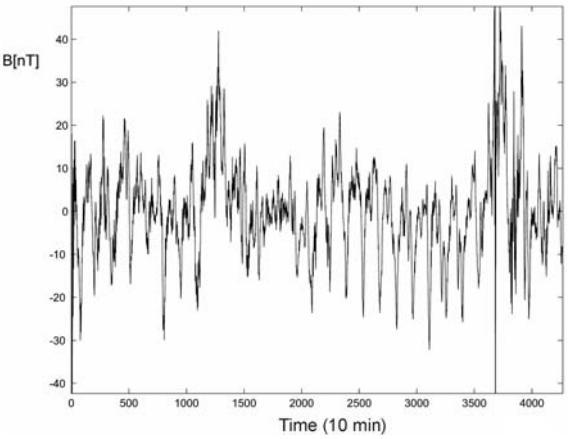

Figure 14. Modeling errors during June 1999. The standard deviation of error is 6.2.

It should be remarked that Lorenz‘s parameters, achieved by forcing approach, are similar to those computed by the synchroniza-

σ	λ	a	b	c_1	c_2	c_3	c_4	I(p)
10	30.1	-2.8819	-3.7399	7.31444	-9.56175	3.04234	-2.97002	14.5511

Table III. Lorenz parameters and weight coefficients for the minimum value of I(p).

tion method. This result lends support to the hypothesis that these parameters are related to the dynamics of the system. Instead, the weight coefficients quantify the interaction between the signal and the external forcing.

5. Conclusions

Nonlinear time series analysis and chaotic identification methods were employed to detect determinism, non-linearity and sensitivity to initial conditions for geomagnetic time series. These three properties are a necessary condition for a time series to be chaotic. The Kaplan test results permit us to not exclude that a deterministic dynamics of the system leading the geomagnetic variations exists. Furthermore, using a nonlinear forecasting approach, the limited predictive ability has been tested, revealing a strong sensitivity to initial conditions. The dependence on initial conditions represents a difficulty when an analogue model describing the geomagnetic variations should be derived. We have overcome this problem by using the synchronization approach as a tool for chaotic identification. The Lorenz system synchronizes well with the geomagnetic time series, when its control parameters are chosen in the range where the dynamical behavior is chaotic. A possible external forcing dynamic of the system has also been introduced. The preliminary results are sufficiently good, but new forcing components must be introduced to obtain better ones. Certainly, the strong coupling between solar wind parameters, magnetosphere and ionosphere constitutes the most significant state variables, which determine the dynamical behavior. Since in the short period band (i.e. less than a month) the geomagnetic field spectrum is essentially led by external contributions (from magnetosphere and ionosphere), we concluded that those external systems are in a nonlinear possibly chaotic state. This is possible and reasonable, but this result could have been affected by using data from a very anomalous site such as a volcano. In volcanic areas both magnetization and conductivity are very anomalous, and a significant effect of electromagnetic induction (magnetization affects mostly the 'static -or more slowing-part', while the conductivity affects the 'changing part' at different periods) is also present in the signal investigated. In conclusion, one cannot completely exclude that the nonlinearities (or some of them) come from nonlinear induction effects. However, the results obtained are a clear evidence of the presence of chaos in magnetic data from volcanic areas. It should be noted that models of the geomagnetic field have already been studied. Our method has the advantage that the system parameters are determined directly from measured data rather than from preconceived notions of the processes governing the geomagnetic system.

Acknowledgments

We are indebted to all personal of Geomagnetism Laboratory of INGV-CT who guarantee the regular working of the permanent magnetic network on Etna volcano. This research was supported by project EPOT of the Gruppo Nazionale per la Vulcanologia of the INGV, and developed in the frame of the TecnoLab, the laboratory for the technological advance in geophysics organized by DIEES-UNICT and INGV-CT.

References

Abarbanel, H. D. I., (1995). *Analysis of observed chaotic data.* Springer Verlag.

Armero, F., Simo J. C., (1996). *Long-term dissipativity of time-stepping algorithms for an abstract evolution equation with applications to the incompressibile MHD and Navier-Stokies equations.* Comput. Methods Appl. Mech. Engrg. 131, 41-90.

Bhattacharjee, J. K., (1987). *Convection and chaos in fluids.* World Scientific, Singapore.

Barraclough, D. R. and De Santis, A., (1997). *Some possible evidence for a chaotic geomagnetic field from observational data.* Phys. Earth Planet. Inter. 99, 207-220.

Currenti, G., Del Negro, C., Fortuna, L., Vicari, A., (2002). *Nonlinear identification of complex geomagnetic models: An innovative approach.* Nonlinear Phenomena in Complex System. In print.

Doxas, I., Horton, W., Smith, J. P., (1999). *A physics based nonlinear dynamical model for the solar wind driven magnetosphere-ionosphere system.* Phys. Chem. Earth. 24, no. 1-3 67-71.

Horton, W., Weigel, R. S., Sprott, J. C., (2001). *Chaos and the limits of predictability for the solar-wind-driven magnetosphere-ionosphere system.* Phys. Plasmas. 8, 6 2946-2952.

Kaplan, T., (1994). *Exceptional events as evidence for determinism.* Physica D, 73, 38-48.

Klimas, A. J., Vassiliadis, D., Baker, D. N., Roberts, D. A., (1996). *The organized nonlinear dynamics of the magnetosphere.* J. Geophys. Res. 101, no. A6 13089-13113.

Lundstedt, H., (1997). *Solar wind magnetosphere coupling: predicted and modeled with intelligent hybrid systems.* Phys. Chem. Earth. 22, no. 7-8 623-628.

Manganaro, G., Arena, P., Fortuna, L., (1999). *Cellular Neural Networks: Chaos, Complexity and VLSI Processing.* Springer-Verlag.

Pavlos, G. P., Diamantidis, D., Amopoulos, A., Rigas, A. G., Daglis, I. A., Sarris, E. T., (1994). *Chaos and magnetospheric dynamics.* Nonlin. Proc. Geophys.1, 124-135.

Pavlos, G. P., Athanasiu, M. A., Diamantidis, D., Rigas, A. G., Sarris, E. T., (1999). *Comments and new results about the magnetospheric chaos hypothesis.* Nonlin. Proc. Geophys. 6, 99-127.

Pecora, L. M., Carrol, T. L., (1990). *Synchronization in chaotic systems.* Phys. Rev. Lett, Vol.64, pp. 821-824.

Pecora, L. M., Carrol, T. L., (1991). *Driving systems with chaotic signals.* Phys. Rev. A, Vol.44, pp. 2374-2383.

Sugihara, G. and May, R. M., (1990). *Nonlinear forecasting as a way of distinguishing chaos from measurement error in time series.* Nature, Vol.344, pp.734-741.

Schreiber, T., (1999). *Interdisciplinary application of nonlinear time series methods*. Physics Reports,Vol.308, pp. 1-64

Takens F., (1981). *Detecting strange attractors in turbulence. In Lecture notes in mathematics.* Ed. by D. A. Rand and L. S. Young,Springer, Berlin, Vol. 898 pp. 366-381.

Tsonis, A. A. and Elsner, J. B., (1992). *Nonlinear prediction as a way of distinguishing chaos from random fractal sequences.* Nature, Vol.358, pp. 217220.

Tsonis, A. A., Triantafyllou G. N., Elsner J. B., (1994). *Searching for determinism inobserved data: a review of the issue involved*. Nonlin. Proc. Geophys.1, 12-25.

Vassiliadis, D. V., Sharma, A. S., Eastman, T. E., Papadopoulos, K., (1990). *Low-dimensional chaos in magnetospheric activity from AE time series.* Geophys. Res. Let. 17, no. 11 1841–1844.

Inverse Modelling of Piezomagnetic and Electrokinetic Data in Volcanic Areas

Giuseppe Nunnari[1] and Ciro Del Negro[2]

[1]Dipartimento di Ingegneria Elettrica, Elettronica e dei Sistemi, Università di Catania
[2]Istituto Nazionale di Geofisica e Vulcanologia, Sezione di Catania

Abstract

The inversion problem dealt with is the identification of the parameters of a volcanic source causing observable changes in magnetic data recorded in volcanic areas. To study the inverse problem, synthetic data was generated by considering two different types of volcanic sources: the traditional Mogi, whose main advantage is the limited number of parameters involved and the Okada type source that seems more realistic to interpret eruptive phenomena in volcanic areas such as Mt. Etna. Two types of magnetic effects were considered, namely the piezomagnetic and the electrokinetic effects. The considered inversion problem was formulated following two different schemes: an optimisation approach based on the use of Genetic Algorithms (GAs) and a neural network based approach based on Multi-layer perceptrons (MLPs). A regular grid centred on the summit volcano area was defined and it was hypothesised that measurements of the magnetic anomalies are performed at the vertices of the grid. Then the two inversion schemes were considered to compute the inverse solution associated with a given set of source parameters and the accuracy of the solution was studied. Appropriate indexes were defined to give an objective measure of the accuracy for each parameter of the source. The results obtained show that both the Mogi and Okada models can be unambiguously inverted. The accuracy obtained by using the GAs based approach is usually higher than that obtained with the neural approach. However, the neural approach is much faster and the accuracy for each individual model parameter is better than 10% in terms of normalised mean absolute error even in presence of data affected by a level of gaussian noise up to 30%.

Key words *inverse modelling – piezomagnetic phenomena – electrokinetic effects*

1. Introduction

Clear correlations between volcanic activity and changes in the local geomagnetic fields have been observed in numerous volcanic areas. Several scientists [Johnston and Stacey, 1969; Johnston, 1989; Yukutake et al. 1990; Tanaka, 1993; Del Negro et al. 1997 and 2000] have investigated the physical mechanisms involved with the observed magnetic anomalies and it seems that they are mainly due to thermal demagnetisation of rocks, to piezo-magnetic effects induced by the stress field generated by the incoming magma and to electrokinetic effects induced by the circulation of ionised fluids. Since the expected changes can be computed in the order of some nano Tesla (nT), very accurate instruments are required to recognise these anomalies from electromagnetic noise. However, accurate instrumentation is not the only ingredient to allow a practical use of recorded geomagnetic measurements. Good numerical methods to model data are of paramount importance also. In particular, this paper deals with the inverse modelling of geomagnetic data, i.e. with the problem of identifying the parameters of a volcanic source that is supposed to generate the changes observed in terms of magnetic data. The main aim of the paper is to assess the feasibility of the inversion problem. Moreover, the accuracy of the solution is studied versus the number of measuring points and the level of noise data. Two different types of volcanic sources were taken into account: the traditional Mogi source [Mogi, 1958], whose main advantage is the limited number of parameters involved and the Okada type sources, which seem more realistic to interpret eruptive phenomena in volcanic areas such as Mt. Etna, where eruptions have their origin in dykes opening from a certain depth toward the surface. Two types of magnetic effects were considered, namely the piezomagnetic and the electrokinetic effects.

In order to provide the necessary information for studying the inverse problem, the direct modelling problem was preliminary addressed based on the original formulas proposed by [Sasai 1991] for the Mogi model and by [Utsugi et. al. 2000] for the Okada source. The electrokinetic effects were computed by using expressions provided by [Murakami, 1989] and [Fitterman, 1979 and 1981].

In this study two different inversion approaches were considered to solve the inverse problem, namely the MLP Artificial Neural Networks (ANNs) and the Genetic Algorithms optimisation approach. MLP neural networks

have already been successfully applied to the inversion of seismic waveforms [Roth and Tarantola, 1996], [Langer et. al. 1996] and for the integrated inversion of geophysical data [Nunnari et al. 2001].

2. Direct Modelling

For the purposes of the application described in this paper, synthetic data generation is performed in order to provide a large enough data set to represent the population of the possible models within the model space. The two considered types of sources are schematically represented in Fig 1 and Fig. 2 respectively.

The basic equations for the direct modelling of piezomagnetic effects are the following. Let us indicate by ΔJ the incremental stress induced magnetisation, by W the associated magnetic potential and by H and B the magnetic field and magnetic induction respectively, then the following equations hold:

$$\begin{aligned} &H = -\mathrm{grad}W\ ; \quad B = H + 4\pi\Delta J; \\ &\nabla^2 W = -\mathrm{div}H = 4\pi\,\mathrm{div}(\Delta J) \end{aligned} \tag{1}$$

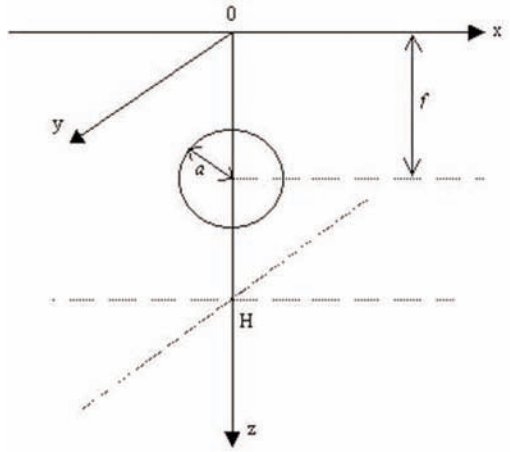

Figure 1. Mogi's source: a hydrostatically pumped pressure source in a homogeneous and isotropic elastic half-space with a uniformly magnetised upper layer centred at (0,0,f) with radius *a*. The Curie point isotherm is at a depth H.

The piezomagnetic field associated with a Mogi model has been investigated by Sasai (1991) who provided the following expressions for the components of the piezomagnetic potential W:

$$\frac{2\mu}{C}W_x = 4\pi C_z\left[\frac{\mu}{3\lambda+2\mu}\left(\frac{x_0}{\rho_1^3}-\frac{x_0}{\rho_2^3}\right)+\frac{6(\lambda+\mu)}{3\lambda+2\mu}H\frac{3x_0D_3}{\rho_3^5}\right] \tag{2}$$

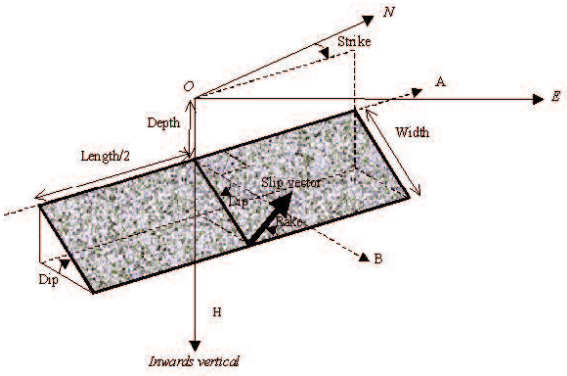

Figure 2. The Okada source: a fault occurring in a homogeneous and isotropic elastic half-space with a uniformly magnetised upper layer. H is the depth of the Curie point isotherm. Depth is the distance between the origin O and the upper edge of the fault; Strike is the orientation of the fault with respect to the North; Dip is angle of the fault plane with respect the horizontal plane; Rake is the angle of the strike-slip displacement; Length and Width are the length and width of the fault respectively; Slip is the module of the strike-slip displacement; Opening is the module of the tensile displacement.

$$+\left\{\frac{3(\lambda+\mu)}{(3\lambda+2\mu)}\left(\frac{x_0}{\rho_1^3}-\frac{x_0}{\rho_2^3}\right)\right\} \quad \text{if (H>D)}$$

$$\frac{2\mu}{C}W_x = 4\pi C_z\left[\frac{\mu}{3\lambda+2\mu}\left(\frac{x_0}{\rho_1^3}-\frac{x_0}{\rho_2^3}\right)+\frac{6(\lambda+\mu)}{3\lambda+2\mu}H\frac{3x_0D_3}{\rho_3^5}\right] \text{ if (H<D)}$$

$$\frac{2\mu}{C}W_z = 4\pi C_z\left[\frac{\mu}{3\lambda+2\mu}\left(\frac{D_1}{\rho_1^3}-\frac{D_2}{\rho_2^3}\right)+\frac{6(\lambda+\mu)}{3\lambda+2\mu}H\left(\frac{-1}{\rho_2^3}+\frac{3D_2^2}{\rho_2^5}\right)\right]+ \tag{3}$$

$$+\left\{\frac{3(\lambda+\mu)}{(3\lambda+2\mu)}\left(\frac{D_1}{\rho_1^3}-\frac{D_2}{\rho_2^3}\right)\right\} \quad \text{if (H>D)}$$

$$\frac{2\mu}{C}W_z = 4\pi C_z\left[\frac{\mu}{3\lambda+2\mu}\left(\frac{D_1}{\rho_1^3}-\frac{D_2}{\rho_2^3}\right)+\frac{6(\lambda+\mu)}{3\lambda+2\mu}H\left(\frac{-1}{\rho_2^3}+\frac{3D_2^2}{\rho_2^5}\right)\right] \text{if (H<D)}$$

where (x_0, y_0, z_0) represents the observation point, C is the moment of the strain nucleus, λ and μ are the Lamè's constants,

$$\rho_i = \sqrt{x_0^2 + y_0^2 + D_i^2}, \quad \text{(i=1,2,3)},$$

and $D_1 = D - z_0$; $D_2 = 2H - D - z_0$; $D_3 = 2H - D - z_0$.

Under the condition that the radius a is sufficiently small as compared with f, the moment C is given by $C = -1/2a^3\,\Delta P$, being ΔP the hydrostatic pressure. Differentiation of the piezomagnetic potential with respect to x,y and z gives the components of the geomagnetic field changes respectively. In table I the average

model parameters that have been used in this study together with the corresponding ranges of random fluctuation are reported.

For the Okada model, the piezomagnetic effects are due to fault motions that are supposed to occur in a homogeneous and isotropic elastic half space with a uniformly magnetized upper layer with a constant piezomagnetic stress sensitivity (see Fig. 2). Here a semi-infinite elastic medium occupies $z<0$ and the magnetised region is limited to the layer $0 \leq z \leq H$, where H is the depth of the Curie point isotherm. The piezomagnetic potential W due to a finite fault can be obtained by integrating the elementary piezomagnetic potential over the fault plane. Analytical solutions for the piezomagnetic potentials for strike-slip, dip-slip and tensile-opening fault motions with arbitrary dip and strike angles were derived [Utsugi et al., 2000]. These solutions, despite being expressed as the composition of elementary functions, look like rather complicated non-linear expressions and are not reported here for the sake of simplicity. In table II the average model parameters used in this study, together with the corresponding ranges of random fluctuation, are reported.Electrokinetic effects in a faulted half space were computed by Fitterman [1981] and [Murakami, 1989] who obtained analytical solutions for the magnetic fields generated by an inclined electrokinetic source (see Fig. 3).

Inside the rectangular region the source intensity is expressed by $S = (C_1\text{-}C_2)\ P$, and is considered a constant; outside this region the source intensity is zero. P is the pore pressure; on the upper side of the contact, the electric conductivity is σ_1 and the streaming potential coefficient is C_1. On the lower side the properties are σ_2 and C_2, respectively. The depth of the source is a; the length and the width are L and W *(=(b-a)/sin(Dp))* respectively and the dip angle of the source is indicated by *Dp*. The boundaries of the electrocinetic source are: $L/2 \geq X_0 \geq -L/2$, $y_2 \geq Y_0 \geq y_1$, $b \geq Z_0 \geq a$.

Symbol	*Parameter*	*Unit of Meas.*	*Range*
a	Radius	Meters	500÷1000
f	Depth	Meters	3000÷7000
ΔP	Pressure	Bars	0÷2000

Table I. Ranges for Mogi's model parameters.

The magnetic field (with components B_x, B_y and B_z) produced by the inclined electrocinetic source described is represented by the following equations:

$$B_x = \frac{\mu \alpha S}{2\pi} \left| \left| T_1 + \tan(D_p) \arctan \frac{T_2}{T_3} \right|_{X_0 =}^{+L/2} \right|_{Z_0 =}^{b} \qquad (4)$$

where:

$$T_1 = \tan(Dp) - \arctan\left[\frac{y\sin(Dp) - Z_0\cos(Dp)}{(x - X_0)\sin(Dp)}\right] \qquad (5)$$

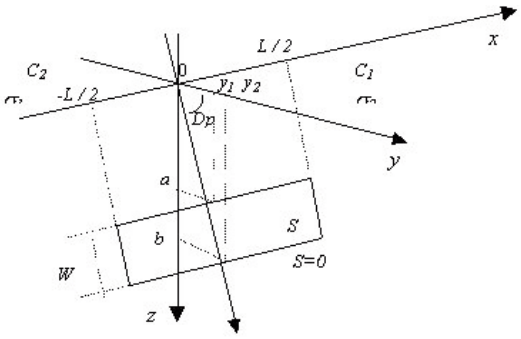

Figure 3. Geometry of the Murakami inclined model.

Parameter	*Unit of Meas.*	*Range*
Depth	Meters	1000÷5000
Strike	Degrees	0÷360
Dip	Degrees	0÷90
Rake	Degrees	0÷360
Crack Length	Meters	3000÷7000
Width	Meters	1000÷5000
Slip	Meters	0÷5
Opening	Meters	0÷10
North Coordinate	Meters	-5000÷5000
East Coordinate	Meters	-5000÷5000

Table II. Ranges for the Okada's model parameters.

$$T_2 = \sin(Dp)\left[y^2\tan(Dp) + (x - X_s)^2\tan(Dp) - yZ_s\right] \quad (6)$$

$$T_3 = (x - X_s)\left[(Z_s - y\sin(Dp)\cos(Dp))^2 + y^2\sin^4(Dp) + (x - X_s)^2\sin^2(Dp)\right]^{-2} \quad (7)$$

Here μ is the magnetic permeability, X_S, Y_S, Z_S are the source coordinates and σ is expressed by $\sigma = \sigma_1\,\sigma_2 / (\sigma_1 + \sigma_2)$.

$$B_y = \frac{\mu\cos S}{2\pi}\left|\left| T_4 + \frac{\sin^2(D_p)}{\cos(D_p)}T_5 + T_6 - T_7\right|_{X_0}^{+L/2}{}_{-L/2}\right|_{Z_s=a}^{b} \quad (8)$$

where

$$T_4 = \frac{\tan(Dp)}{2}\log\left\{(x - X_s)^2 + \left(y - \frac{Z_s}{\tan(Dp)}\right)^2\right\} \quad (9)$$

$$T_5 = \log\left\{(Z_s - y\sin(Dp)\cos(Dp)) + \left[(Z_s - y\sin(Dp)\cos(D\right.\right. \quad (10)$$
$$\left.\left. + y^2\sin^4(Dp) + (x - X_s)^2\sin^2(Dp)\right]^{\frac{1}{2}}\right\}$$

(11)

$$T_6 = \tan\frac{Dp}{2}\log\left\{(x - X_s)^2\sin^2(Dp) + (y\sin(Dp) - Z_s\cos(Dp))^2\right\}$$

$$T_7 = \tan(Dp)\log\left\{Z_s\sin(Dp) + \left[(Z_s - y\sin(Dp)\cos(Dp))^2 + \right.\right. \quad (12)$$
$$\left.\left. + y^2\sin^4(Dp) + (x - X_s)^2\sin^2(Dp)\right]^{\frac{1}{2}}\right\}$$

$$B_z = \frac{\mu\cos S\sin(Dp)}{2\pi}\left|\left| T_3\right|_{X_s}^{+L/2}{}_{-L/2}\right|_{Z_s=a}^{b} \quad (13)$$

3. **Inverse modelling with ANN**

Consider a nonlinear input-output mapping described by the functional relationship:

$$d = f(x) \quad (14)$$

where x and d are the input and output vectors respectively. The vector-valued function $f(\cdot)$ can be considered to be unknown, but it is assumed that a set of pairs (x_i, d_i), referred to as *examples* or *learning patterns* in typical neural network terminology, describing our knowledge about the function $f(\cdot)$ are given.

A typical way of approximating static systems using the popular single-hidden-layer Multi-layer Perceptron (MLP) is the following:

$$y_k(x) = \sum_{j=1}^{MH} c_j\varphi\left(w_j^T \cdot x + t_j\right) + c_0 \quad (15)$$

where $y_k(x)$ is the k-th entry of the approximated function, $\varphi(\cdot)$ represents the sigmoid function (i.e. $\varphi(z) = 1 / (1+e^{-\alpha z})$, $x \in \Re^d$ is the MLP input vector, w_j is a vector of coefficients (weight of the connections), and c_j, t_j are additional adjustable coefficients.

The approximation problem has an inverse that consists of constructing a system that produces the vector x in response to the vector d. The inverse system may thus be described by

$$x = f^{-1}(d) \quad (16)$$

where the vector-valued function f^{-1} denotes the inverse of f. The theoretical aspects concerning the use of MLPs for function approximation lie in the so-called Universal Approximation Theorem [Cybenko 1989], which can be invoked to prove that an MLP with a single hidden layer is sufficient to compute a uniform approximation with a prefixed degree of accuracy. Further results about these aspects can be found in [Barron 1993].

Below, the vectors relating to the data sets and source parameters will be referred to as D and P respectively. As the vector P varies in the space of model parameters the data set D is obtained. The data can be measured or, as done here, generated synthetically. It is therefore possible to produce a population of pairs (D, P) that represent the whole "data space" observed. This population will be used as the *learning* set for the neural network. Identifying the source model on the basis of the data observed using a neural approach thus means finding an approximated function of f^{-1} as indicated by

$$f^{-1}(D) \rightarrow P \quad (17)$$

below.

4. Experimental Framework and Results

The experimental framework was formulated as follows. A regular grid 10 by 10 Km wide centred on the summit volcano area was defined and it was hypothesised that piezomagnetic and electrocinetic magnetic anomalies are computed at the vertices of the grid (direct modelling) by using an appropriate software tool that implements the models mentioned in the previous section. Then a MLP neural network was trained to learn the inverse solution associated with a given set of source parameters. Several trials were performed with a different number of training patterns and distance between the grid vertices in order to characterise the accuracy of the inverse solution in varioust measuring conditions. Appropriate indexes were

	BIAS	MAE	RMSE	NMAE%	d
$a^3 \bullet \Delta P$	$9.99 \bullet 10^7$	$8.12 \bullet 10^9$	$3.07 \bullet 10^{10}$	2.079%	0.9628
f	-33.203	34.705	203.728	0.496%	0.9973
X_S	9.202	9.276	60.815	0.0928%	0,9988
Y_S	-18.941	27.454	227.207	0.275%	0.9983

Table III. Performance indexes of the Mogi inverse model obtained by using GAs. The symbol Xs and Ys represents the x, y coordinates of the source. Evaluating the BIAS, MAE and RMSE for the product $a^3\Delta P$ it is necessary to consider that the order of magnitude for this parameter is 10^{11}.

	Depth	Strike	Dip	Rake	Length	Width	Slip	Opening	Xs	Ys
Bias	-49.77	1.01	0.13	0.12	-5.37	23.61	0.03	-0.06	-13.02	-7.7
MAE	124.31	2.35	1.11	3.04	109.77	106.55	0.07	0.08	85.4	78.64
NMAE%	3.11	0.65	1.23	0.84	2.74	2.66	1.40	0.80	0.85	0.78
RMSE	158.43	4.95	2.37	6.27	140.59	139.09	0.26	0.45	117.14	104.21
d	0.9958	0.9994	0.9979	0.9990	0.9959	0.9967	0.9909	0.9944	0.9995	0.9997

Table IV. Performance indexes of the Okada inverse model obtained by using GAs.

defined to give a measure of the accuracy for each parameter of the source (i.e. for the solution of the inverse problem). For the Mogi model, only piezomagnetic data were considered since for this type of source no electrocinetic effects are expected. Moreover, since the magnetic potential for this kind of source depends on the product $a^3\Delta P$ (a and ΔP being the source radius and the hydrostatic pressure respectively), it does not make sense to invert a and ΔP individually since the inverse problem becomes undetermined.

Before making the model inversion by using ANN, an inversion approach based on the use of Genetic Algorithms (GAs) was studied. GAs is one of the most powerful optimization strategies available and hence a high accuracy of the inverted parameters is guaranteed. One hundred models uniformly distributed in the space of parameters were inverted hypothesizing a grid with 21x21 vertices (i.e. 441 measuring points). The results obtained for the Mogi model are shown in Table III. The meaning of the performance indexes considered is described in the Appendix. From these results it is possible to recognize that the Mogi inverse problem can be solved with very high accuracy by using GAs. The Okada model involved ten parameters as described in Table II. The framework considered for the inversion problem is similar to the one described for the Mogi model. One hundred models were inverted by using the GAs optimization approach and the results obtained are summarized in the following Table IV.

Also in this case it is possible to recognise a high level of accuracy for all the considered parameters demonstrating that the inverse problem can be unambiguously solved. The main drawback with the GAs inversion scheme is the relatively high computation effort required.

In order to overcome this drawback the MLP approach is proposed. As described in the previous section, inversion methods based on MLP aim essentially to approximate the function f^{-1} thus allowing to speed up the computation of the source parameters that best matches the observed data. The availability of this function allows to avoid searching for the minimum, as happens with a traditional optimisation algorithm such as GAs. As traditional optimisation algorithms cannot "learn", i.e. they cannot benefit from solutions obtained previously for similar problems, each new inversion requires the whole search procedure to be re-iterated. In order to avoid the use of MLP with a large number of inputs, the number of grid vertices was drastically reduced from 441 to 9. Moreover, in order to have a *more realistic* data set, synthetic data was corrupted by using various levels of gaussian noise up to 70%. The results obtained by using the MLP based approach are synthesised in the following figures. In particular, in Fig. 4 the NMAE% obtained for some of the parameters of the Okada model for different numbers of learning patterns is shown. It is possible to recognise that using MLP a larger number of learning patterns usually leads to more accurate solutions. However, since the learning process requires an increasing computational effort with a larger number of learning patterns, then a compromise must be found. The accuracy obtained for each parameter of the Mogi and

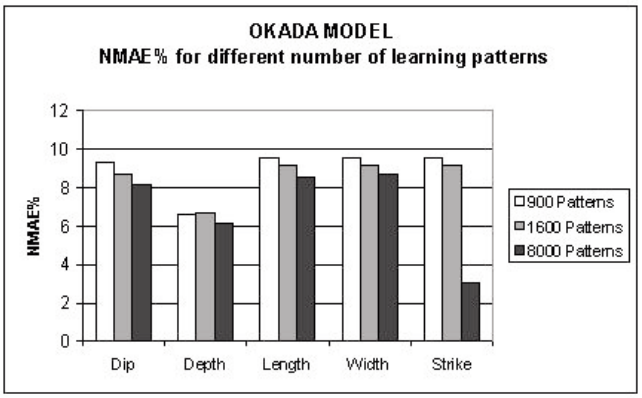

Figure 4. NMAE% obtained by using the neural inversion approach with different number of training patterns.

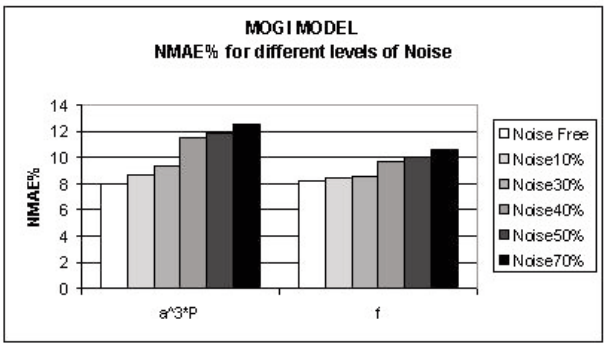

Figure 5. Accuracy obtained for the two inverted parameters of the Mogi model by using the neural approach. Different levels of gaussian noise were considered.

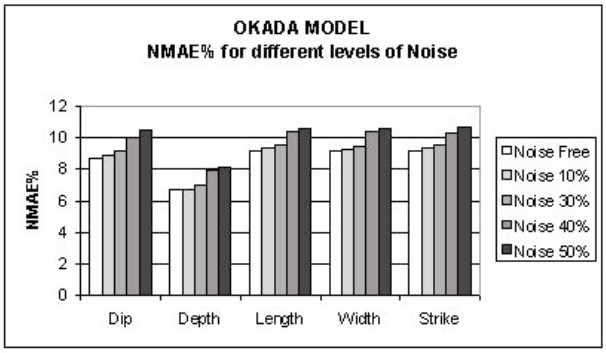

Figure 6. NMAE% obtained by using the neural inversion approach for the Okada model.

Okada sources for increasing levels of gaussian noise is shown in Fig. 5 and Fig. 6 respectively. The neural approach proves less accurate than the GAs optimisation approach, but it is possible to appreciate that all the parameters are estimated with an accuracy, in terms of NMAE%, that is better than 10% even in presence of a noise level up to 30%. On the other hand, it must be stressed here that the neural inversion approach is based on a considerably lower number of measuring stations (only 9 compared with the 441 used for the GAs approach).

5. Conclusions

In this paper the problem of inverting magnetic data of piezomagnetic and electrocinetic type has been addressed. The results show that in spite of the high nonlinearity of the considered inverse problems they can be unambiguously solved. The inversion scheme was set up based on two different techniques: the GAs optimization approach that guarantees high accuracy but requires a considerable computation effort, and the MLP neural network approach

that once appropriately trained assures very low computation efforts and acceptable accuracy even in presence of noise data and limited number of stations. Future work is still required to make the experimental framework more realistic. In particular, since the considered inverse model refers to single sources, which might not be realistic, we plan to consider the presence of multiple sources.

Acknowledgements

This work was supported by the Italian GNV (Gruppo Nazionale per la Vulcanologia) under the coordinate project EPOT (Technological Innovation and Automation in Integrated Application of Electromagnetic Methods and Potential Fields in Volcanic Active Areas).

References

Barron A. R., (1993). *Universal Approximation Bounds for Superposition of a Sigmoidal Function*, IEEE Trans. on Information Theory, vol. 39, pp. 930-945.

Cybenko G., (1989). *Approximation by Super Precision of a Sigmoidal Function Math of control signals & systems*, Springer, New York, vol. 2, pp. 303-314.

Del Negro C. , Ferrucci F. ,Napoli R. (1997). *The Permanent Network for Magnetic Surveillance of Mt, Etna: Changes in the Geomagnetic Total Intensity Observed in 1995*, Acta Volcanologica, no. 9, pp 1-7.

Del Negro C., Ferrucci F., Napoli R., 2000, *A review of the volcano-magnetic effects observed between 1981 and 1995 on Mount Etna (Italy)*, Phys. Chem. Earth, 25, 725-730.

Fittermann D.V. (1979). *Theory of electrokinetic-magnetic anomalies in a faulted half-space*, J. Geophys. Res., vol. 84, pp. 6031–6040, 1979.

Fittermann D.V. (1981). *Correction to theory of electrokinetic-magnetic anomalies in a faulted half-space*, J. Geophys. Res., vol. 86, pp. 9585–9588.

Johnston M.J.S., Stacey F. D., (1969). *Volcano-magnetic effects observed on Mt Ruapehu, New Zealand*, J. Geophys. Res., 74, 6541-6544.

Johnston M.J.S, (1989). *Review of magnetic and electric field effects near active faults and volcanoes in the U.S.A.,* Earth Planet Sci. Lett., 57, 47-63.

Mogi, K., (1958). *Relations between the eruptions of various volcanoes and the deformations of the ground surfaces around them,* Bulletin of Earthquake Research Institute, Univ. Tokio.

Murakami H., (1989) *Geomagnetic fields produced by electrokinetic sources*, J. Geomagn. Geoelectron., vol. 41, pp. 221–247.

Nunnari G., Bertucco L., Ferrucci F., (2001). *A Neural Approach to the Integrated Inversion of Geophisical Data Types*, IEEE Transaction on Geosciences and Remote Sensing, Vol. 39, N. 4, pp 736-748, April 2001.

Okada, Y., (1992). *Surface deformation due to shear and tensile faults in a half-space*, Bulletin of Seismological Society of America.

Röth G., Tarantola A., (1996). *Neural Network and Inversion of Seismic Data*,. J. Geoph. Res. 99, pp. 6753-6768.

Langer H., Nunnari G., Occhipinti L. (1996), *Estimation of Seismic Waveform Governing Parameters with Neural Networks*. J. Geophys. Res., vol. 101, pp. 20109-20118.

Sasai, Y., (1991). *Tectonomagnetic modeling on the basic of the linear piezomagnetic effect*, Bulletin of Earthquake Research Institute, Univ. Tokio.

Tanaka Y., (1993). *Eruption Mechanism as inferred from geomagnetic changes with special attention to the 1989-1990 activity of Aso volcano*, J. Volcan. Geitherm. Res., 56319-338.

Utsugi, M., Nishida, Y. And Sasai, Y, (2000). *Piezomagnetic potentials due to an inclinated rectangular fault in a semi-infinite medium*, Geophys. J. Int..

Yukutake T., Utada H., Yoshino T., Watanabe H., Hamano Y., Sasai Y., Kimoto E., Otani K., Shimomura T., (1990). *Changes in geomagnetic total intensity observed before the eruption of Oshima Volcano in 1986*, J. Geomagn., Geolectr., 42, 277-290.

Appendix A – Performance Indexes

$\overline{O}$, $\overline{P}$ Mean of the observed (O) and computed (P) values

σ_O, σ_P Standard deviation of the observed (O) and computed (P) values

Bias $\frac{1}{N}\sum_{i=1}^{N}(P_i - O_i)$, mean bias error is the degree of correspondence between the mean computed and the mean observation. Lower numbers are best. Values < 0 indicate under-estimation.

MAE $\frac{1}{N}\sum_{i=1}^{N}|P_i - O_i|$, The Mean Absolute Error is the mean of the absolute value of the residuals from a fitted statistical model. Lower numbers are best.

NMAE% $\frac{100}{(N \cdot Range)}\sum_{i=1}^{N}|P_i - O_i|$, The normalised MAE in percent.

RMSE $\sqrt{\frac{1}{N}\sum_{i=1}^{N}(P_i - O_i)^2}$, Root Mean Square Error. The weighting of (P-O) by its square tends to inflate *RMSE*, particularly when extreme values are present. In a good model, the root mean square error should approach zero.

d $d = 1 - \frac{\sum_{i=1}^{N}(P_i - O_i)^2}{\sum_{i=1}^{N}(|P_i - \overline{O}| + |O_i - \overline{O}|)^2}$, Index of agreement, Bounded, relative measure which is capable of measuring the degree to which computed values are error-free. The denominator accounts for the model's deviation from the mean of the observations as well as the observations deviation from their mean. It does not provide information regarding (un)systematic errors. In a good model, the index of agreement should approach one.

A Graphical Computer Program for Modeling of Volcanomagnetic Fields: a Case Study Mount Vesuvius

Rosalba Napoli[1], Gilda Currenti[1,2], Ciro Del Negro[1], Takeshi Hashimoto[3], and Annamaria Vicari[1,2]

[1]*Istituto Nazionale di Geofisica e Vulcanologia – Sezione di Catania, Italy*
[2]*Dipartimento di Ingegneria Elettrica, Elettronica e dei Sistemi – Università di Catania, Italy*
[3]*Institute of Seismology and Volcanoly Graduate School of Science, Hokkaido University, Japan*

Abstract

A graphical computer program for volcanomagnetic modeling, called VMM, has been developed. It is applicable to a variety of volcanomagnetic problems concerning piezomagnetic, thermomagnetic, and electrokinetic effects. The capability and limitation of the program are presented. We applied this tool for computing the volcanomagnetic fields expected to accompany eruptions at Mount Vesuvius. We considered the piezomagnetic and electrokinetic effects due to a regional fault located on the western flank of volcanic edifice, which plays an important role in relation to the activity of the volcano. Relatively intense changes are seen only around both tips of the fault: the amplitudes of calculated piezomagnetic anomalies range from 5-6 nT in the case of tensile-opening (1 m) to 2-3 nT in the case of dip-slip, while the electrokinetic anomalies are less than 1 nT

Key words *magnetic modeling - magnetic monitoring - volcanomagnetism - Mount Vesuvius*

1. Introduction

In real volcanic fields a variety of situations are expected with regard to the manifestation of geomagnetic changes accompanying volcanic activities. Volcanoes are a kind of heat-transfer system from the depths to the ground surface, and hence, in an active period they are frequently accompanied by subsurface hydrothermal convection, which causes changes in temperature, pressure, and fluid motion within the edifice. In addition faults or fissures, which frequently affect volcanoes, give rise to the geomagnetic fields due to piezomagnetic or electrokinetic processes. The correct identification and interpretation of the observed anomalies is crucial to obtain a comprehensive understanding of physical processes taking place beneath the volcanoes and, as such, it is important to distinguish which of them is the most effective for each volcano and for each stage of its activity. However, attempts of modeling magnetic fields expected to accompany volcanic eruptions often involve a great deal of effort, since [i) the solutions are scattered throughout the literature; (ii) they may have only limited applicability to certain locations and regimes; and (iii) are found using algorithms that are frequently complex and iterative. This can be especially frustrating because forecasting and monitoring of volcanic activity requires short-term decision-making.

The need for the development of a volcanology oriented software is thus derived from the desire of being able to model many kinds of volcanomagnetic signals in a way that could match software monitoring standard. That is the software should at least enable users to have a user-friendly tool to calculate and visualize a wide spectrum of volcanomagnetic fields through a mouse-click operation, and to have an option to generate image files in commonly available formats, which could be easily exported for the purpose of exchange of data in a visualized form. With this in mind, we have collected several theoretical solutions of geomagnetic anomalies into a unified computer program. The software, named VMM (Volcano Magnetic Modeling), has been released recently to the public domain, especially offered to the volcanological community. In the present paper we firstly illustrate the capability of this program and its graphical user interface. Secondly, we apply this toolbox for estimating the magnetic anomalies expected to accompany eruptions at Mount Vesuvius (southern Italy). Finally, we also suggest an adequate configuration of the magnetic station arrays for magnetic monitoring purposes.

2. Summary of physical mechanisms

The volcanomagnetic fields rely upon three main endogenous causes. The first is that uprising melt may heat the superficial rocks to a temperature above the Curie point, with a consequent decrease in the intensity of the total field. Due to the thermal inertia of the rocks and the generally small dimensions of magmatic intrusions at shallow depths, this phenomenon is probably (i) slow and (ii) restricted to a limited area. The other two causes of volcanomagnetic transients bring into play the piezomagnetism of rocks and streaming potentials. Anomalies of

this type show modest maximum values but they are fast, with respect to thermomagnetic changes. The comprehension of the different mechanisms, which can generate volcanomagnetic signals, has advanced considerably since first observations of the phenomena. Several theoretical studies for tectonomagnetic and volcanomagnetic modeling have been elaborated.

The main frame of the piezomagnetic modeling was established by Stacey [1964] and Stacey et al. [1965], who demonstrated the seismomagnetic and volcanomagnetic effects using the volume element method. Based on their basic theory, subsequently, Davis [1976], Johnston [1978] and Oshiman [1980] investigated more realistic models. A series of theoretical studies elaborated by Sasai [1979, 1980, 1983, 1991a, 1991b] allow to obtain analytic solutions for the piezomagnetic field due to a point-pressure source and to a strike-slip and tensile-opening vertical rectangular fault. Recently, Utsugi et al. [2000] extended Sasai's analytic solution to cases of an inclined fault including dip-slip.

There has also been theoretical progress in the research field of the electrokinetic effect. Nourbehecht [1963] was the pioneer of such a study formulating the basic theory of electrokinetic phenomena based on irreversible thermodynamics. Mizutani et al. [1976] proposed the possibility of an electrokinetic field produced by underground water-flow for the origin of the geomagnetic variation accompanying the Matsushiro earthquake swarm. While Ishido and Mizutani [1981] provided fundamental data of the parameters for the electrokinetic coupling through laboratory experiments, a series of studies elaborated by Fitterman [1978; 1979; 1981] demonstrated analytic and semi-analytic solutions for the electric and magnetic fields due to electrokinetic sources in horizontally-layered and vertically-faulted half-space. Murakami et al. [1984; 1987] and Murakami [1989] extended Fitterman's solutions to the case of inclined fault using Edwards' [1974] approximation.

When we consider the thermomagnetic effect, we sometimes take a rather simpler calculation approach compared to the other two effects mentioned above. Namely, we assign the temperature distribution and the thermomagnetic property of the ground a priori. In many cases the simplest approximation is adopted: the magnetized host rock with some completely demagnetized sources within. Magnetic anomalies due to thermal demagnetization with arbitrary shape can be calculated by integrating dipole sources. We can also utilize some semi-analytic solutions to reduce the dimension of volume integral such as those proposed by Talwani [1965] and Bhattacharyya [1980]. However, in many cases a point-source or spherical-source approximation practically works in application to volcanic fields as a model of demagnetized source below the volcano, implying that the heterogeneity of the magnetized media is not crucial in the case of thermomagnetic effect.

3. Capability of the VMM software

Although there are several numerical and analytic solutions for volcanomagnetic modeling in the literature, they are rarely user-friendly for those not familiar with the research fields. In order to improve the efficiency of volcano monitoring, we have implemented some of these works in a unified toolbox with the aid of graphical user interface under MatLab® (The MathWorks, Inc.), which is a general purpose programming system with extensive libraries of functions for any programming task. Here we call this procedure VMM (Volcano Magnetic Modeling). The VMM toolbox consists of a collection of MatLab m-files that are distributed as source code. It is designed in a modular fashion so that different components can be combined as necessary, depending on the specific measurements available and parameters desired. MatLab is available on a wide variety of operating systems and platforms and it is widely used in the scientific community. In addition, the vectorized nature of MatLab lends itself to a more transparent presentation of the underlying algorithms. The toolbox structure is designed to facilitate quality-control checks at intermediate stages in the processing of a particular data set.

The VMM basically consists of four modules for computing the volcanomagnetic fields. The first is for the piezomagnetic effects due to a fault based on the analytic solutions by Sasai [1991b] and Utsugi et al. [2000]. Computations for strike-slip, dip-slip, and tensile-opening of a rectangular fault with an arbitrary dip angle are available. The second is for the piezomagnetic effects due to a point pressure source (Mogi model in volcanology) based on the analytic solutions proposed by Sasai [1991a]. The third is for the electrokinetic effects due to a rectangular fault using the analytic solutions by Murakami [1989]. The fourth is for the thermomagnetic effects due to a spherical body using the analytic solution of a magnetic dipole. As an option, the displacement and stress fields, which are based on the analytic expressions of Okada [1992], are also available. In the present version of VMM all fields are calculated in the plane of the ground surface. We have also installed the

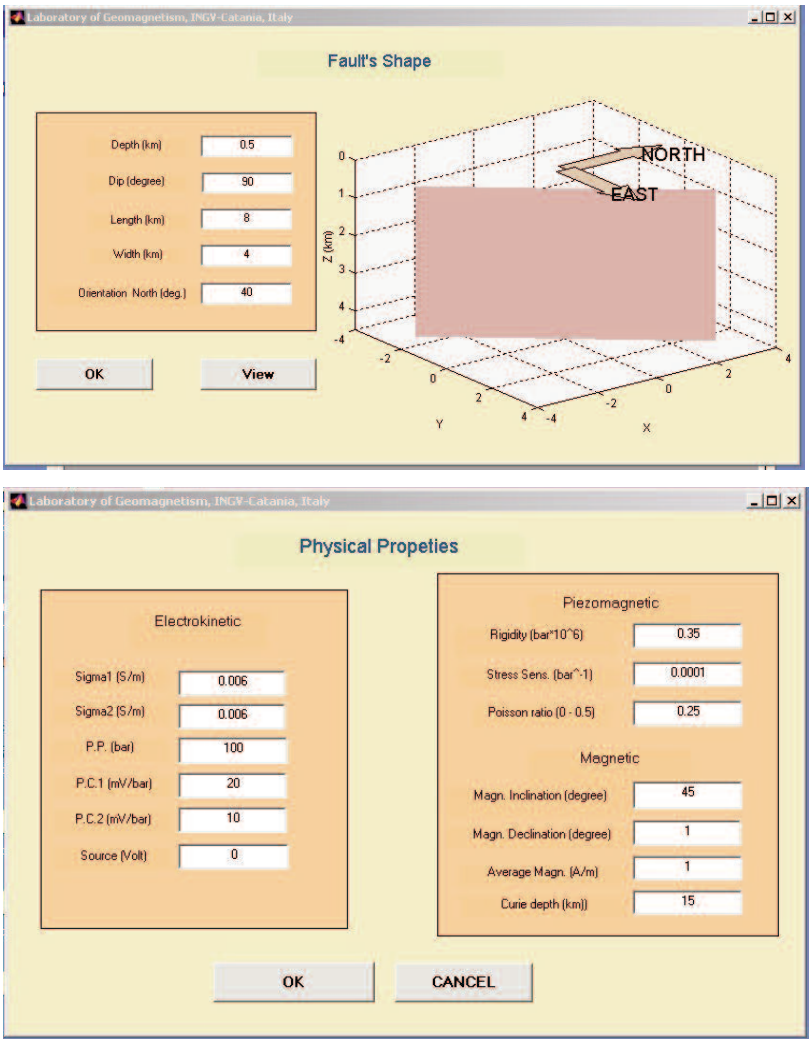

Figure 1. An example of input data windows of VMM: (a) the geometry fault window and (b) the physical properties window.

VMM code on Website of our Geomagnetism Laboratory for remote applications via Internet (the address is: http://maglab.ct.ingv.it).

VMM is characterized by a high automation level and development flexibility. For instance, if you want to add a new process code to the library, all you need to do is to write a simple code. An example of the two input data windows of VMM configuring the fault parameters is shown in Fig. 1.

In the geometry fault window (Fig. 1a) we can define the length, width, burial depth, dip and strike angles of the fault. Calculation of the magnetic field will be done with the parameters here as well as with others (length and type of dislocation) given in the main menu. Visualization of the fault shape is realized in 3-D manner in the right-hand side of the figure. In the physical parameters window (Fig. 1b) it is possible to configure the physical properties of the media. Here you can define the rigidity, Poisson's ratio, and piezomagnetic stress-sensitivity of the media as well as the geomagnetic inclination, declination, average magnetization of the media, and the depth of Curie point isotherm, below which the media is assumed to be completely demagnetized. Figure 2 displays examples of piezomagnetic fields of *Bx* (northward), *By* (eastward), *Bz* (downward), and *Bt* (total force) due to a rectangular fault with strike-slip. It is also possible to compute a case for multiple sources. For example, in the physical property menu we can define both of the piezomagnetic and electrokinetic properties of the ground as shown in Fig. 1b. Thus we can obtain a superposed field of the two as demonstrated in Fig. 3 (fields can be displayed in 3-D expression).

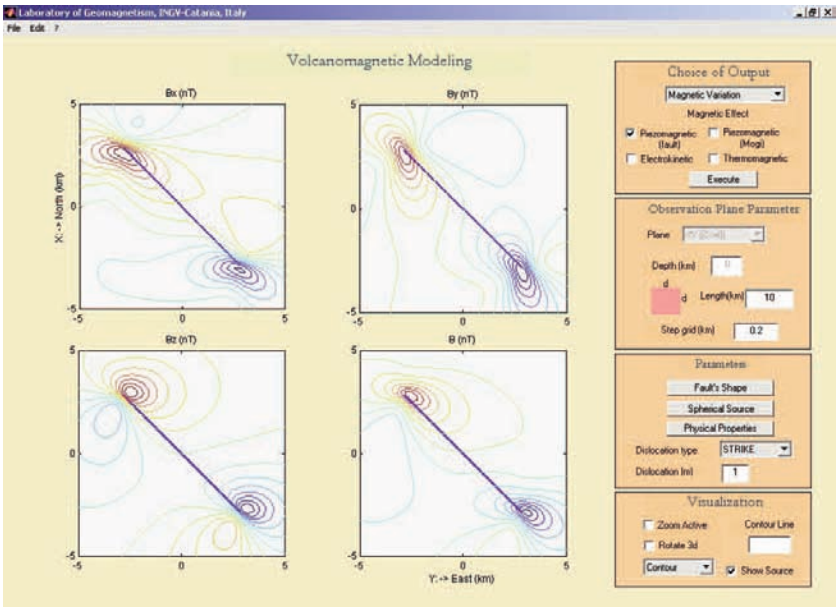

Figure 2. An example of piezomagnetic field due to a rectangular fault with strike-slip calculated with VMM. The components Bx (northward), By (eastward), Bz (downward), and Bt (total force) of piezomagnetic fields produced by an inclined strike-slip fault trending NE-SW direction are shown.

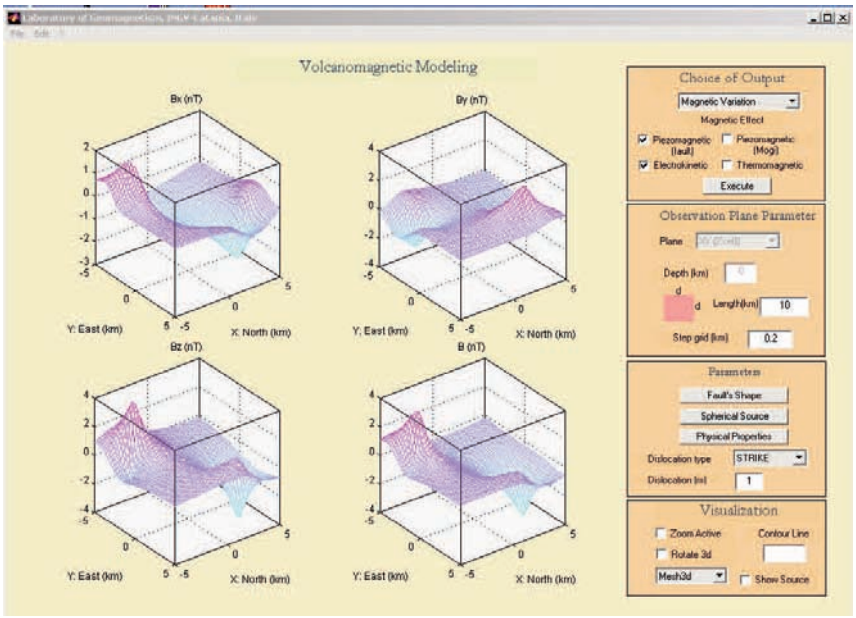

Figure 3 - An example of multiple-source fields of piezomagnetic and electrokinetic effects. Fields are displayed in 3-D expression in this case.

4. Application to Mount Vesuvius

The last eruption at Vesuvius volcano took place in March 1944. Since then the volcano has been in a state of complete quiescence and no particular indication suggesting a renewal of activity has been observed. Nevertheless, Vesuvius must be considered an extremely hazardous volcano because in the course of its long eruptive history, it has often shown long periods of quiescence, sometimes protracted for centuries, which are followed by even more violent renewals.

From a tectonic point of view there seems to be an indirect connection between Vesuvius' eruptive activity and the dynamics of the Calabrian arc. Vesuvius is situated on a NE-SW regional fault [Finetti and Morelli, 1974; Cassano and La Torre, 1987], which crosses all the recent formations and fed various eruptions [Scandone et al., 1991]. The existence of the regional fault is obvious both in gravimetric

data on land [Florio et al., 1999; Cassano and La Torre, 1987] and submarine seismic profiles [Finetti and Morelli, 1974]. In particular, the seismic profiles imply the presence of volcanic events along this fault. Two historic fissure eruptions of Vesuvius in 1794 and 1861 occurred along its inland continuation. This fault belongs to the tectonic system trending perpendicular to the Apennines (NE-SW) and arranges the tensile tectonic field along the NW-SE direction due to the backward retreat of the Calabrian arc. The movement of the arc produces strain variations propagating in the bordering areas. From a volcanological viewpoint, the arrival of an impulsive tensile strain in the Vesuvian area sets off the movement of magma, which is in an unstable equilibrium at the volcanic base [Marzocchi et al., 1993]. Under such an extensional tectonic field, the region between Vesuvius and Campi Fregrei shows a kind of graben structure composed of a group of normal faults. The fault on the NW flank of Vesuvius forms the SE boundary of this graben system and hence dipping to SW direction.

Taking these features of Vesuvius into account, magnetic transients due to electrofiltration and piezomagnetic effects associated with fault activity are more important than slower variations due to the thermal demagnetization process. Hence here we focus on the former effects, for which it is easy to imagine a strong link. At Vesuvius, these two causes of magnetic anomalies can co-exist. Here we first examine the piezomagnetic effects due to a tensile-opening (dike-intrusion) and a dip-slip along the fault. Secondly, we calculate the electrokinetic effects due to the same fault.

Magnetic properties

Total magnetization of volcanic rocks can be calculated from laboratory measurements of thermoremanent magnetization and magnetic susceptibility. Magnetic susceptibility values of the main samples of Vesuvius range between 1 and $3x10^{-2}$ SI for solid rocks and between 0.3 and $2x10^{-2}$ SI for ejecta [Pierattini, pers. com.]. $1x10^{-2}$ SI is adopted as a representative value. Intensity of remanent magnetization is extremely variable: practically nil for sediment emplaced at low temperatures; it can exceed 5 A/m in intrusive bodies. Despite the strong variability of this parameter, it is believed that 2 A/m constitutes a representative value. Therefore the remanent component is the main agent of the total magnetization. For the computation of the magnetic anomaly, we neglected the induced magnetization and used only the remanent component, which is considered uniform and equals 2 A/m. Generally, the direction of natural remanent magnetization is the same as that of the present mean field in accordance with recent age (20-25 ky) of emitted products [Santacroce, 1987]. We assume the geomagnetic inclination and declination as 54 and 1 degree, respectively.

Piezomagnetic field

Magnetic changes associated with a NE-SW tensile-opening and dip-slip faulting are shown in Fig.4. The values of the parameters used for the computation of the anomaly with VMM are indicated in table I. Parameters concerning the fault shape are based on the result of seismic and gravimetric studies [Cassano and La Torre, 1987; Finetti and Morelli, 1974]. Relatively intense changes are seen only around both tips of the fault: the amplitudes of calculated anomalies range from 5-6 nT in the case of tensile-opening (Fig. 4a) to 2-3 nT in the case of dip-slip (Fig. 4b).

These anomalies are intense enough to distinguish them from the normal variations of the Earth's magnetic field, but their shapes are so similar that it will be difficult to distinguish to each other. We should also be careful in that piezomagnetic effect due to a fault is quite sensitive to the position of the edges of the fault. The large values of geomagnetic variation are limited to small areas in the vicinity of the tips. This fact implies that we do not detect anything

Fault length	$2L$	10 km	Poisson's ratio	ν	0.25
Fault width	W	5 km	Average magnetization	J	2.0 A/m
Depth of burial	D	0.5 km	Stress sensitivity	β	$1.0x10^{-4}$ bar^{-1}
Fault dip	Ψ	80° W	Curie isotherm depth	H	15 km
Fault strike	ϕ	N45° E	Average magnetic inclination	I_0	54°
Dislocation	ΔU	1 m	Average magnetic declination	D_0	1°
Rigidity	μ	$3.5x10^{11}$ cgs	Source intensity	S	1 V
Conductivity	σ_1, σ_2	0.005 S/m			

Table I. Fault parameters used for the piezomagnetic and electrokinetic calculation in Fig. 4.

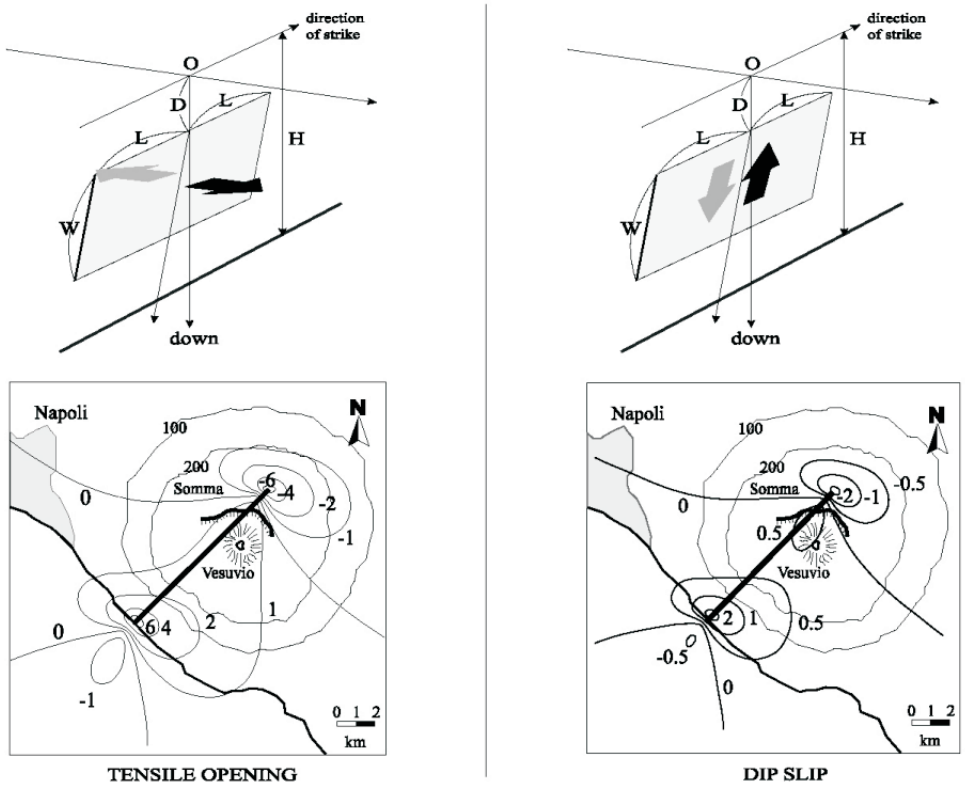

Figure 4. Piezomagnetic fields in total force due to a tensile-opening fault (left panel) and a dip-slip fault (right panel) in Vesuvian area. Parameters used in the calculation are shown in table I. Units are in nanoteslas. The thick line shows the location of the fault.

significant if we lose the position of the tips. Accordingly, it is strongly recommended to investigate the position of the fault before installing magnetometers. Attention must also be paid to the possibility that a fault we are modeling is not always uniform throughout the dimension. In many cases, a large fault consists of some patches within. Geomorphologically a group of such small patches are considered as the parts belonging to a single fault system. In such cases, piezomagnetic anomalies will appear at each edge of these patches. Considering such situations it is preferable to deploy magnetometers as densely as possible along a fault system.

Electrokinetic field

Electrokinetic phenomena require the movement of fluids within the volcanic edifice. Fluid motion in the vicinity of a boundary separating regions with different streaming-potential coefficients can produce an external magnetic field. The electrokinetic field is related to changes in the stress field and to thermal or chemical changes of fluids within the interconnected crack and fissure nets [Nourbehecht, 1963]. Explosive sequences of Vesuvius are characterized by deposits whose composition and structure show an interaction with aquifers during the early stage of the eruptions. Many studies have revealed the presence of aquifers at some depths inside the Vesuvian substratum, both in the carbonate basement as well as in the volcanic covering [e.g. Marzocchi et al., 1993]. Therefore, the volcanic edifice is plausibly the site of water circulation and any modification of the circulation regime might induce local disturbances of the geomagnetic field.

To estimate an order of magnitude and the shape of a possible electrokinetic magnetic field at Vesuvius, we calculated the electrokinetic fields due to the fault using the VMM. The fault geometry is hypothesized the same as the case of piezomagnetic effect and with source intensity S equal to 1 V (equivalent to the over-pressure of 10 bar for 0.1 V/bar of the streaming potential coefficient). We assumed the conductivity of the ground as uniform with a value of 0.005 S/m (200 Ωm). The calculated anomaly is shown in Fig. 5 displaying the amplitude less than 1 nT. Also the greatest component of this field, orientated parallel to the strike of the anisotropy structure, shows relatively small maximum values (< 1 nT). As is the case in piezomagnetic effect, we observe that anomalies

are centered at both ends of the fault. We have to mention that the intensity of electrokinetic field is proportional to the conductivity of the ground. Thus we expect more intensive electrokinetic field if the ground is more conductive. We calculated here assuming the conductivity of the ground is homogeneous. Although the value of 0.005 S/m used here seems reasonable for at least the superficial layer of Vesuvius, we expect a more conductive layer below. The magnetic field should be greater than those demonstrated above if we take such a conductive layer into account.

5. Concluding Remarks

In order to facilitate the identification and interpretation of the sources of a wide spectrum of magnetic signals, we have implemented a graphical computer procedure for modeling magnetic fields associated with volcanic activity. It is applicable to the variety of problems for piezomagnetic, thermomagnetic, and electrokinetic effects with user-friendly interfaces. We applied this tool to Mount Vesuvius. We considered the piezomagnetic and electrokinetic effects due to a regional fault, which lies on the northwestern flank of Vesuvius. The outcomes of our study show that moderate-scale magnetic anomalies of a few nanoteslas should be expected to accompany the volcanic activity. The intensity of the theoretical anomalies proved to be above the minimum level of detection, or rather, volcanomagnetic fields are intense enough to claim the possibility of distinguishing them from the environmental magnetic noise. In the light of the volcanological history of the Vesuvius, which mainly experienced explosive eruptions, this possibility may be relevant for detecting the modifications within the volcanic edifices of the stress field or of the thermodynamic state forerunning future eruptive episodes.

Finally, regarding the diversity of the spatial pattern of these magnetic anomalies, and neglecting the time scales of phenomena, computation of synthetic anomalies may be useful for the advance planning of the configuration of measurement devices oriented to the detection of eruptive forerunners. Considering the results demonstrated above, we can now propose a desirable configuration of instruments aiming to detect geomagnetic variations associated with possible activity of Vesuvius as shown in Fig. 6.

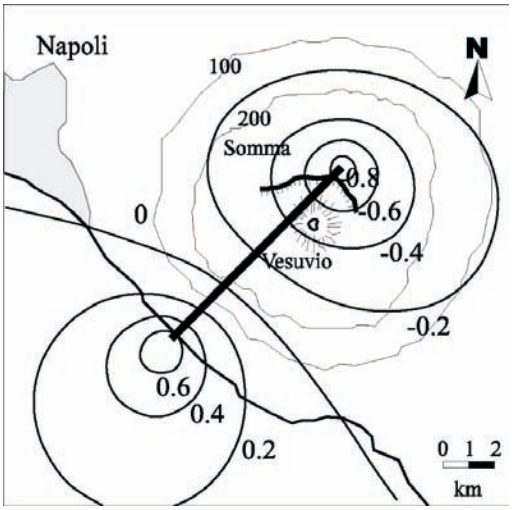

Figure 5. Electrokinetic magnetic fields due to the same fault as Fig. 4. Units are in nanoteslas.

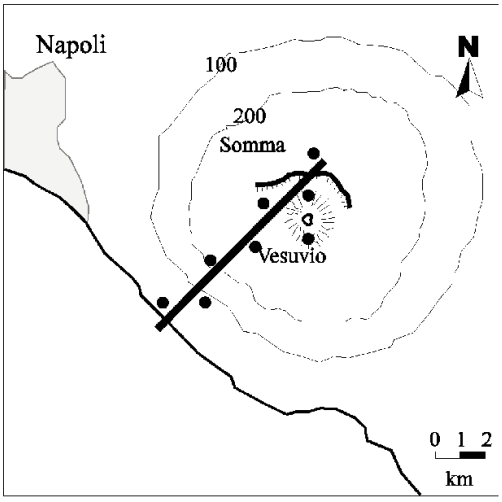

Figure 6. A desirable configuration of geomagnetic monitoring at Vesuvius. The thick line represents the fault while the solid circles show the points of observation.

As was seen above, the dominant effect expected in this area is the piezomagnetic field due to a tensile-opening fault that lies on the western flank of the volcano. Accordingly, it is preferable that we deploy the instruments in parallel alignment to the fault. In addition, considering the possibility of summit activity, some of them are to be deployed in a N-S alignment across the summit.

Acknowledgments

This research was carried out in the framework of the project EPOT, which is supported by Gruppo Nazionale per la Vulcanologia of the INGV.

References

Bhattacharyya, B. K., (1980). *A generalized multibody model for inversion of magnetic anomalies*. Geophys., 45, 255-270.

Cassano, E. and La Torre, P., (1987). *Geophysics*. In: R. Santacroce (Editor), Somma-Vesuvius, CNR Quad. Ric. Sci., 114, vol. 8, 175-192.

Davis, P.M., (1976). *The computed piezomagnetic anomaly field for Kilauea volcano, Hawaii*, J. Geomag. Geoelectr., 28, 113-122.

Edwards, R.N., (1974). *The magnetometric resistivity method and its application to the mapping of a fault*, Can. J. Earth. Sci., 11, 1136-1156.

Finetti, I. and Morelli, C., (1974). *Esplorazione sismica a riflessione nei golfi di Napoli e Pozzuoli*, Boll. Geofis. Teor. Appl., 16, 175-222.

Fitterman, D.V., (1978). *Electrokinetic and magnetic anomalies associated with dilatant regions in a layered earth*, J. Geophys. Res., 83, 5923-5928.

Fitterman, D.V., (1979). *Theory of Electrokinetic magnetic anomalies in a faulted half space*, J. Geophys. Res., 84, 6031-6040.

Fitterman, D.V., (1981). *Correction: Theory of electrokinetic-magnetic anomalies in a faulted half-space*, J. Geophys. Res., 86, 9585-9588.

Florio, G., Fedi, M., Cell, F. and Rampolla, A., (1999). *The Campanian Plain and Phlegrean fields: structural setting from potential field data,* J. Volcanol. Geotherm. Res., 91, 361-379.

Ishido, T. and Mizutani, H., (1981). *Experimental and theoretical basis of electrokinetic phenomena in rock-water systems and its application to geophysics*, J. Geophys. Res., 86, 1763-1775.

Johnston, M.J.S., (1978). *Local magnetic field observations and stress changes near a slip discontinuity on the San Andreas fault*, J. Geomag. Geoelectr., 30, 607-617.

Marzocchi, W., Scandone, R. and Mulargia, F., (1993). *The tectonic setting of Mount Vesuvius and the correlation between its eruptions and the earthquakes of the Southern Apennines*. J. Volcanol. Geotherm. Res., 58, 27-41.

Mizutani, H., Ishido, T., Yokokura, T., and Ohnishi, S., (1976). *Electrokinetic phenomena associated with earthquakes*, Geophys. Res. Lett., 3, 365-368.

Mogi, K., (1958). *Relations between the eruptions of various volcanoes and the deformations of the ground surfaces around them*, Bull. Earthq. Res. Inst., Univ. Tokyo, 36, 99-134.

Murakami, H., (1989). *Geomagnetic fields produced by electrokinetic sources*, J. Geomagn. Geoelectr., 41, 221-247.

Murakami, H., Mizutani, H., and Nabetani, S., (1984). *Self-potential anomalies associated with an active fault*, J. Geomag. Geoelectr., 36, 351-376.

Murakami, H., Mizutani, H., and Nabetani, S., (1987). *Correction: Self-potential anomalies associated with an active fault*, J. Geomag. Geoelectr., 36, 351-376.

Nourbehecht, B., (1963). *Irreversible thermodynamic effects in inhomogeneous media and their applications in certain geoelectric problems*, PhD thesis, MIT, Cambridge.

Okada, Y., (1992). *Internal deformation due to shear and tensile faults in a half-space*, Bull. Seism. Soc. Am., 82, 1018-1040.

Oshiman, N., (1980). *Local magnetic changes associated with fault activity*, M. Sc. Thesis, Tokyo Inst. Tech., 178 pp.

Santacroce, R., (1987). *Somma-Vesuvius*. CNR Quad. Ric. Sci., 114, vol. 8, 251 pp.

Sasai, Y., (1979). *The piezomagnetic field associated with the Mogi model*, Bull. Earthq. Res. Inst., Univ. Tokyo, 54, 1-29.

Sasai, Y., (1980). *Application of the elasticity theory of dislocations to tectonomagnetic modeling*, Bull. Earthq. Res. Inst., Univ. Tokyo, 55, 387-447.

Sasai, Y., (1983). *A surface integral representation of the tectonomagnetic field based on the linear piezomagnetic effect*, Bull. Earthq. Res. Inst., Univ. Tokyo, 58, 763-785.

Sasai, Y., (1991a). *Piezomagnetic field associated with the Mogi model revised: analytic solution for finite spherical source*, J. Geomag. Geoelectr., 43, 21-64.

Sasai, Y., (1991b). *Tectonomagnetic modeling on the basis of the linear piezomagnetic effect*, Bull. Earthq. Res. Inst., Univ. Tokyo, 66, 585-722.

Scandone, R., Bellucci, F., Lirer, L. and Rolandi, G., (1991). *The structure of the Campanian Plain and the activity of the Neapolitan volcanoes*, J. Volcanol. Geotherm. Res., 48, 1-31.

Stacey, F.D., (1964). *The seismomagnetic effect*, Pageoph, 58, 5-22.

Stacey, F.D., Barr, K. G. and Robson, G. R., (1965). *The volcanomagnetic effect*, Pageoph, 62, 96-104.

Talwani, M., (1965). *Computation with the help of a digital computer of magnetic anomalies caused by bodies of arbitrary shape*, Geophys., 30, 797-817.

Utsugi, M., Nishida, Y. and Sasai, Y., (2000). *Piezomagnetic potentials due to an inclined rectangular fault in a semi-infinite medium*, Geophys. J. Int., 140, 479-492.

Project and Manufacturing of an Autolevelling Vectorial Magnetometer for Volcanic Areas Monitoring

Paolo Palangio, Claudia Rossi, Achille Zirizzotti, Antonio Meloni and Lili Cafarella

Istituto Nazionale di Geofisica e Vulcanologia, Roma, Italy

Abstract

In the frame of EPOT project (technological innovation and automation in the integrated applications of Electromagnetic and POTential field methods in active volcanic areas) an auto levelling magnetometer for geomagnetic field monitoring in volcanic areas, was proposed. In this paper a brief description of this magnetometer and some preliminary tests are described. In particular some characteristics of the non-diagonal elements of the field transform matrix **A** between the observatory system and the magnetometer placed in a far location are discussed with the relative implication when one of the two magnetometers would be located in a volcanic area.

Key words *autolevelling magnetometer – magnetic monitoring - thermal drift*

1. Introduction

Magnetic monitoring of volcanoes is made generally by means of proton precession magnetometers for total field measuring. However these observations, although very useful and effective [Stacey et al., 1965; Johnston and Stacey, 1969a; Johnston and Stacey, 1969b; Johnston and Muller, 1981; Johnston and Muller, 1987; Zlotnicki et al., 1993; Zlotnicki and Bof, 1996; Avdeev et al., 1997], provide only partial information because changes of local magnetic inclination and declination could cause null changes of the total field. Moreover the scalar measure of the local field does not furnish information on changes of the X, Y and Z components. On the other side the employment of vector magnetometers in the uninterrupted monitoring of the geomagnetic field, presents different problems in relation to the physical conditions of the volcanic areas: fluctuations of the apparent vertical, torsional movements, strong distortion of the geomagnetic field lines, intense local magnetic field gradients, are in fact only some of the most important remarkable characteristics of these areas [Rikitake and Yokoyama, 1955; Davis et al., 1979; Muller and Johnston, 1981; Meloni et al, 1998; Sasai et al, 2001; Sasai et al. 2002]. In particular, the fluctuations of the apparent vertical can cause effects on the X, Y and Z components; therefore the reference system materialised by the sensor axes, should be inertially coupled to an absolute reference frame. The distortion of the local field lines is reflected on the sensor orientation while the field gradients are reflected on the precision of the measurement since the field is integrated over the space occupied by the sensor.

In order to try to solve these problems we propose here the theory and realization of our autolevelling vector magnetometer that can properly operate in volcanic areas. The new designing criteria have been oriented towards a high long term stability and a low thermal drift. This instrument can be employed for continuous measurements of the geomagnetic field in remote stations, where regular carrying out of absolute measurements cannot be guaranteed.

2. The magnetometer

A prototype of the autolevelling magnetometer here proposed was realized at the geomagnetic observatory of L'Aquila, Italy. The magnetometer consists of a flux gate sensor, its driving electronic circuits (Fig. 1) and data acquisition system. The magnetometer allows fluctuation adjustments of the bearing surface with an indeterminateness of less than 4" and a dynamic extension of ±5°. The geomagnetic fluxgate sensor was designed in order to strictly fit the proposed technical requirements.

The sensor hanging system was made using a compound gimbals with amagnetic ballbearing made with copper and beryllium alloy (Fig. 2). The non-orthogonality of the hanging planes (materialized by the suspension) is less than 0.1°.

Since the best geometric shape for a fluxgate sensor is the toroidal one, the sensor was constituted of two torus each with two copper windings. Each nucleus measures two geomagnetic field components: the first sensor measures horizontal elements X and Y while the second one measures Y and Z components. In this way two different measurements of Y component are obtained. This opportunity is used to minimize the noise using appropriate software.

In order to choose the best material for the sensor realization, measurements of background noise in crystalline and amorphous materials have been implemented in different

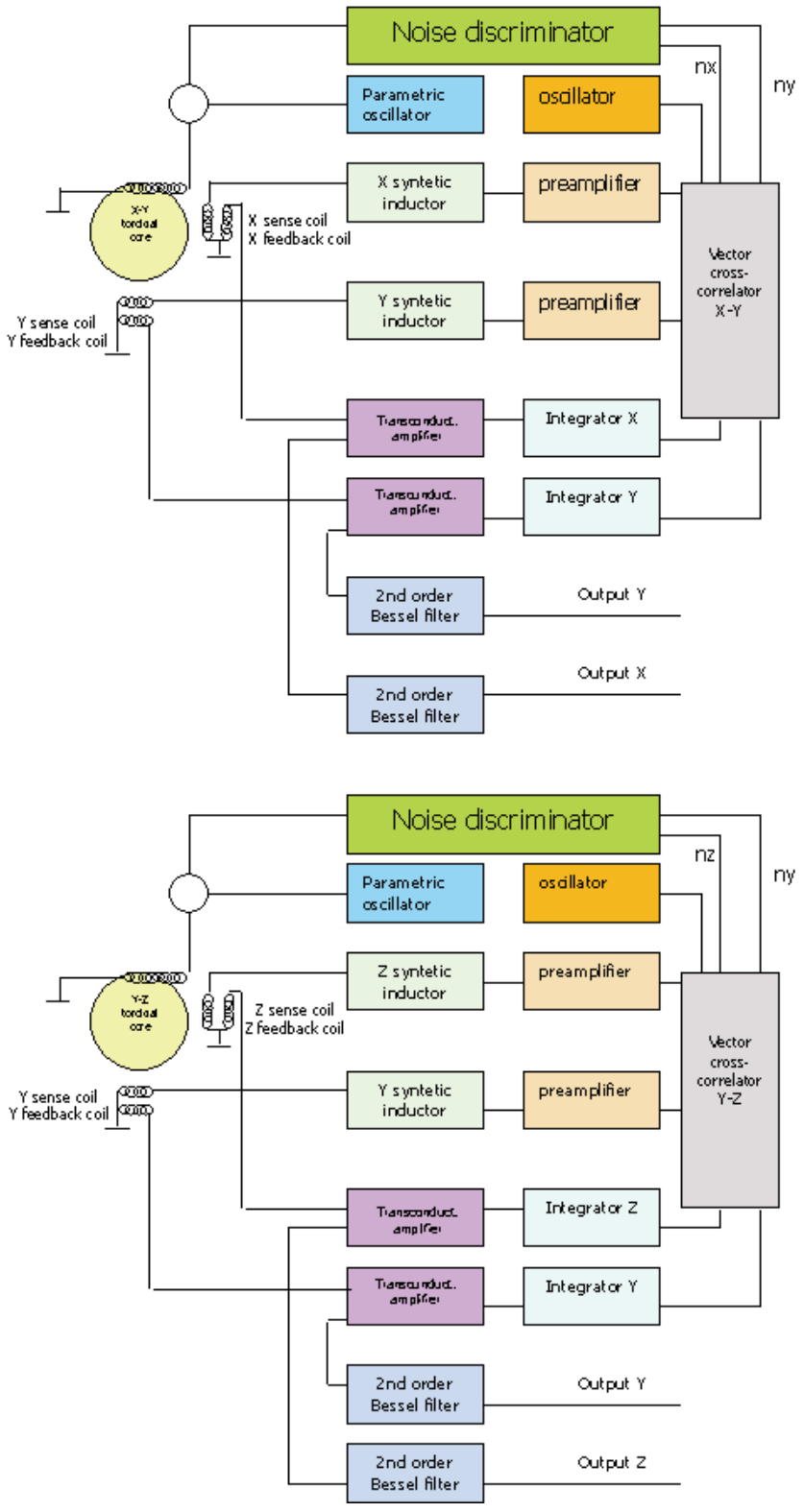

Figure 1. Synoptic scheme of the tri-axial two core magnetometer sensor.

environmental conditions. With respect to crystalline materials, amorphous materials were found to satisfy the following peculiar characteristics [Igoshin and Sholpo, 1979]:

1. 5-10 times lower magnetostriction coefficient
2. lower Barkhausen noise
3. lower general noise (1/f)

The analysis of the collected data in fact shows best results by materials with low level of internal structure of crystallization. In particular the VITROVAC 6025 showed the best perform-

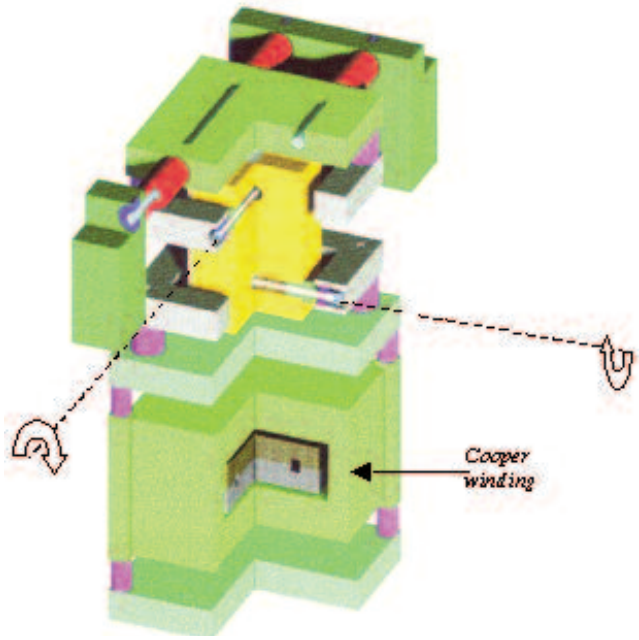

Figure 2. Project of the gimbals of the sensor. One of the two biassial parts of the sensor is visible in the lower part of the figure.

ance.

The two torus size and the choice of the carrying structure, are extremely critical factors. Each torus was realized using a 27 mm diameter aluminum hold on which 10 layers of amorphous material 25 μm wide have been wrapped.

The toroidal sensor linearity depends essentially on the surrounding magnetic field. Therefore in order to minimize the non-linearity error the torus must be constantly immersed in a null field. To realize this condition the nucleus has been surrounded with proper size coils (on a quartz support) in order to create a magnetic field always opposite to the measured one. The measurements of the electric currents in the compensation coils can give preliminary values for the X, Y and Z DC base line current with an error less the 10 nT. In order to check the stability of the vector magnetometer, these values can be used to compare the estimated total intensity of the field (from X, Y and Z) with the intensity measured independently by a proton precession magnetometer. The principal instrumental characteristics are summarized in table I.

3. L'Aquila preliminary test

Magnetic field measurements were conducted for a long period to determine the geo-

Parameter	*Value*
Resolution	50pT
Noise	30 pT/sqr(Hz)
Sensitivity	10 mV/nT
Electronic temperature coefficient	0.007 nT /°C
Sensor temperature coefficient	0.01 nT /°C
Range	1000 nT
Bandwidth	5 Hz
Positioning Error	4"
Sensor Orthogonality Error	0.1°
Compensation Dynamic	10°
Dimension and Weight	26x20x20 cm, 2 Kg
Temperature range	-10°C…40°C

Table I. Characteristics of the autolevelling vectorial magnetometer.

magnetic field transform matrix **A** from the auto levelling magnetometer station to the reference system of the observatory magnetometer. The observatory magnetometer has the same characteristics of the suspended one. The magnetometers were placed 40 km far apart.

The experiment aim was the determination of the nine elements of the geomagnetic field transform matrix **A**.

The elements of this matrix take into account the reciprocal orientation of the two sensors, the non-orthogonality of the axes and the two sensor transfer function differences.

In figure 3 the geomagnetic field components as recorded at the different sites are reported. In figure 4 and 5 the non diagonal elements of **A** when the magnetometers are in the same site and in two different sites are shown respectively. In the ideal case in which the sensors are perfectly aligned, the transfer functions are the same, **A** is an unit matrix. In a more realistic situation, the non diagonal elements of **A** are different from 0 and the diagonal elements are different from 1.

Once the installation of the magnetometers is realized, 120 samples are sufficient in order to define the matrix elements A_{ij} with an error less than the experiment indeterminateness.

The magnetic field H of the suspended magnetometer can be written in the fixed magnetometer coordinate system thanks to **A:**

$$H_x=A_{11}H_{rx}+A_{12}H_{ry}+A_{13}H_{rz}$$
$$H_y=A_{21}H_{rx}+A_{22}H_{ry}+A_{23}H_{rz}$$
$$H_z=A_{31}H_{rx}+A_{32}H_{ry}+A_{33}H_{rz}$$

Where $X_1...X_n$, $Y_1...Y_n$ e $Z_1...Z_n$ are the suspended magnetometer measurements and $X_{r1}...X_{rn}$, $Y_{1r}...Y_{rn}$ e $Z_{r1}...Z_{rn}$ are the observatory magnetometer measurements, n=120 and A_{11}, A_{22} e A_{33} are the diagonal elements of **A**

$$\begin{pmatrix} X_1 \\ X_2 \\ \dots \\ X_n \end{pmatrix} = \begin{pmatrix} X_{r1} & Y_{r1} & Z_{r1} \\ X_{r2} & Y_{r2} & Z_{r2} \\ \dots & \dots & \dots \\ X_{rn} & Y_{rn} & Z_{rn} \end{pmatrix} \begin{pmatrix} A_{11} \\ A_{12} \\ A_{13} \end{pmatrix}$$

$$\begin{pmatrix} Y_1 \\ Y_2 \\ \dots \\ Y_n \end{pmatrix} = \begin{pmatrix} X_{r1} & Y_{r1} & Z_{r1} \\ X_{r2} & Y_{r2} & Z_{r2} \\ \dots & \dots & \dots \\ X_{rn} & Y_{rn} & Z_{rn} \end{pmatrix} \begin{pmatrix} A_{31} \\ A_{32} \\ A_{33} \end{pmatrix}$$

$$\begin{pmatrix} Z_1 \\ Z_2 \\ \dots \\ Z_n \end{pmatrix} = \begin{pmatrix} X_{r1} & Y_{r1} & Z_{r1} \\ X_{r2} & Y_{r2} & Z_{r2} \\ \dots & \dots & \dots \\ X_{rn} & Y_{rn} & Z_{rn} \end{pmatrix} \begin{pmatrix} A_{21} \\ A_{22} \\ A_{23} \end{pmatrix}$$

that in this case are constant. A_{ij} depend on the orientation of the reference frame only in the hypothesis that the geomagnetic field variations

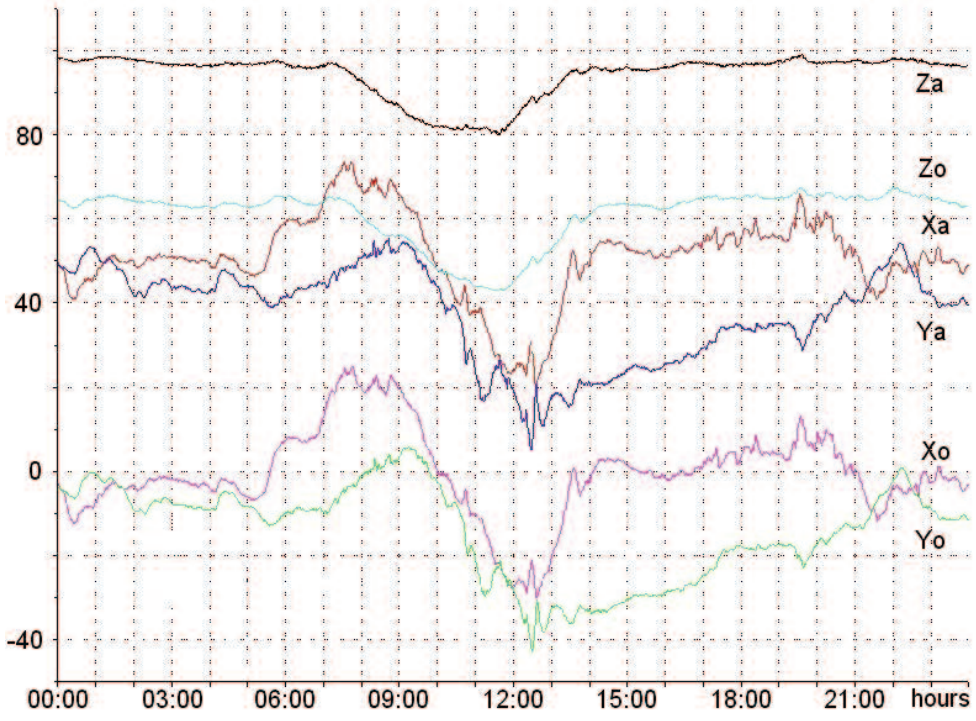

Figure 3. Geomagnetic field component X, Y and Z as recorded in two different sites placed 40 km far apart. In the first site the new autolevelling magnetometer (a in the figure) while in the second site an observatory magnetometer were installed (o in the figure).

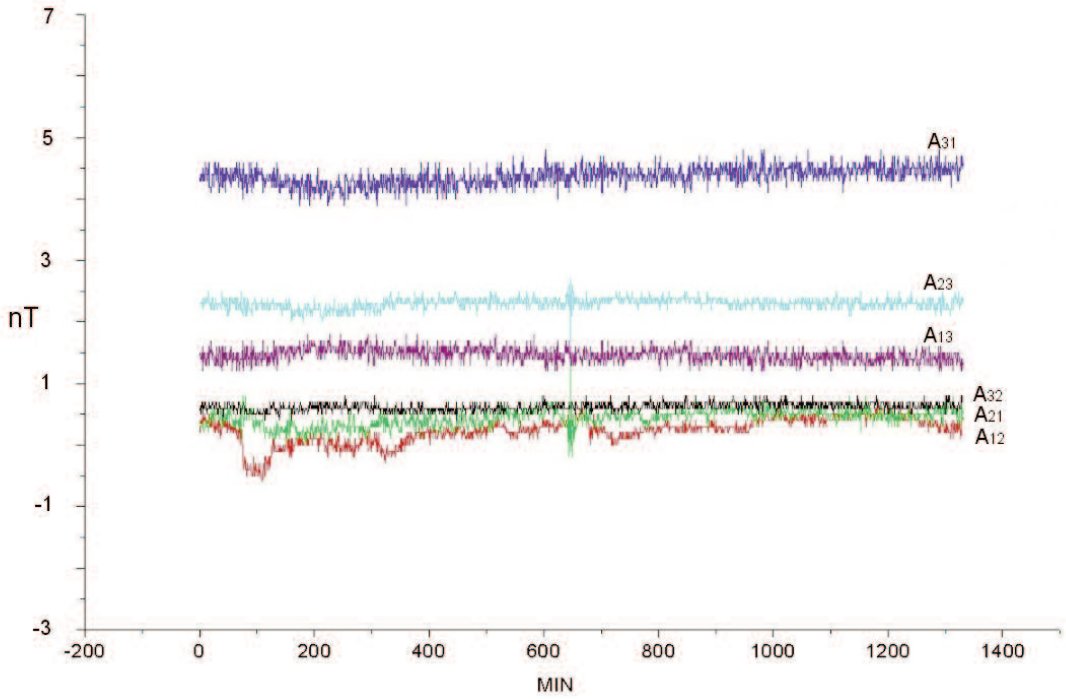

Figure 4. Plot of non-diagonal elements of **A** matrix when the magnetometers are placed in the same site.

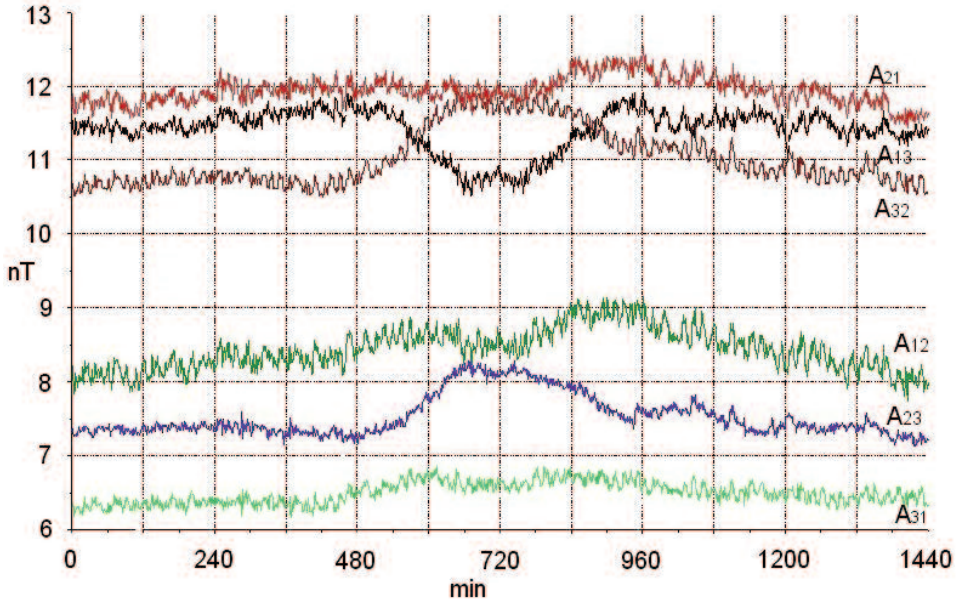

Figure 5. Plot of non-diagonal elements of A matrix when the two magnetometers are placed in two different sites 40 km far apart.

at the two sites are the same. This hypothesis unfortunately is not true if we choose two sites far apart also few kilometers. Necessarily we can find a local geomagnetic field anomalous behaviour using these non diagonal elements only fixing some parameters in the preliminary operations considering that, thanks the magnetometer characteristics, they will not change during the measurements.

In figure 4 and 5 the values of the non diagonal elements are reported: as we can see, they are complex functions depending essentially on the non homogeneity of the geomagnetic field and on inductive phenomena (figure 4: the magnetometers are in the same site, figure 5 the magnetometers are 40 km far apart).

These considerations suggest that the required procedures to evaluate the background noise elements are very laborious also in the simple case in which soil deformations are not

present.

4. Conclusions

The magnetometer described in this paper was proposed in order to compensate the movements of the ground in volcanic areas. The sensor was suspended using a compound gimbals while the problem concerning the azimuthal movements of the sensor frame was compensated monitoring the sensor orientation using a remote reference frame (installed far from the volcanic area). The proposed method is based on the determination of the nine geomagnetic field transform matrix elements every 120 minutes. The plots of these parameters can indicate possible local anomalies linked to the geomagnetic filed variations and to ground movements at the reference system. Ground movements (earthquake) at the volcanic station cannot disturb the measured geomagnetic components due to the auto levelling characteristics of the magnetometer.

The characteristics of the anomalies can be defined considering various contributions of the background noise using **A** matrix. The non-diagonal elements of the matrix are complex functions of the anomaly characteristics. The analysis of the factors of a geomagnetic anomalous behaviour can give important information in order to choose a procedure to investigate signals and consequently isolate the anomalies.

Acknowledgements

This research was partially supported by the GNV through the Epot project.

References

Avdeev, D. B., Kuvshinov, A. V. and Pankratov, O. V, (1997). *Tectonic process monitoring by variations of the geomagnetic field absolute intensity*, Annali di Geofisica, 40, 2, 281.

Davis, P. M., Stacey, F. D., Zablocki, C. J. and Olson, J. V., (1979). *Improved Signal Discrimination in Tectonomagnetism: discovery of a Volcanomagnetic effect at Kilauea, Hawaii*. Physics of the Earth and Planetary Interiors, 19, 331.

Igoshin, L. A. and Sholpo, L. E., (1979). *Effects of Pressure on the Magnetic state of the Rocks*. Izvestiya, Earth Physics, 15, 9.

Johnston, M. J. S. and Stacey, F. D., (1969). *Transient Magnetic Anomalies accompanying Volcanic Eruptions in New Zealand*, Nature, 224, 1289.

Johnston, M. J. S. and Stacey, F. D., (1969). *Volcano-magnetic effect observed on Mt. Ruapehu, New Zealand*. Journal of Geophysical Research, 75, 6541.

Johnston M. J. S. and Muller R. J., (1981). *Volcano-magnetic observations during eruptions May-August 1980*. U.S. Geologhycal Survey, 1250, 183.

Johnston, M. J. S. and Muller, R. J., (1987). *Seismomagnetic Observation During the 8 July 1986 Magnitude 5.9 North Palm Springs Earthquake*, Science, 237, 1201.

Meloni, A., Mele, G. and Palangio, P., (1998). *Tectonomagnetic field observations in central Italy 1989–1995*, Physics of the Earth and Planetary Interiors, 105, 145.

Muller, R. J. and Johnston, M. J. S., (1981). *Precision of magnetic measurements in a tectonically active region*, Trans. Am. Geophys. Un., 62, 1054.

Rikitake, T. and Yokoyama, I., (1955). *Volcanic Activity and Changes in Geomagnetism*. Journal of Geophysical Research, 60, 2.

Sasai, Y., Zlotnicki, J., Nishida, Y., Uyeshima, M., Yvetot, P., Tanaka, Y., Watanabe, H. and Takahashi, Y., (2001). *Evaluation of electric and magnetic field monitoring of Miyake-jima volcano, Central Japan*, Annali di Geofisica, 44, 239.

Sasai, Y., Uyeshima, M., Zlotnicki, J., Utada, H., Kagijama, T., Hashimoto, T. and Takahashi, Y., (2002). *Magnetic and electric field observations during the 2000 activity of Miyake-jima volcano, Central Japan*, Earth and Planetary Science Letters, 769.

Stacey, F.D., Barr, K.G. and Robson, G.R., (1965). *The Volcano-magnetic Effect. Pure and Apllied Geophysics*,62, 96

Zlotnicki, J., Le Mouel, J. L., Delmond, J. C., Pambrun, C. and Delorme, H., (1993). *Magnetic variations on Piton de la Fournaise volcano. Volcanomagnetic signals associated with the November 6 and 30 eruptions*. Journal of Volcanology and Geothermal Research, 56, 281.

Zlotnicki, J. and Bof, M., (1996). *Volcanomagnetic signals associated with the quasi-continuous activity of the andesitic Merapi volcano (Indonesia): 1990-1995*. Physics of the Earth and Planetary Interiors, 105, 119.

Technoplogical Improvements in Gravity Monitoring of Active Volcanoes

Gennaro Budetta, Daniele Carbone,
Filippo Greco

Istituto Nazionale di Geofisica e Vulcanologia – Sezione di Catania
Piazza Roma 2, 95123 - Catania, Italy

Abstract

The conditions at a site close to an active crater are far from the clean, ideal laboratory and so it is quite difficult to attain the required precision in the continuous gravity data. Because of this, continuous gravity observation at active volcanoes have not developed as quickly as other geophysical techniques. However, technological improvements in recent years have allowed most of these difficulties to be overcome. Since 1998, to couple the network for discrete measurements and extend the range of periods of measurable anomalies down to a few minutes, three continuous gravity stations at distances from the active craters ranging between 1 and 10 Km have been installed at Mount Etna. The stations, equipped with LaCoste and Romberg spring gravimeters, acquire, at 1 datum/min sampling rate, gravity and other parameters which are used to reduce the gravity signal in order to assess the volcano-related signal. To improve the possibilities of continuous gravity observation at active volcanoes and to achieve a better signal/noise ratio we have developed (i) a special station setup aimed to reduce the influence of external perturbations on the gravity sensor; (ii) a software under the LabVIEW® environment to quickly analyse long gravity data-sequences and (iii) algorithms aimed to model how the meter output depends on the interfering meteorological signals.

Key words *microgravity - volcano monitoring - continuous recording - data reduction - Mt. Etna*

Introduction

During the past few years, microgravity studies at active volcanoes have become increasingly important and have yield valuable results. Numerous studies have directly associated the systematic variations of the gravity field to volcanic processes [Jachens and Eaton 1980; Eggers 1983; Rymer and Brown 1987; Sanderson 1982; Rymer et al. 1993; 1995; Budetta and Carbone, 1998; Budetta et al. 1999; Carbone et al. 2003a].

Temporal gravity changes at volcanic areas are usually detected by discrete (repeated) measurements. Discrete gravity measurements have been carried out at Mt Etna since 1986. The Etna gravity network (Fig. 1) for discrete measurements is now composed of about 70 stations 0.5 to 3 km apart, covers an area of about 400 km^2 and consists of four integrated subarrays [Budetta and Carbone, 1998; Budetta et al. 1999; Carbone et al., 2003a]. The quality and space resolution of gravity data acquired along the Etna network through discrete measurements is now more than suitable for assessing mass redistributions occurring over a wide range of depths along Etna's plumbing system (roughly between 8 km b.s.l and a few hundred meters below the surface). The limit of this technique is the time interval at which the networks are reoccupied, ranging typically from several weeks to one year, which allows only long-period variations, related to long term magmatic processes, to be recorded and studied. Shortcomings such as snow coverage on the summit zone of high volcanoes often make gravity changes not identifiable on a timescale of less than 6 months during the winter time. If one also considers the need to reduce the exposure of personnel in active areas, the importance of developing effective continuous gravity monitoring appears clear.

Continuous gravity observations can furnish excellent temporal resolution, with measurements collected every second if desired, but the spatial resolution is limited by the number of instruments available. Given the high cost of gravimeters, it is necessary to place the instruments in a position where there is the greatest chance of detecting meaningful gravity changes. Often this is close to an active crater.

Continuous gravity observations aimed to monitor active volcanoes have been scarcely performed in the past [Davis, 1981; De Meyer et al. 1995; Berrino et al. 1997] because of the logistic difficulties of running them in non-laboratory conditions. However, technological improvements in recent years have allowed some of the difficult linked to the inadequacy of the site to be overcome.

The combined use of discrete and continuous gravity measurements is an unique tool both for studying the internal dynamic of a volcano and for surveillance purposes [Carbone, 2001; Carbone et al. 2003b]. Discrete measurements allow both the actual magnitude of the subsurface mass change and the position and spatial characteristics of the source to be

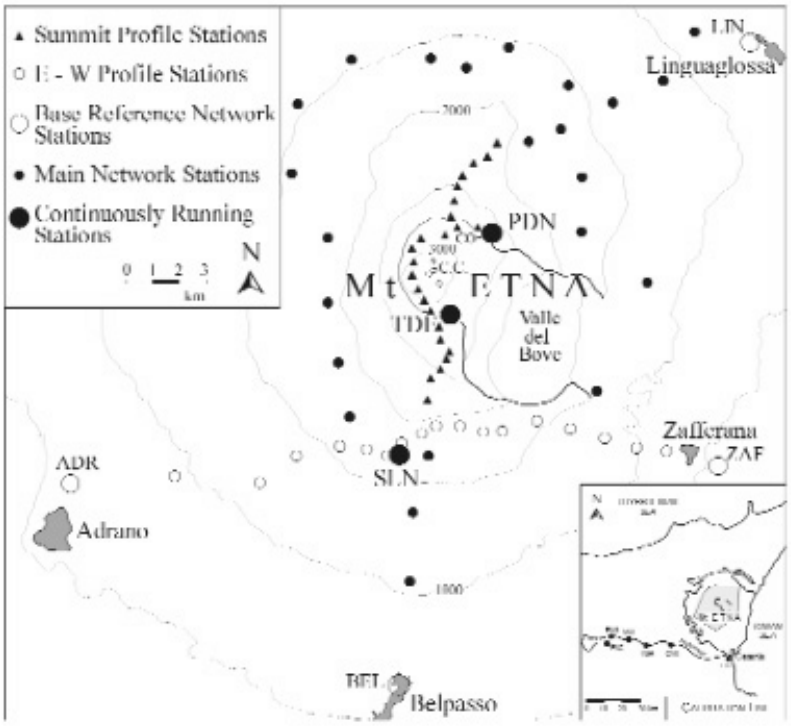

Figure 1. Sketch map of Mt Etna showing (a) stations on the Main Network (small filled circles), (b) the Summit Profile (triangles), (c) the East-West Profile (small open circles), (d) the Basal Reference Network (large open circles) and (c) the continuously recording gravity stations (large filled circles). The stations on the Calibration Line (filled circles, inset) are also shown. The shaded area in the inset represents the area covered by the gravity network. The TDF station was removed from Torre del Filosofo refuge during the October 2000 eruption.

defined. Continuous measurements, on the other hand, allow the temporal evolution of the source to be followed all the year long and with a temporal resolution which would be unthinkable if only discrete measurements were available.¶

¶

¶

2. Continuously recording Etna stations¶

¶

2.1. Review¶

¶

Mt Etna is Europe's most active volcano. It is also one of the most closely monitored volcanoes in the world. Previous continuous microgravity studies at Mt Etna have been carried out at sites remote from the summit craters of the volcano (a) to determine whether there is an anomalous tidal response [Davis, 1981], (b) to determine correction algorithms for the main external perturbations of each instrument employed [El Wahabi et al. 1997] and (c) to obtain precise tidal gravity factors on Mt Etna [d'Oreye et al. 1994]. Before 1998 stations close to the summit craters were not occupied continuously for long time periods and comparisons between the continuously recorded data and data acquired by discrete surveys were never attempted.¶

At Mt Etna we developed a continuously recording mini-array, which was completed in April 1998 (Fig. 1). The stations are located ca. 10 km south of the active craters at the Serra la Nave Astrophysical Observatory (SLN; 1740 m a.s.l.), 2 km NE of the summit NE Crater at the Pizzi Deneri Volcanological Observatory (PDN; 2920 m a.s.l.) and just 1 km S of the summit SE Crater at the Torre del Filosofo refuge (TDF; 2919 m a.s.l.). In October 2000, during a summit eruption, the TDF gravity station was removed from the Torre del Filosofo refuge.¶

¶

2.2. Basic station setup¶

¶

The adverse conditions typically encountered on a volcano include high altitude, inaccessibility for several months at a time, lack of mains electricity for power, variable temperature, pressure and humidity, seismicity, corrosive gases and the risk that the instrumental setup may be destroyed in the event of a large eruption. Therefore the setup of a gravity station continuously recording against such environment needs to be robust, easy to remove and re-establish quickly and cheap (the gravity meter being by far

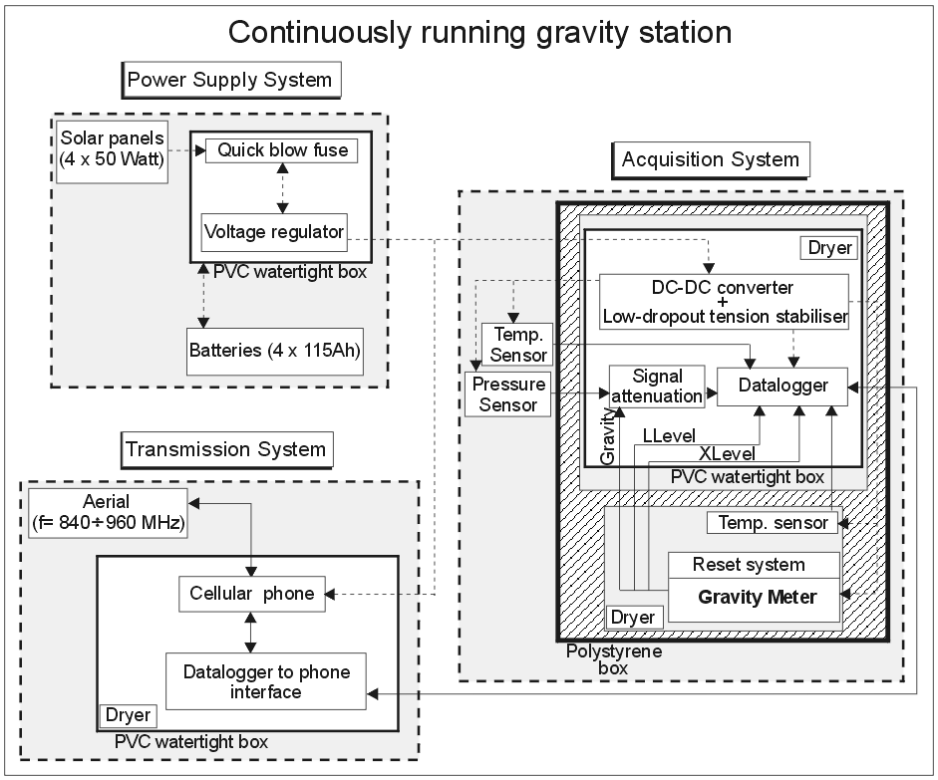

Figure 2. Block diagram showing the three component setup (power supply system, acquisition system and transmission system) developed for continuous gravity stations at Mt. Etna.

the most expensive item). Some sort of building is also essential, but it can be very basic provided that it has a firm basement floor and provides protection from the elements. We have developed a setup for continuous gravity measurements at active volcanoes which consists of 3 components [Budetta et al. 2002; Carbone et al. 2003b]: the power system, the acquisition system and the transmission system (Fig. 2).

The power system comprises equipment to generate, store and feed electricity to the instrumentation. It employs solar panels connected to trickle-charged batteries. The power requirement of the whole setup is approximately 12 W assuming external temperatures around the freezing mark; four 115 Ah batteries can thus maintain the system for at least 10 days without additional power input. To provide a constant power supply to the feedback of continuously recording L&R meters (must be within a few hundredth of a Volt not to affect the quality of data) a dc-dc converter coupled with a low-dropout tension stabilizer is used. The acquisition system comprises the gravity meter itself, equipped with any feedback system [Torge, 1989; VanRuymbeke, 1989] and outputting analogue signals representing the feedback force and the long and cross levels, and sensors for the atmospheric temperature, pressure and humidity. For a gravity meter that is to be left operating without intervention for extended periods of time, instrumental drift [Torge, 1989] may become important (if the instrument drifts beyond the range of operation of the feedback system). The meters installed at Etna's continuous stations are thus equipped with remote controlled stepper motors to reset them. The whole acquisition system is placed inside a thermally insulating polystyrene container. Data are acquired every second by CR10X dataloggers by Compbell Scientific. The average over 60 measurements is than calculated and stored in the solid-state memory of the data logger (at 1 datum/min). Data, after being temporally stored, are dumped automatically every 24 hours by the transmission system which employs a cellular phone. Using a suitable software on a remote computer is also possible a) to remotely activate the stepper motor which turns the meter dial allowing the meter to be reset and b) to monitor in real time all the parameters recorded.

3. Improving the signal-to-noise ratio of continuous gravity sequences

Gravity changes on active volcanoes are caused by the redistribution of subsurface mass-

es and by changes in surface elevation as the edifice inflates and deflates. To evaluate the contribution of subsurface mass redistribution, therefore, it is necessary also to monitor the elevations of the measuring stations. The elevation of each continuous gravity station is not systematically monitored. Nevertheless, discrete ground-deformation surveys routinely performed on Etna provide enough data to evaluate Etna's vertical deformation to a detail suitable for our purposes. Local height variations on Etna are usually too small to significantly affect surface gravity measurements [Budetta and Carbone, 1998; Budetta et al. 1999; Carbone et al. 2003a]. Accordingly, where adequate elevation data are not available, large gravity changes can be assumed to be the result only of subsurface variations in mass.

Continuous gravity sequences acquired on volcanoes can be split into two main components: i) anomalies linked to the activity of the volcano itself (useful signal) and ii) signal due to tides, instrumental and meteorological effects (assumed as noise).

The improvement of the signal-to-noise ratio is fundamental to recognize the anomalies due to volcanic activity within a gravity sequence. To achieve this goal the three main path described below have been followed.

3.1. Reducing the influence of external perturbations

To assess reliable gravity sequences, it is vital to measure all the perturbations which can affect the gravity signal (tilt, temperature, pressure, humidity, etc.) at each station and to suitably remove their effect from the gravity signal. Ours and other Author's experience has shown that gravimeters are affected mostly by temperature changes which can cause strong apparent gravity anomalies. To reduce the effect of atmospheric temperature changes on the gravity signal, we place the whole acquisition system inside a two level thermally insulating polystyrene container. The gravity meter together with a temperature sensor is kept on the lower level and the data logger on the upper level in a watertight PVC container (IP65 standard). Both compartments are dosed with silica gel. The temperature inside the low level of the box is maintained at 15-20°C above ambient; this strategy also reduces the power consumption of gravity meters (whose sensor usually works at about 50°C). A new system for actively thermosetting the environment around the meter is also under development.

3.2. Designing software to quickly analyse long gravity data-sequences

We have designed an advanced software package which allows the large data sets coming from the remote stations to be analyzed quickly and with a high level of automation. The software allows a quick visual pre-analysis which is very important for addressing further analysis steps (i.e. strategies for removing the effect of

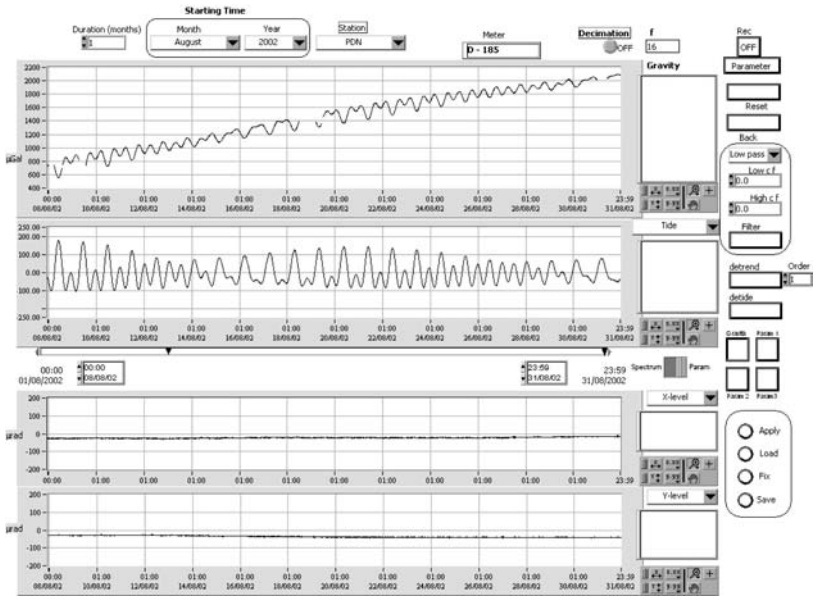

Figure 3. Interface of the program developed under LabVIEW® for real-time (pre-) analysis and presentation of data coming from each continuously recording gravity station. Rectangular buttons are controls, rectangular windows with arrows are selectors, other windows are indicators.

external perturbations). Since this software is quite easy to implement, it allows changes in the continuously recording array to be accommodated on one hand, and can be used to handle data from other similar arrays on the other.

The above software package has been designed under LabVIEW® (Laboratory Virtual Instrument Engineering Workbench), a software which features a graphical programming environment and all the tools needed for data analysis and presentation.

Great care was taken in designing the program interface to make it usable even by the inexperienced operator and to allow a quasi-real-time visualization of the reduced sequences which is vital for volcano monitoring purposes. LabVIEW® features a large library of analysis tools (spectra, Furier Transform, filters, curve fit, probability and statistic, etc.) through which even complex analyses on large data sequences can be performed in near real time.

The program features controls to perform the following operations:

- choose a temporal window within which all subsequent operations will be performed;
- correct the gravity data for the earth tide;
- correct the data for the instrumental drift (modelled as a linear or polynomial curve);
- filter unwanted frequencies from the data sequences;
- performs time-domain to frequency-domain transformations (spectra).

Figure 3 shows the interface of this program (data refer to PDN station). The program interface consist of four charts. The top one displays gravity whereas the parameter to be displayed in the other ones can be set by the operator via menu rings on the right side of each chart (the default from top to bottom is: raw gravity, theoretical tide, X level, Y level). Also there is a rectangular frame on the side of each chart where the list of all the operations performed on the data presented in the chart are reported.

3.3. Modelling how the meter output depends on the interfering meteorological signals

Meteorological perturbations (temperature, pressure, humidity) affect continuous gravity sequences and give rise to a pseudo-signal which is often stronger than the useful one.

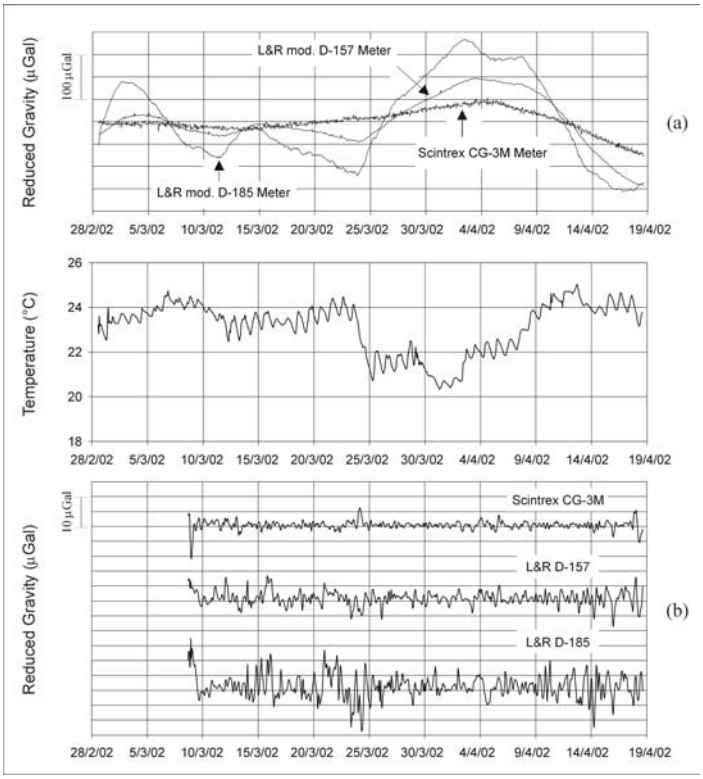

Figure 4. Data set from three gravimeters which worked continuously for about 50 days at a site far away from active zones. The figure shows (a) the reduced gravity sequences, after removal of the best linear fit and the theoretical Earth Tide and (b) the reduced gravity sequences, after removal of the best linear fit, the theoretical Earth Tide and the effect of atmospheric temperature modelled through a Neuro-Fuzzy algorithm. Final residuals are within a few μGal peak-to-peak.

To remove the effect of these perturbations is not easy given that the transfer functions are frequency-dependent and are different for each gravimeter employed. We have tested various algorithms to model the effect of meteorological perturbations on the gravity signal. Using a one-year-lasting data-set from SLN station, Andò and Carbone (2001) showed that a - linear (Neuro-Fuzzy) algorithm can be used to model satisfactorily how the meter output depends on atmospheric temperature and pressure.

The same algorithm was also tested over a data set from three gravimeters which worked continuously for about 50 days at a site far away from active zones. After accomplishing the reduction of the gravity series, residuals were within a few μGal peak-to-peak, thus confirming the capabilities of the Neuro-Fuzzy algorithm (Fig. 4a, b).

4. Concluding remarks

At Mt Etna we have developed a new system for continuous gravity monitoring. Through the experiments accomplished since 1998 many steps forward have been made towards the regular acquisition of high-quality data. We have designed both a suitable station setup and algorithms to reduce the signal for the effect of perturbations.

Our current target is to consolidate our experience (in particular as for the algorithms for continuous data reduction) using the longer sequences now available. Once the gravity signal from continuously recording stations is suitably reduced for the effect of external perturbations (which proved to be stronger by one order of magnitude than the volcanic effect) events with amplitude and/or characteristic anomalous with respect to the “normal” signal will be evidenced within different frequency bands. Possible time correlations between such anomalous items and the volcanic activity will be also tentatively evidenced to define gravity forerunners of paroxysmal eruptive episodes.

We also expect the combined use of discrete and continuous gravity measurements to provide, through the detection of phenomena with a wide range of evolution rates (periods ranging from minutes to years), both substantial improvements in the knowledge of the dynamics of the shallow plumbing system of the volcano and the identification of any possible gravity transient before and during volcanic eruptions.

Acknowledgements

This research was supported by the Epot project of the GNV.

References

Andò, B. and Carbone, D., (2001). *A Methodology for Reducing the Signal from a Continuously Recording Gravity Meter for the Effect of Meteorological Parameters*. IEEE Transactions on Instrumentation and Measurement, 50 (5), 1248-1254.

Berrino, G., Corrado, G., Magliuolo, R. and Riccardi, U., (1997). *Continuous record of the gravity changes at Mt. Vesuvius*. Annali di Geofisica, Vol. XL. N. 5, 1019-1028.

Budetta, G. and Carbone, D., (1998). *Temporal variations in gravity at Mt Etna (Italy) associated with the 1989 and 1991*. Bull. Volcanol., 59, 311-326.

Budetta, G., Carbone, D. and Greco, F., (1999). *Subsurface mass redistribution at Mount Etna (Italy) during the 1995-96 explosive activity detected by microgravity studies*. Geophy. J. Int., 138, 77-88.

Budetta G., Carbone D., Greco F. (2002). *Installazione ad alta quota di una stazione gravimetrica in telemetria: applicazioni all’Etna*. Quaderni di Geofisica, n. 23 – 8 pp.

Carbone, D., (2001). *Gravity monitoring of Mount Etna (Italy) through discrete and continuous measurements*. PhD Thesis, The Open University, Milton Keynes, UK.

Carbone, D., Budetta, G. and Greco, F., (2003a). *Possible mechanisms of magma redistribution under Mt. Etna during the 1994-1999 period detected through microgravity measurements*. Geophys. J. Int., 152, 1-14.

Carbone D., Budetta G., Greco F. and Rymer, H., (2003b). *Combined discrete and continuous gravity observations at Mt. Etna*. J. Volcanol. Geotherm. Res., 2581, 1-13.

d’Oreye, N., Ducarme, B., Hendicks, M., Laurent, R., Somerhausen, A. and Van Ruymbeke, M., (1994). *Tidal gravity observations at Mount Etna volcano*. In: Volcanic deformation and tidal gravity effects at Mt. Etna, Sicily, Final Report. Project no. ERB40002PL900491, pp 60-80, EEC SCIENCE.

Davis, P. M., (1981). *Gravity and tilt earth tides measured on an active volcano, Mt Etna, Sicily*. J. Volcanol. Geotherm. Res., 11, 213-223.

De Meyer F., Ducarme B. and El Wahabi A., (1995). *Continuous gravity observations at Mount Etna (Sicily)*. IUGG XXI General Assembly, Boulder, Colorado, July 2-14.

Eggers, A. A., 1983. Temporal gravity and elevation changes at Pacaya volcano, Guatemala, *J. Volcanol. Geotherm. Res.*, 19**,** 223-237.

El Wahabi, A., Ducarme, B., Van Ruymbeke, M., d’Oreyè, N. and Somerhausen, A., (1997). *Continuous gravity observations at Mount Etna (Sicily) and Correlations between temperature and gravimetric records*. Cahiers du Centre Européen de Géodynamique et de

Séismologie 14, 105-119.

Jachens, R. C. and Eaton, G. P., (1980). *Geophysical observations of Kilauea volcano, Hawaii, 1. Temporal gravity variations related to the 29 November, 1975, M = 7.2 earthquake and associated summit collapse*. J. Volcanol. Geotherm. Res., **7,** 225-240.

Rymer, H. and Brown, G. C., (1987). *Causes of Microgravity change at Poás volcano, Costa Rica: an active but non-erupting system.* Bull. Volcanol., 49**,** 389-398.

Rymer, H., Murray, J.B., Brown, G.C., Ferrucci, F. and McGuire, J., (1993). *Mechanisms of magma eruption and emplacement at Mt Etna between 1989 and 1992*. Nature 361, 439-441.

Rymer, H., Cassidy, J., Locke, C.A. and Murray, J.B., (1995). *Magma movements in Etna volcano associated with the major 1991-1993 lava eruption: evidence from gravity and deformation*. Bull. Volcanol., 57**,** 451 461.

Sanderson, T.J.O., (1982). *Direct gravimetric detection of magma movements at Mount Etna*. Nature, 297, 487-490.

Torge, W., (1989). *Gravimetry*. Ed. Walter de Gruyter., Berlin-New York.

VanRuymbeke, M., (1989). *A new Feedback System for Instruments Equipped with a Capacitive Transducer*. In Proceedings of 11th International Symposium on Earth Tides, pp 51-60, Helsinki, 1989.

Fabrication of IPMC and Characterization of its Sensorial Properties: Preliminary Results

Claudia Bonomo[1], Ciro Del Negro[2], Luigi Fortuna[1] and Salvatore Graziani[1]

[1]*Dipartimento di Ingegneria Elettrica, Elettronica e dei Sistemi, Università di Catania, Italy*
[2]*Istituto Nazionale di Geologia e Vulcanologia, Sezione di Catania, Italy*

Abstract

Ionic Polymer Metal Composites (IPMCs) are innovative materials obtained by deposition of a metal on a ionic polymer membrane. IPMCs bend, when an electric field is applied along their thickness, and vice versa generate a voltage when mechanically deformed. Hence, it makes sense to investigate the opportunity to use IPMCs to build either actuators or sensors. A full comprehension of the behavior of IPMCs sensing capability and a corresponding metrological characterization could be useful for their application to build sensing elements in the geophysical field, e.g. to record earthquakes and study their nature, especially because these materials are able to survey also very small displacement, at very low frequencies. To this aim a laboratory was equipped. Applying some variations to the standard fabrication procedure, many samples were fabricated and tested in order to improve the performance of the material. Moreover, some results of the analysis of sensing properties of an IPMC strip are presented. Experimental data suggest that the output voltage is roughly linear in deformation. Moreover, a nonlinear behavior seems to occur in particular working conditions. To authors' knowledge such a behavior never before has been reported in literature.

Key words *ionic polymer metal composites - actuators - sensors*

1. Introduction

Ionic Polymer Metal Composites (IPMCs) are innovative materials obtained by deposition of a metal on a ionic polymer membrane [Arena et al., 2002]. Some details on their structure are necessary in order to understand their sensing properties.

Ionic polymers have inner ionizable groups. These groups dissociate in a fixed part and in a movable one in a variety of solvent media. Usually, the fixed groups have negative charge while cations can freely move. By mechanically bending the material it is possible to change the distribution of the charges with respect to the membrane neutral axis (see Fig. 1): the applied stress will contract one side of the membrane while will spread the other, the mobile ions will move consequently toward the region characterized by a lower charge density parasitically carrying the solvent molecules (i.e. deionized water).

A deficit of negative charges and an excess of the positive ones will therefore result in the expanded side. In the contracted side the opposite will occur. This phenomenon produces a voltage gradient collected at the metal electrodes. It is intuitive as this property results in a sensing capability [Shahinpoor et al., 1998].

In the following some suggestions to

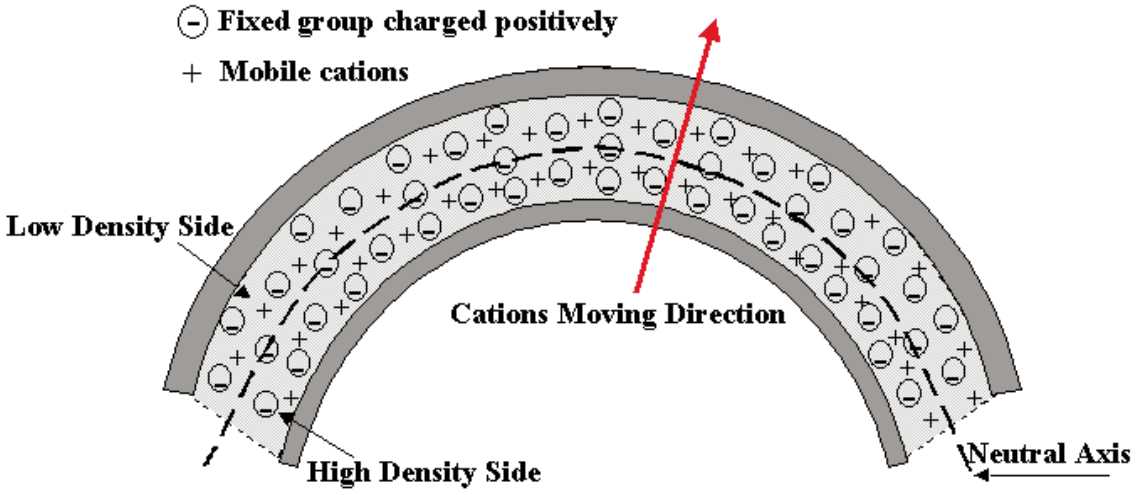

Figure 1. Effect of stress applied to the IPMC strip on charge distribution.

improve the quality of the electrodes and, as a consequence, the performances of the material are given. Moreover, a system for the characterization of the sensing properties of an IPMC strip is described. It allows to investigate the dependence of the voltage generated within the strip on the imposed deformation.

2. Variations to the standard fabrication procedure

One way to fabricate IPMCs refers to the standard procedure [Keisuke Oguro, 2003] to depose the metal layers on the polymer surface. Many matters are with this procedure. First of all the metal particles distribution on the polymer surface does not result uniform. This is because of the sandblasting using emery paper and the formation of metal clusters. These phenomena cause an increase of the surface resistance that means a bad quality of the electrodes.

To reduce the first cause, the sandblasting was obtained by mechanical pressure of the emery paper on the polymer, without scratching the surface; in order to transfer the uniform glass chips distribution. The results of the applied method are shown in Fig. 2.

As regards the second problem, an anti-clotting additive was added to the solution during the plating steps. Also in this case the results were good and they are shown in Fig.3.

3. Experimental setup

A system for the characterization of the sensing properties of an IPMC strip has been built and it is here described. It allows to investigate the dependence of the voltage generated within the strip on the imposed deformation.

The experimental analysis was performed on a strip built by using the ionic polymer Flemion^{TM} (by Asahi Glass) with gold deposed on both sides [Bar-Cohen et al., 2002]. The sample was 38 mm long by 6 mm large; its thick-

Figure 2. Sandblasting effects: microscopic images (20x) of the IPMC surface. To the left a sample fabricated by the standard procedure; to the right a sample where the sandblasting was obtained by mechanical pressure of the emery paper on the polymer, without scratching the surface. The reader can notice the difference in the uniformity of the metal distribution.

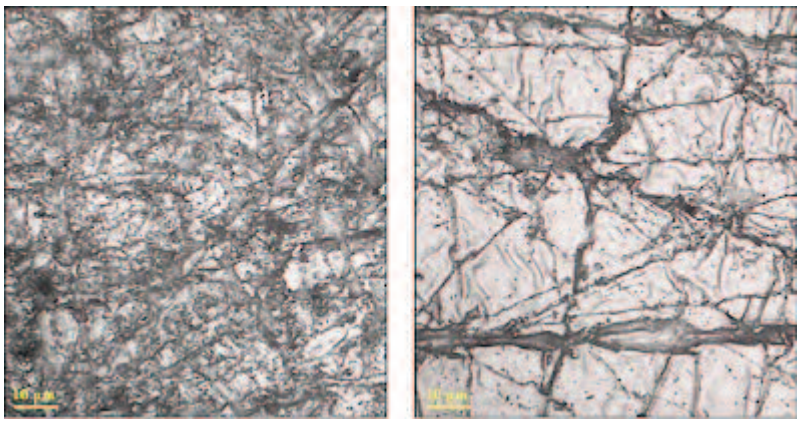

Figure 3. Anti-clotting additive effects: microscopic images (100x) of the IPMC surface. To the left a sample fabricated by the standard procedure; to the right a sample obtained using an anti-clotting additive.

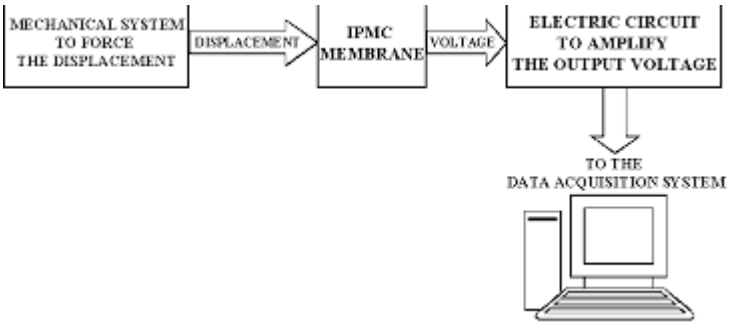

Figure 4. Schematic of the experimental setup used to characterize the sensing properties of an IPMC strip.

ness was about 200 μm.

Before each measuring survey, the strip was opportunely hydrated by immersion in deionized water. In fact a dependence of the sensing properties on the solvent contents was noticed and will be described in the following. The hydrated sample presented a weak curvature probably caused by a non uniform initial distribution of the ions.

The experimental setup is composed of a system to impose a displacement to the membrane tip and a circuit to amplify resulting output voltage. The schematic of the experimental setup is shown in Fig. 4.

The strip was fixed from one end in a cantilever configuration by a clip with cupper contacts, wired to the electronic circuit. The other end was pinned to the wiper of a linear potentiometer. The wiper was moved by a rod connected to a DC motor working at different frequencies, as shown in Fig. 5.

The strip was inserted at all times in such a way that its natural curvature was always in the positive direction of the *x'* axis (Fig. 6).

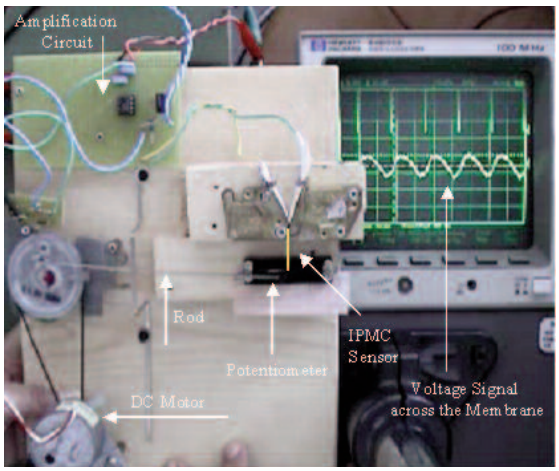

Figure 5. Photo of the mechanical system used to force the displacement on the IPMC strip and of the amplification circuit for the sensor output.

While the motor turns, it moves the rod and the rotational movement is converted in a translatory one by the wiper of the potentiometer and consequently the membrane is bent on both direction.

This causes both a production of a voltage signal V_{IPMC} across the membrane thickness and a variation of the voltage V_1 across the potentiometer. The membrane output signal was opportunely amplified. The gain was fixed to 270, in order to raise the voltage magnitude from less than 1 mV to about 300 mV. Then the amplifier output was acquired by the data acquisition board AT-MIO 16E-10 Series (National Instruments) from a Personal Computer. The potentiometer was used both to move the strip and to transduce its position into a voltage signal, as shown in Fig. 6. It must be noticed that, based on the chosen reference directions, a positive strip displacement corresponds to a negative voltage across it.

A number of data acquisition sessions were performed, tuning the DC voltage applied to the motor and hence changing the frequency

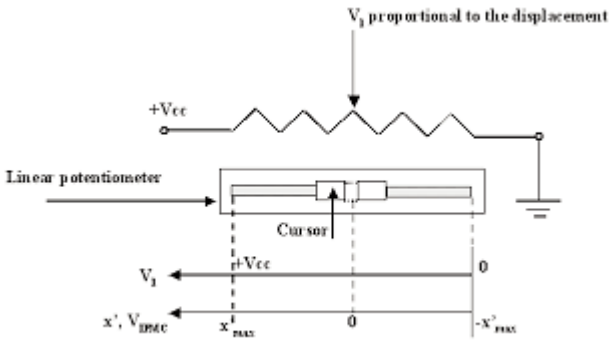

Figure 6. Electric circuit to convert the IPMC displacement into a voltage signal to be related to the voltage generated across the strip. Based on the chosen reference directions, a positive strip displacement corresponds to a negative voltage across it.

of the IPMC strip excitation signal.

Actually, the excitation point on the strip varies while the rod moves the cursor of the potentiometer. However it is possible to neglect this phenomenon being the distance δ between the two farthest excitation points, that is a measure of this variation, much smaller than the distance between the fixed end and the excited one. The wiper displacement, referred to the central position, was $\pm$1.2 cm.

4. Data Analysis

One thousand samples per second were acquired for each frequency and each acquisition lasted ten seconds, i.e. ten thousand samples for each acquisition sessions were collected. The range of the tested frequencies spanned from 1.0 Hz to 10.0 Hz, with steps of 0.5 Hz. These values were fixed because of the inertial constraints imposed by the DC motor. Recorded data were analyzed by using LabVIEW™ software.

The voltage signal V_1, picked up by the wiper of the potentiometer, is a wave oscillating approximately in the range 2.0 ÷ 6.0 V. This signal was translated into a symmetric voltage V_2 and then attenuated to the range –1.2 ÷ 1.2 V in order to give the position of the membrane tip *x'* directly in centimeters.

A second manipulation block was developed to estimate the displacement of a fixed point of the strip. Referring to Fig. 7, it corresponds to the estimation of the displacement x based on x'. Then

$$x = \frac{2.2 * x'}{\sqrt{4.84 + x'^2}} \qquad (1)$$

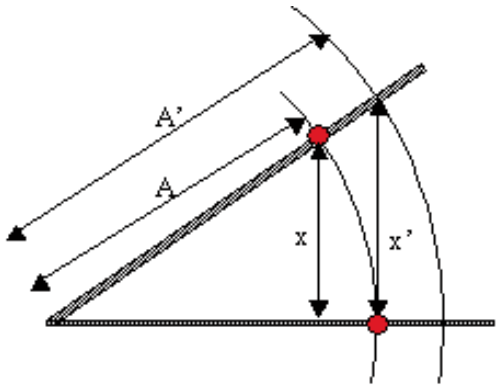

Figure 7. Dependence of the displacement *x* of a fixed point of the strip on the displacement *x'* forced by the potentiometer wiper position.

5. Results

Some typical examples of collected data sets are described in the following. In particular the influence of the input signal frequency is shown in Fig. 8. Both the time plots of the input *x* and of the output V_{IPMC} signals and the corresponding inputoutput plot are shown. In Fig 8a the input signal frequency is 3.69 Hz and in Fig. 8b it is 5.6 Hz.

It can be noticed that the potentiometer output shows a threshold phenomenon at its maximum value. This effect is due to the mechanical resistance met from the rod to invert the slider's motion direction and it is more evident at the lower frequencies. The presence of a non-linearity has to be pointed out on the sensor output signal each time the wiper crosses the zero position superimposed to a ringing signal. Also, the non-linearity effect looks more evident at lower frequencies. The phenomenon could be attributed to the initial deformation of the strip.

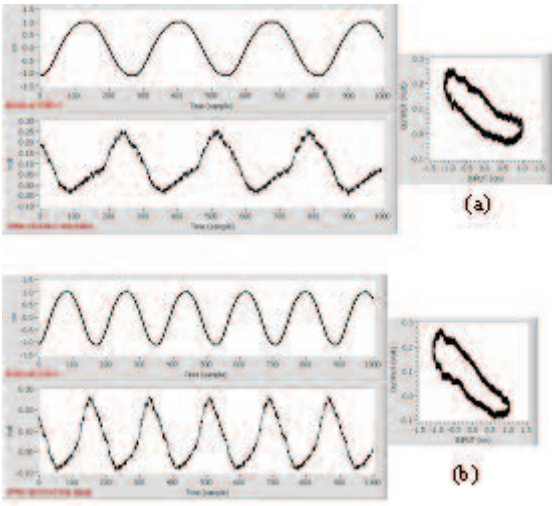

Figure 8. Time plots of the input *x* and of the output V_{IPMC} signals and the corresponding input-output plot: (a) at 3.69 Hz and (b) at 5.6 Hz.

The analysis of acquired data suggests that the input-output peak-to-peak amplitude ratio is constant in the considered range of frequencies.

Also, it is possible to observe the presence of a time delay between the imposed displacement and the voltage response of the membrane. The time delay t_d between the stimulus and the sensor response is frequency dependent as it can be noticed in the data reported in Fig. 8. It seems to decrease as the excitation frequency increase. Indeed as regards the case (a) t_d is 220 ms, and in the case (b) t_d is 160

ms.

The influence of the hydration level on the strip behavior was also addressed. For the sake of comparison the same set of input signal frequencies was considered also in the case of this analysis.

In Fig. 9 the time plots of the input x and of the output V_{IPMC} signals and the relative input-output plot when the strip is partially dehydrated and the input frequency is 5.6 Hz are shown (see Fig. 8b).

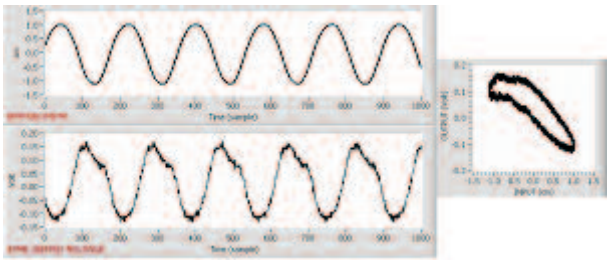

Figure 9. Time plots of the input x and of the output V_{IPMC} signals and the relative input-output plot when the strip is partially dehydrated and the input frequency is 5.6 Hz are shown (see Fig. 8b).

6. Conclusions

In this paper some preliminary results about the sensing properties of an IPMC strip have been presented. A system to gather the required data has been built.

The dependence of a strip of IPMC on both the input signal frequency and on the hydration level of the strip has been addressed.

Further work to extend the frequency range of the acquired data in order to better characterize the sensor is in progress.

A full comprehension of the behavior of IPMCs sensing capability and a corresponding metrological characterization could be useful for their application to build sensing elements in the geophysical field, e.g. to record earthquakes and study their nature, especially because these materials are able to survey also very small displacement, at very low frequencies.

Acknowledgements

The work was developed in the frame of the TecnoLab, the laboratory for the technological advance in geophysics organized by DIEES-UNICT and INGV-CT. This research was supported in part by the Epot project of the GNV.

References

Arena, P., Bonomo, C., Fortuna, L. and Frasca, M. (2002). *"Electro-Active Polymers as CNN actuator for locomotion control"*, Proceedings of ISCAS 2002, Phoenix, May 26-29.

Yoseph Bar-Cohen1, Xiaoqi Bao, Stewart Sherrit and Shyh-Shiuh Lih (2002). "Characterization of the Electromechanical Properties of Ionomeric Polymer-Metal Composite (IPMC)", *Proceedings of the SPIE Smart Structures and Materials Symposium, EAPAD Conference, San Diego, CA, March 18-21, 2002*

Keisuke Oguro: "*Preparation Procedure of Ionic Polymer Metal Composite membrane*", web page http://ndea.jpl.nasa.gov/nasa-nde/lommas/eap/IPMC_PrepProcedure.htm;

M. Shahinpoor, Y. Bar-Cohen, T. Xue, J. O. Simpson, and J. Smith (1998). "*Ionic Polymer-Metal Composites (IPMC) as Biomimetic Sensors and Actuators"*, Proceedings of SPIE's 5th Annual International Symposium on Smart Structures and Materials, San Diego, CA, March 1-5, 1998.

Beta Version of MADAP: A Modular Architecture for MAgnetic DAta Processing Acquired by Volcanic Monitoring Networks

Gilda Currenti[1,2], Ciro Del Negro[1], Luigi Fortuna[2], Salvatore Graziani[2], Rosalba Napoli[1], Alessandro Rizzo[3] and Annamaria Vicari[1,2]

[1]Istituto Nazionale di Geofisica e Vulcanologia – Sezione di Catania, Italy
[2]Università di Catania – Dipartimento di Ingegneria Elettrica Elettronica e dei Sistemi, Italy
[3]Politecnico di Bari – Dipartimento di Elettrotecnica ed Elettronica, Italy

Abstract
The preliminary version of a modular software architecture is presented. It is devoted to the automated elaboration of magnetic data recorded at volcanic sites. To improve the effectiveness of volcano monitoring, it is essential that data gathered over a volcanic area are processed quickly and effectively. To pursue this goal, our Laboratory of Geomagnetism has been developing an automated system of data acquisition and reduction for magnetic data, called MADAP (by MAgnetic DAta Processing). The software application, designed under Visual C++, consists of three modules. The first, called MagTalk, is a package of procedures for the acquisition and transmission of signals from continuously recording sensors to a central observatory. The second, called MagTool, contains a set of analysis routines able to reduce the incoming data, produce interpretable parameters and store the data in permanent files. The third, called MagWarn, is a methodology devoted to comparing the calculated parameters with prescribed limits; a warning signal is displayed if the limits are exceeded.

Keywords *volcano monitoring - data-handling system - volcanomagnetic signals - Mt. Etna*

1. Introduction

In the recent past the magnetic method has proved its ability to detect small changes of the magnetic field linked to volcanic activity [e.g.: Zlotnicki and Bof, 1998; Del Negro and Currenti, 2003]. This technique is now relevant to give valuable and specific information on the state of a volcano. Till now the expertise in this domain is not integrated in an automated system in which the data are continuously analyzed and evaluated. A brief examination of the devices installed throughout the world for the magnetic monitoring of active volcanoes generally shows a low degree of automation. State of the art in volcano monitoring as practiced today lags behind the available technology. This delay implies that data cannot be evaluated in real-time or near real-time, with obvious consequences in crisis periods. Information gathered by a wide variety of sensors, which are distributed over a vast area, must be transmitted on-line to an observatory with specialized staff, where conditions for receiving and evaluating the data have to be tuned to maximum efficiency and reliability. It is therefore fundamental to minimize the workload as much as possible by means of technological innovation to resolve the main burden of standard reduction process of data and give the operators already elaborated information as far as the software available will allow.

Our Laboratory of Geomagnetism (MagLab) has been developing methods, hardware and know-how for the automated acquisition and management of data simultaneously acquired at a variety of remote magnetic stations. We aim to provide a basis for real-time response during eruptive events, therefore, there is the wish to realize an automated system that starting from a reconstruction of the physical behavior of the volcano, provides a model and which, when on-line data are available, allows to observe and foresee the propagation/evolution of phenomena. The structure of classical computations proves to be inadequate to resolve problems of this kind, which require information from a certain number of cases to be generalized. As a consequence, the necessity to resort to innovative computational paradigms, which operating in integrated mode may efficiently confront such problems, has arisen. In particular, we refer to those techniques, known as soft computing, which allows problems requiring the intervention of human experts to be solved. These techniques are able to give an estimate of the uncertainty with which a model of a dynamic system is obtained (the volcano), having in-out value couples available.

Automation in volcano monitoring can be divided into three steps: (i) signal transmission, (ii) signal evaluation, and (iii) notifying of a warning signal. With this aim we have been developing a graphic user interface based application, called MADAP (MAgnetic DAta Processing), which is able to rapidly manage a wide variety of data coming from remote stations of monitoring networks and to execute

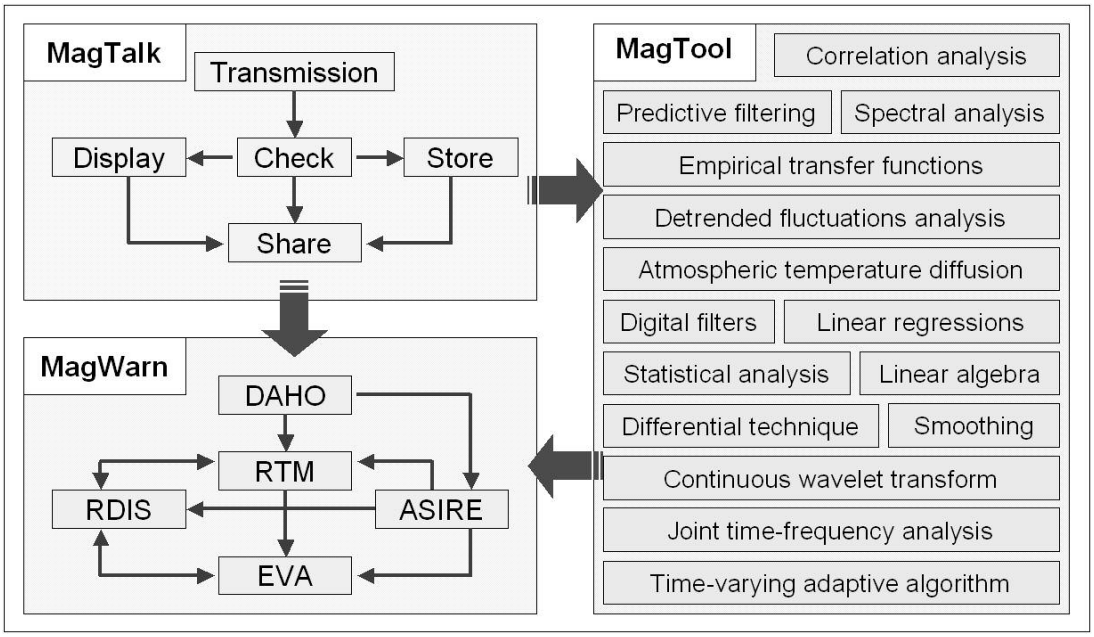

Figure 1. MagWarn system expressed through a block-diagram representation.

quickly different analysis techniques. The software, designed under Visual C++, consists of three modules, one for each step, characterized by high automation level and development flexibility (Fig. 1). The first two modules have been completely implemented. The former, called MagTalk (Communication module), is a package of procedures for the acquisition and transmission of signals from continuously recording sensors to a central observatory. The latter, called MagTool (Analysis module), contains a set of analysis routines for reduction and evaluation of the incoming data to produce interpretable parameters and store the data in permanent files. Currently, we are developing the third module, called MagWarn (Warning module), which aims to develop the best possible methodology to compare the calculated parameters with prescribed limits and subsequent activate a warning signal if the limits are exceeded. The automation process also requires the results of the analyses to be integrated to provide an estimate on the state of volcano. We will briefly summarize the preliminary achievements related to the planning of MADAP, and its application on Etna. This report describes work that is still in progress, but sufficiently mature to warrant attention.

2. The Communication Module

The architecture of MADAP system has been developed taking into account the specific requirements by the magnetic network installed on Mt. Etna. During the last two decades, the MagLab has been intensively monitoring the magnetic field on Mt. Etna. We have observed significant correlations between volcanic activity and changes in the local magnetic field, up to a few tens of nanoteslas [e.g.: Del Negro et al., 1997; Del Negro and Ferrucci, 1998]. Detection of clear magnetic signals associated with the renewal of the volcanic activity has led to an increase in the magnetic monitoring of Mt. Etna. Since the end of 1998 a permanent magnetic array equipped with Overhauser effect magnetometers has been set up [Del Negro et al., 2002]. All remote stations are equipped with Overhauser effect magnetometers (0.01 nT sensitivity) and synchronously sample the Earth's magnetic field every 10 seconds.

MADAP uses data from the array of continuously recording remote stations (RS) spread over the volcanic area and linked by mobile phone to the control center (CC) at the local observatory (e.g. at the INGV-CT). The control center is a computer-based magnetic data acquisition system situated in a local observatory where mains electricity and telephone services are available. At this location a computer receives the data and performs data sorting and reduction as well as limited evaluation to detect abnormal behavior or breakdown of remote sensors. A communication module, called MagTalk and linking CC to RS, has been developed with a client/server structure (Fig. 2). At predetermined intervals (e.g. once a day) the client (CC) connects to the server (RS) to download the latest data. Data coming from each station are collected in the host-computer at the observatory where they are preliminarily examined to iden-

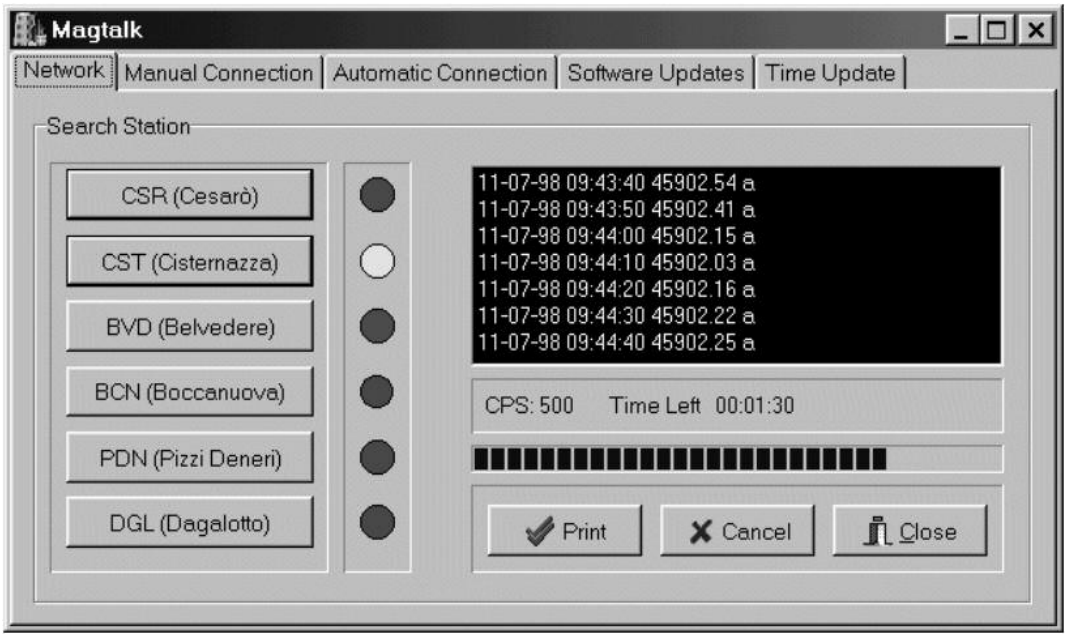

Figure 2. Output screen of the communication module.

tify and correct possible errors. In particular four main functions are applied:

- check for possible time gaps within data sequence or repetition of the same sample;
- verify the standard of the format of data transmission, the possible incoherence in the examined string is immediately indicated to the operator who can decide to eliminate or correct the string;
- select data measured by the magnetometer on the grounds of the quality index associated with each datum. This application deletes data that do not fall within the quality range previously defined by the operator;
- store data in the local database from which they can be easily retrieved at any moment to be processed.

In order to ensure problem-free running the computer system is furthermore programmed to provide a daily report to check if all data have come through normally. The computer system is also programmed to calculate automatically and display in real-time simple differences and spectral content of incoming signals, providing a quantitative measure of magnetic activity. These data can be the basis for rudimentary alarm systems, notifying observatory staff that something has happened and requires further evaluation. An operator can then investigate the problem and decide which action is needed, such as changing the transmission frequency, if greater information is required, or if some equipment failure needs correcting.

Web Site

The local control center has also been devised to upload data to a distant user immediately after acquisition and re-formatting. Data processed at the "distant desk" can be downloaded a few hours later and used by the personnel in charge of the volcano forecast. The on-line availability of crude or pre-processed data to authorized users connected to a wide-area network, fosters the possibility of monitoring active volcanoes without concentrating all human resources in a single observatory. Provided that the field maintenance and support are available at the volcano observatory chosen, such a scheme would allow special instruments to be run even without any expertise in processing and interpretation of specific data.

Some new pages have been added to the INGV-CT Web site under the item Laboratory of Geomagnetism to share the measurements throughout the world. At the address **http://maglab.ct.ingv.it** it is possible to examine geomagnetic observations carried out at Mt. Etna. In the Web site the 10-minute average of the magnetic field total intensity and the related standard deviation for each station are plotted (Fig. 3). In particular, any external users having a password are able to download directly data acquired at the stations of the magnetic network of Mt. Etna.

3. The Analysis Module

To handle rapidly the huge amount of data coming from a continuously recording monitor-

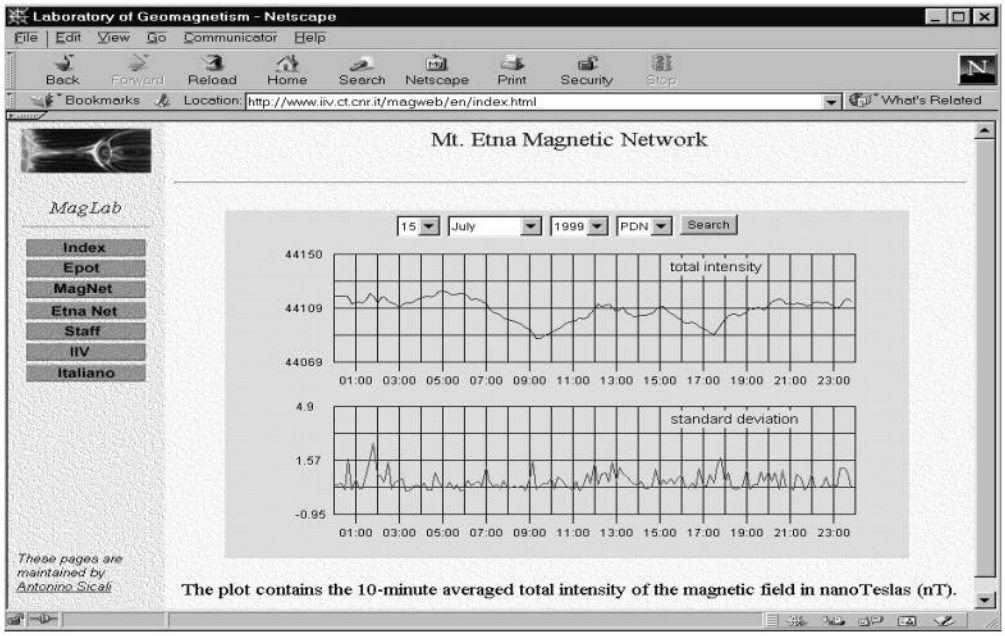

Figure 3. The web site at the address http://maglab.ct.ingv.it**.**

ing network (e.g.: 8640 measurements per day from each station, using a 10 s sample rate) and to apply faster different analysis techniques we have developed a second module, called MagTool, which allows a high skill level to be achieved by the operator. Our application is built to be user friendly and specifically to minimize time taken in data reduction processes and improve the ability to recognize magnetic events due to geophysical sources. MagTool includes a powerful, comprehensive package of analysis routines for processing acquired data. This package is rich in statistics, regressions, linear algebra, time and frequency domain algorithms, windowing routines, and digital filters (Fig. 4). Described below are some dedicated routines available in the package.

Simple differences

The observation of a volcanomagnetic event (a few nT or less) attributable to the dynamics of a volcano is strongly tied to the ability to cancel out the normal variation in the Earth's main and transient fields. To date, the most used and reliable method is the classical differential technique, based on simultaneous simple differences among the magnetic field amplitudes recorded at several points on a volcano. This method was implemented with the option to verify the synchronization between signals recorded at different stations. To do this a cross-correlation function has been included, since if two signals are perfectly synchronized they are also cross-correlated with each other. Thus, when two signals are not synchronized, the cross-correlation function computes the delay/advance of the signals and re-synchronizes them on the grounds of these results. We also included Steppe's [1979] method to find differences between a given station and a weighted linear combination of the remaining stations in a total field array, where the weights are determined by linear regression.

Empirical transfer functions

Recently a vector magnetometer for continuous monitoring of the inclination and declination of the Earth's magnetic field has been tested in the reference station of Mt. Etna magnetic network. We implemented a more detailed data analysis by employing the method developed by Poehls and Jackson [1978], which relates the vector field at the reference site to the total field at the observation sites by transfer functions to filter out residual variations caused by transitory fields. The use of complex, frequency-dependent transfer functions to relate the vector field at a reference site to the total magnetic field effectively filters out residual variations caused by atmospheric disturbances, their associated ground currents, and local variations in magnetic susceptibility. This method is especially effective in reducing the residuals associated with diurnal variations, thus allowing tectonomagnetic events even shorter than a few days duration to be detected.

Correlation analysis

In order to distinguish between transients

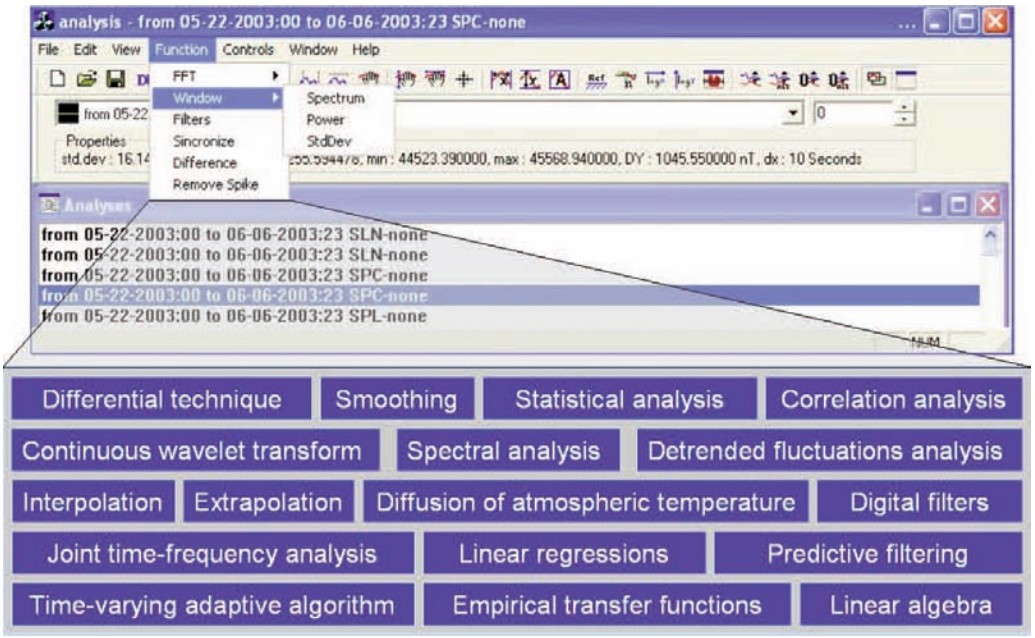

Figure 4. Output screen of the analysis module.

of volcanomagnetic origin and transients generated by strong variations in the external transitory magnetic field, we implemented the method devised by Del Negro and Ferrucci [2000]. This method was inspired by the observation that at two stations spaced a few kilometers apart the transients in one signal were proportional in magnitude to those in another signal. This led to the hypothesis that the contribution to the signal generated by the transitory magnetic field may be broken down into two parts: one of external origin, which is identical for both stations given their geographical proximity, and another of internal origin, proportional to the former, but dependent on the site. Following on from this simple description of the magnetic field, an accurate analysis, which takes into account the correlation between the measurements at two stations, was developed.

Spectral analysis

Another method for the detection of the volcanomagnetic transients is that of analyzing the spectral amplitude changes in signals gathered at continuously recording stations [Del Negro et al., 1997]. The spectral analysis is performed on mobile windows, and the window maximum peak of the spectral amplitude is associated with each time window. An amplitude increase in the power spectrum, caused by a significant change in the local magnetic field, is expected to occur in the presence of volcanic activity. This method is suitable to detect noise-corrupted signals, especially when the signal-to-noise ratio (SNR) is very low. In such cases the time window averages are affected by large statistical error, and the simple difference method for the detection of the volcanomagnetic transients quickly becomes ineffective.

Joint Time Frequency Analysis

Conventional analysis can describe a given signal as a function of time, showing the signal amplitude changes over time, or alternatively as a function of frequency, defining its frequency content but without clearly indicating how those frequencies evolve with time. Given the intrinsically time-varying nature of magnetic signals, a module for the Joint Time-Frequency Analysis (JTFA), a signal processing technique in which signals are analyzed in both the time and the frequency domain simultaneously, has been implemented (Fig. 5). Moreover, the JFTA module uses a rather sophisticated time-dependent spectrum analysis that allows the instantaneous spectrum of a signal to be extimated. Time changes of the spectrum provide a more complete representation of the signal and consequently a better understanding of its nature.

Predictive filtering

Currently, we are concerned with reduction of changes in the difference fields due to contrasting responses at magnetometer sites, using methods of predictive filtering, with the filters giving the relative responses between sites. Davis et al. [1981] developed the first type

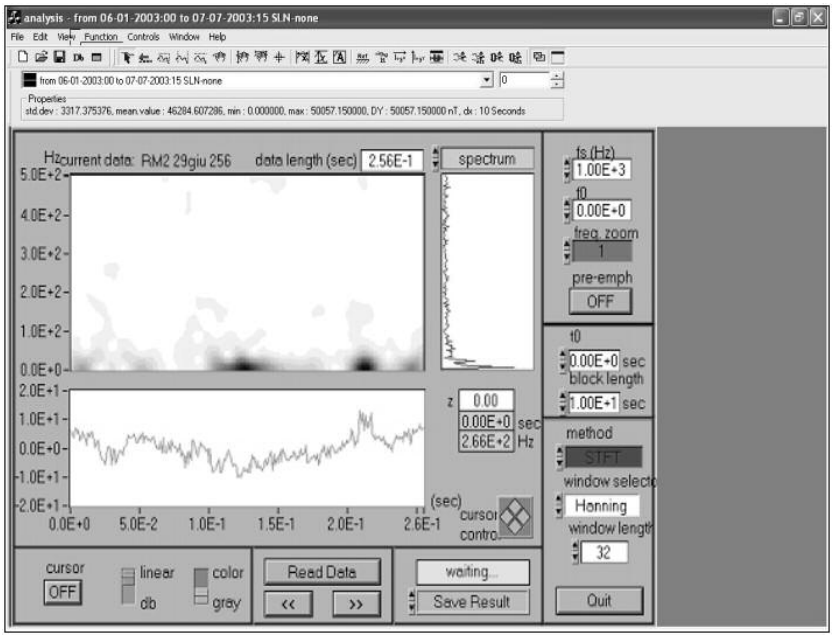

Figure 5. Interface of the joint time-frequency analysis routine.

of approach based on Wiener's classic filters theory. The predictive analysis allows some time-intervals where important statistical variations of the signal are present to be identified. These intervals are also called non-stationary zones. Considering that this phenomenology is time-variant, a non-stationary approach is more suitable to describe the physical effects tied to volcanic processes. For this reason we have also been implementing an adaptive type approach. In the non-stationary analysis all the variables are time varying. Therefore the weight vector of prediction as well as the cost function (mean squares error) will also depend on time. The technique of analysis is based on a set of adaptive mutual predictors, trained on a sliding time-window, which describe the changing statistical characteristics of the observed time series. In practice, each sample within a sliding window is weighted through a time-varying vector in order to obtain a minimization of the cost function. This procedure allows the time intervals where the predicted time series is different from the original sequence to be identified. These intervals are likely to be affected by volcanomagnetic effects.

Diffusion of atmospheric temperature change into the ground

From recent observations an annual component clearly appears in the reduced signals. The amplitude of these annual changes is about 4 nT at all sites. These periodic fluctuations are present even when there was no volcanic activity and they well correlate with seasonal temperature variations (the correlation coefficient is 0.88). Recent and more accurate studies claim that annual variations in the geomagnetic total intensity could be caused by seasonal changes in the heterogeneous magnetization of near-surface rocks due to a diffusion of atmospheric temperature change into the ground. Using the method proposed by Utada et al. [2000], the features of annual variations (ΔF_T) can be quantitatively estimated by a simple one-coefficient filter as:

$$\Delta F_T(t) = h_0\, \Delta T(t - t_0)$$

where ΔT is time variation in the ground temperature, h_0 is the amplitude ratio of annual changes estimated by a least squares method, and t_0 is the time lag calculated from the phase differences between total intensity and temperature. Although the simple linear filtering is effective a residual annual component remains. It is supposed to be due to non-linear effect of the temperature. To model this effect, we propose a non-linear filter based on a fuzzy logic algorithm. The effectiveness of this filtering technique can be tested through the statistical measures of residual component.

4. The Warning Module

In order to integrate the results of the analyses with modelling, and provide an estimate of the level of volcanomagnetic activity, we have implemented a third module, called MagWarn. It is a complex environment still

under realization. To be run on-line it was built with "blocks". This way, the system just needs to load each block onto memory once. The working process was hard to design, but once implemented, it allowed complicated scenery to be built quickly. MagWarn is divided in five main blocks:

- Data homogenization on a common time base (DAHO block),
- Relating information from different sources (RIDS block),
- Automatic signal recognition and classification (ASIRE block),
- Real time modelling (RTM block),
- Evaluation of the volcanomagnetic activity (EVA block).

In the following the most important function performed by each block are described. Each block processes the output from the previous ones and outputs data to the following blocks.

DAHO block

The first block, called DAHO, handles the large amount of heterogeneous data acquired in volcanic areas. Visualizing these data on a common time base is critical to interpreting them correctly and reacting suitably to possible geophysical changes (Fig. 6). DAHO gathers and classifies the available information in homogeneous domains readable by the automated system. Three specific databases are continuously upgraded in the same software environment. The first corresponds to the eruptive history of the volcano (past activity, dynamism, etc.). The second concerns the disturbances (ground temperature, solar wind velocity, K index, etc.) that affect the magnetic field measurements. The third is devoted to the magnetic time series obtained by the real-time monitoring network on the field. These databases homogenize the data format and classify all the different parameters, which will be the input data for both ASIRE and RTM blocks.

RIDS block

The second block, called RIDS, assembles and properly organizes all the dispersed information that contains a location reference, placing that information at some point on the volcano. The whole information is collected in a global GIS (Geographic Information System), which ensures the compatibility among all data and the flexibility and easy running to users [Carrara and Guzzetti, 1995]. A GIS is a computer system capable of capturing, storing, analyzing, and displaying geographically referenced information (data are identified according to a location). The power of a GIS comes from the ability to relate different information in a spatial context and to reach a conclusion about this relationship. RIDS is constituted of three particular GIS (Fig. 7). The first is mainly filled by the knowledge of the volcanic activity: the lava flows distribution, the thickness of ejecta, regional geodynamics, and the time and spatial evolution of fractures. The second collects different types of geophysical reconstruction of the

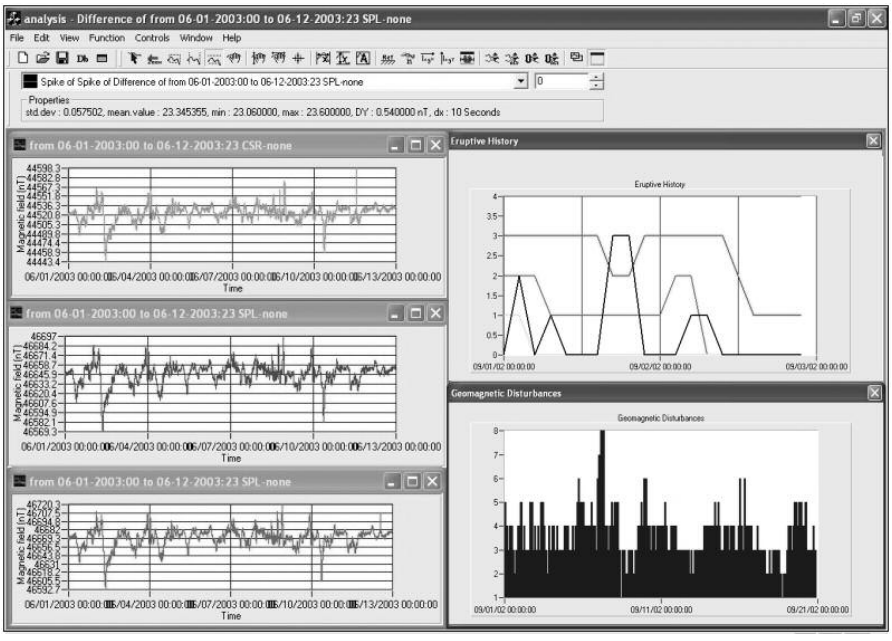

Figure 6. Output screen of the DAHO block.

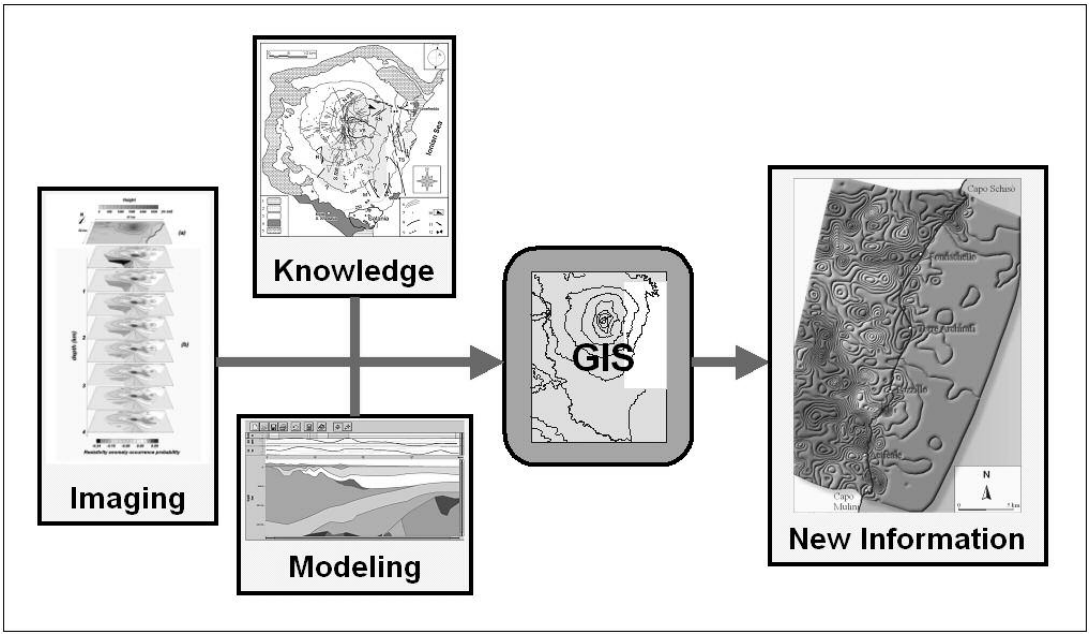

Figure 7. Volcanological and geophysical information stored in a global GIS by RIDS block.

volcano. Some of them integrate information of the volcano structure: location of magma complex, tectonic discontinuities, ground water flows and resistivity structure or earthquakes foci. The third pulls together the results of the forward modelling obtained by RTM block. These models are based on laboratory experiments and constrained by the anomalies evidenced by the ASIRE block. Human experts will validate all this information, before combining them in the global GIS [Emmi and Horton, 1995].

ASIRE block

The third block, called ASIRE, is devoted to the automatic signal recognition and classification by cross correlation analysis. The block is a fuzzy logic based technique [Sugeno, 1985], which aims to recognize intervals of anomalous behavior of the recorded and homogenized geophysical parameters under investigation. A critical point is the identification of the most reliable criteria that permit discriminating the occurrence of a volcanomagnetic event. In particular, these criteria could not be viewed as a simple threshold system that rigidly classifies the activity level. Generally, geophysical processes are not sufficiently well known to be quantitatively described and human knowledge and experience inevitably play a crucial role in making decisions about the state of volcano. A key point in studying geophysical signals is related to the difficulties to deal with the natural uncertainty of the available data, resulting from the imprecise knowledge of the underlying phenomena. Moreover, the needed information is not completely available and/or too complex to be studied with the most traditional algorithms. While conventional computing requires a deep understanding of a system, exact equations and precise numeric values, soft computing is tolerant of imprecision, uncertainty and partial truth [Zadeh, 1965]. Soft computing mimics the human ability to find precise solutions in an environment of uncertainty and imprecision. One of the principal constituents of soft computing is fuzzy logic that, in this perspective, provides a remarkably simple way to draw exact decision from inaccurate information. Since fuzzy logic can handle approximate information in a systematic way, it is an appropriate tool for modelling complex systems when accurate math equations, governing the process, are not known. Fuzzy logic is able to describe complex systems by mapping human knowledge and experience in simple rules. The linguistic information is represented by mathematical functions which map the linguistic expression into exact numeric ranges. Fuzzy rules are very easy to learn and use (Fig. 8). It typically takes only a few rules to describe systems that may require several lines of conventional software. As a result, fuzzy logic could improve significantly the ability to recognize the "events" among the signals.

RTM block

The fourth block, called RTM, calculates

models in real time and integrates the results in a global GIS. It is worth stressing that real-time modelling is now possible thanks to recent improvements in hardware and software performance. Fine adjustments to models can be performed continuously on the grounds of (i) analysis of the latest data, and (ii) new constraints available (Fig. 9). For example the magnetic stations on Mt. Etna are located along a S-N profile crossing the volcano summit. This layout, symmetrical with respect to the central craters, allows continuous prospecting of the volcanomagnetic field along this section of Mt. Etna. The alignment of such continuous stations will deliver – in real time and for a given time window – a 2 or 2½ D forward modelling of the magnetization versus depth [Del Negro and Currenti, 2003].

After individual evaluation of the compatibility between the observed anomalies detected by ASIRE and the independent forward modelling, all the results will be integrated in the global GIS upgraded by RIDS, in which all 3D reconstructions, forward modelling and volcanic activity will be cross-correlated. In this block the time duration of the magnetic anomalies, their number and the location on the volcano will be taken into account in order to recognize the typology of sources. The degree of compatibility with the possible anomalies sources deduced from the different modelling will graduate levels of volcanomagnetic activity. A high coherence level between detected anomalies and the integrated forward modelling

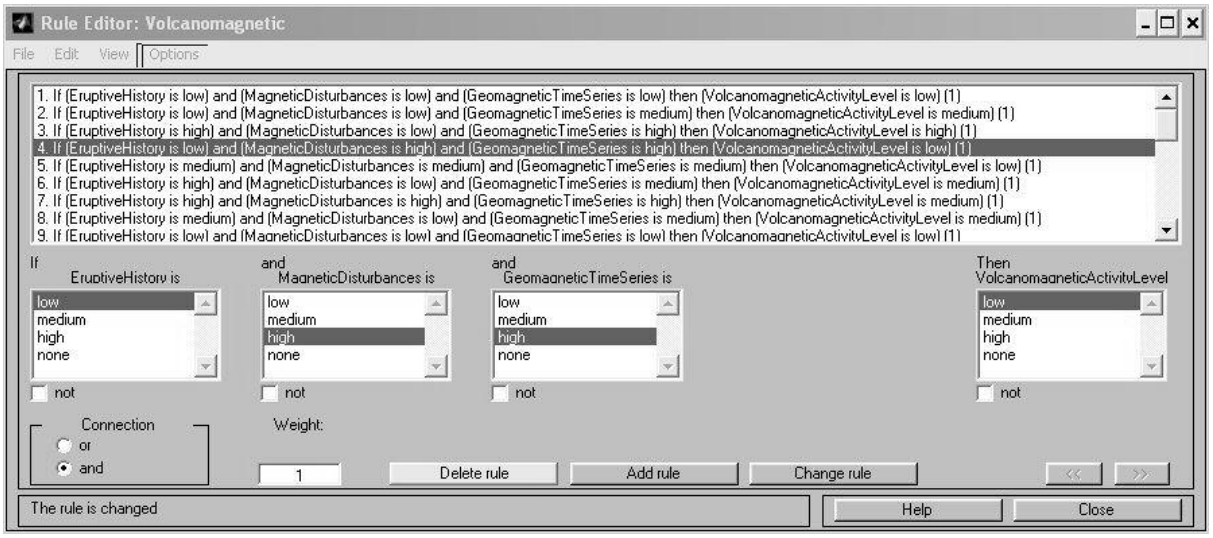

Figure 8. Fuzzy rules contained in ASIRE block.

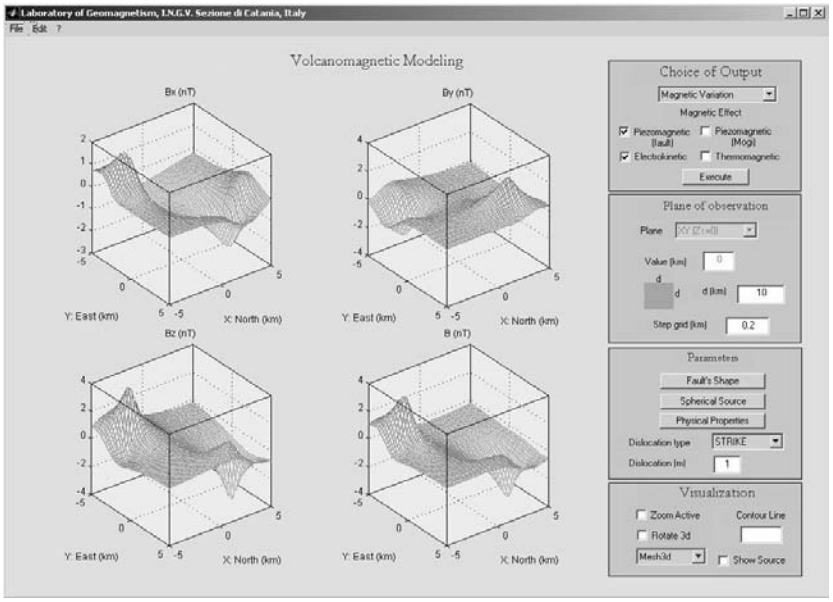

Figure 9. Piezomagnetic field due to a rectangular fault with strike-slip calculated by RTM block.

will lead to evaluate the state of activity.

EVA block

The fifth block, called EVA, starting from a reconstruction of the physical behavior of the volcano, provides a model and, when on-line data are available, allows to describe its time evolution. Modelling involves an analysis of eruptive history and monitoring results in order to find patterns that can be applied to future activity. This allows us to build a model for making foresees that focus our efforts on the most probable activity of the volcano. Therefore, two different typologies of information interfere in this block:
First, the information given by the lower blocks that will detect anomalous and correlated changes, the sources of which will be in agreement with the characterization of the volcano,
Second, the knowledge base deduced from the past activity of the volcano.
At this stage, EVA prepares a report of findings from all available information (Fig. 10):

- The stations which indicate a reliable anomaly.
- The level of reliability of the anomalies.
- The duration of their changes.
- The amplitude and their distribution.
- The correlations between the different parameters.
- The possible locations of the sources of the anomalies.
- The similar changes that have occurred in the past.

EVA's reports are based on a fuzzy decision making method [Zimmermann, 1996] with effective visualization of all processed data and intermediate results. Such information is continuously re-evaluated by the lower levels (blocks). The reports will have to be secured by man-made expertise. Different cases could appear which cannot be considered with the same level of activity. Even if MagWarn is able to make recommendations, the final decision of the level of volcanomagnetic activity will be ensured by experts who will take into account the past activity knowledge base.

5. Conclusions

The computer-based system MADAP was designed and implemented at the MagLab for magnetic monitoring of Etna volcano. The system is intended to solve the problem of monitoring the volcano at large distances from the local observatory, with the requirement of providing an estimate of the level of geomagnetic activity. When studying a system as complex as a volcano, to be able to simplify it without losing relevant information is vital. MADAP is a modular structure using physical building blocks that allow the global problem to be split into smaller and easier sub-problems, each solved within a single module. The multi-resolution approach allows data with diverse characteristics to be elaborated effectively. A variety of blocks with different procedures, depending on the nature of available data, were implemented.

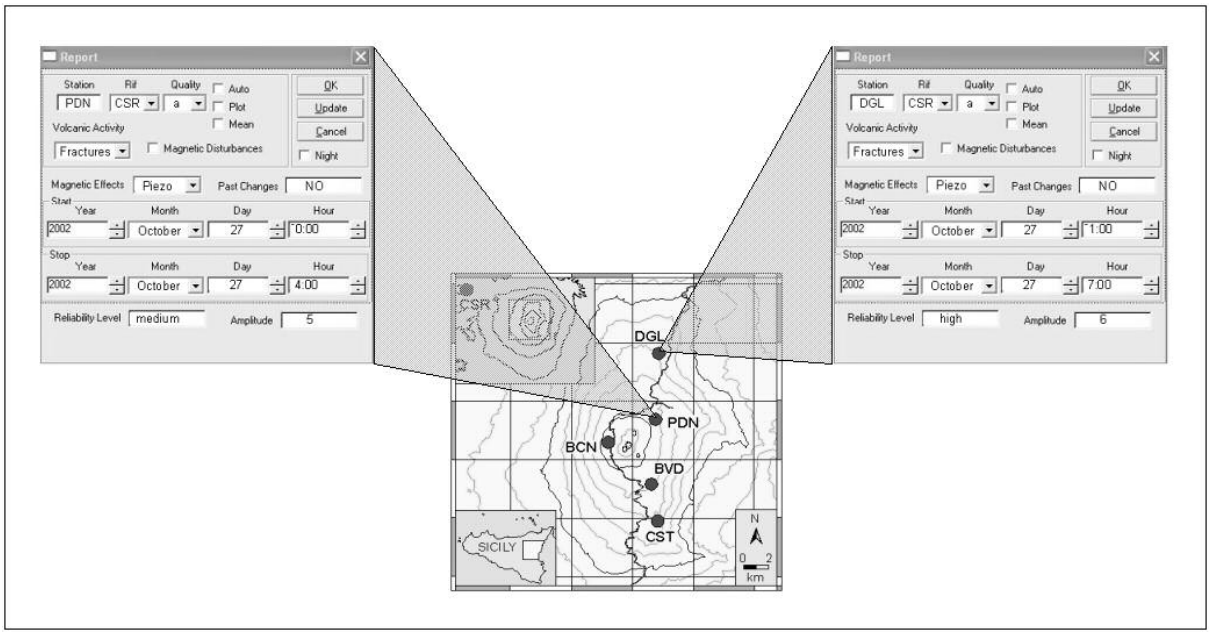

Figure 10. Reports of findings made by EVA block.

In particular, both traditional elaboration procedures and innovative ones were used. The interaction among the various blocks was organized in a complex computing structure that uses an integrated approach based on the techniques known as soft computing to extract, as efficiently as possible, information from the available data [Jang, Sun, and Mizutani, 1997]. The flexibility of the proposed structure allows both changes to the current modules and implementation of new modules to be easily performed. This architecture will avoid dispersion in human resources and will drastically decrease the time response to evaluate the volcanomagnetic activity as well as to notify a warning signal.

We aim to develop the best possible methodology to understand, monitor and foresee the volcanic activity by focusing researches on magnetic monitoring. Such methodology must allow the available information to be handled quickly and effectively. To act "quickly", automated systems able to correlate incoming information with a set of predefined policies and decision strategies are necessary, so that a response can be given when needed. Acting "effectively" means that operators must be able to evaluate the success of their policies and strategies and continually refine them to improve the performance. And, the concept that "methodologies" must accomplish this indicates that actions must be consistent across all operations and not be restricted to individual employees, systems, locations, or communication channels. The methodology we have been building up is founded on a fuzzy-logic based architecture. The approach pursues a main target: to build up an architecture in which new inputs can be continuously integrated. Such a system automatically delivers levels of geomagnetic activity. Higher levels will be controlled by both the automated system itself and by human experts, before a warning signal is delivered.

Finally, MADAP is an example of the rapidly growing technologies involved in managing geophysical data. It is centered on three major themes, including World Wide Web (WWW) database access systems and methodologies; development of Graphical User Interface (GUI) based data processing applications; and recovery of pre-digital analog data records (i.e. the eruptive history of the volcano). As databases grow in size and complexity, new capabilities are needed to access the data rapidly and efficiently. New software for faster processing and analyzing magnetic data recorded by monitoring networks was produced. GIS technologies able to analyze results from forward modelling and to manage geological and geophysical data were also included.

Acknowledgments

We are indebted to all personal of Geomagnetism Laboratory of INGV-CT who ensure the regular working of the permanent magnetic network on Etna volcano. The MagWarn system was developed in the frame of the TecnoLab, the laboratory for the technological advance in geophysics organized by DIEES-UNICT and INGV-CT. This research was supported by project EPOT of the Gruppo Nazionale per la Vulcanologia of the INGV.

References

Carrara, A., and Guzzetti, F., Editors (1995). *Geographical Information Systems in Assessing Natural Hazards*. Kluwer Academic Publishers.

Davis, P. M., Jackson, D. D., Searls, C. A. and McPhernon, R. L. (1981). *Detection of tectonomagnetic events using multichannel predictive filtering.* J. Geophys. Res., 86, 1731-1737.

Del Negro, C. and Currenti, G. (2003). *Volcanomagnetic signals associated with the 2001 flank eruption of Mt. Etna (Italy)*. Geophys. Res. Letters., 30 (7), 1357.

Del Negro, C., and Ferrucci, F. (1998). *Magnetic history of a dyke on Mt. Etna*. Geophysical Journal International, 133, 451-458.

Del Negro, C., and Ferrucci, F. (2000). *Volcanomagnetic effects at Vulcano Island (Aeolian archipelago, Italy).* Geophysical Journal International, 140, 83-94.

Del Negro, C., Ferrucci, F., and Napoli R. (1997). *Retrieval of large volcanomagnetic effects observed during the 1981 eruption of Mt. Etna*. Annali di Geofisica, Vol. XL, 2, 547-562.

Del Negro, C., Napoli, R., and Sicali, A. (2002). *Automated system for magnetic monitoring of active volcanoes*. Bull. Volcanol., 64, 94-99.

Emmi, P.C., and Horton, C.A. (1995). *A Monte Carlo simulation of error in a GIS-based assessment of seismic risk.* Int. J. of GIS, 9, No. 4. pp. 447-461.

Jang, J.-S. R., Sun, C.-T., and Mizutani, E. (1997). *Neuro-Fuzzy and Soft Computing*. Prentice Hall.

Poehls, K., A., and Jackson D. D. (1978). *Tectonomagnetic event detection using empirical transfer functions*. J. Geophys. Res., 83, B10, 4933-4940.

Steppe, J. A. (1979). *Reducing noise in tectonomagnetic experiments by linear regression*. J. Geophys. Res., 84, B6, 3063-3067.

Sugeno, M. (1985). *Industrial Application of Fuzzy Control*. Elsevier Science Publishers Co.

Utada, H. M. Neki, and Kagiyama, T. (2000). *A study of annual variations in geomagnetic total intensity with special attention to detecting*

volcanomagnetic signals. Earth Planets Space, 52, 91-103.

Zadeh, L. A. (1965). *Fuzzy Sets*. Information and Control, vol. 8, pp. 338-353.

Zimmermann, H. J. (1996). *Fuzzy Set Theory and Its Applications*. 3rd ed., Kluwer Academic Publishers, Boston, MA.

Zlotnicki J., and Bof, M. (1998). *Volcanomagnetic signals associated with the quasi-continuous activity of the andesitic Merapi volcano, Inodonesia: 1990-1995*. Physics of the Earth and Planetary Interiors, 105, 119-130.

Istituto Nazionale di Geofisica e Vulcanologia
Via di Vigna Murata, 605 - 00143 Roma - Italy
www.ingv.it